September 2009

THERAPEUTIC TESTING AND EPIGENETIC CHARACTERIZATION OF FRIEDREICH ATAXIA

a thesis submitted for the degree of Doctor of Philosophy

by

Ricardo Mouro Pinto

Division of Biosciences
School of Health Sciences and Social Care

Abstract

Friedreich ataxia (FRDA) is an autosomal recessive, neurodegenerative disorder with severely debilitating effects and no current cure. FRDA is mainly caused by the hyper-expansion of a GAA repeat present in intron 1 of the *FXN* gene, which results in decreased gene expression and consequently a deficiency of the mitochondrial protein frataxin. In the first instance, frataxin deficiency renders an impaired protection from oxidative stress.

Antioxidant therapy with cannabinoids (CBD and THC) and CTMIO was investigated in GAA repeat *FXN* YAC transgenic mouse models of FRDA, but no significant improvements were detected on functional measurements such as rotarod performance and locomotor activity. Additionally such compounds failed to protect the brain of treated mice from oxidative insults. Therefore, the use of such antioxidant compounds cannot be advocated for FRDA therapy.

Recent findings indicate that *FXN* silencing in FRDA may be mediated by repressive heterochromatin, suggesting the use of histone deacetylase inhibitors (HDACi) as *FXN* up-regulators. Therefore, therapy with a benzamide-type HDACi (106) was similarly investigated on the *FXN* YAC GAA mouse model. No significant improvements were detected by functional and histochemical analysis. However, significant changes were produced in global acetylation levels of H3 and H4 in the brain of treated mice, suggesting that the drug is capable of crossing the blood-brain barrier and producing an effect. Additionally, significant increases in frataxin expression were detected in the brain of treated mice.

To identify further FRDA disease mechanisms, characterization of the *FXN* gene for the presence of the CCCTC-binding factor (CTCF) was also performed on FRDA patient cerebellum samples. Overall, lower levels of CTCF were detected in FRDA-associated *FXN* alleles, suggesting the potential involvement of CTCF in the regulation of *FXN* transcription.

Acknowledgements

First and foremost I would like to express my total gratitude to Dr Mark Pook for accepting me as his student. He has always been extremely supportive and has provided me with critical help and guidance throughout the last 4 years.

I would also like to address special thanks to Dr Sahar Al-Mahdawi for her invaluable assistance in the lab. Additionally I would like to thank her and all the other members of the ataxia group, Chiru, Ozy, Dhaval, Daniah and Vahid, for creating such lively and always cooperative atmosphere.

It is my very pleasant duty to thank Ataxia UK for providing the financial support. I would also like to acknowledge GW Pharmaceuticals, RepliGen Corporation and Dr Nuri Gueven for kindly making available the cannabinoid extracts, HDACi 106 and CTMIO, respectively.

For the invaluable assistance with the maintenance of the mouse colony I would like to acknowledge Steve, Julie and Sue. I would also like to thank Lorraine Lawrence from Imperial College London for kindly training me in the art of histology and for preparing most of the histological sections. I must also acknowledge Sahar and Daniah for performing expression analysis and histone investigations, and Chiru for his assistance with the functional studies.

I would also like to thank my Mum, my Dad and my Sister, who did not see me much during the last years, for believing in me.

Finally, I would like to address a special “THANK YOU” to Reyna...

...for always being there for me.

Table of contents

List of figures

List of tables

List of abbreviations

106	N^1-(2-aminophenyl)-N^7-*p*-tolylheptanediamide (4b derivative)
4b	N^1-(2-aminophenyl)-N^7-phenylheptanediamide (BML-210 derivative)
AC	adenylate cyclase
AD	Alzheimer disease
ALS	amyotrophic lateral sclerosis
AMV RT	avian myeloblastosis virus reverse transcriptase
APS	ammonium persulfate
A-T	ataxia-telangiectasia
ATP	adenosine triphosphate
BAC	bacterial artificial chromosome
BCA	bicinchoninic acid
BDS	botanical drug substance
BME	β-mercaptoethanol
BML-210	N^1-(2-aminophenyl)-N^8-phenyloctanediamide (SAHA derivative)
BPB	bromophenol blue
BSA	bovine serum albumin
cAMP	cyclic adenosine monophosphate
CBD	cannabidiol
ChB	Church buffer
ChIP	chromatin immunoprecipitation
CoQ	coenzyme Q
CTCF	CCCTC-binding factor
CTMIO	5-carboxy-1,1,3,3-tetramethylisoindolin-2-yloxyl
DEPC	diethyl pyrocarbonate
DMR	differentially methylated region
DMSO	dimethyl sulfoxide
DNA	deoxyribonucleic acid
DNPH	2,4-dinitrophenylhydrazine
dNTP	deoxynucleotide triphosphate
DRG	dorsal root ganglion

DTT	dithiothreitol
EDTA	ethylene diamine-tetra acetic acid
EMSA	electrophoretic mobility shift assay
EtOH	ethanol
FISH	fluorescent in situ hybridisation
FRDA	Friedreich ataxia
GAPDH	glyceraldehyde-3-phosphate dehydrogenase
H&E	haematoxylin and eosin
HAT	histone acetyltransferase
HCM	hypertrophic cardiomyopathy
HD	Huntington disease
HDβB	high-dose beta-blocker
HMTases	histone methyltransferases
HMW	high molecular weight
HP-β-CD	hydroxypropyl-β-cyclodextrin
i.p.	intraperitoneally
IMS	industrial methylated spirit
kb	kilo base
LMW	low molecular weight
mRNA	messenger RNA
MS	multiple sclerosis
NMR	nucleic magnetic resonance
NSE	neuron-specific enolase
OD	optical density
ODN	oligodeoxyribonucleotides
PAGE	polyacrylamide gel electrophoresis
PBS	phosphate-buffered saline
PBS/T	phosphate-buffered saline / Tween-20
PCR	polymerase chain reaction
PD	Parkinson disease
PEG400	polyethylene glycol 400
PNK	polynucleotide kinase

PVDF	polyvinylidene fluoride
Q-PCR	quantitative real-time PCR
Q-RT-PCR	quantitative real-time RT-PCR
rhu-EPO	recombinant human erythropoietin
RNA	ribonucleic acid
RNAP	RNA polymerase
rpm	rotations per minute
RT-PCR	reverse transcriptase PCR
SAHA	suberoylanilide hydroxamic acid
SBHA	suberoyl bis-hydroxamic acid
SDS	sodium dodecyl sulphate
SE	standard error
SP-PCR	small-pool PCR
SSC	salt sodium citrate
TBE	Tris-borate-EDTA
TE	Tris EDTA
TEMED	tetramethylethylenediamine
THC	Δ-9-tetrahydrocannabinol
TNR	trinucleotide repeat
Tris	tris(hydroxymethyl)aminomethane
TRS	trinucleotide/triplet repeat sequence
TSA	trichostatin A
Tween-20	polyoxyethylene-sorbitan monolaurate
Tween-80	polyoxyethylene-sorbitan monooleate
UTR	untranslated region
UV	ultra violet
VPA	valproic acid
WR	working reagent
YAC	yeast artificial chromosome
ZF	zinc finger

Chapter 1 – Friedreich ataxia: literature review

Friedreich ataxia (FRDA) is an inherited autosomal recessive neurodegenerative disorder – OMIM #229300 (OMIM 2006). Being the most common inherited ataxia, it affects approximately 1.8/100,000 individuals in the UK (Schulz *et al.* 2009).

Generally the first symptoms appear in childhood but age of onset may vary from infancy to adulthood (Pandolfo 2002a). Clinical features include progressive limb and gait ataxia, absent lower limb reflexes, extensor plantar responses, dysarthria, and cardiomyopathy. Other common problems include kyphoscoliosis, pes cavus, and, in 10% of patients, diabetes mellitus (Pandolfo 2002b). The main sites of pathology include the dorsal root ganglia (DRG), posterior columns of the spinal cord, corticospinal tracts and cardiac muscle (Durr *et al.* 1996). On average, patients lose the ability to walk 15 years after the onset of symptoms and have a reduced life expectancy. The commonest cause of death is cardiomyopathy (Delatycki *et al.* 2000).

Although the above clinical features certainly identify the typical cases of FRDA, the disease shows a remarkable clinical variability involving age of onset, rate of progression, severity and extent of disease involvement (Montermini *et al.* 1997c).

1.1 – *FXN* gene: structure and expression

The Friedreich ataxia gene (*FXN*) was mapped to chromosome 9 in 1988 (Chamberlain *et al.* 1988) and is localised in the proximal long arm at position 9q13 (Figure 1.1).

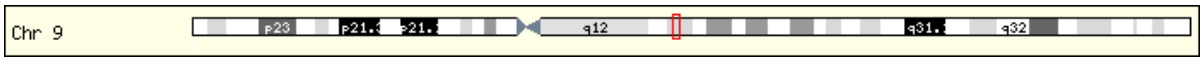

Figure 1.1 – Schematic representation of human chromosome 9. The area in the red box identifies the location of the *FXN* gene as 9q13 (Ensembl 2006).

The *FXN* gene, initially called X25, spans 95 kb of genomic DNA and contains seven exons: 1-5a, 5b and 6 (Campuzano *et al.* 1996) (Figure 1.2). The gene is transcribed in the centromere to telomere direction. The major, and probably only functionally relevant mRNA, has a size of 1.3 kb. This corresponds to the first five exons, 1 to 5a, and encodes a 210 amino acid protein named frataxin (Campuzano *et al.* 1996). By alternative splicing, exon 5b can be transcribed and here a 171 amino acid protein arises. Exon 6 is non-coding (Campuzano *et al.* 1996).

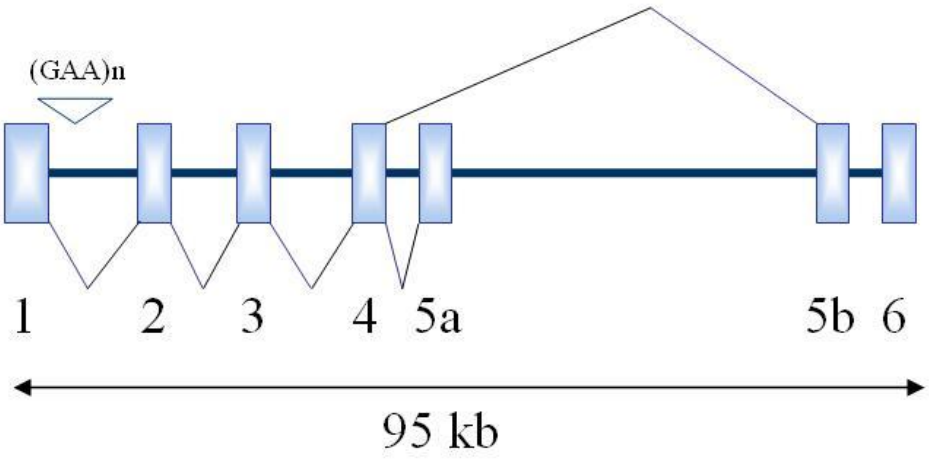

Figure 1.2 – Schematic representation of exons and splicing pattern of the *FXN* gene. The GAA repeat in intron 1 is indicated (▽). Diagram adapted from Cossee *et al.* (1997).

The *FXN* gene is expressed in all cells, but at variable levels in different tissues and during development (Campuzano *et al.* 1996; Koutnikova *et al.* 1997). In adult humans, frataxin mRNA is most abundant in the heart and spinal cord, followed by liver, skeletal muscle, and pancreas. In mouse embryos, the highest levels of frataxin mRNA are found in the spinal cord and in the dorsal root ganglia. The developing brain is also very rich in frataxin mRNA. In the adult mouse brain the level of frataxin mRNA is reduced, but remains high in the spinal cord and dorsal root ganglia. However, protein levels remain high in the adult human and mouse brain and cerebellum (Koutnikova *et al.* 1997).

Frataxin expression is generally higher in mitochondria-rich cells, such as cardiomyocytes and neurons. There is, however, a still unexplained additional cell specificity, which in the nervous system is reflected in a higher abundance of frataxin in specific neuronal types, as primary sensory neurons (Koutnikova *et al.* 1997).

1.1.1 – The GAA triplet repeat mutation

The most common mutation causing FRDA (~95%) is the hyperexpansion of a GAA triplet repeat sequence (TRS) in the first intron of the *FXN* gene (Figure 1.2). Because of the recessive nature of the disease, affected individuals generally have expansions in both alleles of *FXN*, while heterozygous carriers are clinically normal. Occasional patients (~5%) are heterozygous for a GAA expansion and a missense or nonsense point mutation disrupting the frataxin coding sequence (Campuzano *et al.* 1996). No patients have been identified so far that carry point mutations in both copies of the frataxin gene.

Normal alleles contain <30 triplets, and disease-causing expansions (66–1700 triplets) arise via hyperexpansion of premutations (30–65 triplets) (Cossee *et al.* 1997; Montermini *et al.* 1997a). The severity and age of onset of the disease are in part determined by the size of the expanded repeat sequence, in particular of the smaller allele (Pandolfo 2002a).

To date, no other disease has been recognised to be caused by an expansion of GAA·TTC. This is also the most common disease-causing triplet repeat expansion identified so far, with a carrier frequency of 1 in 90 Europeans (Cossee *et al.* 1997).

1.1.2 – Instability of GAA expanded repeats

The FRDA-associated expanded alleles - E alleles - show meiotic (intergenerational) and mitotic (somatic) instability.

Intergenerational instability

When transmitted from parent to child, expansions and contractions of expanded GAA repeats can both be observed (Campuzano *et al.* 1996; Durr *et al.* 1996; Montermini *et al.* 1997c). Expanded alleles are equally likely to further expand or contract during maternal transmission, but most often contract during paternal transmission (Monros *et al.* 1997; Pianese *et al.* 1997), a result also supported by sperm analysis (Pianese *et al.* 1997). Parental age and the intergenerational change in expansion are directly correlated in maternal transmission and inversely in paternal transmission (Kaytor *et al.* 1997; De Michele *et al.* 1998).

Somatic instability is age dependent

Small-pool PCR analysis from tissues of an 18-week fetus homozygous for expanded GAA alleles revealed very low levels of instability compared with adult-derived tissues (4.2% versus 30.6%, $p<0.0011$, Figure 1.3A) (De Biase *et al.* 2007b). Mutation load in blood samples from multiple patients and carriers increased significantly with age, ranging from 7.5% at 18-weeks gestation to 78.7% at 49 years of age ($p=0.0001$, Figure 1.3B). Therefore, somatic instability in FRDA occurs mostly after early embryonic development and progresses throughout life, lending further support to the role of postnatal somatic instability in disease pathogenesis (De Biase *et al.* 2007b).

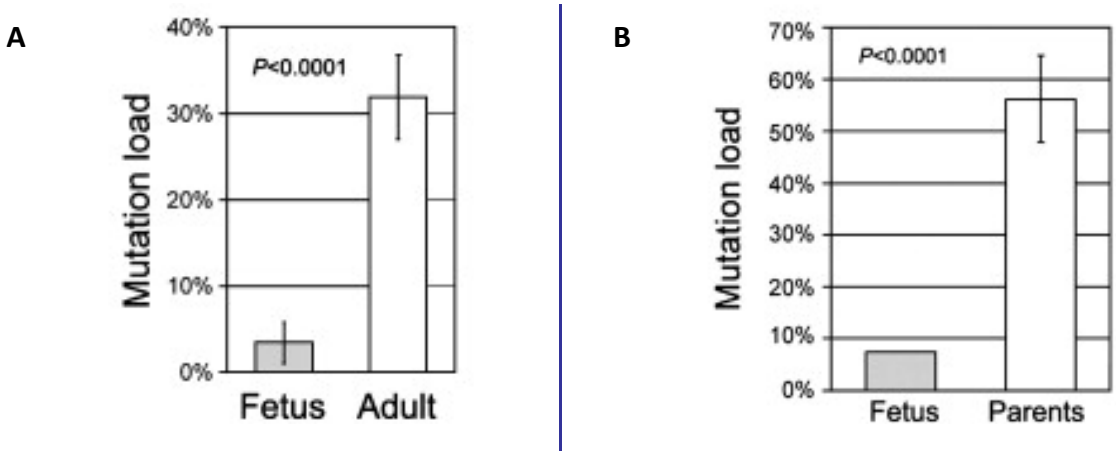

Figure 1.3 – SP-PCR analysis showing differential GAA mutation load in fetus versus adults. (**A**) Mutation load of fetal (18 weeks old) versus adult (24 years old) tissues analyzed by SP-PCR showing a highly significant, 7.3-fold lower level of somatic instability in fetal tissues compared with adult tissues. Error bars depict ±2 SEM. (**B**) Bar graph of mutation load in the blood of fetus versus both parents (combined) showing a highly significant, seven-fold lower level of somatic instability in fetal tissues compared with adult tissues. The error bar depicts ±2 SEM (De Biase *et al.* 2007b).

Somatic instability is tissue dependent

Mitotic instability, leading to somatic mosaicism for expansion sizes, can also be observed in FRDA (Montermini *et al.* 1997c), with a significant predilection for large contractions (Sharma *et al.* 2002). Analysis of GAA expansions reveals ample variations in different cell types or tissues from the same patient. Moreover, heterogeneity among cells occurs at a variable degree in different tissues: whilst cultured fibroblasts and cerebellar cortex show very little heterogeneity in expansion sizes among cells, lymphocytes are more heterogeneous, and most brain regions show a quite complex pattern of allele sizes, indicating extensive cellular heterogeneity (Montermini *et al.* 1997b).

Recently, SP-PCR was used to analyze somatic instability of the expanded GAA triplet-repeat sequence in multiple tissues obtained from six autopsies of FRDA patients (De Biase *et al.* 2007a), showing that DRGs had a significantly greater frequency of large expansions and a relative paucity of large contractions compared with all other tissues (Figure 1.4).

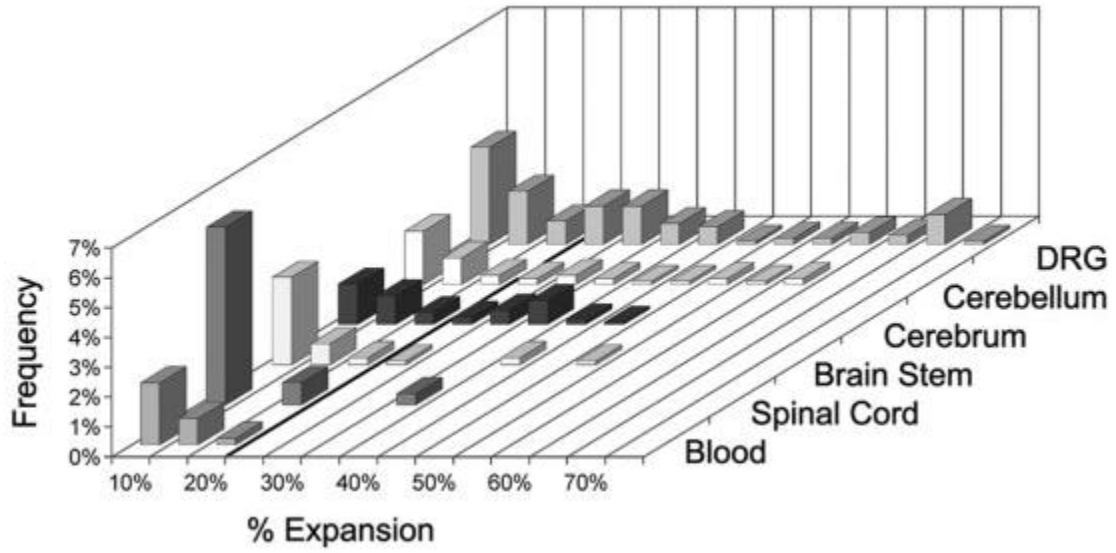

Figure 1.4 – SP-PCR analysis showing greater prevalence of large expansions in DRG Frequency distribution (plotted on the y-axis) of expansions (magnitude plotted on the x-axis as increase in size [%] over the constitutional allele) seen in various tissues from a FRDA patient ($GAA_{950/950}$). All data points to the right of the bold line, plotted at 20%, represent large expansions (De Biase *et al.* 2007a).

While some of these differences could be accounted for by a major period of instability during the first weeks of embryonic development, GAA expanded repeats seem to be inherently more stable in some cell types. Therefore, determining the size of a patient's expansion in peripheral blood lymphocytes, from which DNA is usually obtained, only provides a single sample of the overall repeat size distribution occurring within the patient, and consequently only an approximate estimate of expansion sizes in affected tissues (Pandolfo 2002b).

1.1.3 – Mechanism of expansion of the GAA repeat

Although various mechanisms for trinucleotide repeat instability are under debate, a common theme is that the triplet is able to form stable non-*B*-DNA structures (LeProust *et al.* 2000). Recent evidence proposes that triplet repeat instability specific to GAA·TTC results from strand displacement during DNA replication together with hairpin formation (Figure 1.5), leading to reiterative synthesis and expansion/contraction (Heidenfelder *et al.* 2003). The discontinuous nature of lagging strand replication is characterized by the presence of single-stranded regions in the template and free 5'-ends in the growing strand (Okazaki fragment). The template single-stranded DNA presents the opportunity for formation of secondary structures such as hairpins. Lagging strand replication is predicted to lead to contractions by replication across hairpins formed in the template strand and expansion by DNA slippage to give hairpin formation in the Okazaki fragment (Heidenfelder *et al.* 2003).

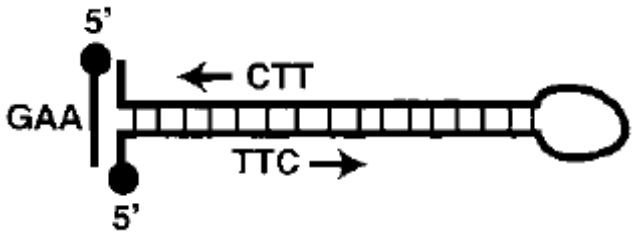

Figure 1.5 – Representation of GAA·TTC secondary structure: hairpin formation (Heidenfelder *et al.* 2003).

1.1.4 – *FXN* becomes truncated at the transcriptional level

FRDA is the consequence of frataxin deficiency. It has been shown that the reduced *FXN* mRNA and frataxin levels are the result of inhibition of transcription and not at the level of post-transcriptional RNA processing (Delatycki *et al.* 2000). The current explanation for this phenomenon is that long GAA repeats adopt a specific secondary structure that impedes transcription. To date, two secondary structures have been associated with expanded GAA tracts: triplexes and sticky DNA (Figure 1.6).

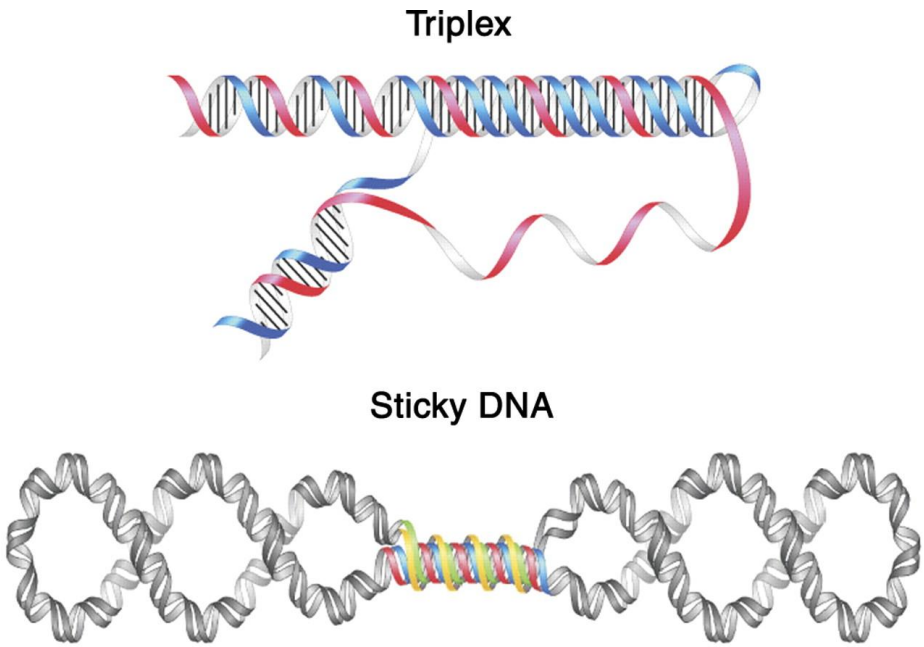

Figure 1.6 – Models of an intramolecular DNA triplex and a sticky DNA structure in a closed circular plasmid (Wells 2008).

Triplex formation

The GAA·TTC tract is a purine·pyrimidine (or R·Y) polymer and may adopt a number of unusual nucleic acid structures, including triple helices – triplexes (Frank-Kamenetskii and Mirkin 1995). Triplexes in general may take the form R·R·Y or Y·R·Y, depending on whether the third strand is purine-rich or pyrimidine-rich, and can be formed as intermolecular structures or as folded intramolecular structures (Figure 1.7) (Grabczyk and Usdin 2000b).

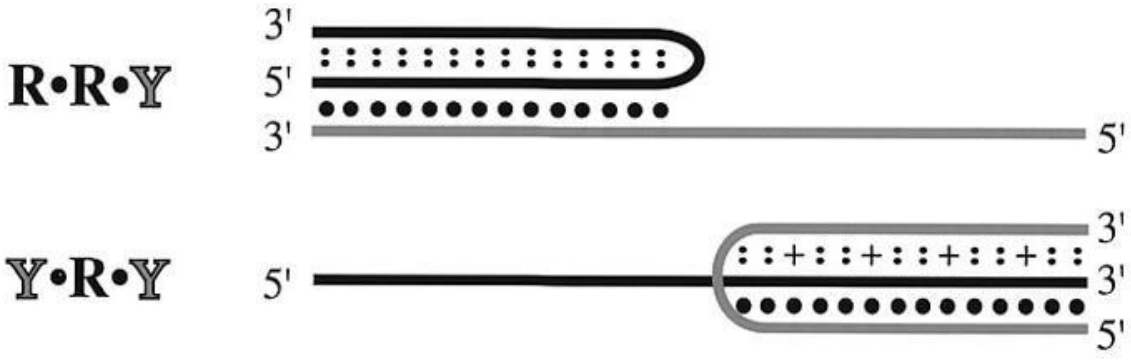

Figure 1.7 – Schematic representation of intramolecular R·R·Y and Y·R·Y triplexes. The purine (R) strand is black; the pyrimidine (Y) strand is grey. The single black dots indicate normal Watson–Crick base pairs and the smaller double dots indicate alternative hydrogen bonding interactions that are pH independent. Hoogsteen base pairs involving a protonated cytosine are indicated with a plus sign (Grabczyk and Usdin 2000b).

Although the actual molecular mechanism by which the GAA·TTC repeat tract expansion reduces frataxin mRNA levels is still unknown, models based on different triplex variants have been suggested to explain the effects of GAA·TTC tract expansion as a possible block to transcription elongation in *FXN* (Sakamoto *et al.* 1999; Grabczyk and Usdin 2000b).

One mechanism proposed is that a transient R·R·Y intramolecular triplex forms behind the RNA polymerase (RNAP) during transcription of a long GAA·TTC tract, trapping the polymerase (Grabczyk and Usdin 2000b) as illustrated in Figure 1.8. The movement of RNA polymerase along the template locally unpairs the DNA duplex and generates a wave of

negative supercoiling in its wake (Figure 1.8A). This creates conditions favourable for triplex formation. At the transcription bubble the polymerase covers the Y (TTC) template strand but the single-stranded portion of the GAA non-template strand is available to initiate triplex formation, promoting formation of the R·R·Y structure. The initial folding may be analogous to the formation of the folded R·R·Y structure by an oligodeoxy-ribonucleotide (Figure 1.7). The spread of triplex formation (Figure 1.8B) is driven by the release of the standing wave of negative superhelical energy that had formed behind the polymerase. It has been suggested that the polymerase has trouble negotiating the junction between the triplex and the duplex in the distal end of the repeat tract (indicated by the black arrow in Figure 1.8C), resulting in a transcript truncated at the 3' end of the structure (Grabczyk and Usdin 2000b).

In addition, recent evidence suggests that the transcription of the *FXN* GAA·TTC repeat sequence results in the formation of a persistent RNA·DNA hybrid (Grabczyk *et al.* 2007). During *in vitro* transcription of longer repeats, T7 RNA polymerase arrested in the promoter distal end of the GAA·TTC tracts and an extensive RNA·DNA hybrid was tightly linked to this arrest (Figure 1.8D). The authors (Grabczyk *et al.* 2007) propose that, initially, the repeating DNA d(TTC)$_n$ strand serves as the template for synthesis of r(GAA)$_n$ to form a moderate length of DNA·RNA hybrid. Due to the stability of this hybrid, the DNA triplex is dislodged behind the growing transcription complex to give an even longer RNA·DNA hybrid. The waves of negative supercoiling behind the translocating RNA polymerase facilitate these processes from a topological standpoint. In summary, this model advocates that *FXN* transcription seems to be truncated in FRDA as a consequence of the formation of a quasi-stable DNA triplex and a DNA·RNA hybrid, generating a pause site at the TRS (Grabczyk *et al.* 2007).

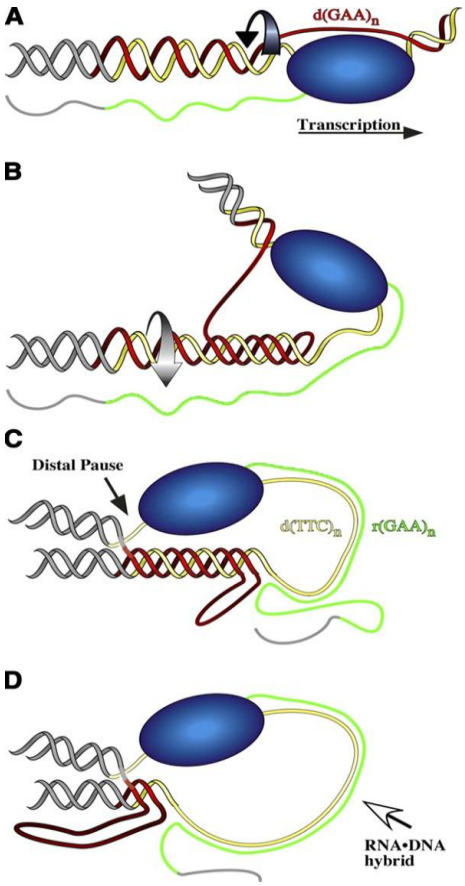

Figure 1.8 – Model for transient transcription-dependent triplex formation leading to an RNA polymerase pause and RNA·DNA hybrid formation (Grabczyk *et al.* 2007). The purine (GAA or R) strand of the repeat is red, the pyrimidine (TTC or Y) strand is yellow, and the flanking DNA is gray. (**A**) A standing wave of negative supercoiling follows RNA polymerase. At the transcription bubble, the nontemplate (GAA) strand is available to fold back in an R·R·Y interaction; the template strand is covered by RNA polymerase. (**B**) Rotation of the helix (curved arrow) as it winds in the third strand relaxes the negative supercoils caused by transcription and leaves a length of the template single-stranded. (**C**) RNAP is impeded at the distal template-triplex junction and the nascent transcript (green) can anneal to the single-stranded stretch of template. (**D**) The RNA·DNA hybrid displaces the much less stable triplex structure.

Sticky DNA

Another proposed mechanism is based on the finding that a new type of DNA structure, that implies intramolecular triplex formation, is adopted by lengths of GAA·TTC. This structure was called "sticky DNA" and is formed by the association of two R·R·Y triplexes (Sakamoto *et al.* 1999) (Figure 1.9). Correlation was found between the lengths of GAA·TTC and the formation of this novel conformation: FRDA patients have 66 or more repeats, sticky DNA was found only for repeats longer than 59 units (Sakamoto *et al.* 1999). The proposed molecular mechanism of transcriptional inhibition by sticky DNA is a sequestration of the RNAP by direct binding to the complex DNA structure (Pandolfo 2002b).

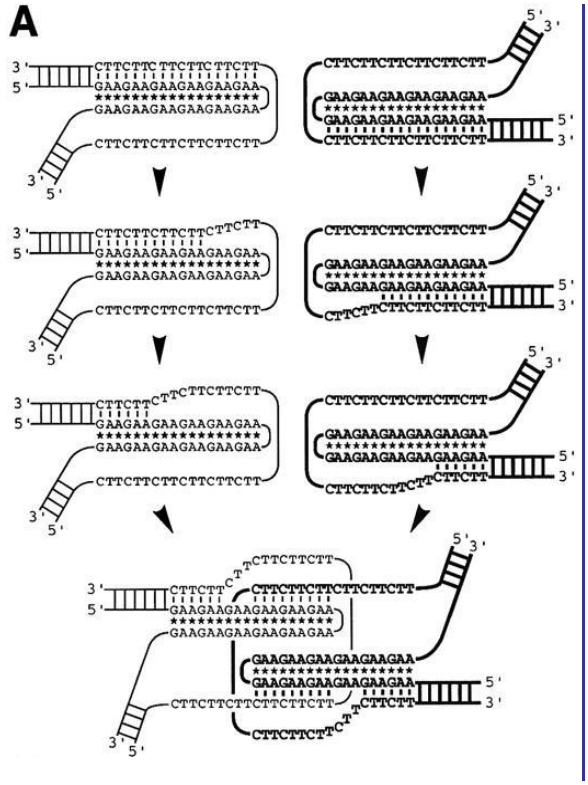

Figure 1.9 – A Model of the association of two triplexes formed by long GAA·TTC tracts. (**A**) Schematic picture of the strand exchange model. The two triplexes are represented as thin and thick lines. The short vertical lines between the bases represent Watson-Crick pairs, and the stars represent the reversed Hoogsteen base pairs. (**B**) Three-dimensional picture of the strand exchange model. Different colours represent different strands. In the left molecule, blue shows the purine strand, while yellow shows the pyrimidine strand. In the right molecule, green shows the purine strand and red shows the pyrimidine strand (Sakamoto *et al.* 1999).

It has been suggested that interruption in the GAA·TTC sequence may destabilize sticky DNA structure and facilitate transcription: a systematic analysis of the effects of introducing interruptions into a $(GAA{\cdot}TTC)_{150}$ repeat by substituting an increasing number of As with Gs has confirmed that the sticky DNA/triplex structure is progressively destabilised and it fails to form when the sequence becomes $(GAAGGA{\cdot}TCCTTC)_{75}$ (Ohshima *et al.* 1999). As the tendency to form a sticky DNA/triplex structure decreases, less and less inhibition of transcription is observed *in vivo* and *in vitro* (Ohshima *et al.* 1999).

Heterochromatin mediated silencing

In contrast to the DNA structure-based mechanism for gene silencing by long GAA·TTC repeats, a study employing artificial transgenes for the lymphoid cell surface marker protein hCD2 has shown that expanded GAA·TTC repeats induce repressive heterochromatin *in vivo*, in a manner reminiscent of position effect variegated (PEV) gene silencing (Saveliev *et al.* 2003).

Recent studies have confirmed that FRDA may be caused by a heterochromatin-mediated gene silencing of *FXN* (Figure 1.10), characterised by a differential DNA methylation profile accompanied by histone acetylation/methylation changes (Herman *et al.* 2006; Greene *et al.* 2007; Al-Mahdawi *et al.* 2008).

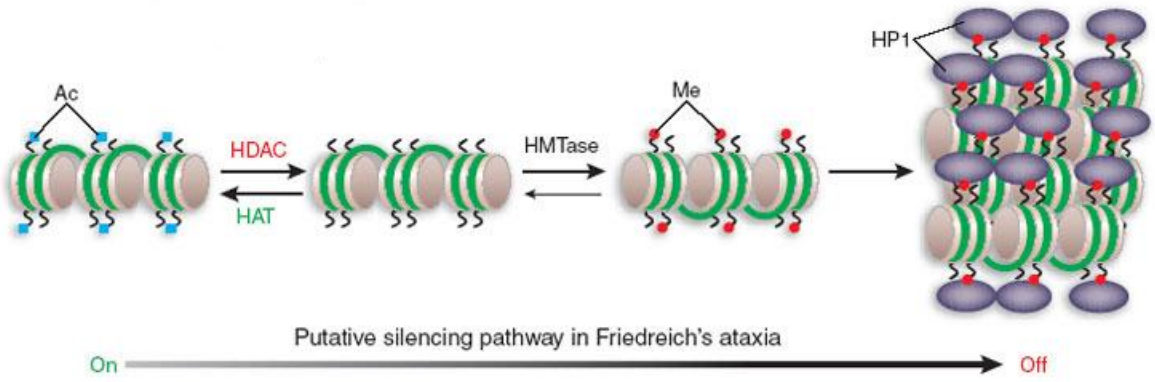

Figure 1.10 – Putative heterochromatin-mediated silencing pathway in FRDA. The chromatin organization of an active *FXN* gene is shown on the far left. Protruding from the nucleosomes are acetylated histone tails (Ac, acetyl). The presence of GAA repeats might nucleate heterochromatin formation, pushing the pathway to the right through several stages. An early step in this process may be the deacetylation of the lysines on histones, which would provide a substrate for histone methyltransferases (HMTases). Methylation of the histone H3 tail (on Lys9) would provide a binding site for HP1, consistent with a histone code for silencing. If the nucleosomes were sufficiently close (possibly because of the repetitive nature of the DNA), then HP1 dimers might stabilize a condensed higher-order heterochromatin structure that prohibits access of the transcriptional machinery to the *FXN* locus (Festenstein 2006).

DNA methylation changes

Bisulfite sequence analysis of the *FXN* flanking GAA regions in FRDA patient brain, cerebellum and heart tissues, reveals a shift in the FRDA DNA methylation profile, with upstream CpG sites becoming consistently hypermethylated and downstream CpG sites hypomethylated. Differential DNA methylation at three specific CpG sites within the *FXN* promoter and one CpG site within exon 1 were also identified (Figure 1.11) (Al-Mahdawi *et al.* 2008).

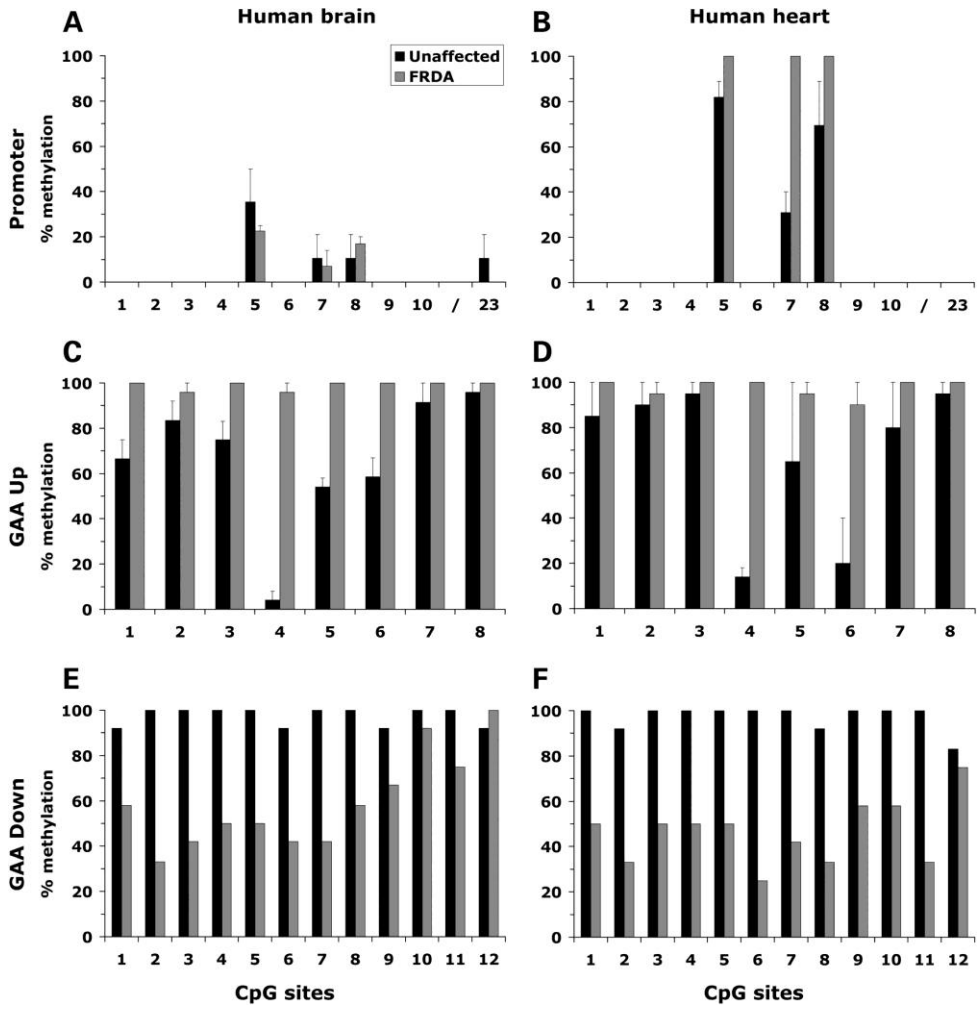

Figure 1.11 – DNA methylation analysis of the *FXN* promoter (**A** and **B**), upstream GAA (**C** and **D**) and downstream GAA (**E** and **F**) regions of human brain and heart tissues. In each case the mean percentage (+SEM) of methylated CpG sites is shown as determined by bisulfite sequencing (Al-Mahdawi *et al.* 2008).

Histone modifications

Heterochromatin hallmarks such as reduced levels of histone H3 and H4 acetylation, accompanied by increased H3K9 trimethylation, are particularly noticeable in FRDA immediately upstream and downstream of the expanded GAA repeat tract (Figure 1.12) (Herman *et al.* 2006; Al-Mahdawi *et al.* 2008).

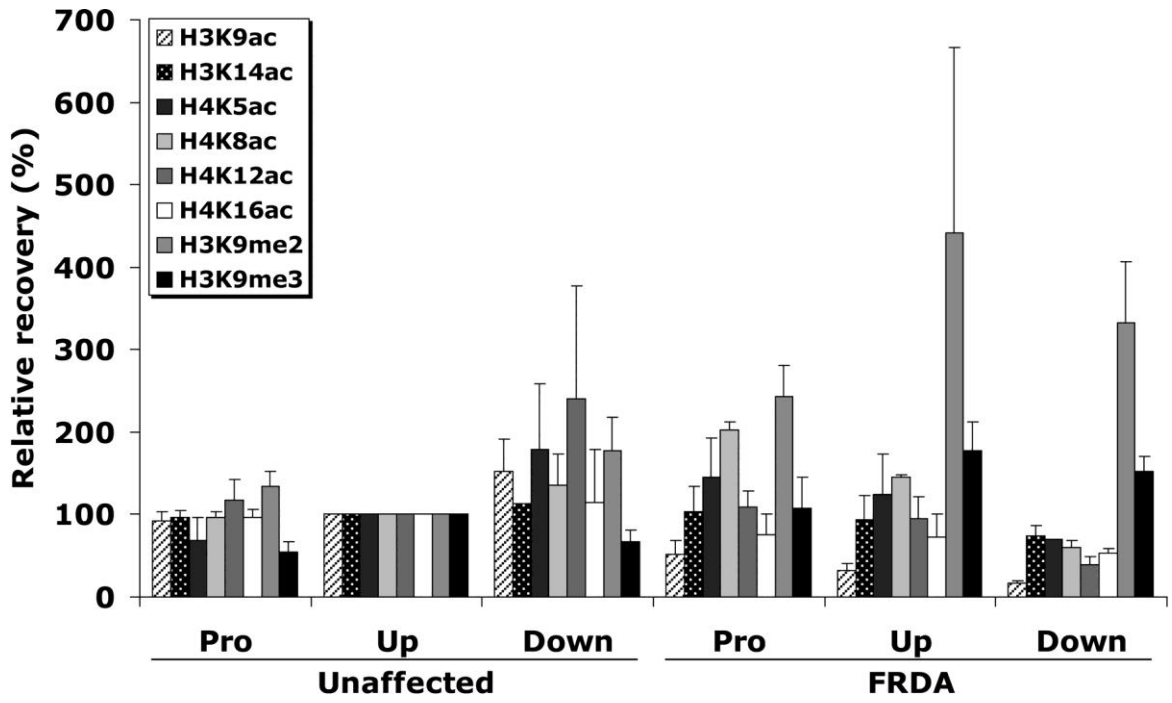

Figure 1.12 – Analysis of histone modifications in human brain tissue. ChIP Q-PCR results for the *FXN* promoter/exon1 (Pro), upstream GAA (Up) and downstream GAA (Down) amplified regions are represented as the relative amount of immunoprecipitated DNA compared with input DNA, having taken negligible –Ab control values into account. *FXN* values were normalized with human *GAPDH* and all values have been adjusted so that all of the upstream GAA mean values from the unaffected individuals are 100%. In each case two individual ChIP samples from two FRDA patients and two unaffected controls were analysed in triplicate. The means and SEMs of these values are shown (Al-Mahdawi *et al.* 2008).

Similarly, it was shown that long intronic GAA·TTC repeats (560) induce comparable epigenetic changes (hypoacetylation and hypermethylation of histones in the vicinity of the repeats) and reporter gene silencing in a molecular model of FRDA (Soragni *et al.* 2008).

1.1.5 – Genotype/phenotype correlation

As expected by the experimental finding that smaller expansions allow a higher residual frataxin gene expression (Campuzano *et al.* 1997), probably because they form less stable triplexes and sticky DNA, expansion sizes have an influence on the severity of the phenotype. A direct correlation has been firmly established between the size of GAA repeats and earlier age of onset, earlier age when confined in wheelchair, more rapid rate of disease progression, and presence of non-obligatory disease manifestations indicative of more widespread degeneration (Durr *et al.* 1996; Filla *et al.* 1996; Monros *et al.* 1997; Montermini *et al.* 1997c). However, differences in GAA expansions account for only about 50% of the variability in age of onset, indicating that other factors influence the phenotype (Pandolfo 2002a). These may include somatic mosaicism for expansion sizes, possibly variation in the triplet repeat sequence, modifier genes and environmental factors.

1.2 – Frataxin: structure and function

Mature frataxin is a compact, globular protein containing an N-terminal α helix, a middle β sheet region composed of seven β strands, a second α helix, and a C-terminal coil (Musco *et al.* 2000) (Figure 1.13). The α helices are folded upon the β sheet, with the C-terminal coil filling a groove between the two α helices. The size and nature of the conserved surface regions suggest that they interact with a large ligand, probably a protein. However, experiments aimed to identify a protein partner of frataxin, mostly by using the yeast two-hybrid method, have so far failed (Pandolfo 2002b). A possibility is that the surface is necessary for frataxin oligo- and multimerization, or that interaction with other proteins only occurs when frataxin has oligomerized. This is particularly relevant in the light of the proposed ability of frataxin to form high molecular weight complexes with iron (Cavadini *et al.* 2002). Frataxin monomers do not have any feature resembling known iron-binding sites. However, the negatively charged ridge confers some resemblance to a unique bacterial ferritin in which an iron-binding pouch is formed by two adjoining subunits, so structural studies are compatible with iron-binding by frataxin oligo- or multimers (Corsi *et al.* 2002).

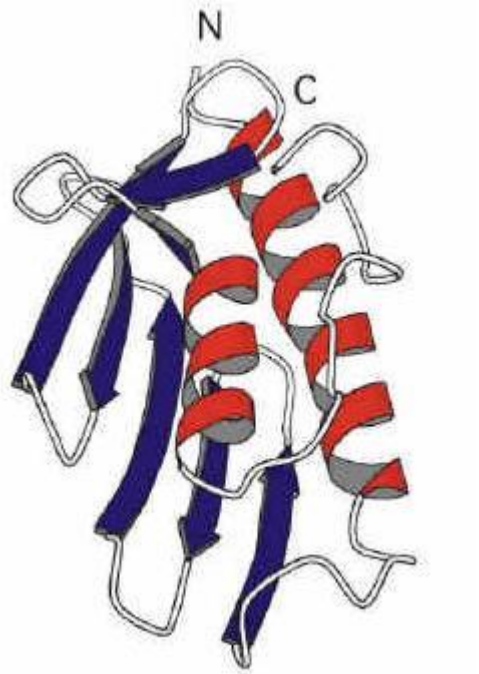

Figure 1.13 – Ribbon representation of the solution structure of the C-terminal domain of frataxin (Musco *et al.* 2000).

1.2.1 – Frataxin is a mitochondrial protein

Frataxin does not resemble any protein of known function. However, the lack of any patients homozygous for a null mutation, and the early embryonic lethality displayed by mice containing a knockout of the murine *FXN* homologue (*Fxn*) (Cossee *et al.* 2000), suggest that frataxin is essential for life. Its aminoacid sequence predicts a small soluble protein with no transmembrane domain. It is highly conserved during evolution (Campuzano *et al.* 1996), with homologs in mammals, invertebrates, yeast and plants. The protein is targeted to the mitochondrial matrix (Branda *et al.* 1999a) (Figure 1.14).

Frataxin has an N-terminal mitochondrial targeting sequence, which is proteolytically removed by the mitochondrial processing peptidase (MPP) after the protein is imported into mitochondria. Recent evidence suggests that mature human frataxin is encoded by amino acids 81–210 (m_{81}-*FXN*) (Schmucker *et al.* 2008).

1.2.2 – FRDA pathogenesis

Reduced levels of frataxin result in mitochondrial dysfunction. Studies incorporating FRDA patients, conditional knockout mouse models, and yeast mutants containing a disruption of the *FXN* homologue, YHF1, have shown intramitochondrial iron accumulation, oxidative stress, and reduced activity of iron-sulphur (FeS) cluster-containing subunits of the mitochondrial electron transport chain (ETC) (complexes I–III) and of aconitase (Koutnikova *et al.* 1997; Cavadini *et al.* 2000; Puccio *et al.* 2001). The exact physiological function of frataxin is unknown but it may be involved in mitochondrial iron homeostasis and/or the assembly of FeS proteins (Bradley *et al.* 2000) (Figure 1.14 & Figure 1.15).

While the exact mechanism by which frataxin is involved in mitochondrial iron homeostasis is unknown, investigation of the yeast frataxin homologue indicates that the protein is involved in iron efflux from mitochondria (Radisky *et al.* 1999). Recent evidence has shown that yeast frataxin homologue (Yfh1p) interacts with mitochondrial intermediate peptidase (MIP), a metalloprotease required for maturation of ferrochelatase and other iron using proteins (Branda *et al.* 1999b). When there is diminished Yfh1p, there is activation of MIP leading to mitochondrial iron uptake (Branda *et al.* 1999b). Thus it appears that Yfh1p regulates mitochondrial iron directly at the level of iron efflux and indirectly through regulation of YMIP activity (Figure 1.16).

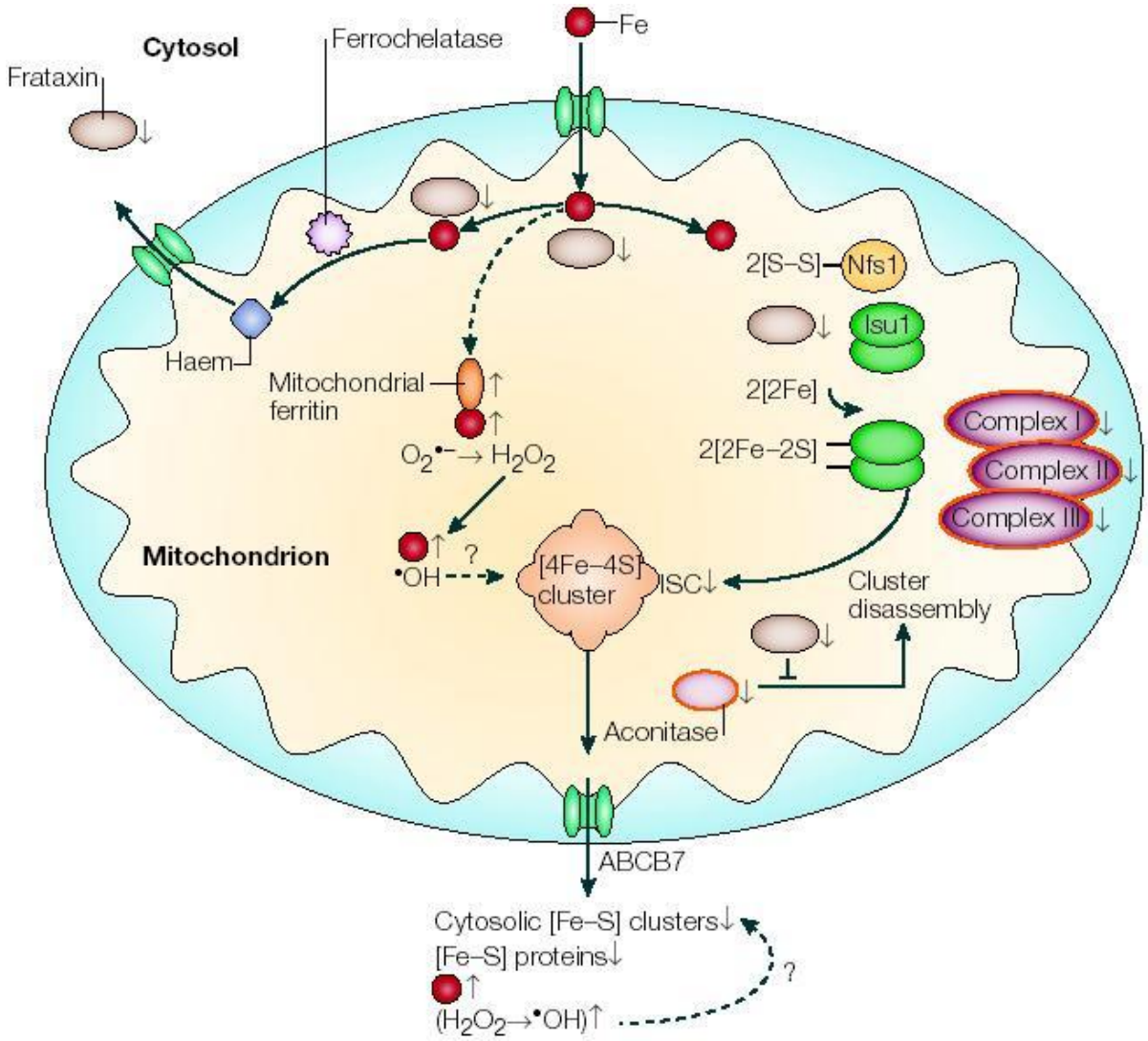

Figure 1.14 – Alterations in mitochondrial biochemistry associated with reduced frataxin levels in FRDA. Frataxin is a highly conserved nuclear-encoded mitochondrial protein for which specific functions are unknown. The proposed roles include as an iron-binding protein (carrying out a function as a mitochondrial ferritin); the protection and synthesis of FeS clusters; in haem metabolism as a binding partner for ferrochelatase; or as a metabolic switch between haem metabolism and FeS cluster synthesis. In FRDA, when frataxin levels are low, FeS cluster containing proteins, such as respiratory transport complexes I–III and aconitase, are reduced. Cytoplasmic proteins that contain FeS clusters can also be affected. The accumulation of iron in the mitochondria leads to free-radical generation; this could feedback to further decrease the levels of FeS clusters, which are sensitive to the oxidative state. ABCB7, ATP-binding cassette, sub-family B, member 7 (ABC transporter 7 protein); ISC, iron–sulphur cluster (Gatchel and Zoghbi 2005).

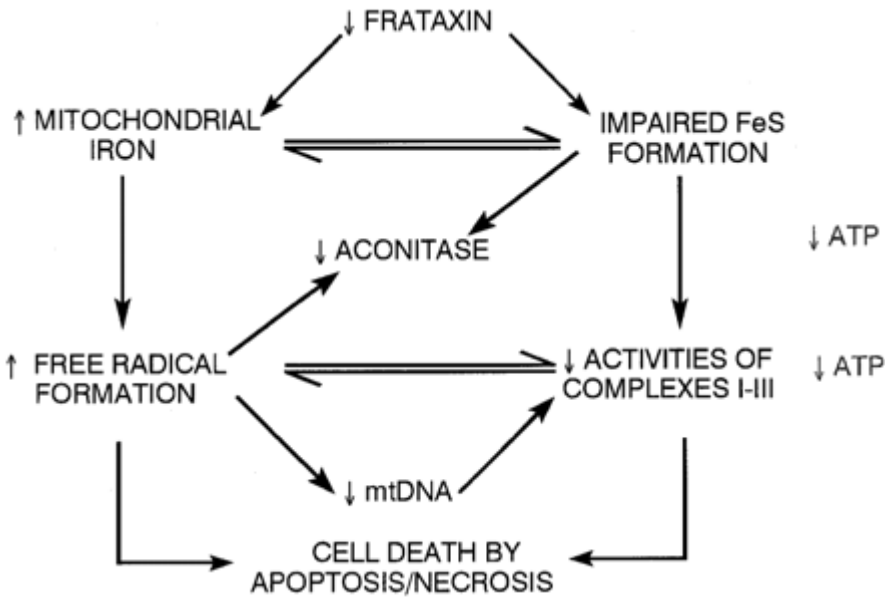

Figure 1.15 – Schematic representation of the proposed events leading to cell death in FRDA. The precise sequence of events in FRDA pathogenesis is uncertain. It is suggested that impaired intramitochondrial iron metabolism results in defective Fe-S formation resulting in decreased complex I–III and mitochondrial aconitase activities and iron overload. Increased free iron levels and a defective mitochondrial respiratory chain will result in increased free radical generation, which will cause oxidative damage including further inhibition of aconitase activity. Impaired respiratory chain activity and decreased aconitase activity will impair ATP synthesis, which, together with oxidative damage to cellular components, will compromise cell viability (Bradley *et al.* 2000).

It has been suggested that excess mitochondrial iron catalyses the production of hydroxyl radicals ($OH^{\bullet}$) by Fenton chemistry. The Fenton reaction is:

$Fe^{2+} + H_2O_2 \rightarrow Fe^{3+} + OH^- + OH^{\bullet}$ (Delatycki *et al.* 2000).

$OH^{\bullet}$ is known to be highly toxic to cells leading to inactivation of FeS enzymes, lipid peroxidation and damage to nucleic acids and proteins, ultimately resulting in cell death (Pandolfo 1999). However, studies with conditional knockout mouse models indicate that deficiencies in FeS enzymes occur prior to iron accumulation within the mitochondria (Puccio *et al.* 2001). Recently, it has also been suggested that mitochondrial iron accumulation does not induce oxidative stress (Seznec *et al.* 2005). Nonetheless, ultimately there remains some

uncertainty as to whether mitochondrial iron accumulation is the result or the cause of the oxidative stress responsible for mitochondrial damage.

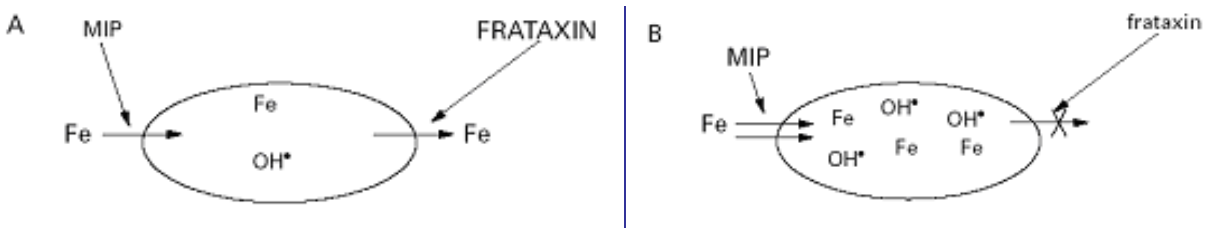

Figure 1.16 – Schematic representation of the likely pathogenesis of FRDA. (**A**) The normal situation in the mitochondrion is shown with iron influx and efflux maintaining low mitochondrial iron (Fe) and free radical ($OH^{\bullet}$) levels. Frataxin is likely to be acting directly at the level of iron efflux. Yeast data suggest that frataxin may also be indirectly limiting the influx of iron into mitochondria by reducing mitochondrial intermediate peptidase (MIP) activity. (**B**) The situation believed to exist in FRDA. Reduced frataxin results in inhibition of the efflux of mitochondrial iron. This leads to reduced cytosolic iron, which results in induction of iron uptake systems and this in turn results in further iron uptake into mitochondria. The increased iron uptake may be in part the result of overactivity of MIP owing to the absence of frataxin. The excess mitochondrial iron leads to excess production of toxic free radicals leading to cell damage and death (Delatycki *et al.* 2000).

Another question that arises is why some tissues are affected in FRDA and not others. Part of the explanation relates to frataxin expression. Additionally, different tissues have different sensitivity to oxidative stress and may use different ways of dealing with that stress (Fridovich 1995). Thus the organ specificity of pathology in FRDA may be explained by the combination of different expression patterns of frataxin and different requirements for frataxin in dealing with ATP production, mitochondrial iron and oxidative stress.

1.3 – Therapeutic approaches

There is currently no effective treatment for FRDA. However, the growing understanding of the role of frataxin and the disease pathogenesis has led to the consideration of four primary potential therapeutic targets (Table 1.1).

Table 1.1 – Identification of the major signs of FRDA pathogenesis and respective suggestion of potential therapeutic strategy.

Target		Potential Therapeutic Strategy
↓ frataxin		Increase of frataxin levels
↑ intramitochondrial iron accumulation		Removal of excess mitochondrial iron
↑ free radical formation		Protection from oxidative stress
↓ mitochondrial ETC activity ↓ aconitase activity	↓ ATP	Decrease of ATP demand

1.3.1 – Removal of excess mitochondrial iron

The removal of excess iron accumulated in the mitochondria should resolve the issues concerning the formation of free radicals. However, the use of iron chelators such as desferrioxamine (DFO), the major chelator in widespread clinical use, has proven to be problematic since it lacks the property to specifically enter and target mitochondrial iron pools (Richardson 2003), suggesting that DFO would cause severe generalised iron deficiency before it could reduce mitochondrial iron levels. Curiously, a recent study reports that when cytosolic iron is chelated by DFO treatment, frataxin mRNA and protein levels decrease, further compromising cellular function (Li *et al.* 2008).

Nevertheless, there is ongoing research into the development of iron chelators, namely the 2-pyridylcarboxaldehyde isonicotinoyl hydrazone (PCIH) analogues, as agents to

specifically remove intramitochondrial iron deposits (Richardson *et al.* 2001; Richardson 2003).

On a contrary note, a recent study challenges current concepts favouring the use of mitochondrion-specific iron chelators (Sturm *et al.* 2005a). According to this study, in FRDA patient lymphoblast and fibroblast cells the concentration of intramitochondrial chelatable iron is not increased, despite a profound reduction in the mitochondrial frataxin content, suggesting that frataxin deficiency does not affect the mitochondrial labile (chelatable) iron pool (Sturm *et al.* 2005a).

1.3.2 – Protection from oxidative stress

Taking into account the difficulties associated with the removal of intramitochondrial iron, the use of antioxidant agents to protect from increased oxidative stress has been suggested as an alternative. Initial clinical trials utilising antioxidants such as coenzyme Q_{10} (CoQ_{10}) and idebenone (CoQ_{10} short-chain synthetic analogue), a potent free radical scavenger, have shown some promise (Rustin *et al.* 1999; Lodi *et al.* 2001a).

Idebenone has been shown to rescue respiratory chain complex II activity, decreased by ferrous iron in heart homogenate. Consequently, the treatment of three patients with FRDA and left ventricular hypertrophy (LVH) with idebenone 5mg/kg/day for 4 to 9 months was accompanied by substantial decreases in interventricular septum (IVS) and left ventricular posterior wall thickness, as well as in left ventricular mass (LVM) index (Rustin *et al.* 1999). However, there was no clear benefit for neurologic findings (Rustin *et al.* 1999). Similar results were confirmed on 38 patients, treated with the same dosage in a 6-month open-label trial. A 20% decrease of the LVM was observed in about half of the patients with no serious side effects reported (Hausse *et al.* 2002). Complementarily, idebenone

treatment has also resulted in decreased levels of urinary 8-hydroxy-2'-deoxyguanosine, which is a peripheral marker of oxidative DNA damage (Schulz *et al.* 2000).

Recently, two studies have been reported where the idebenone treatment has been applied for a 1-year period (Buyse *et al.* 2003; Mariotti *et al.* 2003). Mariotti *et al.* report on a randomized, placebo-controlled, double-blind trial to evaluate the efficacy of 5mg/kg idebenone in 29 patients with FRDA (Mariotti *et al.* 2003). A significant reduction of IVS thickness and LVM was found in the idebenone group as compared with the placebo group. This study confirms that idebenone has an effect on echocardiographic measures of LVH. On the other hand, the differences found in IVS and LVM between treated and nontreated patients are small and of uncertain clinical significance. In addition, no evidence that cardiac function improved under treatment was reported. Buyse *et al.* (2003) reported the effect of 5mg/kg/day idebenone in 8 patients in an open-label trial. The study confirmed a decreased LVM index in FRDA patients with LVH and also showed improvement of functional measures (Buyse *et al.* 2003).

These two studies are complementary in showing that whereas idebenone may modestly reduce LVH in FRDA, it has no effect on the progression of ataxia. These studies also raise several important questions. Do they indicate that antioxidants such as idebenone and related agents are likely to reverse the metabolic dysfunctions induced by frataxin deficiency? Is the modest reduction in LVH a signal that idebenone exerts a useful effect on the heart? Does it suggest that idebenone (or a related agent) at higher dosage or for a longer treatment period may stop the progression of neurologic dysfunction in FRDA? Answers to these questions are needed before the use of idebenone can be recommended in the treatment of FRDA patients. Further basic science investigation and additional

controlled clinical trials are needed to establish both the safety and the possible efficacy of idebenone in FRDA.

Mitoquinone (MitoQ) is an antioxidant selectively targeted to mitochondria (Voncken *et al.* 2004). Its ability to move across biological membranes leads to a 100- to a 500-fold accumulation in mitochondria and a 5- to 10-fold accumulation inside the cell, and its antioxidant effects take place by preventing lipid peroxidation and regeneration of vitamin E (Voncken *et al.* 2004). MitoQ was shown to be 800 times more potent than idebenone in protecting FRDA fibroblasts from death due to endogenous oxidative stress generated by inhibition of glutathione synthesis (Jauslin *et al.* 2003).

Recently, the long-term efficacy of a combined antioxidant and mitochondrial enhancement therapy in 10 FRDA patients was reported (Hart *et al.* 2005). This combined therapy of CoQ_{10} and vitamin E caused a prolonged improvement in cardiac and skeletal muscle bioenergetics clearly demonstrating its biochemical efficacy (Hart *et al.* 2005). Heart function, assessed by fraction shortening, significantly improved after 35 and 47 months and, when compared with cross-sectional data, the International Co-operative Ataxia Rating Scale (ICARS) and kinetic clinical scores were improved in 7 of 10 patients. However, the posture and gait scores and hand dexterity scores continued to deteriorate (Hart *et al.* 2005). Therefore, a larger randomized trial focusing on the response to such a therapy of both neurological and cardiological symptoms is required to confirm whether an early diagnosis of FRDA can be exploited to initiate antioxidant treatment and prevent the progression of this disorder.

In summary, thus far, therapeutic studies with antioxidants have shown a limited effect on the progression and pathology of FRDA, and this is probably because these agents cannot reach the primary sites of neuronal pathology and/or because they cannot remove

the iron accumulation. Taking the later matter into consideration, the use of bifunctional drugs targeting oxidative stress and iron chelation was suggested as an approach to neuroprotection in Parkinson's and other neurodegenerative diseases (Youdim *et al.* 2004).

1.3.3 – Decrease ATP demand

The involvement of mitochondrial respiratory chain dysfunction in FRDA pathogenesis has also been considered as a potential target for FRDA therapy. Decreased levels of frataxin lead to a mitochondrial ATP deficiency in tissues with high energy dependency, such as the heart (Lodi *et al.* 2001b). It has also been reported that cardiac hypertrophy is a compensatory phenomenon in response to the metabolic deficit rather than a direct consequence of mutations (Marian and Roberts 1995). Familial hypertrophic cardiomyopathy (HCM) patients have been successfully treated with a high-dose beta-blocker (HDβB) therapy (Ostman-Smith *et al.* 1999).

Therefore, considering that abnormalities of ATP homeostasis do play a central role in any form of HCM, irrespective of the type of mutation or the pathohistology, and that HDβB treatment is capable of inducing the regression of left ventricular hypertrophy in patients with familial HCM (Ostman-Smith *et al.* 1999), it has been suggested that the same effect could be achieved in any patient with myocardial hypertrophy including FRDA patients (Kosutic and Zamurovic 2005). Subsequently, a recent case report presents a 5-year follow-up of symmetrical concentric HCM in an FRDA patient treated with highdose propranolol (β-blocker) (Kosutic and Zamurovic 2005). The HDβB therapy resulted in a reduction in the thickness of the septal and posterior left ventricular walls and complete normalization of diffuse electrocardiographic repolarization abnormalities (Kosutic and Zamurovic 2005), suggesting that the HDβB treatment resulted in a reduction of energy demand and that it

favorably changed the myocardial energy demand–supply mismatch, thereby inducing the regression of cardiac hypertrophy.

Nevertheless, more FRDA patients with HCM should be submitted to HDβB treatment before any definitive conclusions can be drawn. In addition, a therapy protocol combining a potent antioxidant such as idebenone (increases mitochondrial ATP production) and HDβB (decreases ATP demand) might prove to be a promising therapeutic strategy.

1.3.4 – Increase of frataxin levels

While all the therapeutic approaches mentioned above may have the potential to reduce neurological deterioration and retard disease progression, they do not directly overcome the effects of the underlying *FXN* mutation. Since FRDA is caused by a deficiency of frataxin, an obvious solution would be to increase expression of frataxin.

Gene therapy

Ideally, this could be achieved through gene therapy by delivering a fully functional normal *FXN* allele to the main sites of pathology. Although it is unlikely that such an approach will be readily available within the near future, a recent gene therapy strategy consists of using patient's cord blood-derived multipotent stem cells, modified to include a bacterial artificial chromosome (BAC) containing the normal FRDA locus (Zaibak *et al.* 2009).

Inhibition of triplex formation

On a different perspective, since the rate of formation of full-length transcripts has been shown to be inversely correlated with the length of the GAA expansion, a potential therapeutic approach targets the inhibition of triplex formation, or "sticky" DNA, during transcription (Figure 1.17). Oligodeoxyribonucleotides (ODNs) designed to block particular

types of triplex formation have been shown *in vitro* to provide specific and concentration-dependent increases in full-length transcript (Grabczyk and Usdin 2000a).

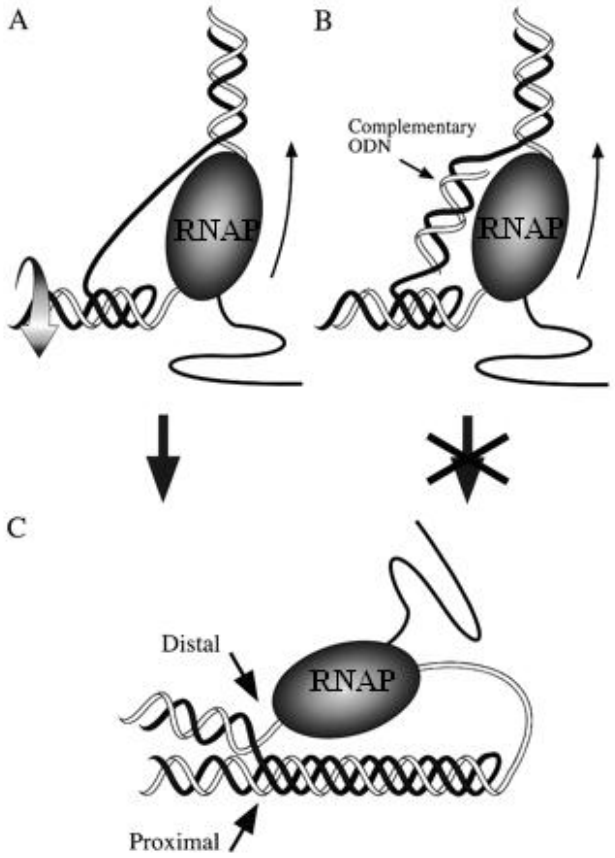

Figure 1.17 – Foundation for ODN antagonism of transcription-driven intramolecular triplex formation. Ribbon diagrams show two points in transcription-driven triplex formation (**A** and **C**) and indicate how ODN hybridization may disrupt it (**B**). (**A**) RNAP with an attached nascent transcript (black wavy line) is shown just after nucleation of an intramolecular triplex in the R·Y tract behind it. The curved arrow indicates rotation of the acceptor helix as it winds in the third strand and relaxes negative supercoils. The supercoil energy-driven spread of triplex formation may rapidly progress to the situation shown in (**C**). (**B**) as in (**A**) but with the addition of an ODN able to bind to the non-template strand. Hybridization by the ODN to the expanded transcription bubble might prevent the initial fold-back that nucleates triplex formation or stop spread of the triplex by blocking additional winding in by the third strand. RNAP continues to transcribe unhindered. (**C**) Once the non-template strand has been wound into a triplex, the RNAP that initiated formation may be paused at the triplex–duplex junction formed ahead of it at the promoter distal end of the triplex. If the triplex is stable, it may serve to block the next transcribing polymerase, which will encounter the triplex at its promoter proximal end (Grabczyk and Usdin 2000a).

Recently, a range of small molecules with the potential to bind selectively to the duplex form of the GAA repeat sequence was identified by competition dialysis (Grant *et al.* 2006). Potentially, such groove binding agents prefer duplex over triplex forms, and would in fact displace the third strand to form a drug-duplex DNA complex (Grant *et al.* 2006). Using cell lines containing a portion of expanded *FXN* intron 1 (GAA_{148}) fused to a green fluorescent protein (GFP) reporter, a selection of the above mentioned small molecules was found to increase frataxin expression through the GAA repeat region (Grant *et al.* 2006). In addition, it has also been shown that one of such small molecules, namely pentamidine (approved drug for the treatment of infections in HIV patients), can increase frataxin levels in cultured patient lymphocytes (Grant *et al.* 2006).

Similarly, polyamides seem to bind GAA·TTC tracts with high affinity and disrupt the intramolecular DNA·DNA-associated region of the sticky DNA conformation (Burnett *et al.* 2006). These synthetic ligands increase transcription of the frataxin gene in cell culture, resulting in increased levels of frataxin protein, while DNA microarray analyses indicate that a limited number of genes are significantly affected in FRDA cells (Burnett *et al.* 2006).

Inhibition of heterochromatin-mediated silencing

In contrast to the above mentioned strategy, an alternative therapeutic approach takes into account the fact that expanded GAA repeats have been shown to induce repressive heterochromatin in a manner reminiscent of PEV gene silencing (Saveliev *et al.* 2003). PEV occurs when a gene is located within or near regions of heterochromatin, and silent heterochromatin is characterized by the presence of particular types of histone modifications, the absence of acetylated histones, and the presence of histone deacetylases (HDACs), DNA methyltransferases, chromodomain proteins and polycomb group proteins (Elgin and Grewal 2003). Since the acetylation and deacetylation of histone proteins (and of

other proteins involved in transcriptional regulations) have a critical role in regulating gene expression, it has been suggested that HDAC inhibitors may revert silent heterochromatin to an active chromatin conformation and restore the normal function of otherwise silenced genes (Figure 1.18) (Herman *et al.* 2006). Pursuing this thought, a recent study has reported the synthesis and characterization of a class of HDAC inhibitors that increase histone acetylation on *FXN* and successfully reverse its silencing in primary lymphocytes from FRDA patients (Herman *et al.* 2006).

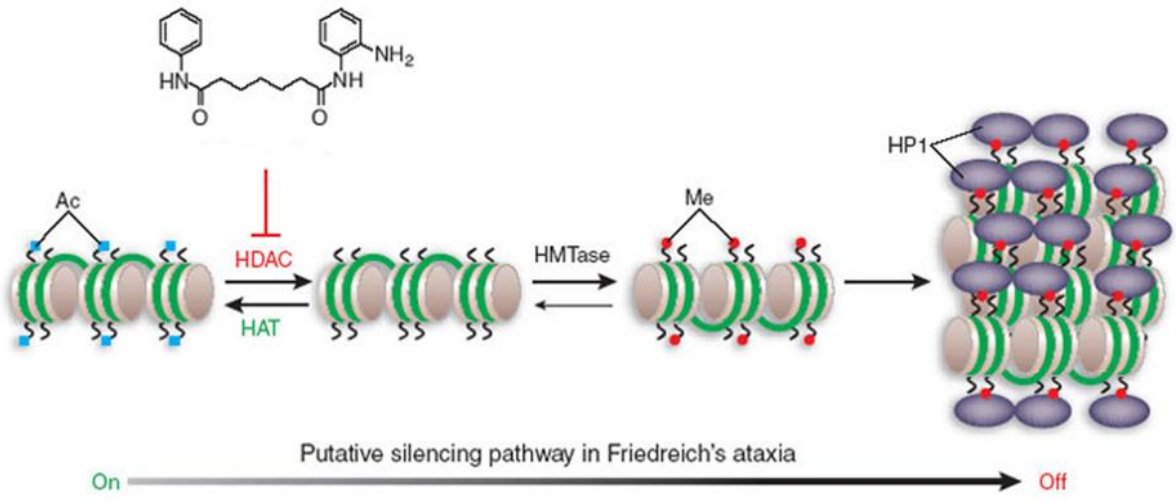

Figure 1.18 – Representation of the use of HDAC inhibitors in FRDA to promote histone acetylation and consequently cancelling out the gene-silencing effect (Herman *et al.* 2006).

Other/unknown mechanisms

A recent report describes recombinant human erythropoietin (rhuEPO) as a potential therapeutic agent for FRDA (Sturm *et al.* 2005b). Over the last decade, the cytokine rhuEPO has proven to be a safe therapeutic agent in haemodialysis patients with minimal adverse events (de Francisco *et al.* 2002). However, in recent times, rhuEPO has received considerable attention owing to its broad neuroprotective and cardioprotective capabilities (Cerami *et al.* 2002; Erbayraktar *et al.* 2003; Smith *et al.* 2003) by a still poorly understood

mechanism. It has been hypothesized that the function of rhuEPO in tissue protection could also be mediated by increasing frataxin expression (Sturm *et al.* 2005b). And in fact, it has been demonstrated that rhuEPO can, additionally to its reported neuro- and cardioprotective properties, increase frataxin expression *in vitro* (Sturm *et al.* 2005b). Significant increases on frataxin expression in primary lymphocytes from FRDA patients were observed following rhuEPO treatment (Sturm *et al.* 2005b). Additionally, rhuEPO was also reported to increase frataxin expression in many other cell types, among them the most affected cell types in FRDA such as neurones and cardiac cells (Sturm *et al.* 2005b).

Curiously, a recent study investigating the effects of rhu-EPO on frataxin mRNA and protein in primary fibroblast cell cultures derived from FRDA patients, reported a slight but significant increase in the amount of frataxin protein, but did not identify any increase in the mRNA expression at any of the times and doses tested, suggesting that the regulatory effects of rhu-EPO on the frataxin protein are at the post-translational level (Acquaviva *et al.* 2008).

High throughput screening

In order to investigate the regulation of *FXN* expression, a sensitive cellular genomic reporter assay was developed, which allows the *in vitro* screening of compounds for their ability to increase frataxin expression (Sarsero *et al.* 2003). A low level of enhancement of FRDA gene expression by hemin and butyric acid was initially demonstrated using this assay (Sarsero *et al.* 2003). Adaptation of this approach to high throughput screening with human cell lines may enable the development of specific inducers of frataxin expression. Further support for this approach has been recently provided by the observation that resistance to cisplatin in a cancer cell line was associated with an increase in frataxin expression

(Ghazizadeh 2003). In addition, 3- nitropropionic acid increases frataxin expression in human lymphoblasts and in transgenic rat PC12 cells (Turano *et al.* 2003).

Recently, an alternative high-throughput system was developed by Soragni *et al.* (2008). This cell line-based molecular model of FRDA is characterized by the introduction of a *GFP* reporter minigene which contains 560 GAA·TTC repeats in intron 1. The GFP_$(GAATTC)_{560}$ minigene recapitulates the molecular hallmarks of the mutated *FXN* gene such as: inhibition of transcription of the reporter gene, decreased levels of the reporter protein and hypoacetylation and hypermethylation of histones in the vicinity of the repeats (Soragni *et al.* 2008).

Finally, a greater understanding of the mechanisms involved in *FXN* gene expression may identify additional genomic targets for drug development, as expression studies should facilitate delineation of the endogenous regulatory elements that determine the tissue and developmental specificity.

1.4 – FRDA mouse models

In order to gain further understanding of the physiological function of frataxin and FRDA pathogenesis, as well as to develop an effective system for testing potential therapies, mouse models of FRDA are considered essential.

1.4.1 – Knockout mouse models

As most recessive mutations reduce or ablate protein function, knockout mice can often replicate most of the features of these diseases (Watase and Zoghbi 2003). However, the production of accurate animal models for recessive diseases is not always so straightforward. For FRDA a basic knockout approach, using targeted deletion of *Fxn* exon 4, to generate a mouse model was unsuccessful: mice that are heterozygous for an *Fxn*-null allele seem normal, but the homozygotes die *in utero* as early as E6.5 (Cossee *et al.* 2000). Even though a model was not achieved this result indicates that frataxin has a critical role in development.

Conditional knockout mice were generated using a loxP-flanked allele and Cre-lines that are driven by the neuron-specific enolase (NSE) and muscle creatine-kinase promoters (Puccio *et al.* 2001). Mutants, in which frataxin protein levels are reduced in the brain and absent in the heart, show large sensory-neuron dysfunction, cardiomyopathy, iron-sulphur enzyme deficiency and premature death. Unfortunately, the primary sites of FRDA pathology, such as the dorsal column of the spinal cord, do not seem to be affected in these mice (Puccio *et al.* 2001).

To obtain specific and progressive neurological models for FRDA, Simon *et al.* (2004) generated an inducible knock-out mouse model expressing the tamoxifen-dependent

recombinase (Cre-ERT) under the mouse Prion protein (Prp) promoter, thus enabling spatiotemporal control of conditional alleles of the target genes. Ablation of frataxin in adult mice caused both spinal cord and DRG anomalies, leading to progressive neurological symptoms resembling FRDA, although with absence of motor neuropathy (Simon *et al.* 2004).

Conditional knockout mice were also generated to investigate the involvement of frataxin deficiency in the development of diabetes mellitus (Ristow *et al.* 2003). These mice had disrupted expression of frataxin selectively in pancreatic β cells. This resulted in an impairment of insulin secretion due to a loss of β cell mass, and consequently in the development of impaired glucose tolerance (Ristow *et al.* 2003).

1.4.2 – Knockin mouse models

Recently, a frataxin knockin mouse was produced by introducing a 230-repeat GAA tract into the mouse frataxin gene (Miranda *et al.* 2002). The homozygous mutation led to a 25% reduction in the levels of frataxin in all the tissues examined. GAA repeat knockin/*Fxn* knockout compound heterozygous mice express 25–36% of wild-type frataxin levels - such levels are typically associated with mild FRDA in humans. Even though a clear microarray gene expression phenotype has been determined (Coppola *et al.* 2006), these double mutants are viable and show no discernible phenotype (Miranda *et al.* 2002), indicating that longer repeats might be necessary to generate an accurate model of FRDA in mice.

The use of mouse models to study both germ-line and somatic repeat instability in CAG, CGG, and CTG trinucleotide-repeat disorders has proved to be very effective in studying the dynamics of trinucleotide repeats and their relation to disease (Kaytor *et al.* 1997; Mangiarini *et al.* 1997; Monckton *et al.* 1997; Sato *et al.* 1999; Shelbourne *et al.* 1999;

Wheeler *et al.* 1999; Fortune *et al.* 2000; Kennedy and Shelbourne 2000; Lorenzetti *et al.* 2000; Seznec *et al.* 2000; Ishiguro *et al.* 2001; Peier and Nelson 2002; Watase *et al.* 2003). However, instability is apparent only when the repeat sequence is introduced within the appropriate genomic context, such as a large human genomic transgene or knockin at the endogenous mouse locus (Shelbourne *et al.* 1999; Wheeler *et al.* 1999; Bontekoe *et al.* 2001; Ishiguro *et al.* 2001; Peier and Nelson 2002; Libby *et al.* 2003). Thus, a similar knockin strategy for FRDA is somewhat hampered by the fact that the *Fxn* intron 1 region of the mouse does not normally contain a GAA repeat sequence. Indeed, the knockin of a 230-GAA repeat sequence into the *Fxn* intron 1 has not reproduced triplet repeat instability in mice (Miranda *et al.* 2002).

1.4.3 – *FXN* YAC transgenic mouse models

As an alternative approach in the generation of FRDA mouse models, Pook *et al.* chose to study the potential applications of *FXN* transgenic mice, suggesting that a human genomic *FXN* transgene that contained a large GAA repeat expansion at the correct intronic position would enable both GAA repeat instability and reduced frataxin expression to be obtained within the one single model (Pook *et al.* 2001).

YAC derived human frataxin is functional and rescues homozygous Fxn knockout mice

In an initial effort to assess whether human frataxin could function in a mouse background and substitute for loss of endogenous murine frataxin, a human wild-type *FXN* yeast artificial chromosome (YAC) (Figure 1.19) transgenic mouse line was generated and crossbred with heterozygous *Fxn* exon 4 deletion knockout mice ($Fxn^{+/-}$) (Cossee *et al.* 2000; Pook *et al.* 2001).

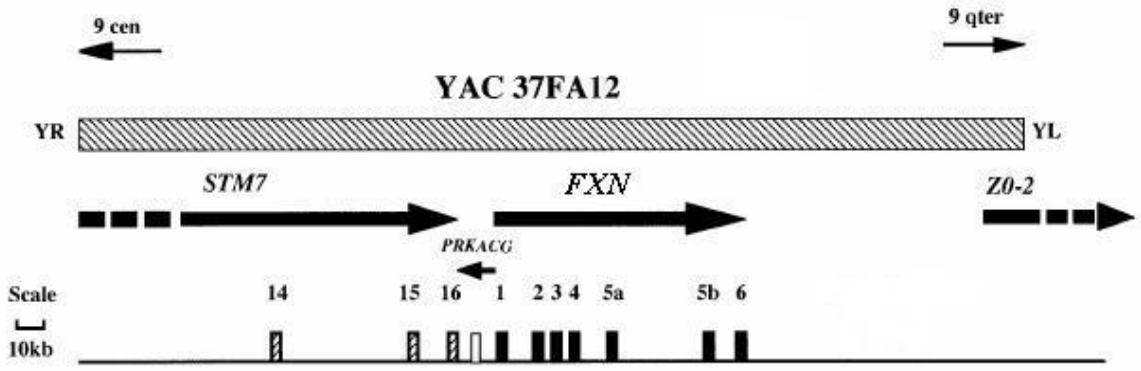

Figure 1.19 – The position of YAC 37FA12 with respect to the *FXN* locus at 9q13. Genes are represented as solid arrows, which indicate the direction of transcription, and the broken lines represent incomplete gene sequence. Individual exons are numbered and are shown below the relevant gene (Pook *et al.* 2001).

The result was phenotypically normal homozygous *Fxn* knockout ($Fxn^{-/-}$) offspring that have no endogenous murine frataxin, but are rescued by expression of functional YAC-derived human frataxin (Pook *et al.* 2001). These results demonstrate that: the 370kb *FXN* YAC transgenic construct (37FA12) is functional and can express frataxin during development; the protein undergoes correct post-translational modification to achieve mitochondrial localisation and is able to interact with other proteins in the cellular environment to achieve its normal function (Pook *et al.* 2001). Furthermore, this assisted in the delineation of a minimal genomic region that drives complete frataxin expression (Pook *et al.* 2001), which can be of great value in FRDA gene therapy studies.

GAA-containing human FXN YAC transgenic mice

Further advances were made by the generation of a *FXN* YAC transgenic mouse model that contains a GAA expansion mutation (Al-Mahdawi *et al.* 2004). This was achieved by GAA repeat modification of the 370-kb human genomic YAC clone, 37FA12 (Figure 1.20). To carry out the GAA modification, a PCR product containing approximately 700 GAA repeats and

1.85 kb of flanking intron 1 sequence was initially amplified from FRDA patient genomic DNA. Subsequent to cloning into pCR2.1 and then YEp24 vectors, the GAA repeat sequence showed contraction to a maximum size of 230 repeats. A very similar degree of contraction has previously been observed upon cloning of large GAA repeat expansion sequences into plasmids (Ohshima *et al.* 1998). Yeast pop-in/pop-out homologous recombination between the 230-GAA plasmid sequence and retrofitted YAC 37FA12 resulted in a final modified YAC, designated 1(38), which contained 190 GAA repeats (Al-Mahdawi *et al.* 2004).

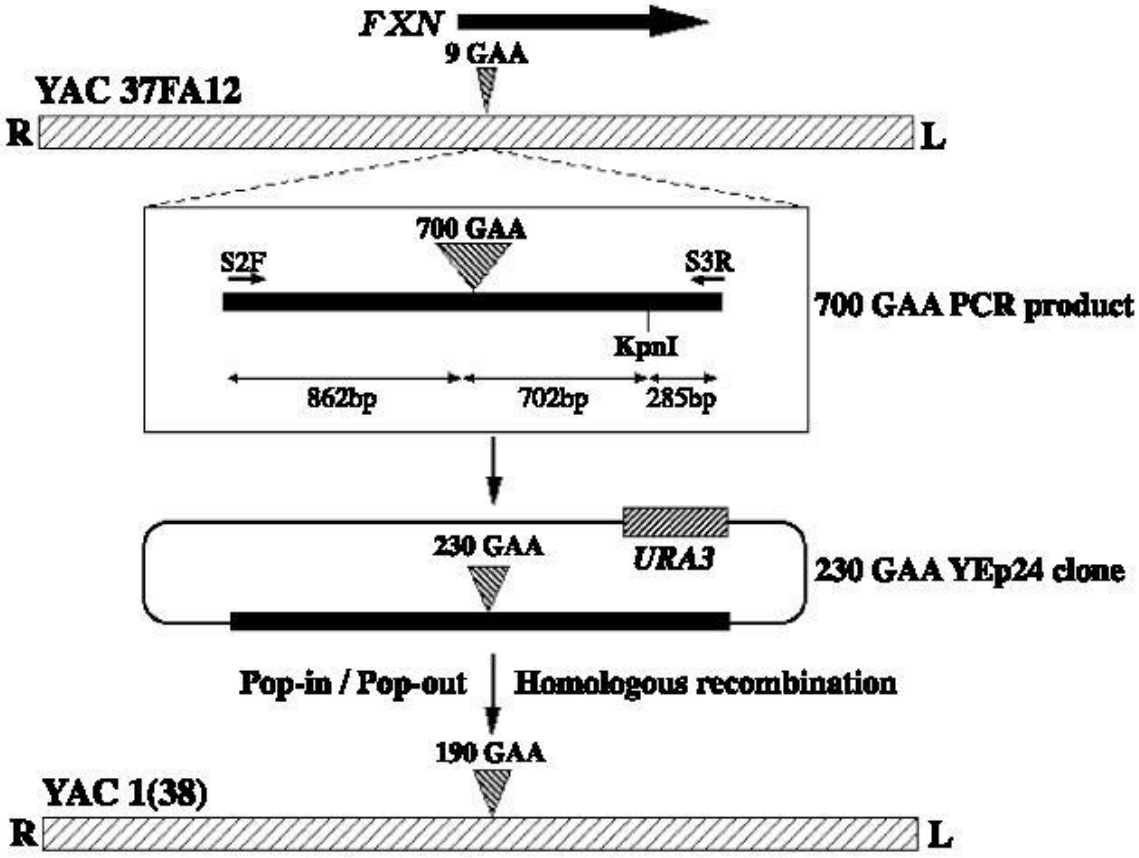

Figure 1.20 – GAA repeat modification of YAC 37FA12. The position and orientation of the normal *FXN* gene (9 GAA repeats) within the human YAC clone 37FA12 are indicated by the arrow. L and R indicate left and right arms of the YAC. A 700-GAA PCR product was amplified from FRDA patient DNA using primers S2F and S3R. The PCR product was first cloned into pCR2.1 and then into YEp24, which contains a selectable *URA3* gene, with resultant contraction to 230 GAA repeats. Pop-in/pop-out homologous recombination between Yep24 and YAC 37FA12 *FXN* sequences produced the 190-GAA-repeat YAC clone 1(38), which was subsequently used to generate transgenic mice (Al-Mahdawi *et al.* 2004).

Two lines of GAA containing human *FXN* YAC transgenic mice have been generated (Al-Mahdawi *et al.* 2004), designated YG8 and YG22 (Table 1.2). Both lines were shown to contain transgene sequences spanning the whole 370-kb human YAC clone, including the left and right arms of the YAC and the entire FRDA gene together with GAA repeat expansions. YG8 contained two GAA sequences of 90 and 190 repeats, while YG22 contained a single 190-GAA repeat sequence. Southern blot hybridization with YAC left arm and right arm probes detected nonsegregating bands in all transgenic offspring for both YG8 and YG22, indicating single sites of integration (Al-Mahdawi *et al.* 2004). By performing human–mouse comparative frataxin exon 3 ^{33}P-labeled PCR amplification, specific restriction enzyme digestion, and subsequent densitometry analysis, it was determined that the YG22 line had a single copy of the *FXN* gene and the YG8 line had two copies of the *FXN* gene (Al-Mahdawi *et al.* 2004).

Table 1.2 – General characterisation of *FXN* YAC transgenic mouse lines. (Al-Mahdawi *et al.* 2004)

Transgenic line	YAC transgene integrity	*FXN* copy number	Founder GAA repeat length(s)	Range of GAA repeats in offspring
YG8	Complete	2	190 + 90	<9 to 223
YG22	Complete	1	190	<9 to 235

GAA-repeat instability in FXN YAC GAA transgenic mice

Intergenerational GAA instability was identified in both the YG8 and the YG22 transgenic mice, ranging from complete contractions (<9 GAA repeats) to substantial expansions (223 and 235 GAA repeats in YG8 and YG22, respectively) (Table 1.2) (Al-Mahdawi *et al.* 2004). However, very large expansions have not been detected yet. The instability of the GAA repeat sequence during transmission from YG8 and YG22 transgenic

parents to offspring was assessed through five generations and eight generations of backcrossing, respectively, onto the C57BL/6J background (Al-Mahdawi *et al.* 2004). Both maternal and paternal GAA expansions and contractions have been identified as they have in FRDA patients. However, neither of the two lines shows patterns of intergenerational GAA repeat instability that are particularly similar to those found in FRDA patients (Al-Mahdawi *et al.* 2004).

Somatic instability of the GAA repeat was assessed in a variety of tissues from YG22 mice 2–12 months of age and YG8 mice 2–6 months of age (Al-Mahdawi *et al.* 2004). No somatic GAA instability was detected in either YG8 or YG22 mice at 2 months of age (Figure 1.21). However, pronounced changes were detected in tissues from older mice of both lines.

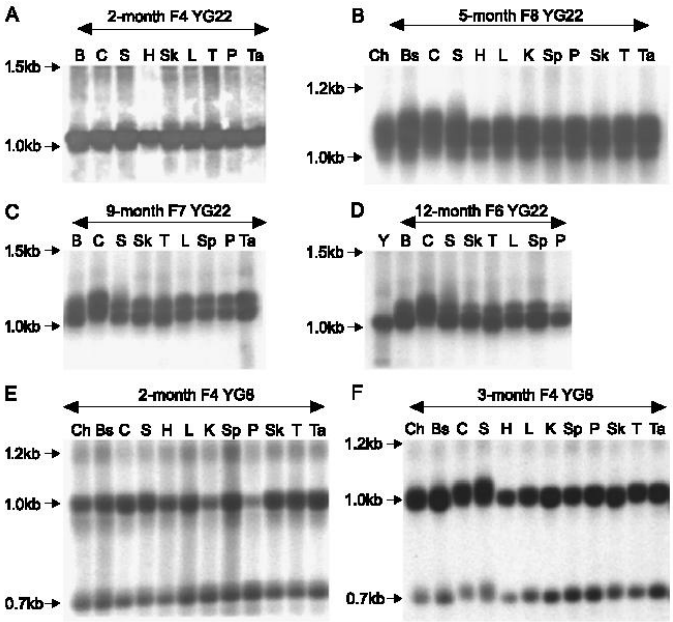

Figure 1.21 – Somatic GAA repeat instability in *FXN* YAC transgenic mice. Autoradiographs of Southern-blotted GAA PCR products from somatic tissues of representative transgenic mice. (**A**) 2-month F4 YG22, (**B**) 5-month F8 YG22, (**C**) 9-month F7 YG22, (**D**) 12-month F6 YG22, (**E**) 2-month F4 YG8, and (**F**) 3-month F4 YG8. No GAA repeat instability is detected in either 2-month-old YG22 or 2-month-old YG8 mice. Instability is greatest in the cerebellum of 9- and 12-month-old YG22 mice and the cerebellum and spinal cord of 3-month-old YG8 mice. Y, YAC 1(38); B, whole brain; Ch, cerebral hemisphere; Bs, brain stem; C, cerebellum; S, spinal cord; H, heart; L, liver; K, kidney; Sp, spleen; P, pancreas; Sk, skeletal muscle; T, testis; Ta, tail (Al-Mahdawi *et al.* 2004).

In contrast to the situation with germ-line instability, there is a marked similarity between the *FXN* YAC GAA transgenic mice and FRDA patients when it comes to observing somatic instability of the GAA repeat as both YG8 and YG22 transgenic mice showed prominent GAA expansion changes in CNS tissues, particularly in the cerebellum (Al-Mahdawi *et al.* 2004). This is a very interesting finding since consistently larger GAA alleles have been described in the cerebellar cortex of FRDA patient autopsy samples, when compared with other CNS tissues (Montermini *et al.* 1997b). Therefore, it is possible that some trans-acting cerebellar tissue or cell factors may be influencing GAA instability within both species.

Recently, a small pool PCR (SP-PCR) approach was used to perform a detailed quantitative analysis of the length-, tissue-, and age-dependent instability of the GAA repeat sequence in the context of the human *FXN* locus, using both YG8 and YG22 mouse lines (Clark *et al.* 2006). This has further confirmed that both lines display tissue specific instability characterized by expansions in the cerebellum and DRG and that somatic instability is age dependent.

The somatic instability of the $(GAA)_{190}$ tract was analysed in multiple tissues from 12-month-old mice derived from both transgenic lines, and over 2,000 molecules, representing individual somatic transgenes, were analyzed from each transgenic line (Clark *et al.* 2006). Although, both expansions and contractions were observed in most tissues, the $(GAA)_{190}$ sequence was most unstable in cerebellum and DRG (Figure 1.22). The mutation load in cerebellum was 20.4% and 39.4% in YG8 and YG22, respectively, and in DRG of YG8 it was 8.3% (DRG was not analyzed in YG22). By comparison, the combined mutation loads of the other tissues (i.e., excluding cerebellum and DRG) were only 1.4% and 4.3% in the YG8 and YG22 lines, respectively (p<0.001 in both lines). Somatic instability in cells derived from

actively proliferating tissues such as peripheral blood and sperm was also much lower than in the cerebellum and DRG (p<0.001; Figure 1.22) (Clark *et al.* 2006).

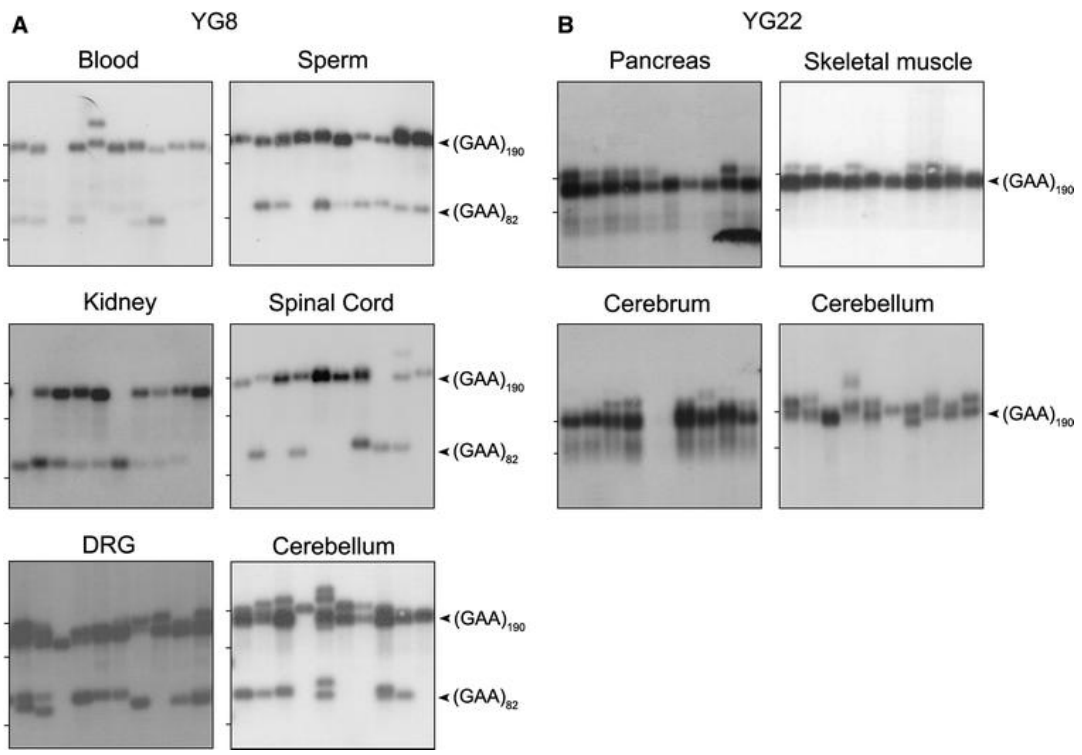

Figure 1.22 – SP-PCR analysis showing somatic instability of the GAA triplet-repeat sequence in multiple tissues from YG8 (**A**) and YG22 (**B**) transgenic mice. Representative gels are shown for the indicated tissues. The locations of the constitutional $(GAA)_{190}$ and $(GAA)_{82}$ alleles, as determined by conventional PCR, are indicated by *arrowheads*. Each *lane* typically contains 5–10 individual molecules. Note that cerebellum and DRG show higher levels of instability. The relative positions of the DNA size markers are indicated by *dashes* on the left margin of each gel; they represent 0.65, 0.85 and 1 kb from the bottom of the gels in (**A**) and 0.85 and 1 kb in (**B**). (Clark *et al.* 2006)

A significant expansion bias was noticed in all tissues, with at least an eightfold greater frequency of expansions over contractions in both lines (p<0.001 in both lines; Figure 1.23). Again, most of the expansions were noted in the cerebellum and DRG, which accounted for 75% and 44% (92/122 and 68/154) of all expansions seen in the YG8 and YG22 lines, respectively. It is noteworthy that the same frequency of expansions was noted for the $(GAA)_{190}$ transgene in both YG8 and YG22 mice (p=0.7; Figure 1.23). The magnitude of

expansions was comparable for the two lines (Figure 1.24), with maximum expansions in cerebellum of 50+ triplets noted in both lines (representing an increase of >30%). Similar instances of expansion by 50+ triplets, although less frequent than in cerebellum, were also noted for the $(GAA)_{190}$ transgene in DRG (Clark *et al.* 2006).

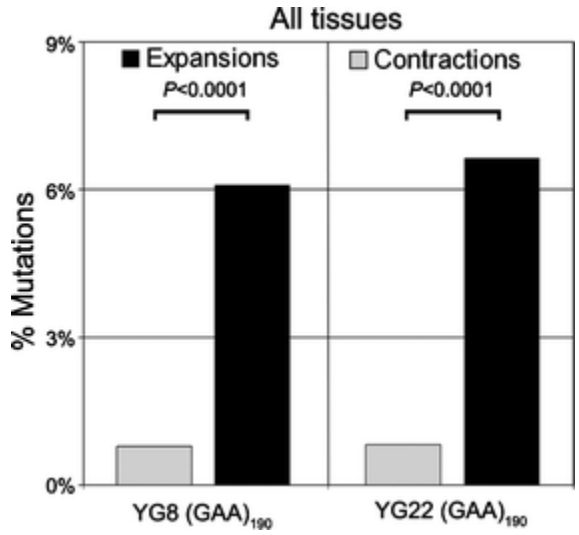

Figure 1.23 – Somatic instability of the $(GAA)_{190}$ allele in tissues from YG8 and YG22 transgenic mice shows a significant bias for expansions. Note that both transgenic mice show a >eightfold excess of expansions over contractions (Clark *et al.* 2006).

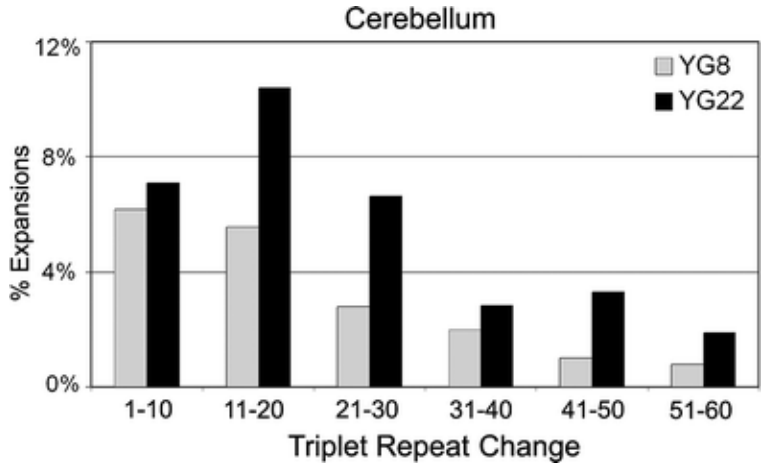

Figure 1.24 – Similar magnitude of cerebellar expansions of the $(GAA)_{190}$ allele in YG8 and YG22 transgenic mice. *Bars* represent the frequency of expansions with the indicated increase in repeat length (measured in triplets) (Clark *et al.* 2006).

The SP-PCR analysis was also used to compare the levels of somatic instability in tissues derived from young (2 month old; 2,400 individual molecules) versus old (12 month old; 2,000 individual molecules) YG8 transgenic mice (Table 1.3) (note DRG was analyzed at 3 and 14 months) (Clark *et al.* 2006). Through 2 months of age, the $(GAA)_{190}$ allele showed low levels of somatic instability (≤1%) including in the cerebellum and DRG (Table 1.3; Figure 1.25A). The $(GAA)_{82}$ allele was completely stable through 2 months, indicating that repeat length determines the age of onset of somatic instability (Figure 1.26). In older mice, a significant increase in mutation load was noted, which was mainly due to the accumulation of expansions. The $(GAA)_{190}$ allele showed a significant age-dependent increase in the frequency of expansions in DRG and cerebellum (p<0.001 for each tissue; Table 1.3). The $(GAA)_{82}$ allele showed a similar age-dependent increase in mutation load in cerebellum and DRG, which at 12 months was indistinguishable from the $(GAA)_{190}$ allele in terms of the proportion of mutant molecules (p=0.12 for all tissues and p=0.36 for cerebellum only) (Figure 1.26). However, as opposed to cerebellum and DRG, low mutation loads (<2.5%) were noted for both alleles even up to 12 months of age in blood and sperm (proliferative cells), spinal cord, and kidney (Table 1.3) (Clark *et al.* 2006).

Table 1.3 – Age-dependent and expansion-biased somatic instability of the $(GAA)_{190}$ allele in YG8 transgenic mice (Clark *et al.* 2006).

	2 Months				12 Months			
	ML (%)	Molecules analyzed	Cont	Exp	ML (%)	Molecules analyzed	Cont	Exp
Blood	0	898	0	0	0.6	711	0	4
Sperm	0	121	0	0	2.3	216	0	5
Kidney	N/a	N/a	N/a	N/a	0	189	0	0
Spinal cord	1	100	0	1	2.4	42	0	1
Brainstem	0.65	306	0	2	5.5	161	2	7
DRG[a]	0.9	112	1	0	8.3	180	2	13
Cerebellum	0.35	862	0	3	20.4	501	10	92
Total	0.29	2399	1	6	6.8	2,000	14	122

N/a not analyzed; *ML* mutation load; [a] DRG was analyzed at 3 and 14 months.

The age-dependent increase in expansions described in the cerebellum of YG8 mice was reproduced in the YG22 mice (Clark *et al.* 2006). The $(GAA)_{190}$ allele, which was only slightly unstable at 2 and 5 months (4.3% of 325 individual molecules at 5 months), by 12 months showed a significant increase in mutation load (39.3% of 211 individual molecules; $p<0.001$ compared with 2 or 5 months), and expansion bias (4.5-fold greater frequency of expansions over contractions; $p<0.001$) (Figure 1.25B) (Clark *et al.* 2006).

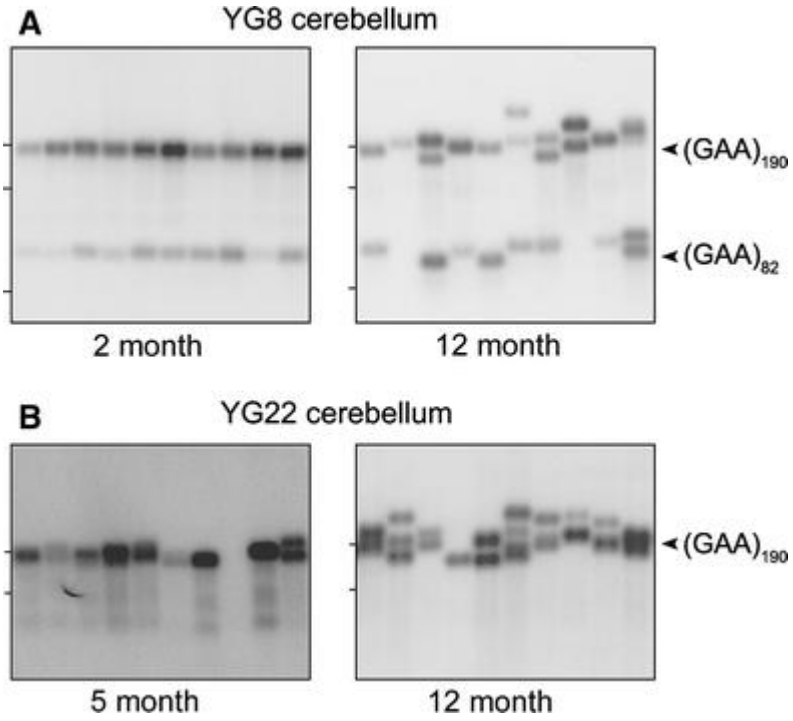

Figure 1.25 – Somatic instability of the $(GAA)_{190}$ and $(GAA)_{82}$ alleles is age-dependent. Representative gels are shown for cerebellar DNA, and the locations of the constitutional $(GAA)_{190}$ and $(GAA)_{82}$ alleles, as determined by conventional PCR, are indicated by *arrowheads*. Each lane contains a comparable number (5–10) of individual molecules. YG8 cerebellum and YG22 cerebellum are shown in (**A**) and (**B**), respectively. Note the increase in instability and bias for expansion, seen in 12 month versus 2 or 5-month-old cerebellum. The relative positions of the DNA size markers are indicated by *dashes* on the left margin of each gel; they represent 0.65, 0.85 and 1 kb from the bottom of the gels in (**A**) and 0.85 and 1 kb in (**B**) (Clark *et al.* 2006).

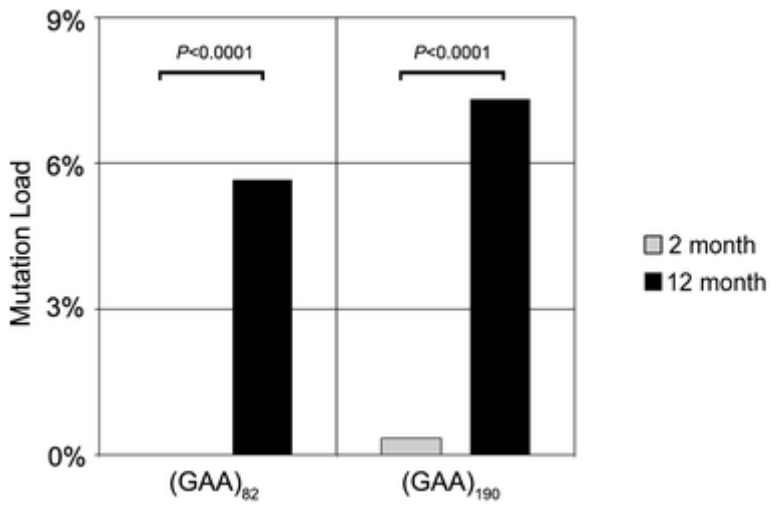

Figure 1.26 – Somatic instability of the $(GAA)_{190}$ and $(GAA)_{82}$ alleles is age-dependent. The graph shows a significant increase in somatic instability of the $(GAA)_{190}$ and $(GAA)_{82}$ alleles in (all tissues of) 12 versus 2-month-old-littermates of YG8 transgenic mice (DRG was collected 14 and 3 months instead) (Clark *et al.* 2006).

In summary, both the YG8 and YG22 mice lines show progressive and tissue-specific expansions of GAA repeats specifically in the regions of the nervous system that show pathology in FRDA patients. This suggests the involvement of *trans* or *cis*-acting factors, likely independent of DNA replication, in the regulation of tissue-specific and age-dependent GAA somatic instability.

The fact that the two *FXN* YAC GAA transgenic mice lines show both intergenerational and somatic GAA repeat instability, when neither was observed with the 230-GAA repeat knockin mouse model (Miranda *et al.* 2002), also suggests that the genomic context of the GAA repeat influences its instability. In addition, such intergenerational and somatic GAA repeat instability observed in both *FXN* YAC GAA transgenic lines represents the first time that such occurrence has been reported in a FRDA mouse model (Al-Mahdawi *et al.* 2004). Therefore, such a model is potentially useful for detailed study of FRDA GAA repeat expansion mechanisms within an *in vivo* mammalian system.

GAA expansion-containing FXN YAC transgene rescues Fxn knockout embryonic lethality

To determine the viability of each GAA *FXN* transgene, both the YG22 or YG8 lines (*FXN*$^{+}$, *Fxn*$^{+/+}$) were crossbred with heterozygous *Fxn* knockout mice (*Fxn*$^{+/-}$) (Al-Mahdawi *et al.* 2006). The *FXN*$^{+}$, *Fxn*$^{+/-}$ offspring from these crosses were further bred with *Fxn*$^{+/-}$ mice to generate *FXN*$^{+}$, *Fxn*$^{-/-}$ "rescues" (Al-Mahdawi *et al.* 2006). Correct Mendelian ratios of rescue mice to overall offspring number were obtained from both YG22 and YG8 crosses, indicating functional frataxin derived from both GAA repeat-containing transgenes (Al-Mahdawi *et al.* 2006). The rescue mice from both lines have exhibited a normal life span, with mice surviving up to at least 2 years of age.

Comparable epigenetic changes in human and transgenic mouse brain and heart tissues

Since the transgene present in the *FXN* YAC transgenic mice consists of the entire human *FXN* gene sequence, it was possible to investigate the DNA methylation profiles and the histone modifications at exactly the same three regions of the *FXN* gene that had previously been analysed in human tissue (Al-Mahdawi *et al.* 2008).

Overall, the DNA methylation profiles of *FXN* transgenic mouse brain and heart tissues resemble the profiles of human tissue (Figure 1.27), particularly on the upstream GAA regions of both YG8 and YG22 transgenic mouse brain and heart tissues (Al-Mahdawi *et al.* 2008).

Similarly, histone modifications of *FXN* transgenic mouse brain tissue are comparable with histone modifications of human tissue (Figure 1.28): overall GAA repeat-induced decreases in histone H3K9 acetylation and increases in H3K9 methylation for both YG8 and YG22 transgenic mice, as previously identified in human FRDA tissue (Al-Mahdawi *et al.* 2008). However, the level of deacetylation in the transgenic mouse tissue was not as great

as that seen in the human tissue, possibly as a consequence of the smaller transgenic GAA repeat expansion sizes. The greatest consistent histone residue changes found between the non-GAA (Y47) and both of the GAA (YG8 and YG22) transgenic brain tissue samples were decreases in acetylated H3K9 and increases in di- and tri-methylated H3K9 (Al-Mahdawi *et al.* 2008).

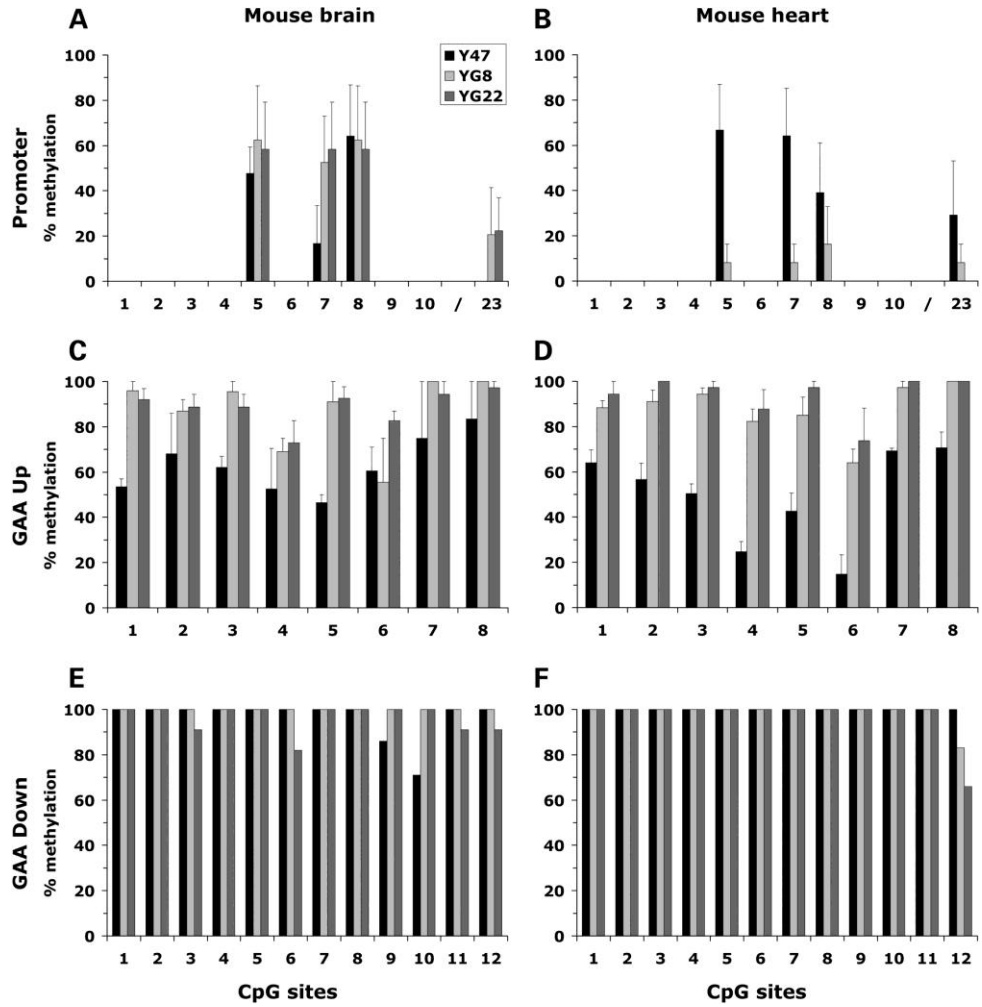

Figure 1.27 – DNA methylation analysis of the *FXN* promoter in *FXN* YAC transgenic mice: (**A** and **B**), upstream GAA (**C** and **D**) and downstream GAA (**E** and **F**) regions of Y47 (black columns), YG8 (light grey columns) and YG22 (dark grey columns) transgenic mouse brain and heart tissues (Al-Mahdawi *et al.* 2008).

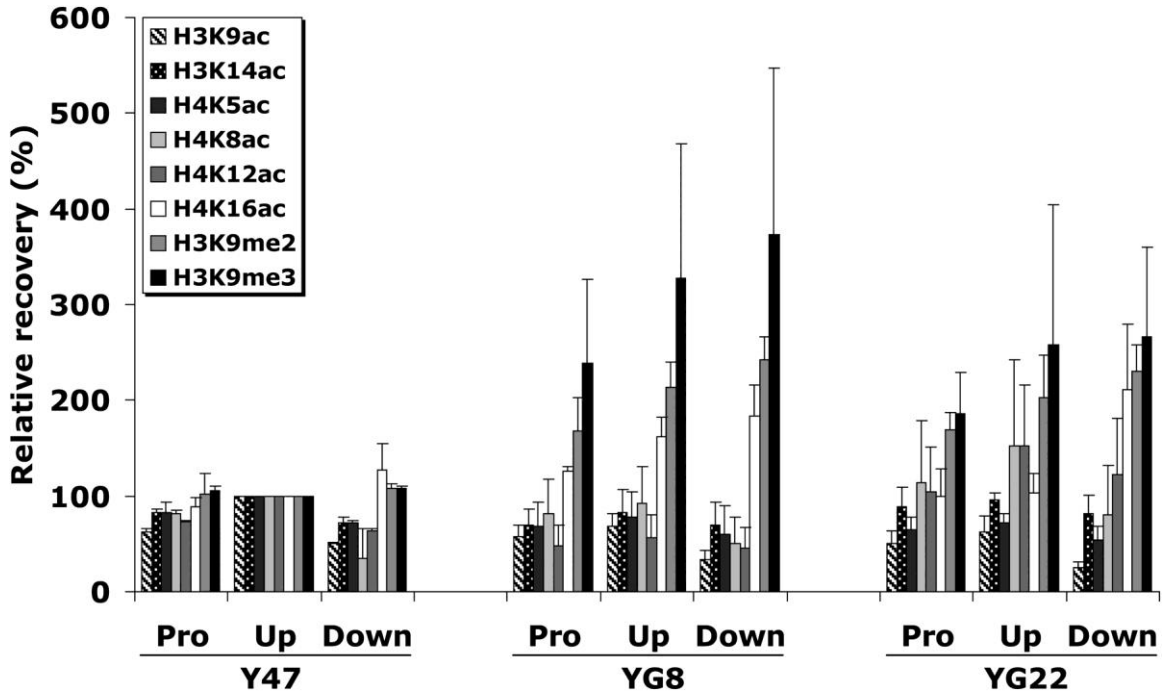

Figure 1.28 – Analysis of histone modifications in transgenic mouse brain tissues. ChIP Q-PCR results for the transgenic *FXN* promoter/exon1 (Pro), upstream GAA (Up) and downstream GAA (Down) amplified regions are represented as the relative amount of immunoprecipitated DNA compared with input DNA, having taken negligible –Ab control values into account. *FXN* values were normalized with mouse *GAPDH* and all values have been adjusted so that all of the upstream GAA values from the non-GAA transgenic mouse tissues (Y47) are 100% (Al-Mahdawi *et al.* 2008).

Decreased levels of frataxin mRNA and protein expression in FXN YAC GAA mouse model

Both the YG8 and YG22 rescue mice express comparatively decreased levels of human frataxin mRNA in all tissues (Figure 1.29) and decreased levels of human frataxin protein in at least some tissues compared with endogenous mouse levels (67% and 42% in cerebellum, 37% and 25% in heart, and 10% and 9% in skeletal muscle of YG22 and YG8 rescue mice, respectively) (Figure 1.31) (Al-Mahdawi *et al.* 2006). Overall the YG8 rescue mice demonstrate slightly less frataxin mRNA and protein expression compared with the YG22 mice.

Recently, real-time reverse transcriptase PCR (Q-RT-PCR), was used to confirm the *FXN* transgene expression levels, showing YG8 and YG22 to have mean decreased mRNA levels of

26% and 35% in brain and 57% and 56% in heart compared with Y47 normal-sized GAA repeat-containing *FXN* YAC transgenic mice (Figure 1.30)(Al-Mahdawi *et al.* 2008).

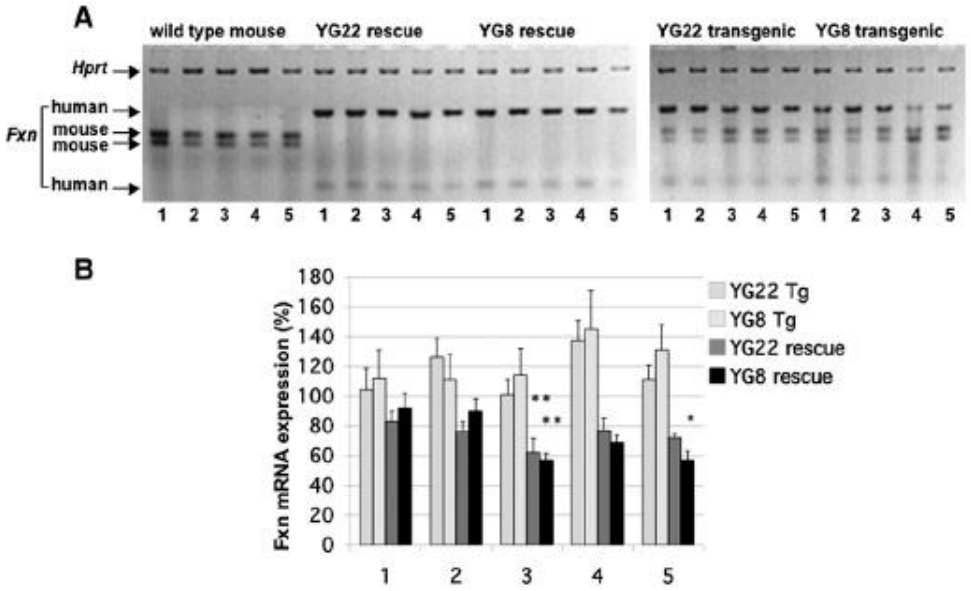

Figure 1.29 – Frataxin mRNA expression analysis in YG8 and YG22. (**A**) A representative RT-PCR image showing restriction-digested human frataxin products (112 and 29 bp) and mouse frataxin products (75 and 64 bp), together with mouse *Hprt* controls. mRNA samples were isolated from tissues of wild-type, YG22 rescue, YG8 rescue, YG22 transgenic, and YG8 transgenic mice (lanes 1, cerebrum; 2, brain stem; 3, cerebellum; 4, heart; 5, skeletal muscle). (**B**) Levels of frataxin mRNA expression as a percentage value of wild-type mouse expression. Values were generated by determining the means of six different RT-PCR experiments, each normalized to *Hprt*. Error bars indicate SEM. **p*<0.05, ***p*<0.01 (Al-Mahdawi *et al.* 2006).

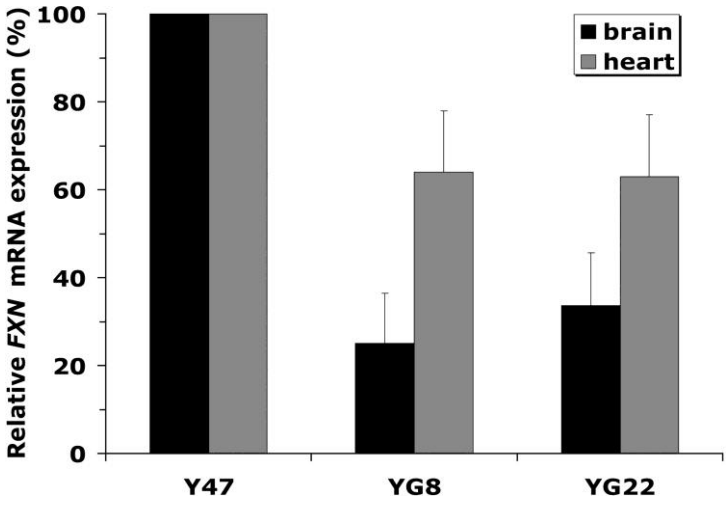

Figure 1.30 – Q-RT-PCR analysis of transgenic *FXN* mRNA isolated from Y47, YG8 and YG22 mouse brain and heart tissues (Al-Mahdawi *et al.* 2008).

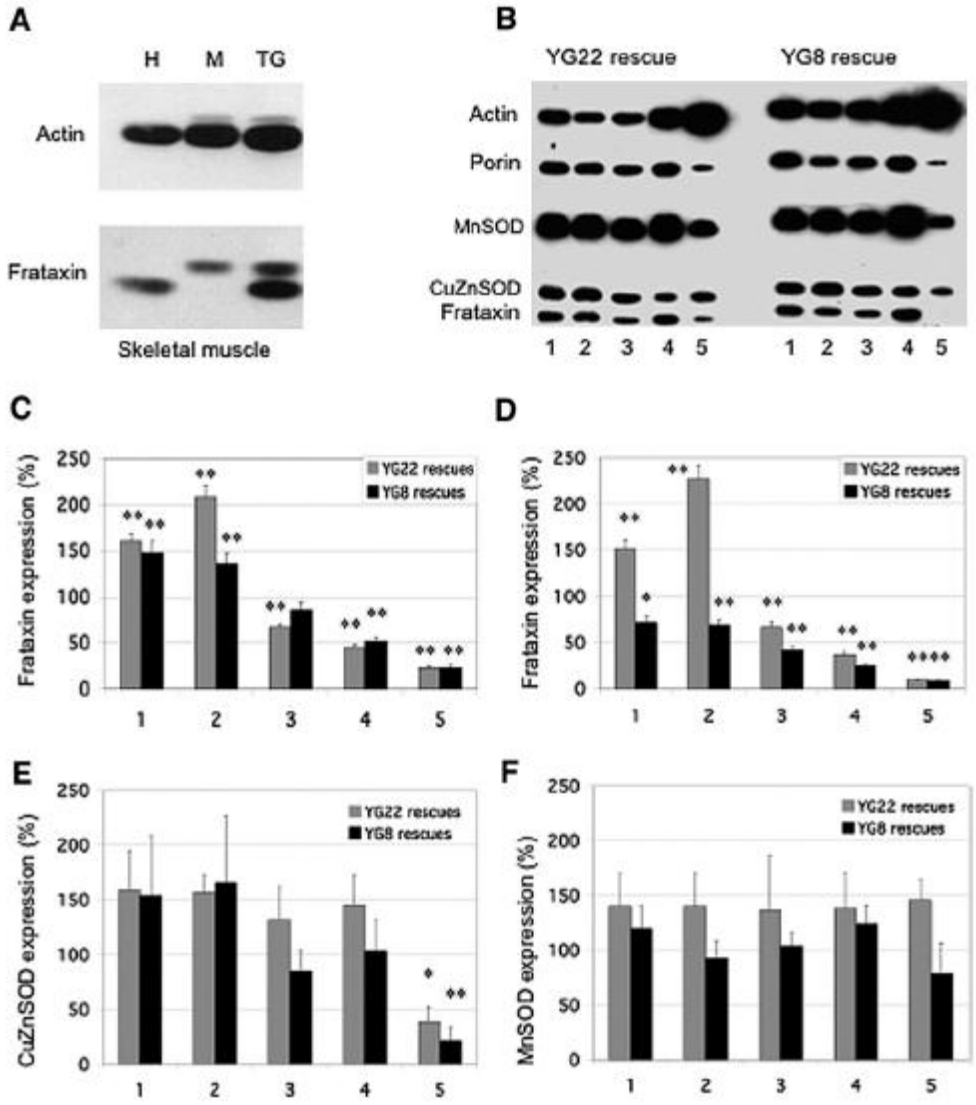

Figure 1.31 – Frataxin and antioxidant enzyme expression levels in YG22 and YG8 rescue mice. (**A**) Western blot showing comparative levels of frataxin relative to actin in skeletal muscle samples from human (H), wild-type mouse (M), and YG22 transgenic mouse (TG). (**B**) Western blot of YG22 and YG8 rescue mouse tissue lysates (lanes 1, cerebrum; 2, brain stem; 3, cerebellum; 4, heart; 5, skeletal muscle) hybridized with antibodies against frataxin, actin, porin, MnSOD, and CuZnSOD. The very low levels of YG8 skeletal muscle frataxin, which appear to be negative in this image, were revealed upon longer exposure. (**C**, **D**) Levels of transgenic human frataxin expression as a percentage value of endogenous wild-type mouse frataxin expression, (**C**) relative to porin controls or (**D**) relative to actin controls (*n*=5–8). Tissues 1–5 are as described for (**B**). (**E**) Levels of CuZnSOD in rescue mice as a percentage value of wild-type mouse expression, normalized to actin (*n*=3–7). Tissues 1–5 are as described for (**B**). (**F**) Levels of MnSOD in rescue mice as a percentage value of wild-type mouse expression, normalized to porin (*n*=3–6). Tissues 1–5 are as described for (**B**). Error bars indicate SEM. **p*<0.05, ***p*<0.01 (Al-Mahdawi *et al.* 2006).

Such differentially reduced levels of frataxin in the *FXN* YAC GAA mouse model have been proven sufficient to induce a mild FRDA-like pathological phenotype. Impaired aconitase activity (Figure 1.32), oxidative stress (Figure 1.33), and functional deficits are apparent (Figure 1.34), although not severe, and neuronal histopathology within the DRG and iron deposition within the heart are later progressive effects (Figure 1.35 & Figure 1.36) (Al-Mahdawi *et al.* 2006).

Oxidative stress in FXN YAC GAA mouse model

The *FXN* YAC GAA mouse models demonstrate an obvious, but not severe, degree of oxidative stress (Figure 1.33) (Al-Mahdawi *et al.* 2006). This may be due to the fact that the models have residual frataxin in all tissues. The mice also have a mitochondrial respiratory chain that shows only a slight overall functional deficit (Figure 1.32) and, therefore, continues to produce damaging free radicals. The greater loss of aconitase activity than MRC complex activity deficits suggests that aconitase impairment is a prominent early feature, even in mild cases of FRDA. The increases described in CuZnSOD and MnSOD are generally consistent with a reaction to oxidative stress in our FRDA mouse model tissues. However, where there is the greatest decrease in frataxin (i.e., skeletal muscle) a decrease in both CuZnSOD and MnSOD was observed. This indicates a different susceptibility or handling of this tissue to mild oxidative stress (Al-Mahdawi *et al.* 2006).

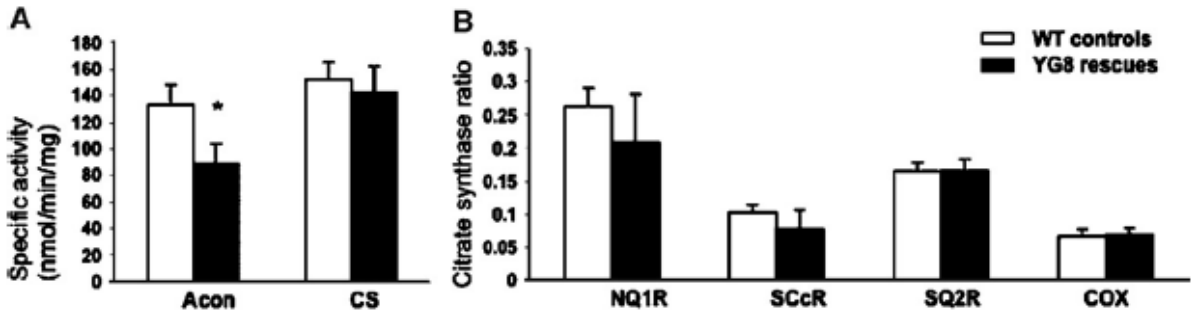

Figure 1.32 – Mitochondrial respiratory chain and aconitase activities in heart tissue from 6-month-old YG8 rescue mutant and control mice. (**A**) The specific activities of aconitase (Acon) and citrate synthase (CS). CS activities were divided by 10 (*n*=6). (**B**) The mitochondrial respiratory chain (MRC) activities expressed as a ratio with citrate synthase; MRC I, NADH coenzyme Q1 reductase (NQ1R); MRC II/III, succinate cytochrome *c* reductase (SCcR); MRC II, succinate coenzyme Q2 reductase (SQ2R); and MRC IV, cytochrome oxidase (COX). COX/CS ratio was multiplied by a factor of 10 (*n*=4). Activities are expressed as means ±SEM. **p*=0.03. (Al-Mahdawi *et al.* 2006)

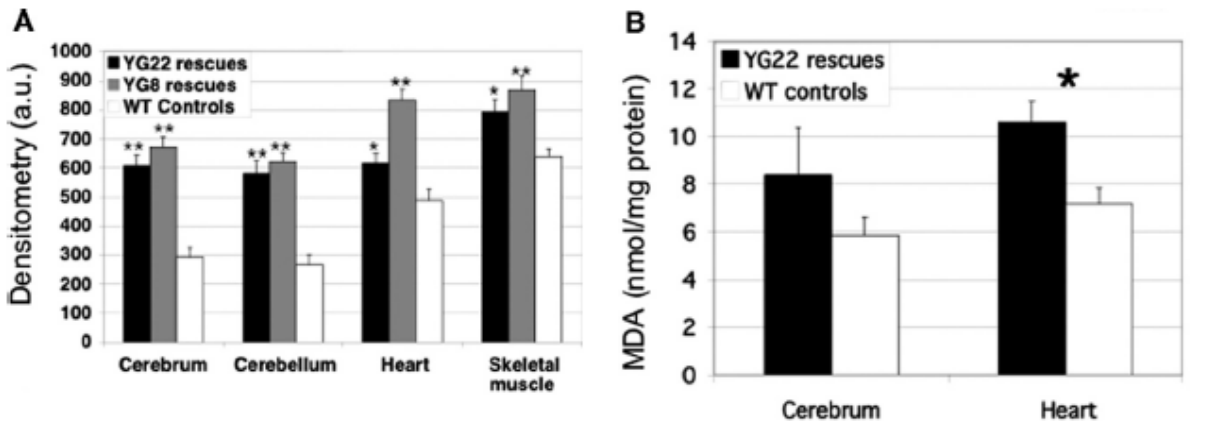

Figure 1.33 – Oxidative stress in YG8 and YG22 mice. (**A**) Protein oxidation analysis (Oxyblot) in cerebrum, cerebellum, heart, and skeletal muscle tissues of 6- to 9-month old YG22 and YG8 rescue mice, compared with wild-type controls, measured in arbitrary units (a.u.) of densitometry (*n*=8–12). Error bars indicate SEM. **p*<0.05, ***p*<0.01. (**B**) TBARS analysis shows levels of MDA (nmol/mg of protein) as a marker of lipoperoxidation in YG22 cerebrum and heart tissue compared with wild-type controls (*n*=6). Error bars indicate SEM. **p*<0.05 (Al-Mahdawi *et al.* 2006).

Neurobehavioral deficits in FXN YAC GAA mouse model

The coordination ability of the YG22 and YG8 rescue mice was shown to be impaired from the age of 3 months as determined by reduced performance on an accelerating rotarod treadmill compared with wild-type littermate controls (p<0.01) (Figure 1.34A) (Al-Mahdawi *et al.* 2006). However, the degree of impairment did not extend to overt ataxia in either line of mice up to the age of 2 years. Locomotor activity, assessed by examining the unrestricted movement of mice in an open field, was decreased in both lines (Figure 1.34B) (Al-Mahdawi *et al.* 2006). The YG22 rescues showed a decreased trend in locomotor activity from 6 months of age, but no statistically significant difference was seen until 1 year (p<0.05). YG8 rescues, on the other hand, showed a significant decrease in locomotor activity from 6 months of age (p<0.05). Both YG22 and YG8 lines demonstrated an increase in weight, with statistically significant differences detected in YG22 rescues from 6 months of age (p<0.01) and in YG8 rescues from 9 months of age (p<0.01) (Figure 1.34C) (Al-Mahdawi *et al.* 2006). One reason for the observed gain in weights may be the decreased locomotor activity identified in the mice.

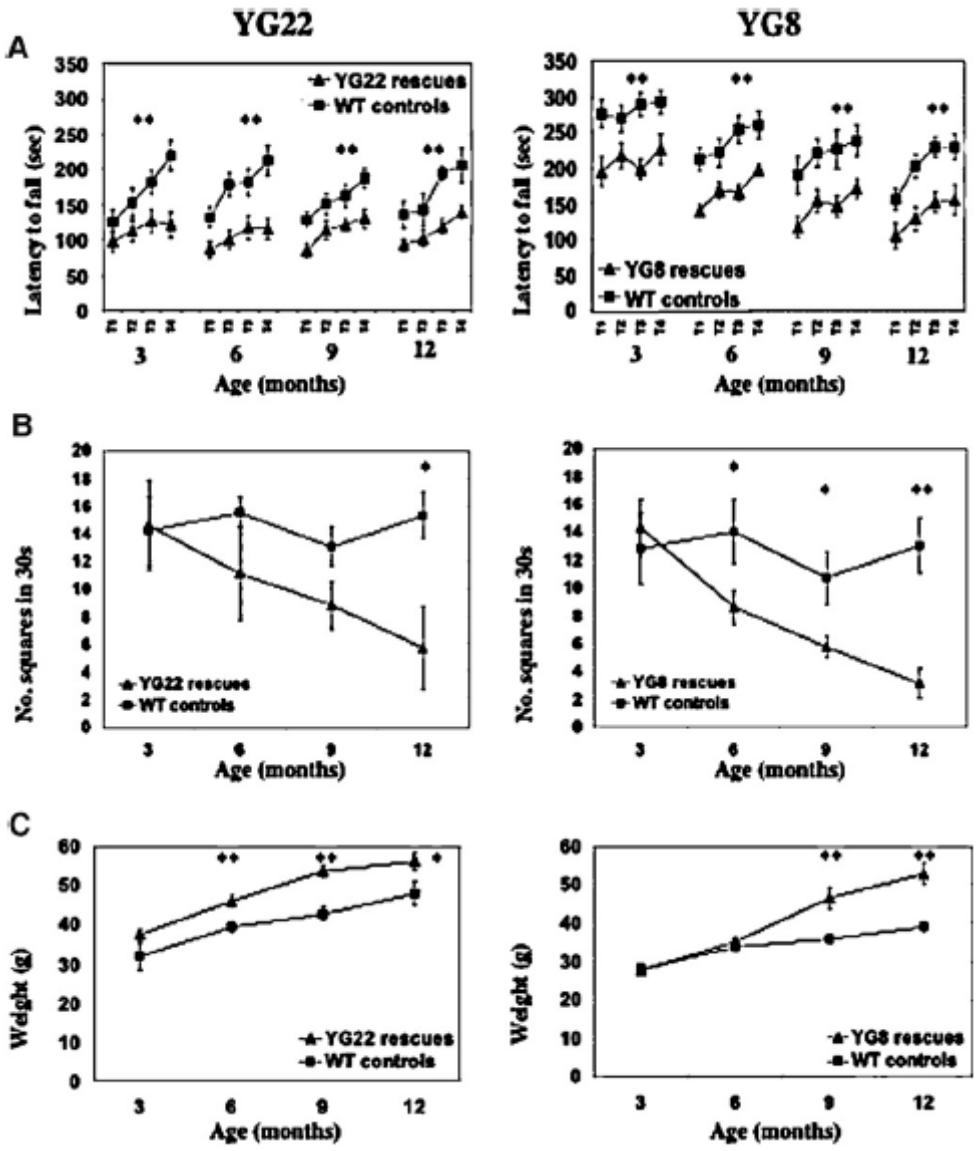

Figure 1.34 – Functional studies of 3, 6, 9, and 12 month old YG22 and YG8 rescue mice, compared with wild-type controls. (**A**) Rotarod analysis of YG22 and YG8 rescue mice compared with wild-type littermate controls shows a coordination deficit in both rescue mice from 3 months of age (*n*=10 and 9, respectively). However, a direct comparison between YG22 and YG8 experiments is not possible due to the use of different rotarod acceleration rate settings carried out at different periods of time. (**B**) Locomotor analysis identifies a progressive decrease in the mobility of both rescue mice (*n*=6–8 and 7–13, respectively). (**C**) Weight increases are detected in both rescue mice (*n*=6–16). Error bars indicate SEM. *p<0.05, **p<0.01 (Al-Mahdawi *et al.* 2006).

Histological abnormalities in the DRG and heart in FXN YAC GAA mouse model

Vacuoles were identified in the DRG of the *FXN* YAC GAA mouse models (Figure 1.35A), similar to those in the "Cb" neuron-specific frataxin conditional knockout model (Simon *et al.* 2004). The vacuolar pathology progressed from affected distal lumbar regions at 6 months of age to more proximal cervical regions at 13–15 months (Al-Mahdawi *et al.* 2006), resembling the dying-back phenomenon of neurodegeneration that is observed in FRDA patients. Although DRG vacuoles have not been described in FRDA patients, loss of large sensory DRG cell bodies is a hallmark of the disease. Thus, it is likely that this represents a milder or earlier effect in the *FXN* YAC GAA mouse models, before the DRG neurons degenerate and are lost completely. Iron deposition was also identified in the hearts (Figure 1.35B) of only older mice, confirming the later onset aspect of this pathology as previously described for cardiac frataxin conditional knockout mouse mutants (Puccio *et al.* 2001).

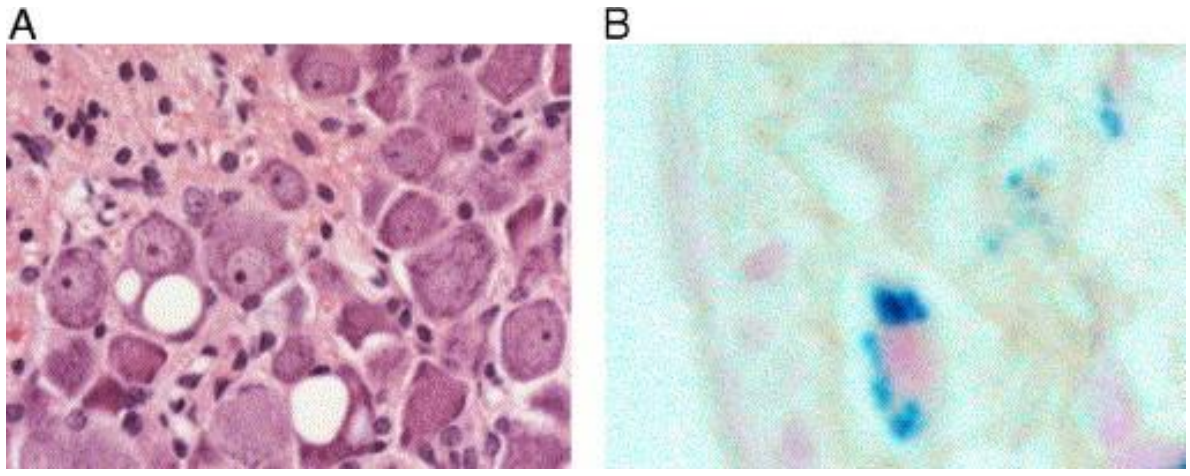

Figure 1.35 – Neuronal and cardiac histopathology. (**A**) H&E-stained section of lumbar DRG from a representative YG22 rescue mouse over 1 year of age, showing two neurons containing large vacuoles. Original magnification 400×. (**B**) Perl's staining of a heart section from a representative YG22 rescue mouse over 1 year of age, showing characteristic blue staining indicating iron deposition. Original magnification 600× (Al-Mahdawi *et al.* 2006).

Ultrastructure pathology in the DRG and heart in FXN YAC GAA mouse model

Electron microscopy of DRG from *FXN* YAC GAA mice identified lipofuscin deposition, chromatolysis, swelling of neuronal cell bodies and demyelination of axons (Figure 1.36) similar to a mouse model of ataxia with vitamin E deficiency, indicating chronic oxidative stress (Yokota *et al.* 2001).

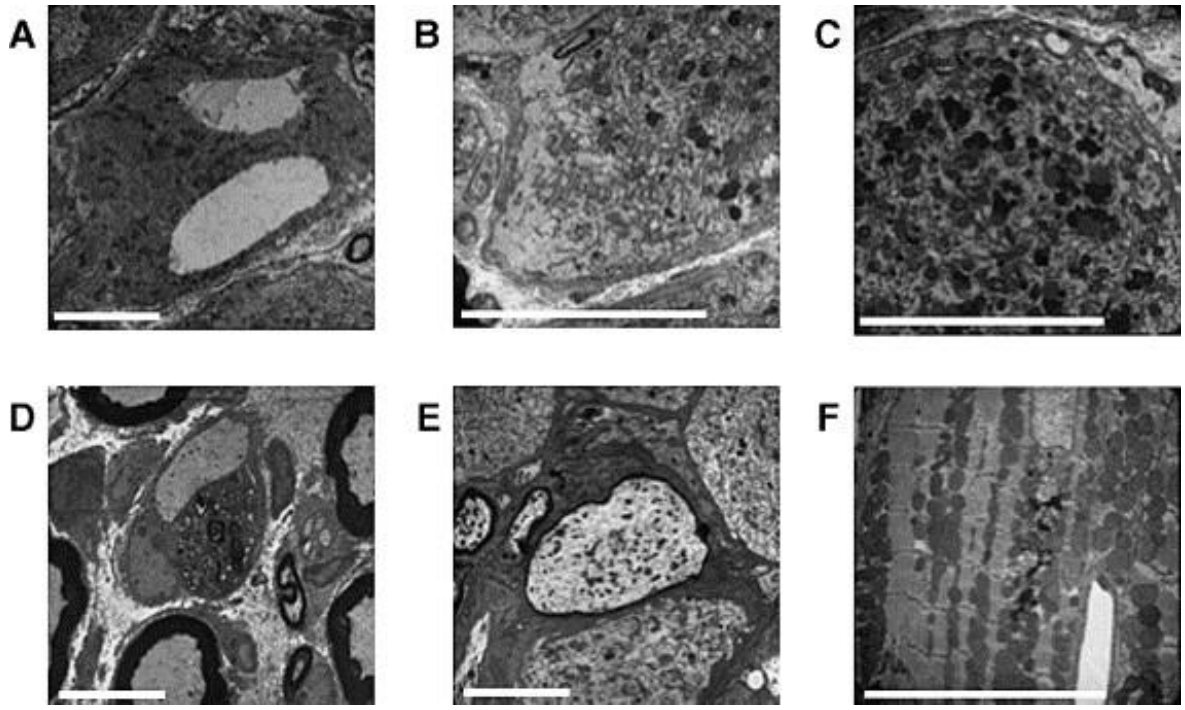

Figure 1.36 – Electron microscopy of lumbar DRG and cardiac muscle of YG8 mice. (**A–E**) Electron micrographs of lumbar DRG from 20-month-old YG8 rescue mice showing examples of: (**A**) giant vacuoles, (**B**) chromatolysis, and (**C**) lipofuscin deposits within the large neuronal cell bodies. Also detected within the lumbar DRG are instances of: (**D**) complete demyelination of a large axon with its associated Schwann cell and (**E**) large axonal swelling with reduced myelination. (**F**) Electron micrograph of cardiac muscle from a 20-month-old YG8 rescue mouse showing lipofuscin deposition and lysosomes disrupting an ordered array of mitochondria. Scale bars represent 10 µm (Al-Mahdawi *et al.* 2006).

In summary, the *FXN* YAC GAA mouse model of FRDA, which expresses only human-derived frataxin, shows comparatively reduced levels of frataxin mRNA and protein expression, decreased aconitase activity, and oxidative stress, leading to progressive neurodegenerative and cardiac pathological phenotypes (Al-Mahdawi *et al.* 2006). This

phenotype is indicative of the early effects of FRDA pathology that precede overt ataxia and the later development of hypertrophic cardiomyopathy. Indeed, these mild mouse models can be considered representative of the less severe, later onset cases of FRDA. The 190 and 190+90 GAA repeat expansion mutation sizes within our mouse models are also in keeping with the cases of later onset FRDA that have smaller GAA allele sizes of fewer than 200 repeats (Gellera *et al.* 1997; Sorbi *et al.* 2000; Lhatoo *et al.* 2001; McDaniel *et al.* 2001; Berciano *et al.* 2002).

Consequently, a GAA-repeat-based mouse model of FRDA has been generated, that would be suitable for the investigation of many different therapeutic strategies. The fact that such FRDA mouse model has been generated by the introduction of a GAA repeat expansion mutation also makes it appropriate for novel therapeutic strategies aimed at interacting with and modifying the GAA repeat expansion itself.

1.4.4 – *FXN* BAC transgenic mouse models

Recently, a similar strategy to the *FXN* YAC GAA transgenic mouse model has been used to generate a *FXN* bacterial artificial chromosome (BAC) transgenic mouse model (Sarsero *et al.* 2004). As with the human wild-type *FXN* YAC transgenic mice, the 188-kb BAC (pBAC265) containing the complete wild-type *FXN* gene has successfully rescued the embryonic lethality that is associated with homozygosity for the *Fxn* knockout mutation (Sarsero *et al.* 2004). Rescued mice displayed normal behavioural and biochemical parameters (Sarsero *et al.* 2004). A *FXN* BAC transgenic mouse model that contains a GAA expansion mutation (around 500 repeats) has also been generated, but these mice do not exhibit GAA repeat instability nor do they exhibit any FRDA-like phenotype, most likely due to an interrupted GAA tract (J. Sarsero, personal communication).

Chapter 2 – General materials and methods

2.1 – Solutions

General solutions:

- Tail digestion buffer: 100mM Tris-HCl (pH 8), 5mM EDTA, 200mM NaCl, 0.2% SDS
- TE buffer: 10mM Tris-HCl (pH 7.5), 1mM EDTA
- Orange G loading dye (6x): 0.35% Orange G dye, 30% sucrose
- 1x TBE: 90mM Tris, 90mM Boric acid, 2mM EDTA
- 1x TAE: 40mM Tris, 20mM Acetic acid, 1mM EDTA
- Tris/glycerol homogenisation buffer: 100mM Tris-HCl (pH 9.0), 15% glycerol
  - filter-sterilised via 0.2µm pore

Chromatin immunoprecipitation (ChIP) analysis

- Cell lysis buffer: 10mM HEPES pH 8, 85mM KCl, 0.5% NP-40 (Igepal)
- Nuclei lysis buffer: 1% SDS, 10mM EDTA, 50mM Tris-HCl (pH 8)
- Low salt buffer: 1% Triton-X100, 0.1% SDS, 150mM NaCl, 2mM EDTA, 20mM Tris
- High salt buffer: 1% Triton-X100, 0.1% SDS, 500mM NaCl, 2mM EDTA, 20mM Tris
- Dilution buffer: 1% Triton-X100, 150mM NaCl, 2mM EDTA, 20mM Tris
- Elution buffer: 1% SDS, 100mM $NaHCO_3$

Western blot analysis

- Running buffer: 25mM Tris, 190mM glycine, 3.5mM SDS
- Sample buffer: 80mM Tris-HCl (pH 6.8), 12.5% glycerol, 10% SDS, 0.5% BPB, 1% BME
- Transfer buffer: 25mM Tris, 190mM glycine, 10% methanol
- PBS/T: 0.2% Tween-20 in PBS
- 5% milk PBS/T: 5% $^{w}/_{v}$ milk, 0.2% Tween-20 in PBS

OxyBlot analysis

- Dilution buffer: 60mM Tris-HCl (pH 6.8), 2% SDS, 10% glycerol
- Loading buffer: 62.5mM Tris-HCl (pH 6.8), 180mM BME, 0.002% BPB
- Transfer buffer: 12mM Tris-HCl (pH 8.3), 96mM glycine, 20% methanol

Electrophoretic mobility shift assay (EMSA) analysis

- Binding buffer: 5mM $MgCl_2$, 0.1mM $ZnSO_4$, 1mM DTT, 0.1% Nonidet P-40, 10% glycerol in PBS

Southern blot analysis

- Church buffer: 340mM Na_2HPO_4, 180mM NaH_2PO_4, 1mM EDTA, 7% SDS

Histological analysis

- Heparinised saline: 2u/ml heparin in PBS
- 4% paraformaldehyde saline (pH 7.4): 4% $^{w}/_{v}$ paraformaldehyde, 30mM NaOH in PBS
- Hillman & Lee's EDTA: 150mM EDTA, 10% formalin
- Acid alcohol: 1% HCl in 70% IMS

2.2 – Primers

Oligonucleotides were obtained from either previous studies (as referred to) or designed using Primer3 software (Rozen and Skaletsky 2000). All primers were purchased from Sigma-Genosys.

Table 2.1 – Primers used for genotyping

Primer name	Sequence (5' – 3')	Product length
GAA repeat (Campuzano *et al.* 1996)		
GAA-F	GGGATTGGTTGCCAGTGCTTAAAAGTTAG	457 bp + 3xGAA_n
GAA-R	GATCTAAGGACCATCATGGCCACACTTGCC	
Fxn knockout (Cossee *et al.* 2000)		
WJ5	CTGTTTACCATGGCTGAGATCTC	
WN39 (Wt specific)	CCAAGGATATAACAGACACCATT	520 bp
WC76 (KO specific)	CGCCTCCCCTACCCGGTAGAATTC	245 bp
Msh2 knockout (Toft *et al.* 1999)		
Msh2-P1	CGGCCTTGAGCTAAGTCTATTATAAGG	
Msh2-P2 (KO specific)	GGTGGGATTAGATAATGCCTGCTCT	194 bp
Msh2-P3 (Wt specific)	CCAAGATGACTGGTCGTACATAAG	164 bp
Msh3 knockout (de Wind *et al.* 1995)		
Msh3-P1 (Wt specific)	CAGGAAGAGGTCACTGGGAAATGG	130 bp
Msh3-P2 (KO specific)	GGTGGGATTAGATAATGCCTGCTCT	250 bp
Msh3-P3	GCTGAGAATACTTAGTCTCTGGCA	
Msh6 knockout (de Wind *et al.* 1995)		
Msh6-P1 (Wt specific)	CAAGTCCTAGGATTAGAGGTCTGG	220 bp
Msh6-P2 (KO specific)	CCGGTGGATGTGGAATGTGTGCG	253 bp
Msh6-P3	CCATGCAAATCAGACTCGATACAA	
Pms2 knockout (designed by Mark Pook)		
Pms2-P1	ACAGTTACATTCGGTGACAG	
Pms2-P2 (KO specific)	TTTACGGAGCCCTGGCGC	189 bp
Pms2-P3 (Wt specific)	ACTAATTCCCCTACGGTTTAG	385 bp
Atm knockout (Liao *et al.* 1999)		
Atm-P1	GACTTCTGTCAGATGTTGCTGCC	
Atm-P2 (Wt specific)	CGAATTTGCAGAAGTTGCTGAG	162 bp
Atm-P3 (KO specific)	GGGTGGGATTAGATAAATGCCTG	441 bp

Table 2.2 – Primers used for Q-RT-PCR analysis of *FXN* expression

Primer name	Sequence (5' – 3')	Product length
FXN (Al-Mahdawi *et al.* 2008)		
FxnRT-F	CAGAGGAAACGCTGGACTCT	172 bp
FxnRT-R	AGCCAGATTTGCTTGTTTGGC	
Gapdh – endogenous control (Al-Mahdawi *et al.* 2008)		
Gapdh-F	ACCCAGAAGACTGTGGATGG	81 bp
Gapdh-R	GGATGCAGGGATGATGTTCT	

Table 2.3 – Primers used for EMSA/ChIP Q-PCR analysis of CTCF

Primer name	Sequence (5' – 3')	Product length
FXN – 5'UTR		
h-FXN-pro - F	AAGCAGGCTCTCCATTTTTG	186 bp
h-FXN-pro - R	CGAGAGTCCACATGCTGCT	
FXN – GAA upstream (Herman *et al.* 2006)		
h-FXN-up - F	GAAACCCAAAGAATGGCTGTG	116 bp
h-FXN-up - R	TTCCCTCCTCGTGAAACACC	
FXN – GAA downstream		
h-FXN-down - F	TGGGTTGTCAGCAGAGTTGT	165 bp
h-FXN-down - R	CCGATAATCCCAGCTACTCG	
DM1 site 1 – CTCF positive (Filippova *et al.* 2001)		
DM1-1-F	GCCTGCCAGTTCACAACC	150 bp
DM1-1-R	AGCAGCATTCCCGGCTAC	
DM1 site 3 – CTCF negative (Filippova *et al.* 2001)		
DM1-3-F	AGCTTTCTTGTGCATGACG	226 bp
DM1-3-R	GGTTGTTGGGGGTCCTGTAG	
H19 – CTCF positive (Burke *et al.* 2005)		
h-H19 - F	CCCATCTTGCTGACCTCAC	165 bp
h-H19 - R	AGACCTGGGACGTTTCTGTG	
*H19*neg – CTCF negative (Burke *et al.* 2005)		
h-H19neg - F	CATCATGGTGTCCTCACAGG	161 bp
h-H19neg - R	AGCTCTAAGGGAGGCTCCAG	

2.3 – General techniques

Centrifugation of samples was performed in different equipment according to sample size and temperature requirements: centrifugation of small samples (≤ 1.5ml) at room temperature using a standard bench top microcentrifuge (16K, BioRad) and at 4°C using a refrigerated microcentrifuge (5415R, Eppendorf); while larger volumes (≤ 50ml) were centrifuged in a Centaur 2 centrifuge (Sanyo/MSE). 96 well plates were centrifuged at room temperature using a Legend T centrifuge (Sorvall).

Incubations at lower temperatures (37-60°C) were performed in waterbaths (Grant), while for higher temperatures a heating block (DB-2A, Techne) was used.

The pH of solutions was determined using a pH meter (Delta 340, Mettler) and pH adjustments were made by adding either concentrated HCl or NaOH.

Agarose gel electrophoresis

Agarose gel electrophoresis was used to separate DNA fragments. 0.8%-2% agarose (UltraPure electrophoresis grade, Invitrogen) gels were prepared in 1x TBE/TAE. The agarose solution was melted using a standard microwave and allowed to cool until approximately 60°C. Ethidium Bromide was then added to a final concentration of 0.5µg/ml and the gel was poured and allowed to set. Small gels (50ml) were run in mini-gel tanks (Flowgen Bioscience) while a midi-gel tank (BRL) was used for larger gels (150ml). Products were loaded on gels by adding 6x Orange G loading dye. Gel electrophoresis was performed in 1x TBE/TAE (same as used to prepare gel) and powered by a power pack at 50-100V.

Gels were visualised and documented using a UV-lighted gel documentation cabinet (Alpha Innotech).

DNA extraction: ethanol method (Wang and Storm 2006)

This method was used to quickly extract genomic DNA from mice tails for routine genotyping. Tail samples (<5mm in length) were collected in eppendorf tubes. 400µl of tail digestion buffer and 10µl of 50mg/ml Proteinase K was added to the tail sample, followed by brief vortexing and overnight incubation at 55°C in a waterbath. After digestion, samples were vortexed and centrifuged at 14K rpm for 5min. Avoiding transferring any of the cell/hair/bone debris, the supernatant was collected into a new eppendorf tube. 1ml of absolute ethanol was added, immediately followed by brisk inversion several times. Samples were incubated for 10min at -80°C followed by spinning at 14K rpm for 30min at 4°C. The ethanol was drained off and the pellet washed with 1ml of 70% ethanol. Samples were recentrifuged at 14K rpm for an extra 20min at 4°C and the ethanol carefully drained off. The tubes were left to dry inverted on paper towels for ~10min. The DNA pellet was resuspended in 50-100µl of TE buffer and stored at 4°C.

DNA extraction: phenol/chloroform method (Sambrook *et al.* 1989)

This method was used to extract genomic DNA from samples where greater DNA quality was necessary. Proteinase K digestion was performed as just described. After digestion, samples were vortexed and 400µl of phenol (equilibrated with Tris-HCl pH 8.0) was added. Samples were mixed by vortexing (2x 15s) and centrifuged at 14K rpm for 5min at 4°C. 380µl of the upper aqueous phase was removed to a fresh eppendorf tube and 380µl of chloroform/isoamyl alcohol (24:1) was added, followed by a brief vortex and spin at 14K rpm for 5min at 4°C. 350µl of the resulting upper aqueous phase was transfered to a fresh eppendorf tube and 35µl of 3M Na-acetate (pH 5.2) was added. 700µl of absolute ethanol was then added and ethanol precipitation performed as previously described.

Determination of DNA concentration and purity

The concentration of DNA was determined using a UV spectrophotometer (BioPhotometer, Eppendorf). DNA samples were diluted 1:20 and the absorbance (A) was measured at 260nm. The DNA purity was determined by the $A_{260/280}$ ratio (≥ 1.8).

Purification of PCR products from agarose gels

This method involves the use of agarose gel electrophoresis and a gene-cleaning kit (Geneclean III, Bio 101) to purify PCR products. PCR products (~20µl) were separated on a 0.8% agarose TAE mini-gel for approximately 2hr at 100V in 1x TAE buffer, leaving an empty well between each sample loaded. Using a scalpel blade and under high wavelength UV light (362nm), the bands were excised from the gel and transferred to eppendorf tubes. The weight of the excised gel block was determined and 3x that was added of NaI volume. The agarose blocks were completely dissolved by incubating at 55°C in a waterbath. 5µl of glassmilk was added to each sample. The samples were incubated on ice for a minimum of 30min with gentle shaking. The tubes were then centrifuged at 14k rpm for 15min and the supernatant discarded. The glassmilk pellet was washed 3x by adding 250µl of "new wash" solution, followed by brief vortexing and centrifugation as described above. The pellet was briefly air-dried and then resuspended in 6µl of dH_2O. The DNA was eluted from the glassmilk by vortexing and incubating at 55°C for 5min in a waterbath. The purified DNA was collected as the supernatant phase, and 1µl was separated in a 1% agarose TBE mini-gel to confirm the success of purification. The DNA sample was stored at -20°C.

Radioactive labelling of PCR products

Gene-cleaned PCR products used for labelling were prepared as previously described.

γ-^{32}P ATP labelling

End-labelling with ^{32}P was performed using T4 polynucleotide kinase (PNK) kit (Invitrogen) and γ-^{32}P ATP (PerkinElmer). Reactions were prepared in a final volume of 10µl by adding the following in order: 1µl of gene-cleaned PCR product, 5µl of dH_2O, 2µl of 5x Forward buffer, 1µl T4 PNK and 1µl of γ-^{32}P ATP. The reaction was performed at 37°C for 1hr and terminated at 65°C for 15-30min. The final volume was adjusted to 100µl with TE.

α-^{32}P ATP labelling

Labelling with ^{32}P was performed using the RadPrime DNA labelling system (Invitrogen) and α-^{32}P dCTP (PerkinElmer). Initially, 5µl of gene-cleaned PCR product was diluted in 15µl of TE buffer and heat-denatured by incubating at 100°C for 5min, followed by immediate incubation on ice for 5min. The labelling reaction was prepared in a final volume of 50µl by adding the following in order: 3µl of 1.5mM dNTP mix (dATP + dGTP + dTTP), 20µl of 2.5x RadPrime buffer, 1µl of α-^{32}P dCTP and 5µl of klenow fragment. The reaction was performed at 37°C for 45min. The final volume was adjusted to 100µl with TE buffer.

Removal of unincorporated nucleotides

Unincorporated radionucleotides were removed using a MicroSpin S-200 HR column (Amersham Biosciences). The column was prepared by re-suspending the resin by vortexing. The column cap was slightly loosened (¼ turn) and the bottom closure was broken. The column was placed in an eppendorf tube and centrifuged for 1min at 3k rpm. The column was transferred to a fresh tube and the sample (100µl) was then carefully applied to the top-centre of the resin bed. The purified ^{32}P labelled PCR product was then eluted by centrifuging for 2min at 3k rpm and either used immediately or stored at -20°C.

Extraction of total RNA

This method involved the use of Trizol (Invitrogen) to isolate total RNA following the supplier guidelines. 30-60mg of frozen mouse brain or heart tissue was collected in a 1.5ml eppendorf tube. 1ml of Trizol solution was added and the tissue was homogenised using an eppendorf homogenising plastic rod. The homogenates were incubated for 5min at 30°C. 0.2ml of $CHCl_3$ was added followed by vigorous shaking by hand for 15sec. The homogenates were incubated for 15min at 30°C and phase separated by centrifuging at 14k rpm for 15min at 4°C. The upper aqueous phase was transferred to a fresh tube and the RNA precipitated by mixing with 0.5ml isopropyl alcohol, incubating for 10min at 30°C, and centrifuging at 12k rpm for 10min at 4°C. The supernatant was discarded and the RNA pellet was washed with 1ml of 75% ethanol. The sample was then centrifuged at 7.5k rpm for 5min at 4°C. The supernatant was discarded and the RNA pellet air-dried. The RNA was finally dissolved in 50-100µl DEPC-treated dH_2O (pre-heated to 60°C), mixed by pipetting and incubated for 10min at 60°C. The RNA quality was crudely checked by separating 5µl in a 2% agarose mini gel in 1x TBE. RNA was either used immediately for cDNA synthesis or stored at -80°C.

cDNA synthesis

This method involved the use of a cloned AMV first-strand cDNA synthesis kit (Invitrogen) to convert mRNA to cDNA following the supplier guidelines. On ice, 2µl of total RNA was added to 9.5µl of dH_2O in an RNase-free eppendorf tube. 1µl of Oligo(dT) primer was added followed by annealing at 65°C for 10min, and then transferred to ice. The following kit reagents were then added in order: 1µl of RNase inhibitor, 4µl of 5x RT buffer, 1µl of 100mM dNTPs, 1µl of 80mM sodium pyrophosphate, and 0.5µl of AMV Reverse

Transcriptase (RT). The 20µl reaction was gently mixed by taping the tube and briefly centrifuged to bring all contents to the bottom of the tube. The RT reaction was then completed by incubating at 42°C for 1hr. The contents were again brought to the bottom of the tube by brief centrifugation. The RT reaction was terminated by incubating at 95°C for 2min. The cDNA was then transferred to ice and either immediately used for RT-PCR or stored at -80°C.

Preparation of protein lysates

Following the method of Campuzano *et al.* (1997), 30-60mg of frozen mouse brain tissue was collected in a 1.5ml eppendorf tube and homogenised on ice in 312µl of Tris/glycerol homogenisation buffer, in the presence of protease inhibitors, using an eppendorf homogenising plastic rod. The homogenate was then passed through a 19G needle 5x, followed by an additional 5x through a 21G needle to shear the DNA. This was followed by the addition of 60µl of 10% SDS. The homogenates were subsequently incubated at 100°C for 10min and then put on ice. The samples were centrifuged at 14K rpm for 10min at 4°C and the clear supernatant was collected in a fresh eppendorf tube. DTT was added at a final concentration of 1mM and the final protein lysates were stored at -80°C. Protein concentrations were determined by the BCA protein assay method, on samples without DTT.

Determination of protein concentration using BCA protein assay

The protein concentration was estimated using the BCA Protein Assay Reagent Kit (Perbio). This is a detergent-compatible formulation based on bicinchoninic acid (BCA) for the colorimetric detection and quantification of total protein. A set of protein standards (samples with known protein concentration) was produced by diluting the contents of one bovine serum albumin (BSA) ampoule [2mg/ml] with Tris/glycerol homogenisation buffer into several eppendorf tubes as shown on Table 2.4.

Table 2.4 – Preparation of diluted BSA standards for BCA analysis

Tube	Volume of homogenisation buffer	Volume and source of BSA	Final BSA concentration
A	–	300µl of stock	2,000µg/ml
B	125µl	375µl of stock	1,500µg/ml
C	325µl	325µl of stock	1,000µg/ml
D	175µl	175µl of tube B dilution	750µg/ml
E	325µl	325µl of tube C dilution	500µg/ml
F	325µl	325µl of tube E dilution	250µg/ml
G	325µl	325µl of tube F dilution	125µg/ml
H	400µl	100µl of tube G dilution	25µg/ml
I	400µl	–	0µg/ml

According to the number of samples studied at one time, two different methods were used: test tube or microplate procedures.

Test tube procedure

This approach was taken when dealing with lower sample numbers (i.e. for Western blotting and EMSA). 2ml of working reagent (WR) was prepared for each sample and was added to appropriately labelled bijou tubes. 100µl of protein lysate, diluted 1:20 with Tris/glycerol homogenisation buffer, was added to the respective bijou, followed by a gentle mix. The bijous were incubated at 37° C for 30min, in a waterbath. Tubes were then left to

cool to room temperature. 1ml of each sample was pipetted into clean cuvettes and the absorbance at 562nm (A_{562}) of the standards and protein lysates was measured using a spectrophotometer (BioPhotometer, Eppendorf).

Microplate procedure

This approach was taken when dealing with higher sample numbers (i.e. for Oxyblot analysis). 200µl of WR was prepared for each sample/standard and added to individual wells of a 96 wells microplate. 25µl of protein lysate, diluted 1:20 with homogenisation buffer, was added to the respective wells, followed by a gentle mix. 25µl of the BSA standards was also added. The plate was incubated at 37° C for 30min in an incubator and then allowed to cool at room temperature. The A_{562} of the standards and protein lysates was then measured using a plate reader (BP800, BioHit).

Following either method, a standard curve was prepared by plotting the blank-corrected measurement for each BSA standard against its concentration. The standard curve was then used to determine the protein concentration of each study sample.

Preparation of nuclear extracts

Nuclear extracts were prepared from normal human cerebellum autopsy tissue. In a 50ml falcon tube, 0.7g of tissue was homogenised in cold PBS using a 5mm dispersing element (S8N-8G, IKA Labortechnik), attached to a rotor (Ultra-Turrak T8, IKA Labortechnik). The homogenisation was performed in increasing volumes of cold PBS up to a final volume of 15ml. The sample was centrifuged at 5k rpm for 5min at room temperature. The supernatant was discarded and the pellet washed 2x with 15ml cold PBS. The cells were pelleted by centrifuging as before and the supernatant discarded. The cells were lysed in the presence of protease inhibitors in 3.5ml of cell lysis buffer, for 10min on ice. The sample was

then split in 4 equal volumes (~1ml each) and transferred to eppendorf tubes. The nuclei were pelleted by centrifuging for 10min at 13K rpm, 4°C. The pelleted nuclei were then lysed in the presence of protease inhibitors in 350µl of nuclei lysis buffer, for 10min on ice. The cell debris was removed by centrifugation for 30min at 13K rpm, 4°C. The supernatants were collected and combined. To reduce the viscosity of the nuclear extract, this was passed through a 25G needle 5x. Nuclear extracts were aliquoted and stored at -80°C. Protein concentration was determined using the BCA assay as described above.

Polyacrylamide gel electrophoresis (PAGE)

PAGE was performed using AE-6200 gel apparatus (ATTO Corp.) powered by BioRad power pack. PAGE was performed differently for Western blot and EMSA analysis.

PAGE for Western blotting

The gel plates were sealed and assembled in an upright position and held in place with bulldog clips. An appropriate well forming comb was slotted in place and the bottom of the wells was marked on the glass plate. A 12% resolving polyacrylamide gel (37.5:1 acrylamide, 0.5mM Tris (pH 8.8), 0.1% SDS) was prepared in a glass flask. Polymerisation was initiated by adding 0.05% APS and 0.05% TEMED. The resolving gel was gently poured between the gel plates up to ~1cm below the comb marking. Water-saturated butanol was immediately added over the gel mix to prevent air contact and the gel was left to polymerise for 30-40min. The butanol was drained and the gel rinsed with dH_2O. A 4% stacking polyacrylamide gel (37.5:1 acrylamide, 0.125mM Tris (pH 6.8), 0.1% SDS) was then prepared in a glass flask and polymerisation was started by adding 0.05% APS and 0.1% TEMED. The stacking gel was gently poured on top of the resolving gel and the well comb was then fitted. The gel was allowed to polymerise for 45-60min. The gel cast was then put inside the PAGE tank and

approximately 1L of 1x running buffer was poured into the two compartments of the tank in order to establish an electric current through the gel, from the upper to the lower end. The comb was then removed and the wells carefully flushed with running buffer, using a syringe and needle. The tank was connected to the power pack and the presence of current was checked. After loading of samples, gels were run at 150V for 3-4hr.

PAGE for EMSA analysis

The gel plates were sealed and assembled in an upright position and held in place with bulldog clips. A 4% nondenaturing polyacrylamide gel (29:1 acrylamide, 0.5x TBE) was prepared in a glass flask and polymerisation was started by adding 0.05% APS and 0.1% TEMED. The gel was carefully poured between the plates, the well forming comb fitted and the gel was left to polymerise for approximately 30min. The gel cast was fitted inside the PAGE tank and approximately 1L of 0.5x TBE buffer was poured into the two compartments of the tank. The comb was then removed and the wells carefully washed out with 0.5x TBE using a syringe and needle. The tank was connected to the power pack and the presence of current was checked. After loading of samples, gels were run at 50-100V for 1-2hr.

X-ray film processing

Radiographic imaging was always performed in a dark room under red safety light. Amersham Hyperfilm ECL films (GE Healthcare) were exposed to radioactive gels/chemiluminescent blots in x-ray cassettes. Exposure was performed for a range of different times (30s-days). Longer exposures (≥ 15min) were performed at -80°C. The films were either developed using an automatic film processing unit (Xograph) or hand-developed using X-OMAT developer and fixer solutions (Kodak). Hand development was performed by soaking the film in developer solution for 1-2min, followed by a brief wash under running tap water. The film was then soaked in fixer solution for 2min, followed by an extensive wash under running tap water. Finally the film was air-dried.

Densitometry analysis

Densitometry was carried out using UN-SCAN-IT software (Silk Scientific Corp.). Initially, developed films were scanned using a desktop scanner (G2710, HP) and the resulting images were saved as high resolution greyscale JPEG files. Images were imported into UN-SCAN-IT and the bands of interest were selected by drawing a rectangle around it. The analysis method was slightly different between Oxyblots and Western blots. For Western blot analysis the segments' size varied from band to band as these were individually drawn to just include the band of interest. On the other hand, for Oxyblot analysis all segments covered exactly the same sized area in order to minimise background effects (Figure 2.1). Nevertheless, background correction was performed for both methods. The pixel average figures (combined intensity of all pixels in each segment divided by the segment size) were used as measurement for graphical/statistical analysis.

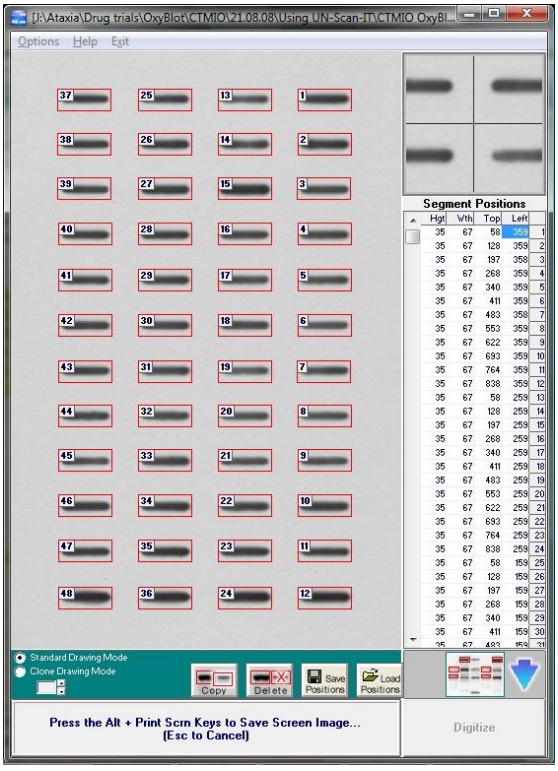

Figure 2.1 – Screenshot capture of UN-SCAN-IT densitometry for Oxyblot analysis.

Statistical analysis

Graphical visualisation and statistical analysis of data was performed using both Microsoft Excel and SPSS software. Student's *t* test and Mann-Whitney test for independent samples were used to determine if the mean values between two different groups of samples were significantly different or not. Two-way mixed analysis of variance (ANOVA) for repeated measures was also performed to investigate the effect of therapeutic compounds over a specific period of time.

2.4 – Genotyping of newborn mice

Newborn mice were weaned at approximately 3 weeks of age. The mice ears were clipped for identification purposes and, after local anaesthesia with Ethyl Chloride BP (Cryogesic, Acorus Therapeutics Ltd) the tip of the tail (<5mm in length) was collected into a sterile eppendorf tube. The tails were digested with proteinase K and the DNA extracted as previously described.

PCR genotyping was performed for the presence/absence of the *FXN* YAC transgene by amplifying the GAA repeat. In addition, PCR analysis was also performed to determine the knockout genotype of *Fxn*, *Msh2*, *Msh3*, *Msh6*, *Pms2* and *Atm*. All primers used for genotyping PCRs are described in Table 2.1. PCR reactions were performed using *Taq* 2x mastermix (Qiagen) in a final volume of 25µl containing appropriate amounts of the respective forward and reverse primers (Table 2.5) and 1µl of DNA. For each PCR experiment DNA samples with known genotype were used as controls (at least one sample used for each possible genotype). In addition, a reaction containing dH_2O in place of DNA was prepared for each experiment as a contamination control.

PCR amplification was performed in 0.25ml tubes using a thermal cycler (PTC-225, MJ Research) and the cycling conditions were as described in Table 2.6. To visualise the results, 10-15µl of PCR product was separated in 1-2% agarose TBE mini-gels along with $1kb^+$ DNA ladder (Invitrogen) at 75V for ~30min.

Additionally, samples positively identified for the presence of the *FXN* YAC transgene were further analysed to obtain a better estimation of the GAA repeat size. This was achieved by separating the GAA PCR products, along with $1kb^+$ and 100bp DNA ladders (Invitrogen), on a 20cm-long 1.5% agarose 1xTBE gel at 50V, overnight.

Table 2.5 – Primer amounts used for various genotyping PCRs

Primer	Amount per reaction	Primer	Amount per reaction
GAA repeat		*Msh2/Msh3/Msh6/Atm* knockout	
GAA-F/R	12.5pmol	P1/P2/P3	12.5pmol
Fxn knockout		*Pms2* knockout	
WJ5/WN39	20pmol	P1	30pmol
WC76	3.5pmol	P2	20pmol
		P3	10pmol

Table 2.6 – Cycling conditions for various genotyping PCRs

GAA	*Fxn*	*Msh2/3/6*	*Pms2*	*Atm*
94°C 2min	94°C 2min	94°C 1min	94°C 1min	94°C 1min
10x 94°C 10s 60°C 30s 68°C 45s	40x 94°C 20s 54°C 20s 72°C 20s	30x 94°C 30s 60°C 30s 72°C 1min	40x 94°C 20s 49°C 20s 72°C 20s	30x 94°C 30s 55°C 30s 72°C 1min
20x 94°C 10s 58°C 30s 68°C 1min *	72°C 6min	72°C 10min	72°C 10min	72°C 10min
68°C 6min				

* - time increased by 20s increments per cycle.

2.5 – Mice breeding for drug treatments

FRDA mice were approximately 84% B6 while Wt mice were 100% B6. Animal husbandry was performed under controlled temperature and light/dark cycles. The breeding of mice was designed to produce litters with maximum numbers of either rescue FRDA mice (YG8 and YG22) or wild type mice. Initially, the main strategy to get rescue FRDA mice consisted on mating hemizygous rescue mice (FXN^{+}, $Fxn^{-/-}$). Although this strategy produced only FRDA rescue mice, a small proportion would have been homozygous rescue mice ($FXN^{+/+}$, $Fxn^{-/-}$). Later, with the identification of a few homozygous rescue mice, it was decided that these would be mated with $Fxn^{+/-}$ mice, to produce known hemizygous rescue mice only. The mice were grouped by gender and age, and up to a maximum of 5 per cage.

2.6 – Functional studies during drug treatments

Weight, rotarod performance and locomotor activity measurements were taken at the start of and periodically repeated throughout the drug treatments.

Rotarod performance analysis

Rotarod analysis was performed using a Ugo-Basille 7650 accelerating rotarod treadmill apparatus. A maximum of 5 mice were assessed per run. The mice were placed on the rotating rod with the speed of the rotation gradually increasing from 4 to 40 rpm (increments of 4 rpm per 30 seconds) over a maximum period of 400 seconds. The time taken for each mouse to fall from the rod was recorded. Four runs were completed and a resting period of approximately 200 seconds (minimum) was allowed between each trial.

Locomotor activity analysis

Locomotor activity was assessed by placing the mice in a 3x5 gridded open-field (33cm x 55cm) perspex box. The number of gridded squares entered by the mouse over a period of 30 seconds was recorded. Four runs were completed for each timepoint and a resting period of approximately 200 seconds (minimum) was allowed between each trial.

2.7 – Sample collection from mice post drug treatment

At the completion of the drug treatment the mice were appropriately culled and samples were collected according to the type of analysis desired.

Preparation of mouse tissue for expression and biochemical analysis

For the preparation of samples intended for molecular biology and biochemical analysis, the mice were culled by cervical dislocation and immediately dissected. The tissues collected were snap-frozen in liquid nitrogen and stored at -80°C. The following samples were collected: brain (B); brain stem (Bs); cerebellum (C); spinal cord (Sc); heart (H); lung (Lu); liver (L); pancreas (P); kidney (K); spleen (Sp); skeletal muscle (Sk); blood (Bl); tail (Ta); lumbar vertebral column (Vl); thoracic vertebral column (Vt); cervical vertebral column (Vc); testis (T) and sperm (S) from males; and ovaries (O) from females.

Preparation of mouse tissue for histological analysis

For histological preparations, mice were terminally anaesthetized by intraperitoneal injection with 5µl/g Pentobarbitone Sodium (Pentoject, Ph. Eur. Animalcare Ltd), followed by a preliminary intracardial perfusion with approximately 50ml of heparinised saline. Fixation of tissues was performed by intracardial perfusion with approximately 100ml of 4% paraformaldehyde in PBS. The fixed mice were dissected and a tissue block containing the exposed brain, spinal cord and heart was collected, as well as other tissues such as the pancreas and liver. The fixation of tissues was completed by means of storage in 4% paraformaldehyde in PBS at 4°C for up to 3 days. The fixed tissues were then washed with dH_2O and immersed in 70% EtOH at 4°C for long term storage.

2.8 – Real-time PCR/RT-PCR

Quantitative real-time PCR (Q-PCR) and RT-PCR (Q-RT-PCR) amplification was performed using SYBR Green (SYBR Green 2x mastermix, Applied Biosystems) in a real-time PCR system (ABI Prism 7900HT, Applied Biosystems).

Reactions were carried out in 96 well plates (MicroAmp, Applied Biosystems), in triplicates, and in a final volume of 20µl containing 2.5-5pmol of each of the respective forward and reverse primers and 5µl of gDNA/cDNA. 5µl of dH_2O was added to control reactions instead of template DNA. The reactions were setup on ice while trying to minimize light exposure. The plates were then sealed with real-time plate sealers (MicroAmp, Applied Biosystems) and the reactions briefly mixed by gently shaking the plate. The plate was then briefly (1min) centrifuged at 1k rpm to collect the reactions to the bottom of the wells.

The cycling conditions varied according to the application and were optimised to amplify the different targets (being co-amplified in the same run) with similar efficiencies, ensuring that a clear exponential phase was produced and the plateau phase was reached before the end of PCR program.

Following each real-time PCR run a dissociation curve run was performed by gradually increasing the temperature from 60°C to 95°C. Relative quantification values were determined by the $2^{-\Delta\Delta Ct}$ method using SDS 2.1 software (Applied Biosystems).

2.9 – Chromatin immunoprecipitation (ChIP) analysis

This procedure was performed as previously described by Al-Mahdawi *et al.* (2008). Initially, 30mg of frozen tissue was homogenised in cold PBS, in a final volume of 1ml, followed by cross-linking of DNA and protein by incubating at room temperature for 20min in 1% formaldehyde (Sigma Aldrich). The cross-linking reaction was stopped by adding glycine to a final concentration of 125mM and incubating for 5min at room temperature. The cells were pelleted by centrifugation for 5min at 13K rpm, 4°C, and washed 2x with 500µl cold PBS. The cells were lysed in the presence of protease inhibitors (Roche) in 250µl of cell lysis buffer, for 10min on ice. The nuclei were pelleted by centrifugation for 5min at 5K rpm, 4°C. The pelleted nuclei were then lysed in the presence of protease inhibitors in 100µl of nuclei lysis buffer, for 10min on ice. The DNA was then sheared by sonicating 5x for 10 seconds at 21-22db. The cell debris was removed by centrifugation for 30min at 13K rpm, 4°C, and the DNA collected as the supernatant phase. To assess the quality of the DNA shearing, 5µl were separated on a 1% agarose 1xTBE mini-gel. DNA fractionation was considered acceptable when the majority of the DNA was ≤600bp. The DNA was either immediately submitted to immunoprecipitation or stored at -80°C.

For the immunoprecipitation (IP), protein A-agarose beads (Upstate) were used. Initially, 40µl of beads were washed 2x with 1ml of cold PBS, and resuspended in a final volume of 40µl. The sonicated sample (100µl) was then added to the washed beads and incubated at 4°C with gentle shaking for 2hrs. The beads were removed by centrifuging for 2min at 13K rpm, and collecting the supernatant. An "Input" sample (10µl) was collected and stored at -80°C for later use as control. The remaining sample was diluted to 1ml in ChIP dilution buffer, in the presence of protease inhibitors (Roche). The sample was split into 2 equal parts, and the following added: "+Ab" – 5µl of antibody specific to the protein of

interest; "-Ab" – 5µl of Immunoglobulin G (IgG) (Upstate). Both samples were incubated, with gentle shaking, at 4°C overnight. The IP was achieved by adding 60µl of beads (previously washed as described above), followed by incubation at 4°C with gentle shaking for 2hrs. The beads were pelleted by centrifugation for 30 seconds at 6K rpm, 4°C, and the supernatant discarded. The beads were washed 3x with 1ml of low salt buffer, each time gently rotating at 4°C for 5min, followed by centrifugation for 30 seconds at 6K rpm, 4°C. The beads were then washed 1x as described above with 1ml of high salt buffer. The chromatin was subsequently eluted by adding 150µl of elution buffer to each bead pellet, followed by incubation at 65°C, for 10min. The samples were centrifuged for 30 seconds at 6K rpm, and the supernatant collected into a fresh tube. The elution was repeated as described above and the resulting supernatant combined with the previous one. At this stage, the "Input" sample was thawed and 300µl of elution buffer was added. The cross-linking was reversed on the 3 samples by adding 0.5mg Proteinase K and incubating at 37°C for 30min, followed by 65°C overnight. The DNA was extracted using the phenol/chloroform method, followed by ethanol precipitation in the presence of 100µg of glycogen (Sigma Aldrich). The DNA was finally resuspended in TE buffer ("Input" in 100µl; "+Ab" and "-Ab" in 50µl) for 2 hrs at 4°C and ultimately stored at -20°C.

Relative Q-PCR amplification was carried out with SYBR Green (Applied Biosystems) in an ABI Prism 7900HT real-time PCR instrument (Applied Biosystems) as previously described. Reactions were carried out in triplicates, in a final volume of 20µl containing 12.5pmol of each of the respective forward and reverse primers (Table 2.3). Relative quantification values were normalised to input and minus antibody samples, and finally determined in relation to a control region.

2.10 – Western blot analysis

Protein lysates were prepared from mouse frozen brain tissue and the protein concentration determined using BCA assay as previously described. For each sample, approximately 40µg of protein was prepared in 1x working sample buffer to a final volume of 20µl. Samples were placed at 100°C for 5min and then put on ice. Low and high molecular weight (LMW and HMW) protein markers (BioRad) were incubated at 37°C for 5min prior to loading. Protein samples were separated, alongside the size markers (17µl), by PAGE in a 4% stacking / 12% resolving polyacrylamide gel, at 150V for 3-4hr (until the smaller band of the LMW protein marker was 2-3cm from the end of the gel). The distance migrated by each of the bands of the protein markers was measured from the end of the stacking gel.

Transfer to membrane – Western blotting

Transfer of protein from gel to membrane was performed using a Hoefer TE22 Transphor tank transfer unit (Amersham Biosciences). The transfer tank was filled with approximately 1L 1x transfer buffer, attached to a water cooling system and placed on a magnetic stirrer. The stacking gel was removed and the resolving gel divided into upper and lower sections by cutting the gel at approximately 30kD, so that the protein of interest and the internal control were in separate gel sections. For each gel section one piece of PVDF membrane (Amersham Biosciences) and two pieces of 3MM Whatman paper were cut to match the gels' size. The PVDF membranes were appropriately labelled with a pencil to distinguish the top from the bottom section of the gel. The blotting sponges and filter paper pieces were soaked in 1x transfer buffer for 5min. Separately, the gel sections were also equilibrated in 1x transfer buffer for 5min. The blotting system was assembled in 1x transfer buffer as shown in Figure 2.2. At every step of layering a 10ml pipette was used to smoothen

the surface and remove any air bubbles. The blotting cassette was placed in the transfer tank in a vertical position oriented so that negatively charged molecules would migrate towards the grey anode, transferring from the gel into the nitrocellulose membranes. Transfer was carried out at constant 400mA and 60-80V for 15min.

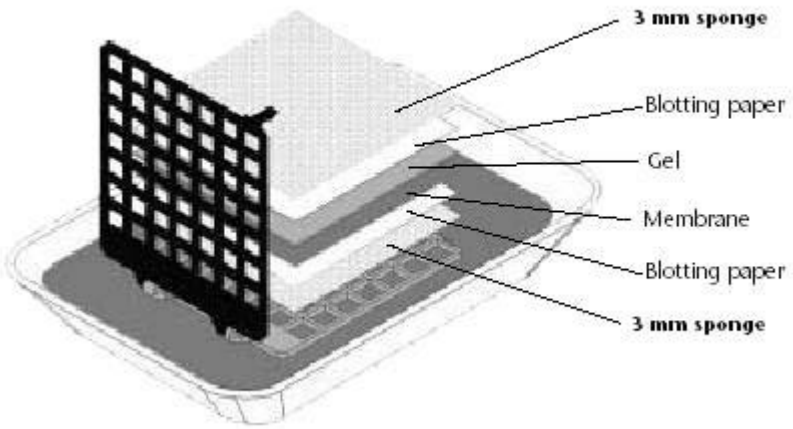

Figure 2.2 – Schematic representation of Western blotting transfer cassette assembly. The cassette panels are colour coded: black is the cathode side and grey the anode side

Gel staining

At the end of the transfer the gel was briefly washed in dH_2O, followed by staining with GelCode blue stain reagent (Perbio) on a shaker for 1h. The gel was washed again in dH_2O for 5-10min. The stained gel was placed on a piece of 3MM Whatman paper, covered with cling film and dried on a gel dryer (5040, Fisherbrand) under vacuum and ramp temperature of 80°C for 2h.

Hybridisation of membrane with antibodies

Separately, each PVDF membrane was briefly washed in PBS/T, transferred to a small plastic box and blocked at room temperature in 10ml 5% milk in PBS/T for 30min with gentle shaking. 5µl of primary antibody was added to the respective box: rabbit anti-tubulin antibody (1:40,000 dilution) (Sigma) was applied to the membrane corresponding to the top section of the gel, and rabbit anti-mature frataxin antibody (1:2,000 dilution) (G. Isaya, Mayo Clinic) was applied to the bottom one. The membranes were incubated at 4°C overnight, with shaking. Each membrane was extensively washed in PBS/T buffer for 2h, at room temperature, with several changes of wash, with shaking. Blocking with 10ml 5% milk in PBS/T was carried out for 30min at room temperature, with shaking. 5µl of secondary antibody (1:2,000 dilution) goat anti-rabbit conjugated with horseradish peroxidase (HRP) (Dako) was added to each membrane. The membrane was then incubated at room temperature for 30min, with shaking. Extensive washing in PBS/T buffer for 2h with several changes of wash was repeated.

Chemiluminescent visualisation and densitometry

SuperSignal West Pico Chemiluminescent Substrate (Perbio) was used to detect HRP on the immunoblots. The membranes were placed on Saran wrap with the protein side upwards. The chemiluminescent reagent mix (1:1 ratio of substrate components) was prepared and 2ml were pipetted onto each membrane covering its entire surface. Incubation was carried out for 5min. The excess reagent was discarded and the membrane was covered with Saran wrap and exposed to Amersham Hyperfilm ECL films (GE Healthcare) for various lengths of time up to 1h. Films were either developed by hand or automatically using a film processing unit (Xograph) as previously described.

2.11 – Oxyblot analysis: detection of protein oxidation

Overall, this method is as previously described by Al-Mahdawi *et al.* (2006) and consists on the use of a protein oxidation detection kit (OxyBlot, Chemicon International). This kit detects protein oxidation by targeting the carbonyl groups introduced into protein side chains by oxygen free radicals and other reactive species.

Derivatisation of protein samples

Initially, protein lysates were prepared from mouse frozen brain tissue and the protein concentration determined using BCA assay as previously described. Protein samples were diluted with dilution buffer so that 30µg of protein was present in a final volume of 15µl. The protein sample was denatured by adding 15µl of 12% SDS and then split into two 10µl aliquots, each containing 10µg of protein. One aliquot was derivatised with 10µl of DNPH while the other was used as a negative control sample and 10µl of derivatisation-control solution was added instead. The derivatisation reaction was performed at room temperature for 15min, and stopped by adding 7.5µl of neutralization solution to both aliquots.

Slot-blotting

This method consisted in the transfer of the derivatised protein samples to a PVDF membrane (Millipore) using a 4x12 slot-blot apparatus. Initially two 6x11cm pieces of PVDF membrane were cut and pencil-labelled for identification and orientation purposes. A single piece of 3MM filterpaper (Whatman) was cut to the same size. The PVDF membrane was activated by soaking in 100% EtOH for 2min and then briefly washed in dH_2O. The membrane was then equilibrated in 50mM Tris-HCl (pH 6.8) for 5min. The 3MM filterpaper was also briefly soaked in this solution. The blotting apparatus was then set up by placing

the 3MM paper over the suction holes (making sure that all holes were completely covered), followed by both PVDF sheets. The slot lid was then applied and the screws tightly tightened. Correct assembly was checked by loading in each slot 100µl of loading buffer and by applying vacuum suction. Each sample was then diluted with loading buffer to a final volume of 100µl and loaded into the appropriate slot. The protein was then transferred to the PVDF membrane by applying vacuum suction. After all samples have filtered through the suction was removed. The membranes were washed by loading 100µl of loading buffer to all wells, followed by suction. A final wash was performed as above but using 100µl of transfer buffer instead. The apparatus was disassembled and the PVDF membranes briefly left to air dry on clean filter paper.

Immunodetection and densitometry

Immunodetection and chemiluminescent visualisation were performed as previously described for the Western blotting, using the primary (rabbit anti-DNP, 1:150 dilution) and secondary (goat anti-rabbit IgG, 1:300 dilution) antibodies included in the OxyBlot kit. Finally, densitometry was carried out using UN-SCAN-IT software (Silk Scientific Corp.) as previously described.

2.12 – Southern blot analysis

This method is based on Sambrook *et al.* (1989). Initially, DNA products were separated on a 1% agarose 1xTBE midi-gel along with 5µl 1kb+ DNA marker at 75V for ~6h.

Transfer to membrane – Southern blotting

A transfer assembly was prepared as depicted in Figure 2.3. The transfer solution used was 0.4M NaOH. The lane containing the DNA marker was excised and the gel was carefully placed with the DNA side upwards on top of the 3MM Whatman filter paper wick. A piece of Hybond N^+ (Amersham Biosciences) membrane was cut to the same size of the gel, labelled for orientation, soaked in 0.4M NaOH and placed over the gel. Two pieces of 3MM Whatman filter paper were also cut to the same size of the gel, soaked in 0.4M NaOH and placed over the membrane. At every step of layering, a 10ml pipette was used to smoothen the surface and remove any air bubbles. A stack of paper towels was placed on top followed by a weight.

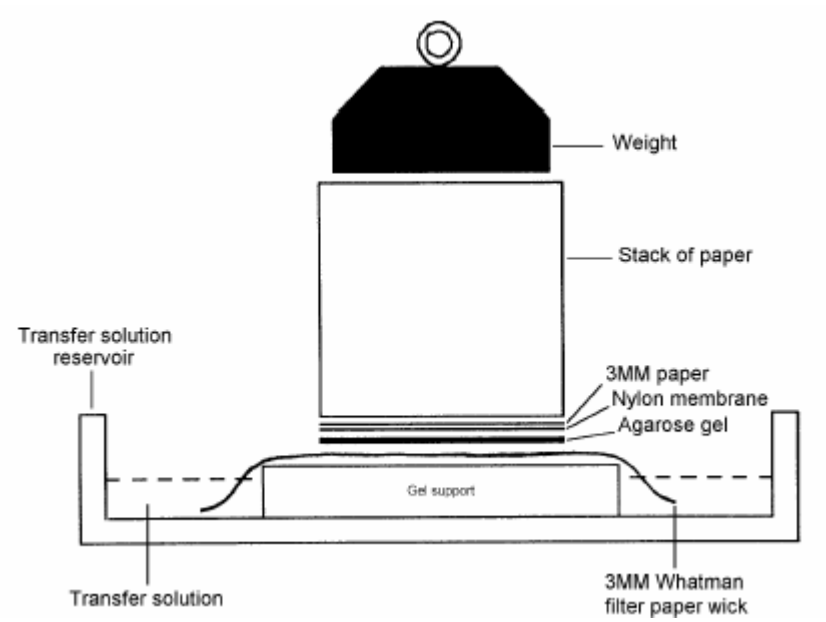

Figure 2.3 – Schematic representation of Southern blotting transfer assembly.

The transfer was carried out overnight by capillary action: the negatively charged DNA was drawn from the agarose gel and bound to the positively charged Hybond N^+ membrane.

Probing of membrane

Following transfer, the membrane was washed twice in 3x SSC. The membrane was then transferred into a hybridisation bottle and pre-hybridisation was carried out in 10ml of pre-warmed Church buffer at 65°C for 2-3h with rotation in a hybridisation oven (HIR12, Grant). An appropriate radioactively ($^{\gamma 32}$P ATP) labelled DNA probe was heat-denatured at 98°C for 10min, followed by 5min incubation on ice. The pre-hybridisation solution was replaced by 10ml of pre-warmed Church buffer containing the denatured radioactive probe. Hybridisation was carried out at 65°C overnight with rotation in a hybridisation oven. Following hybridisation the probe solution was removed and stored at -20°C for future use.

Stringency washing of membrane and development

The membrane was washed inside the hybridisation bottle with pre-warmed 3x SSC / 0.1% SDS at 50°C for 20min with rotation in a hybridisation oven. The blot was monitored with a Geiger counter (Series 900 mini-monitor, Thermo Electron Corp.) and if the background signal was still too strong further stringency washes were performed by initially increasing the incubation period, then increasing temperature to 65°C and finally lowering the SSC concentration all the way down to 0.1x, as necessary. The membrane was exposed to Amersham Hyperfilm ECL films (GE Healthcare) and developed as previously described.

2.13 – Histological analysis of lumbar DRG sections

This method was kindly made available by Lorraine Lawrence, Imperial College London.

Preparation of vertebral column paraffin wax blocks

Paraformaldehyde fixed vertebral column samples were cut into appropriate blocks: using a scalpel blade, cuts were made at the intervertebral disks resulting in 2 blocks, each containing 2 vertebrae: VL_{1+2} and VL_{3+4} (Figure 2.4).

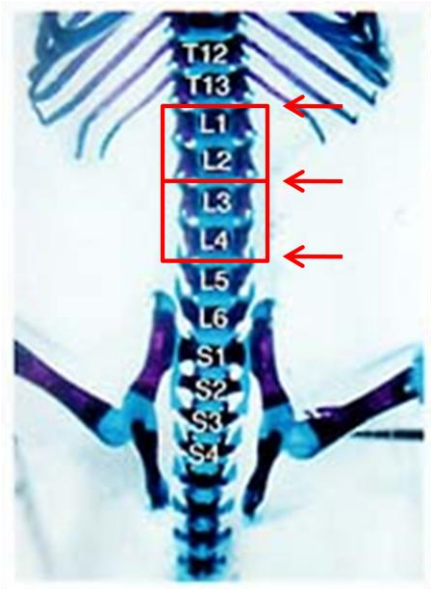

Figure 2.4 – Representation of vertebral blocks processed for histological analysis. The red arrows represent the location of the cutting and the 2 red boxes represent the blocks used.

Excessive muscular and connective tissue surrounding the vertebral column was carefully removed, and the isolated vertebrae block was placed in a tissue-tek cassette. Decalcification was performed by immersing the cassettes in 500ml of Hillman & Lee's EDTA for a minimum of five days, with occasional gentle agitation and changing the solution once a day. The EDTA was then washed off by washing the cassettes under running tap water for at least 4hrs. Using an automated wax embedding unit (Hypercenter XP, Shandon) the cassettes were immersed in increasing concentrations of industrial methylated spirit (IMS),

followed by Histoclear (Sigma Aldrich) and finally in molten paraffin wax-based embedding medium (Kendall), as described in Table 2.7. The final paraffin wax incubation was performed under vacuum for 1 hr.

Table 2.7 – Schedule of incubations performed for paraffin wax embedding.

Solution*	**Duration**
Hillman & Lee's EDTA	5 days (changing solution once a day)
70% IMS	Overnight
90% IMS	4 hr
100% IMS	1.5 hr
100% IMS	1.5 hr
100% IMS	1 hr
Histoclear	Overnight
Histoclear	1 hr
Parafin wax	1.5 hr
Parafin wax	1.5 hr
Parafin wax - Vacuum	1 hr

* - Fresh solutions were used at each incubation step.

The vertebrae block was then vertically positioned in a pre-heated mould, covered with a tissue-tek cassette and submerged by pouring wax. The block was then allowed to cool down on a cold plate and removed from the mould.

Preparation and H&E staining of section slides

DRG-containing transversal sections (6µm thick) were cut using a rotary microtome (AS 325, Shandon) and briefly suspended on the surface of a 37°C waterbath. The sections were then transferred to microscope slides (SuperFrost Plus, VWR) and left to dry overnight at 37°C. The sections were de-waxed by soaking 2x 5min in Histoclear. They were then washed 2x in 100% IMS, followed by 70% IMS, with a brief water rinse in between each wash. The

sections were immersed in Haematoxylin Harris (BIOS Europe) for 2min and put in running tap water until they turned blue. Colour was differentiated by dipping 2x in acid alcohol (1% HCl in 70% IMS). The sections were returned to running tap water until they turned blue. The sections were then immersed in 1% Eosin (BIOS Europe) for 1min and briefly rinsed in running tap water. They were subsequently dehydrated by rinsing with gentle agitation in increasing concentrations of IMS (70%, 90%, 100% and 100%), for 30s each time. Finally, the sections were washed 3 x 5min in Histoclear. Coverslips were applied with DPX mount.

Analysis of neurodegeneration in the DRG

DRG sections were analysed using a light microscope (CH20, Olympus). A minimum of 2 sections was analysed for each vertebrae block. The DRG were screened for the presence of vacuoles within the neuronal cell bodies. For each DRG, as a measurement of neurodegeneration, the number of cells with vacuoles was divided by the total number of neuronal cells.

Chapter 3 – Cannabinoid therapeutic testing in FRDA mice

3.1 – Introduction

Cannabis has been used medicinally in many cultures and civilisations for 5000 years. In China, it was recommended for malaria, constipation, rheumatic pains, childbirth, and was mixed with wine as a surgical analgesic. In India, it has been used as an anticonvulsant, antispasmodic, anti-emetic and hypnotic (Mechoulam 1986). It was used extensively in Britain and America in the second half of the nineteenth century, most notably by Queen Victoria and was prescribed by British doctors up until 1971 (Ashton 1997). However, the use of cannabis as a medicine declined, mainly due to variability in the potency, unpredictable responses with oral use and poor storage stability (Mechoulam 1986). Illegal use of cannabis by patients with Multiple Sclerosis (MS) to treat their symptoms of pain is well established in the literature (Consroe 1998; Pertwee 2002). As a result there is much anecdotal evidence of safety and efficacy.

The *in vitro* and *in vivo* efficacies of cannabis extracts and their individual compounds reported to date in the scientific and medical literature are those of anti-inflammatory (Costa *et al.* 2004), analgesic (Pertwee 2001), anti-anxiety and anti-emetic (Mechoulam *et al.* 2002), anti-cancer (Guzman 2003) and antioxidant (Hampson *et al.* 1998). Antioxidant activity indicates that the extracts and/or compounds derived from cannabis may be effective in preventing and/or treating the development of some cardiovascular and neurodegenerative diseases.

Cannabis based medicines are prepared from the *Cannabis sativa* L. plant. The most abundant potentially therapeutic compounds in the plant are the cannabinoids Δ^9-tetrahydrocannabinol (THC) and cannabidiol (CBD) (Figure 3.1) (Pacher *et al.* 2006). The plant also contains smaller amounts of a wide range of other compounds such as other cannabinoids, terpenoids, flavonoids and sterols (Pacher *et al.* 2006).

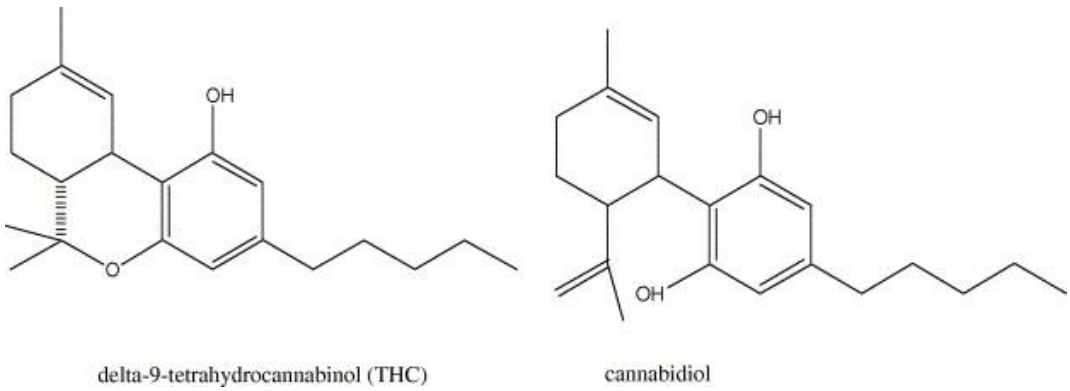

Figure 3.1 – Chemical structures of THC and CBD (Russo and Guy 2006).

3.1.1 – Cannabinoid receptors and ligands

Up until the last two decades, marijuana research was strongly neglected and enjoyed by a rather reserved number of scientists. A contributory factor was the highly lipophilic nature of the biologically active ingredients, which led to the notion that marijuana elicits its effects non-specifically by perturbing membrane lipids (Lawrence and Gill 1975). The first important breakthrough that ultimately led to a rejection of this concept was the identification of the correct chemical structure of THC, the main psychoactive ingredient of marijuana; and the subsequent demonstration that bioactivity resides in the L-stereoisomer of this compound (Mechoulam and Gaoni 1967), which is one of approximately 60 cannabinoids present in the plant (Dewey 1986). This discovery stimulated the generation of a whole range of synthetic analogs in the 1970s that included not only compounds structurally similar to phytocannabinoids but also analogs with different chemical structures, including classic and nonclassic cannabinoids and aminoalkylindoles, as well as the subsequently discovered endogenous arachidonic acid derivatives or endocannabinoids (Howlett *et al.* 2002).

Studies of the biological effects of THC and its synthetic analogs revealed strict structural selectivity (Hollister 1974) as well as stereoselectivity, suggesting drug-receptor

interactions (Jones *et al.* 1974). Definitive evidence for the existence of specific cannabinoid receptors was followed soon by the demonstration of high-affinity, saturable, stereospecific binding sites for a synthetic cannabinoid agonist – [^{3}H]CP-55940 – in mouse brain plasma membranes, which correlated with both the *in vitro* inhibition of adenylate cyclase (AC) and the *in vivo* analgesic effect of the compound (Devane *et al.* 1988). The availability of a radioligand also allowed the mapping of cannabinoid receptors in the brain by receptor autoradiography (Herkenham *et al.* 1991). This mapping turned out to be of key importance in the subsequent identification of an orphan G protein-coupled receptor (GPCR) as the brain receptor for cannabinoids (Matsuda *et al.* 1990), later named CB_1 receptor, based on the overlapping regional distribution of the mRNA for this GPCR and [^{3}H]CP-55940 binding sites. CB_1 receptors are the most abundant receptors in the mammalian brain but are also present at much lower concentrations in a variety of peripheral tissues and cells. A second cannabinoid GPCR, CB_2, is expressed primarily in cells of the immune and hematopoietic systems (Munro *et al.* 1993) but recently has been found to be present in the brain (Van Sickle *et al.* 2005; Gong *et al.* 2006), in nonparenchymal cells of the cirrhotic liver (Julien *et al.* 2005), in the endocrine pancreas (Juan-Pico *et al.* 2006), and in bone (Ofek *et al.* 2006).

An interesting twist on the steric selectivity of cannabinoid receptors has emerged through recent studies of the behaviorally inactive phytocannabinoid CBD and its synthetic analogs, which have negligible affinity for either CB_1 or CB_2 receptors. Paradoxically, some of the synthetic stereoisomers of these compounds were found to bind potently to both CB_1 and CB_2 receptors (Bisogno *et al.* 2001) but to display only peripheral and not centrally mediated cannabinoid-like bioactivity, suggesting that they may act as antagonists rather than agonists at central, but not peripheral, CB_1 receptors (Fride *et al.* 2005).

Among the 60 or so cannabinoids present in marijuana, only THC is psychoactive (Pacher *et al.* 2006). However, some of the other constituents, such as CBD, have well-documented biological effects of potential therapeutic interest, such as antianxiety, anticonvulsive, antinausea, anti-inflammatory and antitumor properties (Mechoulam *et al.* 2002). As previously mentioned, CBD does not significantly interact with CB_1 or CB_2 receptors, and its actions have been attributed to inhibition of anandamide degradation (AEA) or its antioxidant properties (Mechoulam *et al.* 2002), or an interaction with as yet unidentified cannabinoid receptors.

In addition to CB_1 and CB_2 receptors, pharmacological evidence has been accumulating over the years to support the existence of one or more additional receptors for cannabinoids (Begg *et al.* 2005). Two of these possibilities which have been more extensively explored are: an endothelial site involved in vasodilation and endothelial cell migration (Begg *et al.* 2003), and a presynaptic site on glutamatergic terminals in the hippocampus mediating inhibition of glutamate release (Hajos *et al.* 2001).

Although both CB_1 and CB_2 receptors are GPCRs, they share little sequence homology, with only 44% homology at the protein level or 68% in the transmembrane domains, which are thought to contain the binding sites for cannabinoids (Lutz 2002). Despite this, THC and most synthetic cannabinoids have similar affinities for the two receptors, and only recently did synthetic ligands that discriminate between CB_1 and CB_2 receptors emerge (Pacher *et al.* 2006). These include agonists as well as antagonists.

The fact that specific receptors in mammalian cells recognize a plant-derived substance suggested the existence of an endogenous ligand. This theory was confirmed in 1992 with the isolation from porcine brain of the lipid arachidonoyl ethanolamide, named anandamide (AEA), which bound to the brain cannabinoid receptor with reasonably high

affinity and mimicked the behavioral actions of THC when injected into rodents (Devane *et al.* 1992). Three years later a second endocannabinoid, 2-arachidonoylglycerol (2-AG), was discovered (Mechoulam *et al.* 1995; Sugiura *et al.* 1995). Since then, a number of related endogenous lipids with endocannabinoids-like activity have been reported, but follow-up studies about biosynthesis, cellular transport, metabolism, and biological function have focused on AEA and 2-AG, with much less information available about the other compounds with endocannabinoid-like properties (Pacher *et al.* 2006).

The development of potent and highly selective CB_1 and CB_2 receptor antagonists (Rinaldi-Carmona *et al.* 1994; Rinaldi-Carmona *et al.* 1998) is particularly noteworthy as it provided critically important tools to explore the physiological functions of endocannabinoids. For example, the appetite-reducing effects of a particular CB_1 antagonist (SR141716) in various rodent models was the first sign to suggest that endocannabinoids may be active orexigenic agents (Thornton-Jones *et al.* 2005), representing the endogenous counterpart of the “munchies” caused by marijuana smoking.

However, these antagonists, as well as most of the other CB_1 and CB_2 antagonists developed to date, have inverse agonist properties (Bouaboula *et al.* 1999). For this reason, the development of CB_1 and CB_2 receptor-deficient mouse strains (Marsicano *et al.* 2002) was similarly important, as the use of these animals in combination with receptor antagonists can reinforce the presumed regulatory roles of endocannabinoids. More recently, the development of conditional mutant mice that lack the expression of CB_1 receptors only in certain types of neurons represents another milestone, as it allows linking of specific neuronal populations with a well-defined cannabinoid-modulated behaviour (Marsicano *et al.* 2003).

3.1.2 – CBD and THC as potential therapeutics for FRDA

The emerging role of the endocannabinoid system in a variety of CNS disorders should not come as a surprise given the very high level of expression of CB_1 receptors in the brain. The particularly high density of CB_1 receptors in the cortex, cerebellum, hippocampus, and basal ganglia had drawn early attention to diseases affecting movement, mood and anxiety disorders, and conditions related to altered brain reward mechanisms, as well as processes of memory and learning (Pacher *et al.* 2006).

Endocannabinoid involvement in the central regulation of motor functions and in movement disorders is based on multiple lines of evidence (reviewed by Pacher *et al.* 2006). First, CB_1 receptors are highly expressed in the basal ganglia, especially in the substantia nigra and in the cerebellum, areas involved in motor control. Second, endocannabinoids are also abundant in these brain regions. Third, endogenous, plant-derived, and synthetic cannabinoids have potent, mostly inhibitory, effects on motor activity. Fourth, CB_1 receptor and endocannabinoid levels are altered in the basal ganglia both in experimental models and human forms of movement disorders. Fifth, the endocannabinoid system interacts with several neurotransmitter pathways at various levels of the basal ganglia circuitry.

The endocannabinoid system is thought to provide on-demand protection against acute excitotoxicity in the CNS, as endocannabinoids have been shown to be neuroprotective through numerous mechanisms involving blockade of microglial activation (Ramirez *et al.* 2005), increase in brain-derived neurotrophic factor (Khaspekov *et al.* 2004), reduction of calcium influx (Nadler *et al.* 1993), and antioxidant activity (El-Remessy *et al.* 2003), suggesting a role for cannabinoids as therapeutic agents in the CNS.

A number of cell culture and rodent model studies have provided evidence for a cannabinoid neuroprotective effect both in acute neuronal injury, e.g. cerebral ischemia

(stroke) (Hampson *et al.* 1998), and in chronic neurodegenerative disorders such as Alzheimer disease (AD) (Iuvone *et al.* 2004), Parkinson disease (PD) (Brotchie 2003), Huntington disease (HD) (Lastres-Becker *et al.* 2003), and amyotrophic lateral sclerosis (ALS) (Raman *et al.* 2004).

During an ischemic episode, large quantities of the excitatory neurotransmitter glutamate are released, causing neuronal cell death. The neuroprotective actions of CBD and THC have been examined in rat cortical neuron cultures exposed to toxic levels of glutamate (Hampson *et al.* 1998). Both compounds significantly reduced glutamate toxicity. However, the observed neuroprotection was unaffected by cannabinoid receptor antagonist, indicating it to be cannabinoid receptor independent (Hampson *et al.* 1998). Both CBD and THC were shown to be potent antioxidants.

Excessive accumulation of β-amyloid peptide has been proposed as a pivotal event in the pathogenesis of AD, although the precise mechanism by which it induces neuronal death is still unknown. In a study of β-amyloid-induced neurotoxicity, treatment with CBD significantly elevated cell survival, while it decreased ROS production, lipid peroxidation, caspase 3 levels, DNA fragmentation and intracellular Ca^{2+} (Iuvone *et al.* 2004). This has further shown that CBD can exert a combination of neuroprotective, antioxidant and antiapoptotic effects, with the antiapoptotic effect being produced by CBD inhibition of caspase 3 formation.

Previous studies have indicated that CBD is non-toxic, even when chronically administered to humans (Cunha *et al.* 1980) or given in large acute doses [700 mg/day] (Consroe *et al.* 1991). Furthermore, the lack of psychoactivity associated with CBD allows for the administration of higher doses than would be possible with psychotropic cannabinoids such as THC. Recently, it has also been suggested that CBD may achieve synergy with THC

consisting of potentiation of benefits, antagonism of adverse effects, pharmacokinetic advantages, and metabolism (Russo and Guy 2006). Finally, the reported neuroprotective, antioxidant and antiapototic effects of both CBD and THC make them potential candidates for the therapy of FRDA.

3.2 – Aim of study

FRDA is primarily a neurodegenerative disorder with pathological loss of large sensory neurons in the DRG, posterior columns of the spinal cord, and corticospinal tracts. It is generally accepted that such pathology is a consequence of the actions of free radicals. The cannabinoids THC and CBD have been shown to have antioxidant and antiapoptotic properties, and ultimately a neuroprotective effect, thus preventing neuronal cell loss. Additionally, there is anecdotal evidence from FRDA patients that the taking of cannabis relieved their symptoms.

Therefore, it has been hypothesised that such cannabinoids may be of potential benefit to the therapy of FRDA. For that reason, the aim of this research project is to examine the potential neuroprotective effects of the cannabinoids CBD and THC in FRDA by performing drug trials on the two lines of *FXN* YAC GAA transgenic mice available.

3.3 – Materials and methods

3.3.1 – Botanical origin of cannabinoids

The THC and CBD extracts of cannabis were prepared from two strains (chemovars) of *Cannabis sativa* L. These chemovars, unique to GW Pharmaceuticals Plc (UK), contain consistently high levels of either THC or CBD. The plants were grown indoors under strict temperature and light conditions and reproduced asexually, thus providing crop consistency and minimal genetic variation. Both the CBD and THC botanical drug substances (BDS) are a brown viscous semi-solid with an absence of immiscible liquid and have a characteristic smell of decarboxylated cannabis. The THC BDS typically contains not less than 64% THC (more than 90% of the total cannabinoid present), and the CBD BDS not less than 60% CBD (more than 85% of the total cannabinoid present), with the remainder being co-extracted plant material.

3.3.2 – Drug preparation

The cannabinoid extracts were provided by GW Pharmaceuticals and stored in the dark at -80°C. Two distinct drug formulations were prepared as described by Pertwee *et al* (1992):

– *CBD solution [4mg/ml]*: 1 part CBD BDS, 2 parts Tween-80, 247 parts sterile saline.

– *CBD:THC (1:1) solution [4mg/ml]*: 1 part CBD BDS, 1 part THC BDS, 4 parts Tween-80, 494 parts sterile saline.

The BDS was initially completely dissolved in Tween-80 and then saline was added in a series of aliquots of increasing volume, the mixture being shaken between additions. The drug dispersions were stored in 1ml aliquots in the dark at -80°C. A Tween-80/saline solution (1:248) was prepared for placebo administration and stored at room temperature.

3.3.3 – Study design and drug administration

Mice under investigation were treated with courses of CBD, CBD:THC or placebo solution. Mice that started being treated at 6 months of age were administered intraperitoneally (i.p.) with a 10mg/kg CBD drug dose (approximately 6 mice per group) while the mice that started being treated at 3 months of age were administered i.p. with either 20mg/kg CBD or 20mg/kg CBD:THC drug doses (approximately 10 mice per group) (Table 3.1). A corresponding volume of Tween-80/saline solution was administered to the placebo control mice. All treatments consisted of twice-weekly i.p. doses for a period of 3 months.

Initially, treatments were performed on all available mouse lines: Wt, YG8 and YG22. However, the CBD:THC treatment was only performed on Wt and YG8 mice.

Table 3.1 – Study details including the number of mice used in each treatment group

10mg/kg 6-9 months of age				**20mg/kg 3-6 months of age**			
	Wt	**YG8**	**YG22**		**Wt**	**YG8**	**YG22**
Placebo	6	5	6	**Placebo**	19	18	10
CBD	6	6	5	**CBD**	9	10	10
				CBD:THC	10	11	–

3.3.4 – Functional studies during drug treatments

Weight, rotarod performance and locomotor activity measurements were taken just before the start of the drug treatments and repeated thereafter with monthly intervals until the completion of the treatment.

3.3.5 – Sample collection

At the completion of the drug treatment the mice were appropriately culled and samples were collected as described in Chapter 2 according to the type of analysis desired. Preference was given to the collection of samples for molecular biology and biochemical analysis rather than histology (Table 3.2 and Table 3.3).

Table 3.2 – Number of mice sampled for biochemical analysis

	10mg/kg				20mg/kg		
	Wt	**YG8**	**YG22**		**Wt**	**YG8**	**YG22**
Placebo	5	4	5	**Placebo**	17	16	9
CBD	5	5	4	**CBD**	8	9	9
				CBD:THC	9	10	–

Table 3.3 – Number of mice sampled for histological analysis

	10mg/kg				20mg/kg		
	Wt	**YG8**	**YG22**		**Wt**	**YG8**	**YG22**
Placebo	1	1	1	**Placebo**	2	2	1
CBD	1	1	1	**CBD**	1	1	1
				CBD:THC	1	1	–

3.3.6 – OxyBlot analysis

Oxyblot analysis was performed on brain samples of Wt and YG8 mice from the 20mg/kg studies.

Table 3.4 – Number of brain samples investigated by OxyBlot analysis

20mg/kg		
	Wt	**YG8**
Placebo	6	6
CBD	3	3
CBD:THC	3	3

3.3.7 – Histological analysis

Standard H&E histological analysis was performed on brain and DRG paraffin embedded sections. Only YG8 male mice were investigated.

Table 3.5 – Number of brain and DRG samples investigated by histology

10mg/kg	
	YG8
Placebo	1
CBD	1

20mg/kg	
	YG8
Placebo	1
CBD	1
CBD:THC	1

3.4 – Results

3.4.1 – Functional studies

10mg/kg CBD – 6-9 months of age

An initial study consisted of administering 10mg/kg CBD (or placebo) to 6 months old Wt, YG8 and YG22 rescue mice (n=5-6), for a duration of 3 months. The mice were generally matched for age (Figure 3.2A), and despite the fact that all Wt mice tested were males, an attempt was made to keep a balanced proportion of males to females in the YG8 and YG22 groups (Figure 3.2B). No drug/placebo administration-associated deaths were observed.

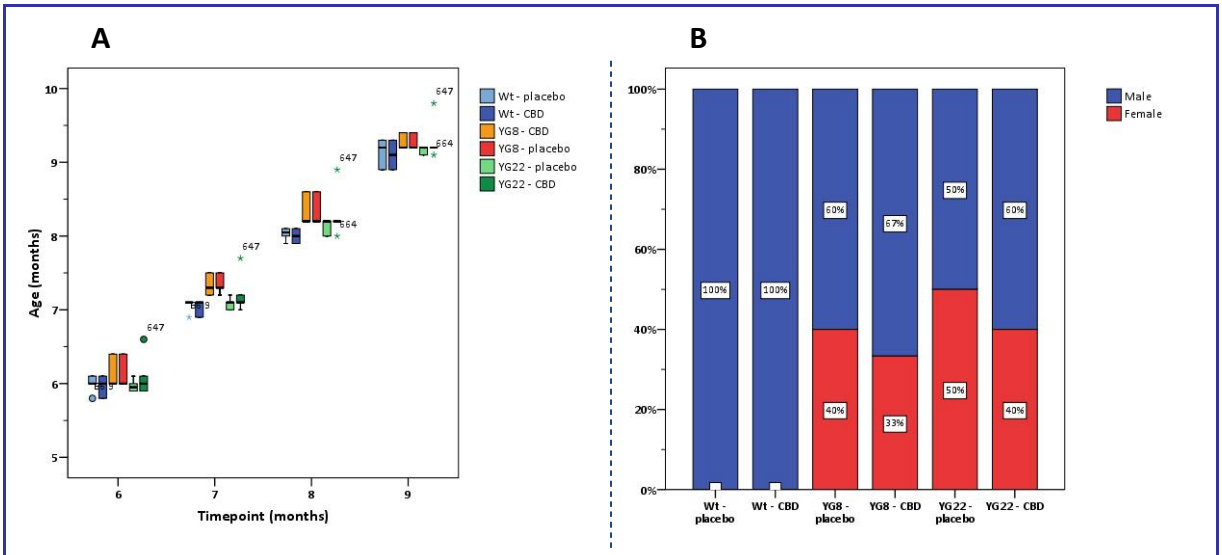

Figure 3.2 – (**A**) Age and (**B**) gender distribution of mice used in the 10mg/kg CBD study.

Although the YG22 mice seemed to be generally heavier mice (in comparison to the Wt and YG8 mice) no difference was observed between drug and placebo taking groups (Figure A.1). The weight gain was by and large consistent (Figure 3.3), with only a few mice deviating from normality. Nevertheless, this was not associated with the drug taking factor since such deviations were observed in both drug and placebo taking mice (Figure A.2).

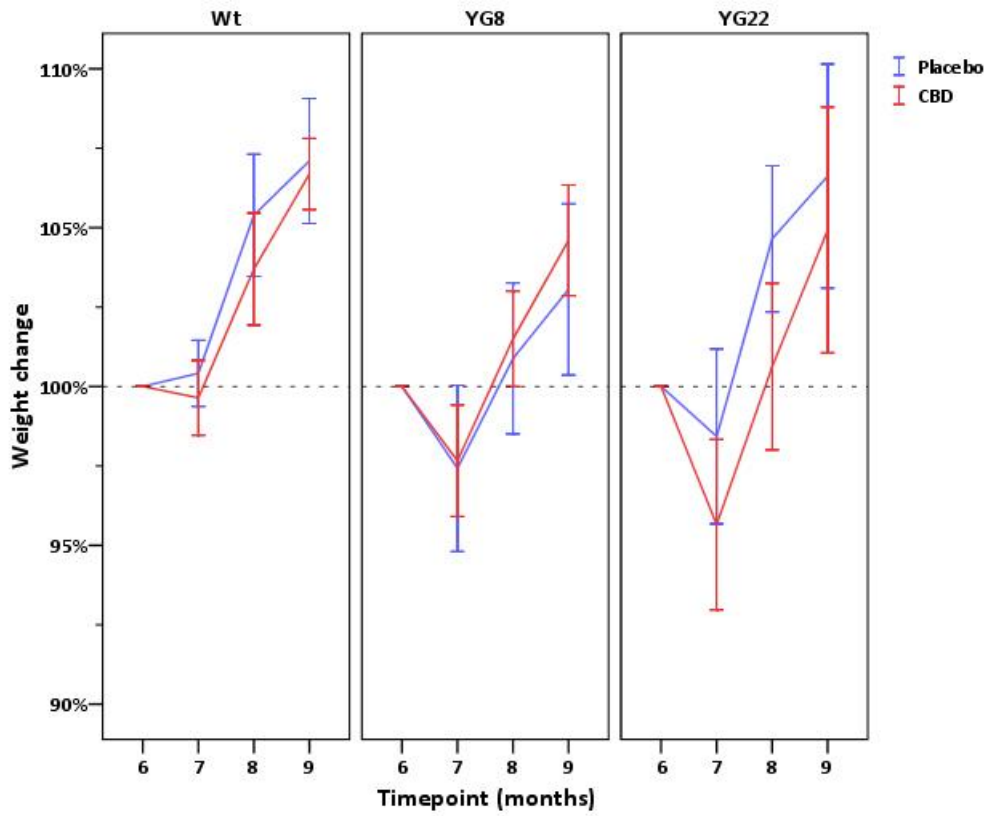

Figure 3.3 – Weight gain/loss during the 10mg/kg CBD study (error bars: +/- 1 SE).

Two-way mixed ANOVA for repeated measures confirmed that the age of the mice (timepoint) had a significant effect on the weight gain (Table 3.6 and Table 3.7). However, no significant effect of either the genotype (Table 3.7) or drug treatment (Table 3.6) on the weight gain was detected over the duration of the study.

Regarding rotarod performance, this was relatively normally distributed with all study groups showing average levels of performance (Figure A.3). The number of high performance mice (scoring near the test maximum of 400s) was reduced, but these mice were observed in all genotypic groups. In contrast, poor performance mice (<100s) were only observed in the YG8 and YG22 line and only after 8 months of age. Regarding individual changes in performance these were also mainly normal distributed (Figure A.4). In general, performance levels were maintained through the first month of the study, but seem to have

Table 3.6 – ANOVA associated *p*-values of timepoint and drug treatment effect on the various functional measurements during the CBD 10mg/kg study.

		ANOVA *p*-values	
Effect on	**Genotype**	**Timepoint**	**Timepoint * Treatment**
Weight	Wt	<0.001	0.819
	YG8	0.001	0.944
	YG22	<0.001	0.702
Rotarod performance	Wt	0.027	0.465
	YG8	0.010	0.603
	YG22	0.134	0.505
Locomotor activity	Wt	0.035	0.819
	YG8	0.114	0.757
	YG22	0.011	0.624

Table 3.7 – ANOVA associated *p*-values of timepoint and genotype effect on the various functional measurements during the CBD 10mg/kg study.

			ANOVA *p*-values	
Effect on	**Genotype**	**Treatment**	**Timepoint**	**Timepoint * Genotype**
Weight	Wt vs YG8	placebo	<0.001	0.321
		CBD	<0.001	0.644
	Wt vs YG22	placebo	<0.001	0.905
		CBD	<0.001	0.472
Rotarod performance	Wt vs YG8	placebo	0.069	0.743
		CBD	0.002	0.415
	Wt vs YG22	placebo	0.818	0.703
		CBD	<0.001	0.234
Locomotor activity	Wt vs YG8	placebo	0.058	0.719
		CBD	0.058	0.869
	Wt vs YG22	placebo	0.043	0.017
		CBD	0.376	0.335

slightly declined after that. Final drops of approximately 10% and 10-30% were observed in Wt and YG8 mice respectively, with some of the later showing drops of 35% in performance. Graphical analysis of the change in rotarod performance over the duration of the study did

not suggest any clear effect of the drug treatment (Figure 3.4). However, at the end of the study, all CBD-treated groups showed lower average performance values when compared to the respective placebo groups. Nevertheless, ANOVA statistical analysis confirmed that the drug effect over the duration of the study was not significant (Table 3.6). Curiously, no significant difference was observed either between Wt and YG8, and Wt and YG22 mice for each of the drug treatments (Table 3.7).

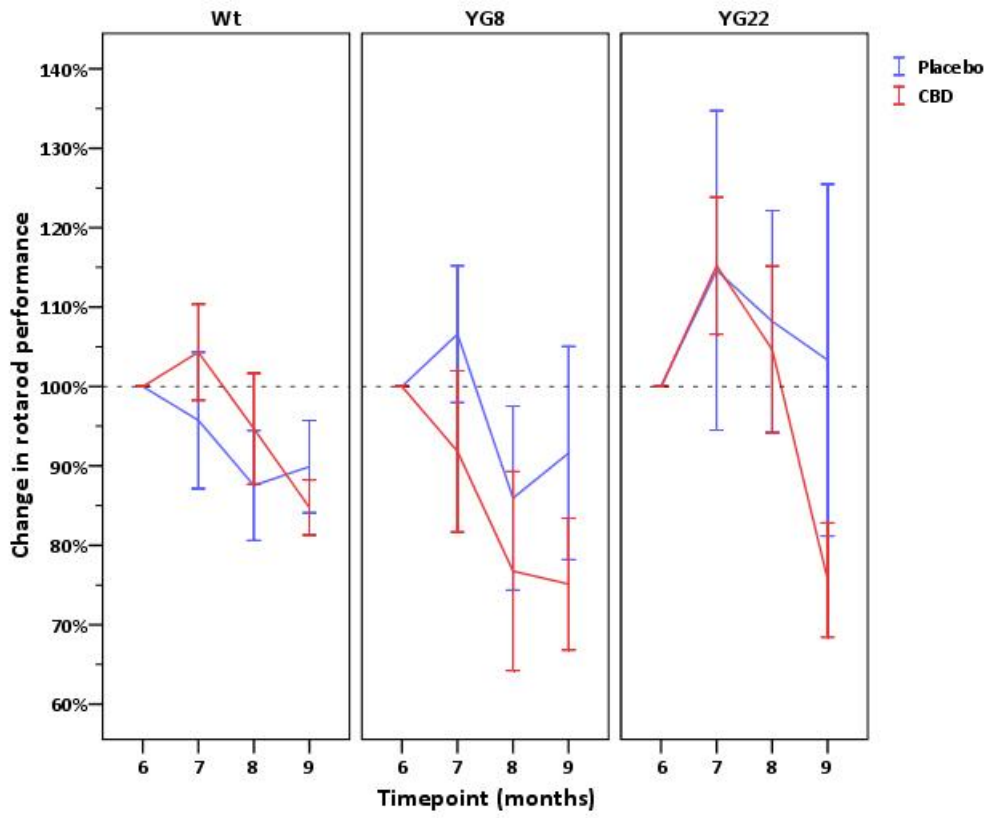

Figure 3.4 – Rotarod performance change during the 10mg/kg CBD study (error bars: +/- 1 SE).

Regarding locomotor activity, little data is available for this study given that only a very small number of mice from each group (n=2-3) was analysed since t=0. The absolute levels of activity were generally consistent among the different study groups (normally around 10 squares covered in 30s), with the exception of the CBD-treated YG22 mice which reached relatively higher levels (15-25 squares covered in 30s) as the study progressed (Figure A.5

and Figure A.6). No timepoint effect can be clearly observed with locomotor activity both reducing (Wt and YG8) and drastically increasing (YG22) over the duration of the study (Figure 3.5). ANOVA analysis confirms that the locomotor activity of Wt groups significantly decreased and significantly increased in YG22 groups, throughout the study (Table 3.6). No clear drug effect was detected, and regarding the genotype effect, this was only significant when placebo-taking Wt and YG22 mice were compared (Table 3.7), where the former showed a final average decrease of 25%, while the latter's activity levels increased by nearly 300% (Figure 3.5).

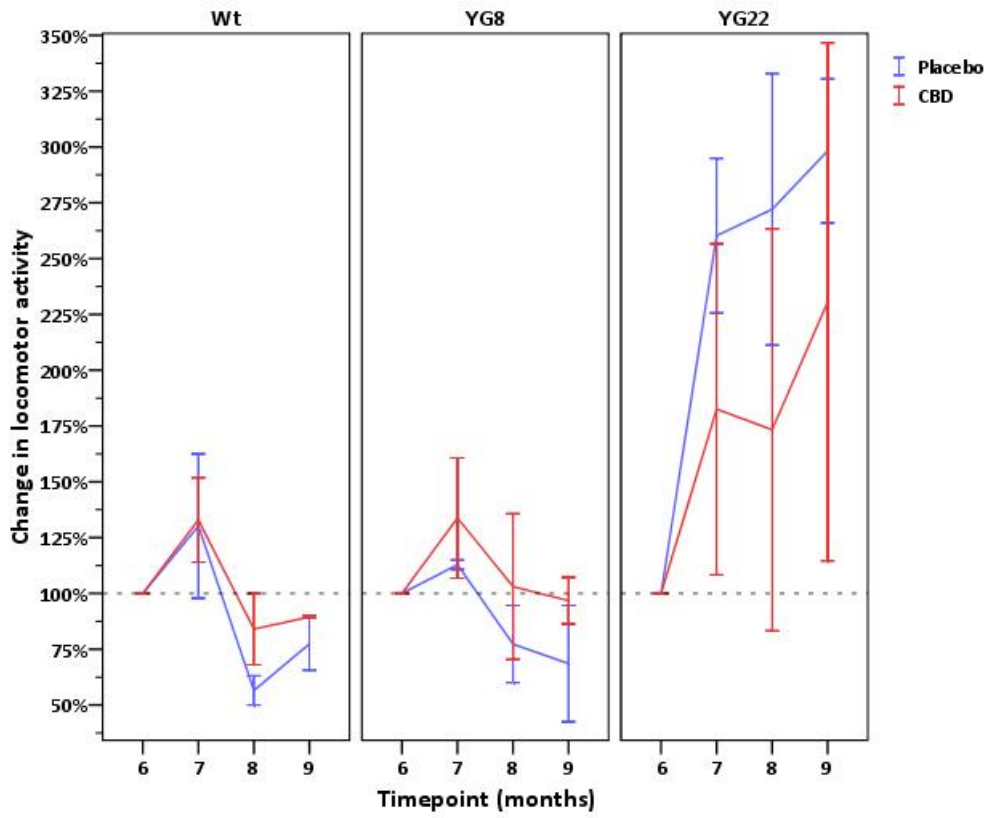

Figure 3.5 – Change in locomotor activity during the 10mg/kg CBD study (error bars: +/- 1 SE).

20mg/kg CBD and CBD:THC – 3-6 months of age

A later study consisted of administering 20mg/kg of either CBD or CBD:THC (or placebo) to 3 months old Wt, YG8 and YG22 rescue mice (n=9-19), for a duration of 3 months. The mice were generally matched for age (Figure 3.6A) and an attempt was made to keep a relatively balanced proportion of males to females in all groups (Figure 3.6B). No drug/placebo administration-associated deaths were observed.

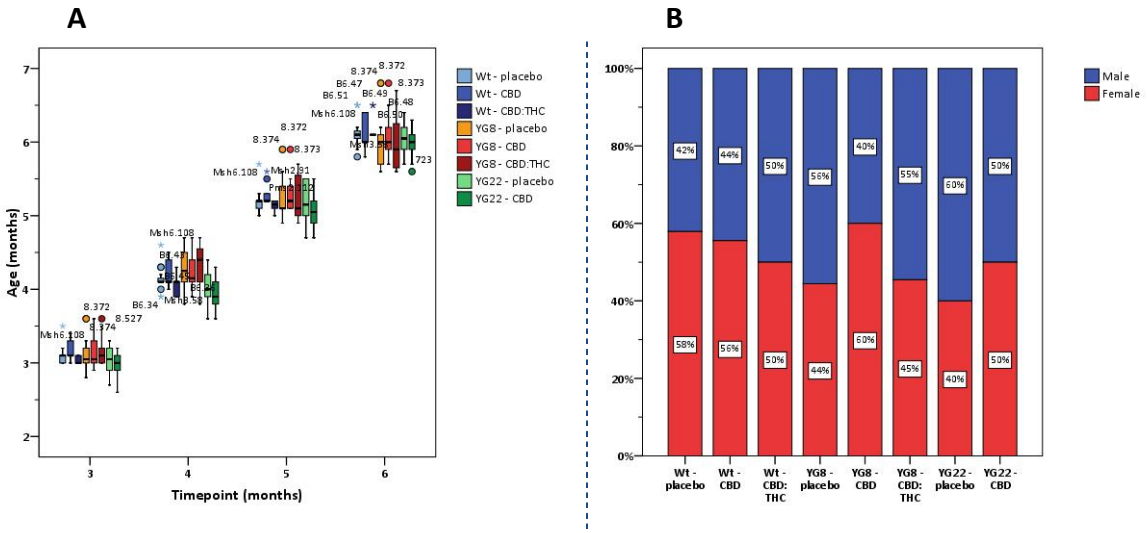

Figure 3.6 – (**A**) Age and (**B**) gender distribution of mice used in the 20mg/kg CBD/CBD:THC studies.

All mice in the different study groups started off with fairly similar weight levels (Figure A.7), and although they all constantly gained weight throughout the study, YG22 mice seem to have gained relatively more than Wt and YG8 mice (Figure 3.7). In fact when comparing CBD-taking Wt vs YG22 mice, the genotype effect appears to a significant nature (Table 3.9). Regarding the drug effect on weight gain, this seems non-existent when CBD is administered on its own. However, both Wt and YG8 CBD:THC-taking mice seem to have put comparatively less weight on throughout the study. In fact, ANOVA analysis confirmed the significance of the drug effect of CBD:THC in Wt mice weight loss (Table 3.8).

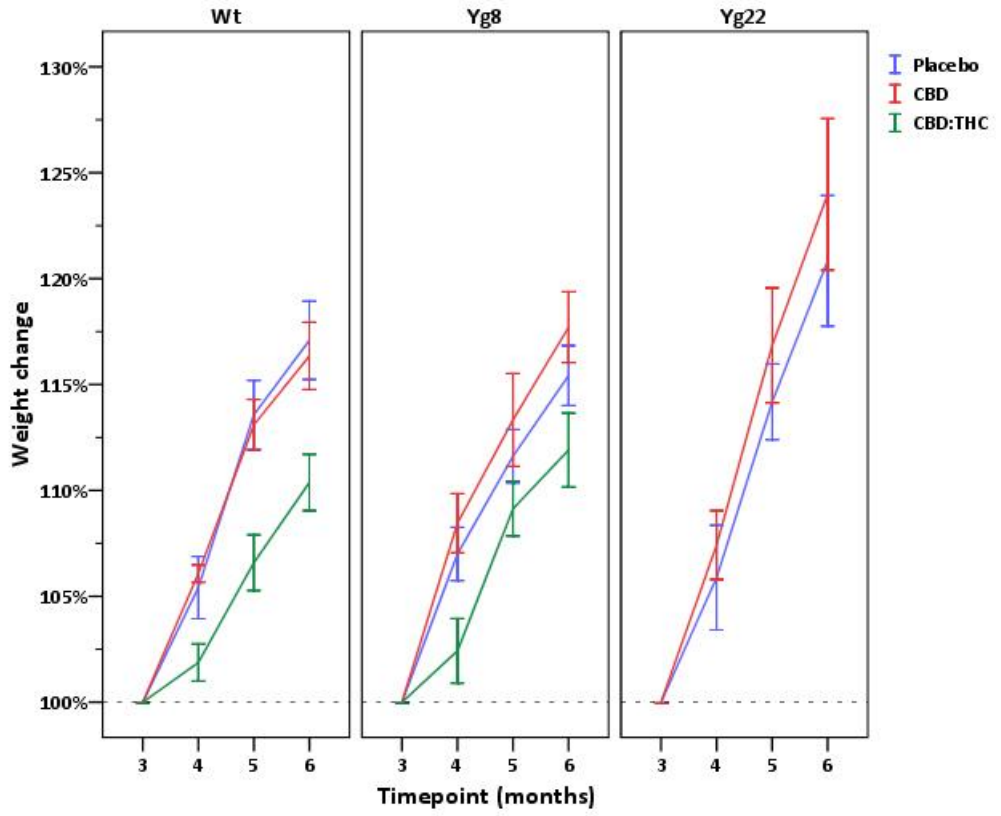

Figure 3.7 – Weight gain/loss during the 20mg/kg CBD/CBD:THC studies. (error bars: +/- 1 SE)

Table 3.8 – ANOVA associated *p*-values of timepoint and drug treatment effect on the various functional measurements during the 20mg/kg CBD and CBD:THC studies.

Effect on	Genotype	Treatment (vs placebo)	ANOVA *p*-values	
			Timepoint	Timepoint * Treatment
Weight	Wt	CBD	<0.001	0.923
		CBD:THC	<0.001	0.004
	YG8	CBD	<0.001	0.759
		CBD:THC	<0.001	0.169
	YG22	CBD	<0.001	0.776
Rotarod performance	Wt	CBD	0.019	0.124
		CBD:THC	0.017	0.548
	YG8	CBD	0.164	0.752
		CBD:THC	0.003	0.455
	YG22	CBD	0.003	0.207
Locomotor activity	Wt	CBD	0.515	0.919
		CBD:THC	0.002	0.077
	YG8	CBD	0.016	0.487
		CBD:THC	0.037	0.446
	YG22	CBD	0.237	0.098

Table 3.9 – ANOVA associated *p*-values of timepoint and genotype effect on the various functional measurements during the 20mg/kg CBD and CBD:THC studies.

			ANOVA *p*-values	
Effect on	**Genotype**	**Treatment**	**Timepoint**	**Timepoint * Genotype**
Weight	Wt vs YG8	placebo	<0.001	0.233
		CBD	<0.001	0.644
		CBD:THC	<0.001	0.592
	Wt vs YG22	placebo	<0.001	0.420
		CBD	<0.001	0.040
Rotarod performance	Wt vs YG8	placebo	0.025	0.374
		CBD	0.183	0.284
		CBD:THC	0.004	0.945
	Wt vs YG22	placebo	0.042	0.339
		CBD	0.099	0.113
Locomotor activity	Wt vs YG8	placebo	0.284	0.848
		CBD	0.033	0.241
		CBD:THC	<0.001	0.267
	Wt vs YG22	placebo	0.638	0.224
		CBD	0.341	0.350

Regarding rotarod performance, a relatively high rate of intra-study group variability was observed (Figure A.9). However, when this was analysed in terms of change in rotarod performance a certain degree of consistency was present, with only few outlier mice detected (Figure A.10). In general, the rotarod performance has changed significantly throughout the duration of the study, with the exception of CBD-treated YG8 mice (Table 3.8). In both Wt and YG8 groups the CBD-taking mice have consistently showed increased improvement (or decreased deterioration) in rotarod performance, while the CBD:THC-taking mice showed the strongest deterioration throughout the study (Figure 3.8). Regarding the YG22 mice, a similar change in performance was observed until 5 months of age, and at the final timepoint placebo-taking mice recovered to original levels, while the CBD-taking mice further deteriorated (Figure 3.8). Nevertheless, no genotype (Table 3.9) or treatment (Table 3.8) effect on rotarod performance was found to be significant.

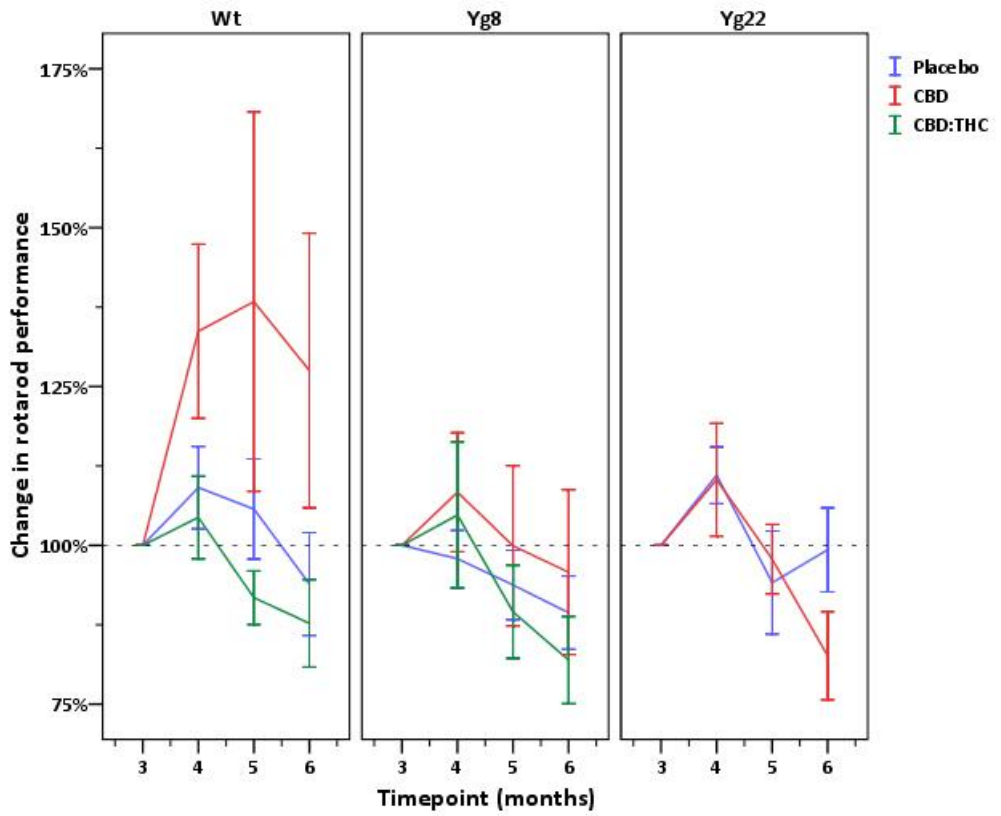

Figure 3.8 – Rotarod performance change during the 20mg/kg CBD/CBD:THC studies. (error bars: +/- 1 SE)

Regarding locomotor activity, with the exception of a CBD-taking Wt mouse which was clearly hyperactive (covering 25-50 squares in 30s), the absolute values were fairly normally distributed, regularly ranging from 5-10 squares (Figure A.11). However, when a change in activity levels was computed, greater levels of variability were observed, with some mice from the same study group doubling their activity while other were showing drops to one quarter of original levels (Figure A.12). In general, activity levels decreased throughout the study, with the exception of placebo-taking YG22 mice which actually showed a gradual increase. The activity of Wt mice dropped approximately 10%-15% for the placebo- and CBD-taking study groups (Figure 3.9). However, the CBD:THC-taking Wt mice showed a steep drop in activity culminating in values of 60% of original levels. Regarding the YG8 mice the placebo-taking showed a final drop of 10%, while both the CBD- and CBD:THC-taking mice

ended up with a 30%-35% drop (Figure 3.9). Nevertheless, neither genotype (Table 3.9) nor drug treatment (Table 3.8) were found to have a significant effect on locomotor activity levels throughout the duration of the study.

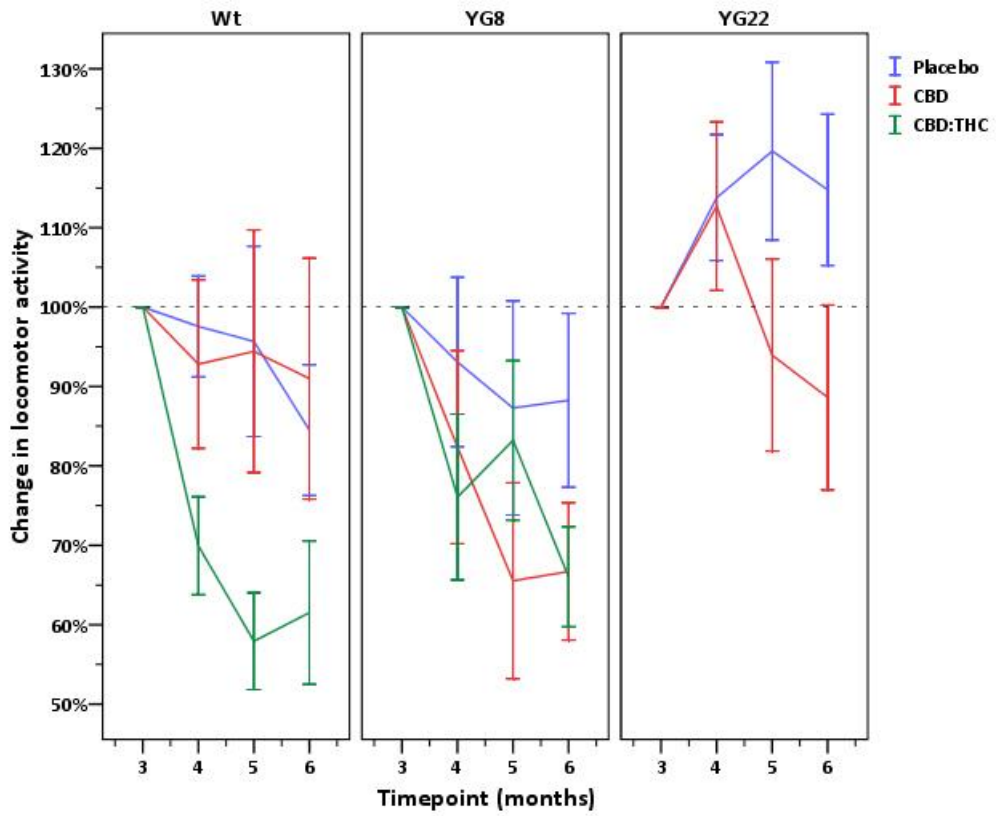

Figure 3.9 – Change in locomotor activity during the 20mg/kg CBD/CBD:THC studies. (error bars: +/- 1 SE)

3.4.2 – Oxyblot analysis

The levels of protein oxidation were determined in the brain of Wt and YG8 rescue mice from the 20mg/kg CBD/CBD:THC studies (n=3-6). Two oxyblots (blot A and B), each containing all samples investigated, were quantified by densitometry (Figure A.13). Slightly different results were obtained between the two oxyblots: although the placebo values were similar, their relation to YG8 mice levels was reversed in the two experiments (Figure A.14). In oxyblot A no significant genotype or drug effect was observed (Table A.2 and Table A.3). However, in blot B a significant difference was observed between Wt and YG8 mice in corresponding treatments, with the YG8 mice showing higher levels of protein oxidation (Table A.2). In addition, in YG8 mice a significant drug effect was observed for both drug treatments, increasing the protein oxidation levels (Table A.3).

Ultimately, after combining the two blots, in both placebo and YG8 mice CBD treatment seems to lower the protein oxidation levels, but CBD:THC seems to slightly cause the opposite effect (Figure 3.10). Nevertheless, the genotype or drug effect was found to be non-significant (Table 3.10 and Table 3.11).

Table 3.10 – Independent samples *t*-test associated *p*-values of drug treatment effect on brain levels of protein oxidation during the 20mg/kg CBD and CBD:THC studies.

Genotype	**Treatment** (vs placebo)	***p*-value**
Wt	CBD	0.065
	CBD:THC	0.645
YG8	CBD	0.685
	CBD:THC	0.076

Placebo n=6, CBD n=3, CBD:THC n=3

Table 3.11 – Independent samples *t*-test associated *p*-values of genotype effect on brain levels of protein oxidation during the 20mg/kg CBD and CBD:THC studies.

Genotype	Treatment	*p*-value
Wt vs YG8	placebo	0.987
	CBD	0.483
	CBD:THC	0.176

Placebo n=6, CBD n=3, CBD:THC n=3

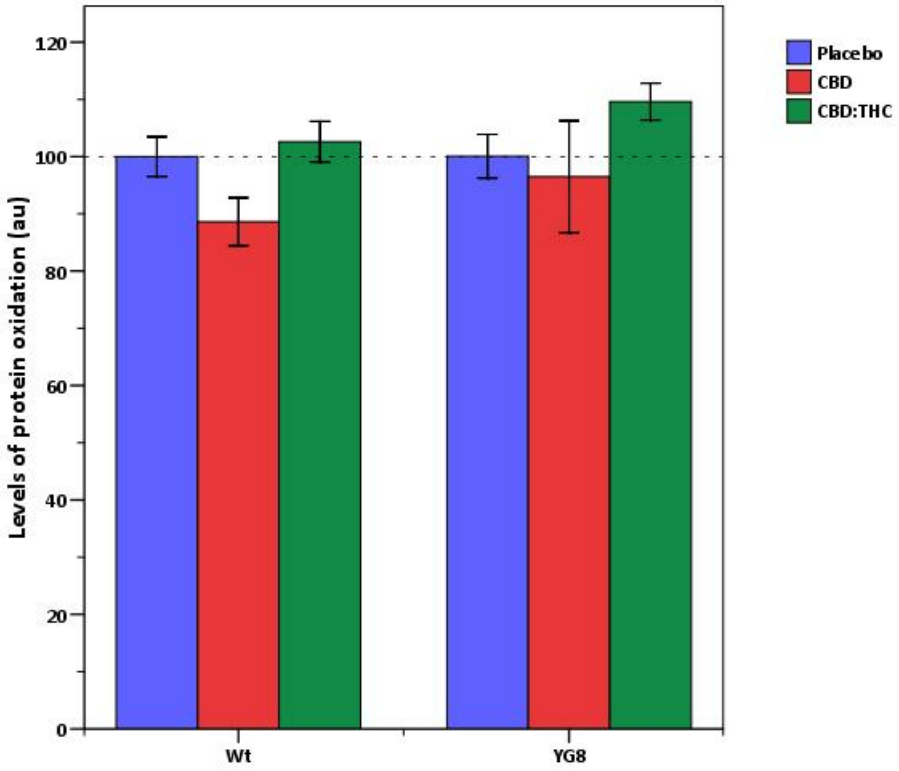

Figure 3.10 – Levels of protein oxidation in the brain of mice from the 20mg/kg CBD/CBD:THC studies, as determined by Oxyblot analysis. Placebo n=6, CBD/CBD:THC n=3. (au = arbitrary units; error bars: +/- 1 SE)

3.4.3 – Histological analysis

Histological analysis was performed by means of H&E staining of lumbar vertebral column sections (Figure 3.11 and Figure 3.12) from a single mouse representative of each YG8 study group, and the levels of DRG neurodegeneration were determined by counting the number of cell bodies displaying vacuoles (Figure 3.12).

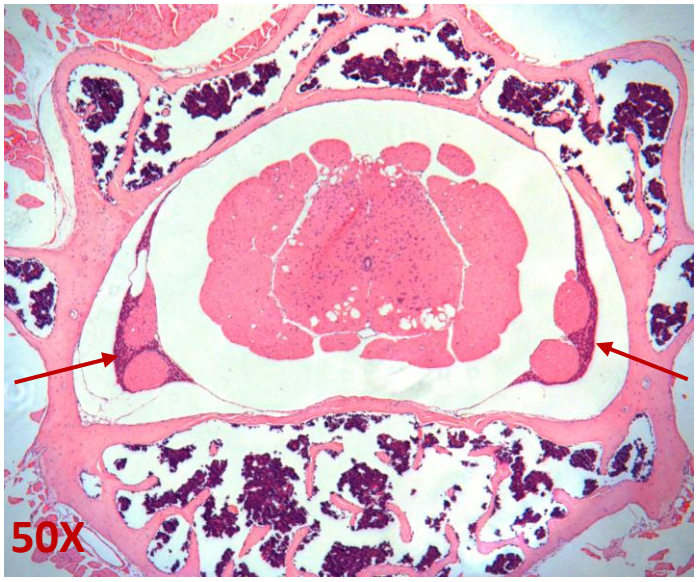

Figure 3.11 – H&E stained vertebral column section from YG8 rescue mouse (placebo). Red arrows point out the DRG.

Very low levels of neurodegeneration were observed in younger mice (6 months of age), where the maximum number of vacuoles observed never exceeded 2 (Figure 3.13). When lower sections of the lumbar region were analysed (VL_{3+4}) the level of neurodegeneration consistently increased, but only marginally (when compared to VL_{1+2}).

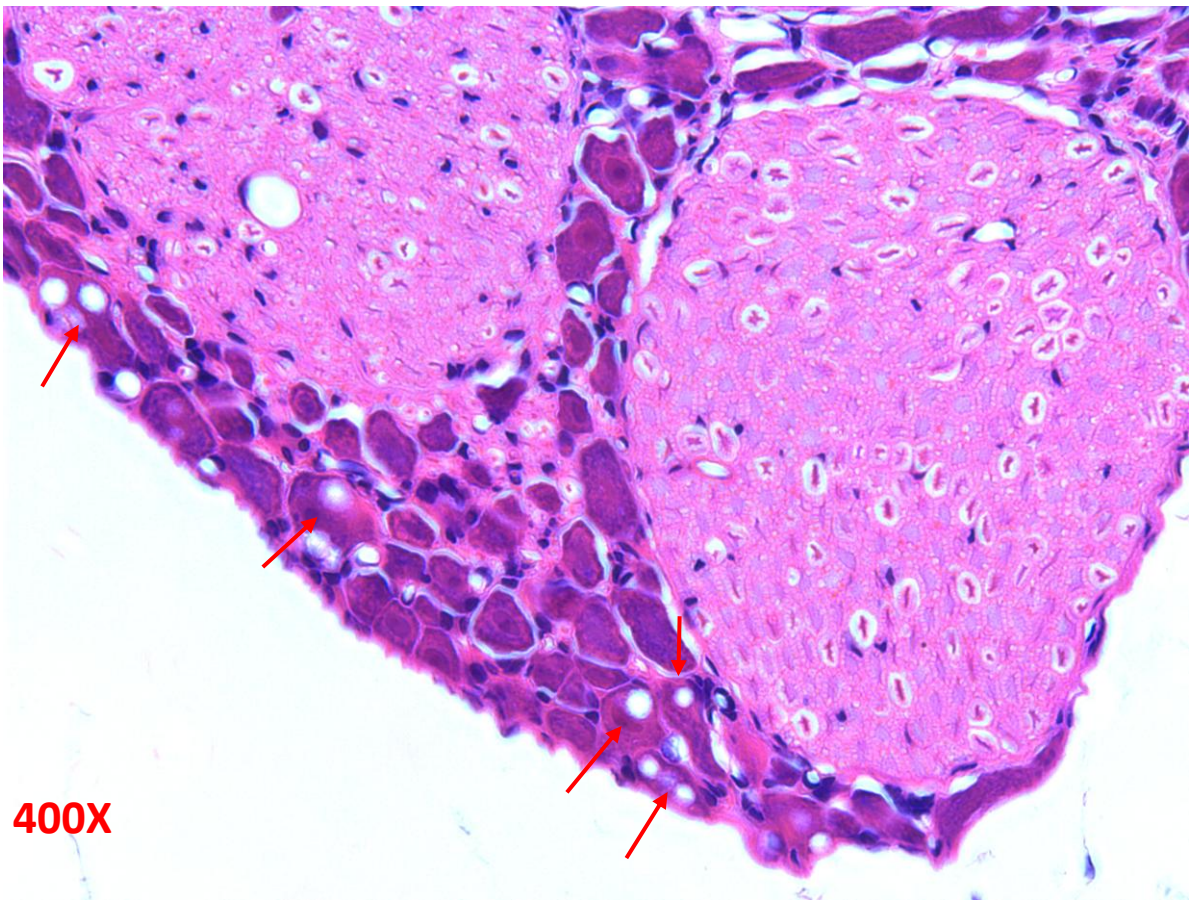

Figure 3.12 – H&E stained DRG section from YG8 rescue mouse (placebo). Red arrows point to vacuoles present in DRG cell bodies.

With the exception of the VL_{1+2} sections from the placebo-taking mouse, older mice showed much higher levels of neurodegeneration. In these mice, much higher levels of neurodegeneration were also observed in the lower lumbar region, with an average of 12 and 25 vacuoles observed in placebo- and CBD-taking mice respectively (Figure 3.13). In fact, in the placebo mouse this represented 14% of the total DRG cell bodies, and for the CBD-treated mouse this level reached 20%.

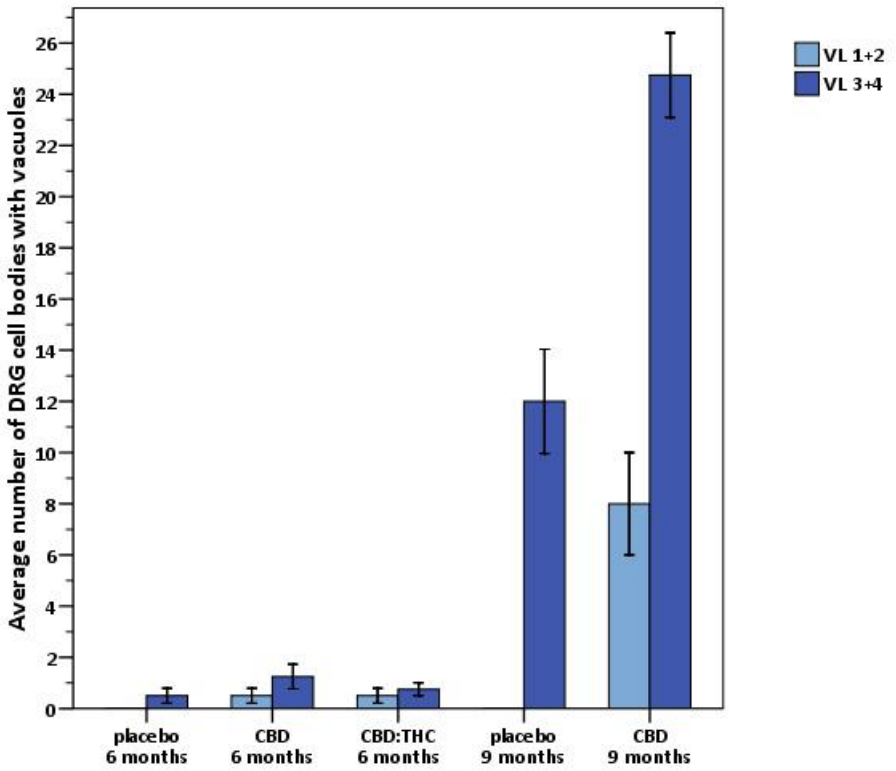

Figure 3.13 – Levels of DRG neurodegeneration in YG8 mice following the CBD and CBD:THC treatments (n=1). (error bars: +/- 1 SE)

3.5 – Discussion

The recently reported antioxidant and neuroprotective effects of the cannabinoids CBD and THC have drawn attention to the fact that such compounds could be of potential therapeutic benefit to FRDA patients by alleviating some of the associated symptoms. Adding to this, anecdotal reports from FRDA patients also advocated such therapeutic properties.

Drug studies were performed on Wt and FRDA mice to investigate such effects. These consisted of administering either a course of: 10mg/kg CBD to 9 months old; or 20mg/kg CBD or CBD:THC (1:1) to 6 months old mice. All treatments lasted for 3 months, and during this period various functional studies were routinely performed, such as: weight monitoring, and assessment of rotarod performance and locomotor activity. Although it does not seem accurate to compare absolute values from functional studies between the higher and lower dose studies because of age differences, the alterations experienced can be evaluated.

Administration of 10mg/kg CBD seems to have had a detrimental effect on the rotarod performance of all study groups (when compared to corresponding placebo groups). After increasing the CBD concentration to 20mg/kg, increased changes in performance were observed (when compared to corresponding placebo groups), with the exception of YG22 mice. On the other hand, administration of 20mg/kg CBD:THC produced the most detrimental changes in rotarod performance, in both Wt and YG8 mice. Administration of the higher doses of cannabinoids seems to have caused reduced levels of locomotor activity, particularly when THC was present.

Based on these findings we could postulate that the higher dose of CBD may be causing this positive change in rotarod performance by protecting neuromotor system from oxidative damage. Regarding the reduced locomotor activity observed this may be related to

the well established anti-anxiety effects of cannabinoids, therefore maybe relaxing the mice and making them less inquisitive. Nevertheless, none of the drug effects on the alterations of both rotarod performance and locomotor activity were found to be statistically significant.

Additionally, although the analysis of performance alterations can provide a better idea of the potential drug effects, the lack of a strong demarcation between Wt and FRDA mice makes the analysis of absolute performance values very difficult to interpret. In fact, no significant difference was observed between Wt and any of the FRDA mice (in corresponding drug treatments).

The antioxidant potential of CBD and CBD:THC was also investigated by analysing the levels of protein oxidation in the brain of YG8 mice. Administration of 20mg/kg CBD seems to have successfully reduced levels of protein oxidation, although only marginally, while CBD:THC seems to have had the opposite effect. However, none of these effects were found to be statistically significant. Again, as far as YG8 mice are concerned, no significant difference was observed in the brain levels of protein oxidation, when compared against Wt mice.

Histological analysis confirmed the presence of neurodegeneration in the YG8 line, but only in older mice (9 months old). Although the investigated YG8 mouse which was treated with CBD showed higher levels of neurodegeneration than the placebo mouse, this cannot be considered definite since only one mouse from each study group was analysed.

One of the points to be taken from this histological investigation is that DRG from distal lumbar vertebrae show much higher levels of neurodegeneration, confirming the FRDA-like “dying back” effect.

Additionally, the fact that the levels of neurodegeneration were significant in 9 months old mice, but not in 6 months old mice, suggests that maybe the mice used in the higher cannabinoid dose studies were simply too young to be displaying a significant phenotype.

In fact, it seems that any general interpretations from this study, concerning the effects of cannabinoid therapy for FRDA, are severely hampered by the fact that any abnormal phenotype exhibited by both the YG8 and YG22 lines of the FRDA mouse model was not very evident. Therefore, based on the findings obtained it is not possible to promote or refute the use of the cannabinoids CBD and THC as therapeutic agents for FRDA patients.

To address this issue, future preliminary studies should be performed in cell lines derived from FRDA patients, followed by *in vivo* studies utilising more severely affected mice. Whether that may consist on performing longer studies with the current FRDA model, until mice are much older and displaying a potentially more significant phenotype, or simply using a better model, yet to be developed.

Chapter 4 – CTMIO antioxidant therapeutic testing in FRDA mice

4.1 – Introduction

The isoindoline nitroxide antioxidant CTMIO

Nitroxides are stable free radicals that protect against oxidative and radiation-induced cytotoxicity (Hahn *et al.* 1994).

An initial study investigating the antioxidant properties of isoindoline nitroxides consisted of exposing plasmid DNA to peroxyl and hydroxyl free radicals damage, and assessing the DNA damage by analysing the proportion of linear/circular plasmid, ultimately revealing that these protect DNA from oxidative damage (Damiani *et al.* 2000).

The isoindoline nitroxide CTMIO (5-carboxy-1,1,3,3-tetramethylisoindolin-2-yloxyl) (Figure 4.1) is a compound that preserves the advantages of the isoindoline systems while possessing water solubility up to 2mM (Chen *et al.* 2003).

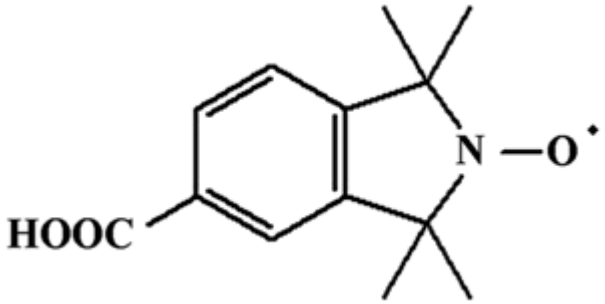

5-carboxy-1,1,3,3-tetramethylisoindolin-2-yloxyl (CTMIO)

Figure 4.1 – Structure of the isoindoline nitroxide CTMIO (Chen *et al.* 2003).

To date, studies with CTMIO have primarily focused on its potential therapeutic effects in ataxia-telangiectasia (A-T) (Chen *et al.* 2003; Hosokawa *et al.* 2004; Gueven *et al.* 2006). A-T is an autosomal recessive disorder that is characterized by early onset progressive cerebellar ataxia, oculocutaneous telangiectasia, susceptibility to bronchopulmonary disease, and lymphoid tumours. Various other abnormalities are also associated with this

disorder, including the absence or the rudimentary appearance of a thymus, immunodeficiency, progressive apraxia of eye movements, insulin-resistant diabetes, clinical and cellular radiosensitivity, cell-cycle checkpoint defects and chromosomal instability (reviewed by Lavin 2008).

Interestingly, when a patient-derived A-T lymphoblastoid cell line was irradiated, not only did CTMIO treatment significantly increase cell survival but also reduced the level of chromosome aberrations (Hosokawa *et al.* 2004). Additionally, in this study, the antioxidant effect of CTMIO was shown to be much more significant than that of vitamin E.

An alternative study investigated the effect of CTMIO on cerebellar Purkinje neuron cultures derived from A-T mice, which are characterized by reduced cell survival. CTMIO treatment dramatically increased the survival rates (from 32% to 77% of Wt) and partially restored dendritic elongation and branching of Purkinje neurons (Chen *et al.* 2003).

More recently, an *in vivo* study was also performed using A-T mice (Gueven *et al.* 2006). Disruption of the *Atm* gene in mice largely recapitulates the human phenotype, with almost all $Atm^{-/-}$ mice succumbing to thymic lymphomas within 5 months (Barlow *et al.* 1996). CTMIO intake through drinking water (40µM) significantly prolonged the survival of $Atm^{-/-}$ mice (median survival of 54 weeks versus 16 weeks, CTMIO versus untreated respectively) (Figure 4.2). The CTMIO chemoprevention mechanism did not appear to involve apoptosis, as tumours from CTMIO treated mice did not show higher levels of apoptosis compared to tumours from untreated $Atm^{-/-}$ mice (Gueven *et al.* 2006).

This study also examined the effect of CTMIO on neuromotor performance by employing a multiparameter test based on performance on a narrow beam. CTMIO treatment significantly improved overall motor performance of $Atm^{-/-}$ mice, correcting the neurobehavior function to levels comparable to Wt mice (Figure 4.3) (Gueven *et al.* 2006).

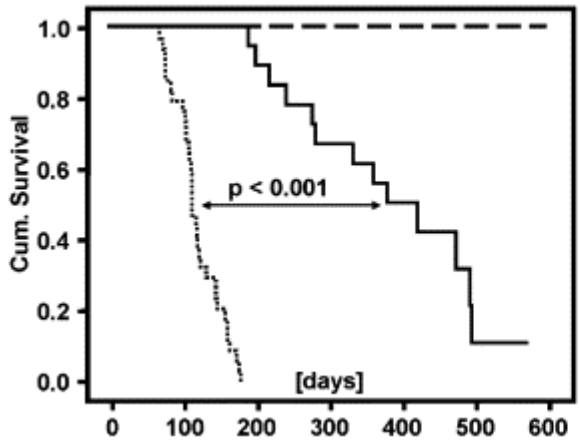

	CTMIO	Median survival (days)	SE (Med)	95% CI lower	95% CI upper
Atm$^{-/-}$	untreated	109.00	4.07	101.01	116.99
	treated	379.00	50.91	279.21	478.79

Figure 4.2 – Effect of CTMIO on survival of *Atm*$^{-/-}$ mice (Gueven *et al.* 2006).

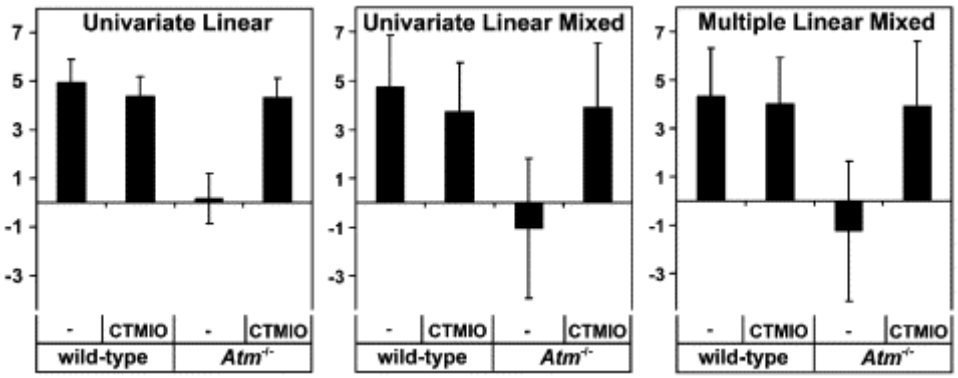

Figure 4.3 – Effect of CTMIO on neurobehavioral function of *Atm*$^{-/-}$ mice. Neuromotor performance assessed by multiparameter test based on performance on a narrow beam. All three statistical models show a significant effect for the CTMIO treatment of *Atm*$^{-/-}$ mice, but not Wt mice (Gueven *et al.* 2006).

Additionally, *Atm*$^{-/-}$ mice show multiple manifestations of oxidative stress in the cerebellar Purkinje cells as determined by 3-nitrotyrosination of proteins and immunoreactivity to 4-hydroxy-2-nonenal Michael adducts. Treatment with CTMIO reduces the levels of oxidative damage to those of Wt mice, suggesting that CTMIO corrects the A-T neurobehavioral phenotype by its antioxidative activity (Gueven *et al.* 2006).

4.2 – Aim of study

The isoindoline nitroxide CTMIO has been shown to have strong antioxidant properties, so much as displaying a neuroprotective effect in A-T cell and mouse models by preventing neuronal cell loss. FRDA, similarly to A-T, is a progressive neurodegenerative disorder, and it is generally accepted that such pathology may be a consequence of the actions of free radicals.

Therefore, it has been hypothesised that such compound may be of potential benefit to the therapy of FRDA. For that reason, the aim of this research project is to examine the potential antioxidant and neuroprotective effects of CTMIO in FRDA by performing drug trials on the *FXN* YAC GAA transgenic mice available.

4.3 – Materials and methods

4.3.1 – CTMIO synthesis and origin

The isoindoline nitroxide antioxidant CTMIO was synthesised as previously described by Bottle *et al.* (2000) and kindly made available by Dr Nuri Gueven from the Queensland Institute of Medical Research, Australia.

4.3.2 – Drug preparation

The CTMIO was provided to us in a solid form and was stored at 4°C. Initially, a 250x stock solution was prepared by dissolving 23mg of the provided CTMIO in 10ml PBS under heating and stirring conditions, resulting in a 10mM stock solution. This stock solution was also stored through the duration of the study at 4°C. Finally, the stock solution was diluted 1:250 in drinking tap water as required, resulting in a 40µM CTMIO solution. A placebo solution was prepared by diluting PBS 1:250 in drinking tap water.

4.3.3 – Study design and drug administration

A long-term CTMIO study was performed on Wt and YG8 rescue mice with 30 animals in each drug/placebo group (Table 4.1). The treatment was initiated as soon as possible after weaning and genotyping, at approximately 2 months of age and, at an initial stage, lasted for 3 months. An additional 3 months of treatment were then performed on only half of the mice, with 15 animals in each group.

The 40µM CTMIO/placebo solution was administered *ad libitum* as a replacement to normal drinking water. The water was changed twice a week.

Table 4.1 – CTMIO study details including the number of mice used in each group

	3 month duration		6 month duration	
	Wt	**YG8**	**Wt**	**YG8**
Placebo	30	30	15	15
CTMIO	30	30	15	15

4.3.4 – Functional studies during drug treatments

Weight, rotarod performance and locomotor activity measurements were taken just before the start of the drug treatment and repeated thereafter every 1.5 months until the completion of the treatment.

4.3.5 – Sample collection

At the completion of the drug treatment the mice were appropriately culled and samples were collected as described in Chapter 2 according to the type of analysis desired: 7 mice from each group were sampled for biochemical analysis and the remaining 8 were sampled for histological analysis (Table 4.2).

Table 4.2 – Number of mice sampled for biochemical and histological analysis

	biochemical analysis				histological analysis			
	3 months		6 months		3 months		6 months	
	Wt	**YG8**	**Wt**	**YG8**	**Wt**	**YG8**	**Wt**	**YG8**
Placebo	7	7	7	7	8	8	8	8
CTMIO	7	7	7	7	8	8	8	8

4.3.6 – OxyBlot analysis

Oxyblot analysis was performed on brain samples of Wt and YG8 mice for both the 3 months and the 6 months duration studies (Table 4.3). The OxyBlot analysis was performed 2x for all samples.

Table 4.3 – Number of brain samples investigated by OxyBlot analysis

	3 month duration		6 month duration	
	Wt	**YG8**	**Wt**	**YG8**
Placebo	6	6	6	6
CTMIO	6	6	6	6

4.3.7 – Histological analysis

DRG paraffin-embedded sections were analysed by standard H&E histology (Table 4.4).

Table 4.4 – Number of DRG samples investigated by H&E histology

	6 month duration	
	Wt	**YG8**
Placebo	2	2
CTMIO	–	2

Additionally, paraformaldehyde-fixed brain and heart samples were sent to Dr John Luff and Dr Nuri Gueven from the Queensland Institute of Medical Research in Australia, where histological and immunohistochemistry analysis was performed in order to investigate levels of: nitrotyrosine (NO-dependent oxidative stress marker), 4HNE (lipid peroxidation marker), p53 (tumour suppressor gene), ATM S1981 (protein phosphorylation marker), 8oxoG (DNA damage marker), Fe deposits, and cardiac hypertrophy.

4.4 – Results

4.4.1 – Functional studies

A CTMIO drug study consisted of administering 40µM CTMIO (or placebo) *ad libitum* in drinking water to Wt and YG8 rescue mice (n=30), for a preliminary duration of 3 months. After this, treatment was continued for an additional 3 months on only half of the mice (n=15). The treatment was initiated as soon as possible after weaning and genotyping, with the mice being generally matched for age, at approximately 2 months of age (Figure 4.4). In the first 3 months of treatment the proportion of males to females was 1:1. However, for the second 3 months period, two thirds were males and the remaining third were females (Figure 4.5). No drug/placebo administration-associated deaths were observed.

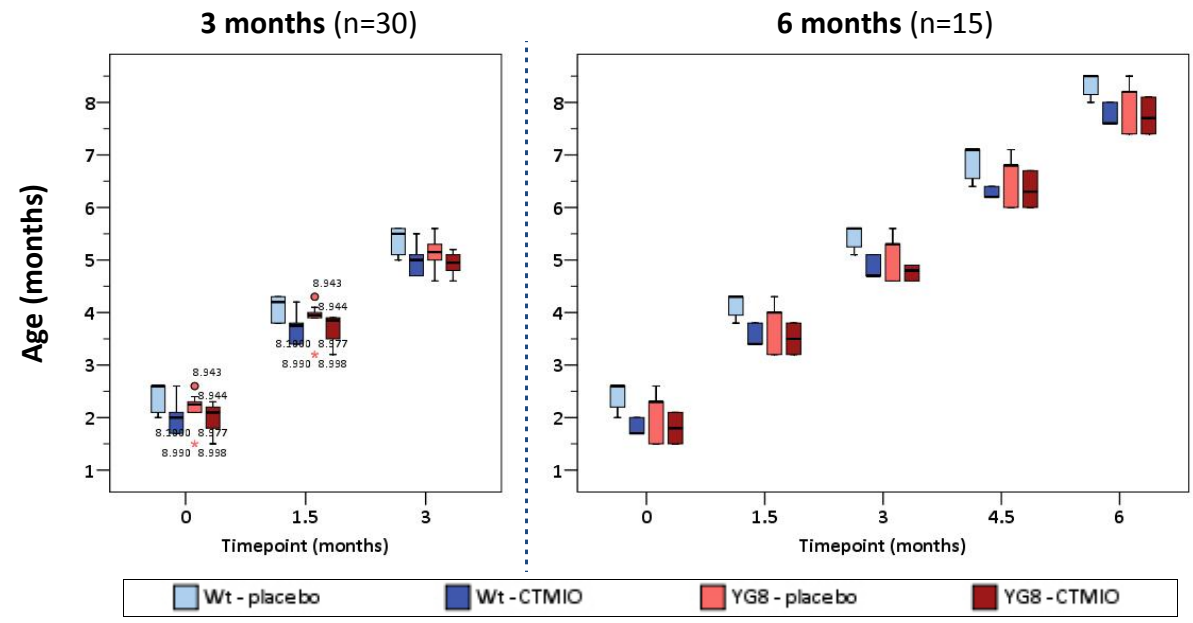

Figure 4.4 – Age distribution of mice used in the CTMIO studies.

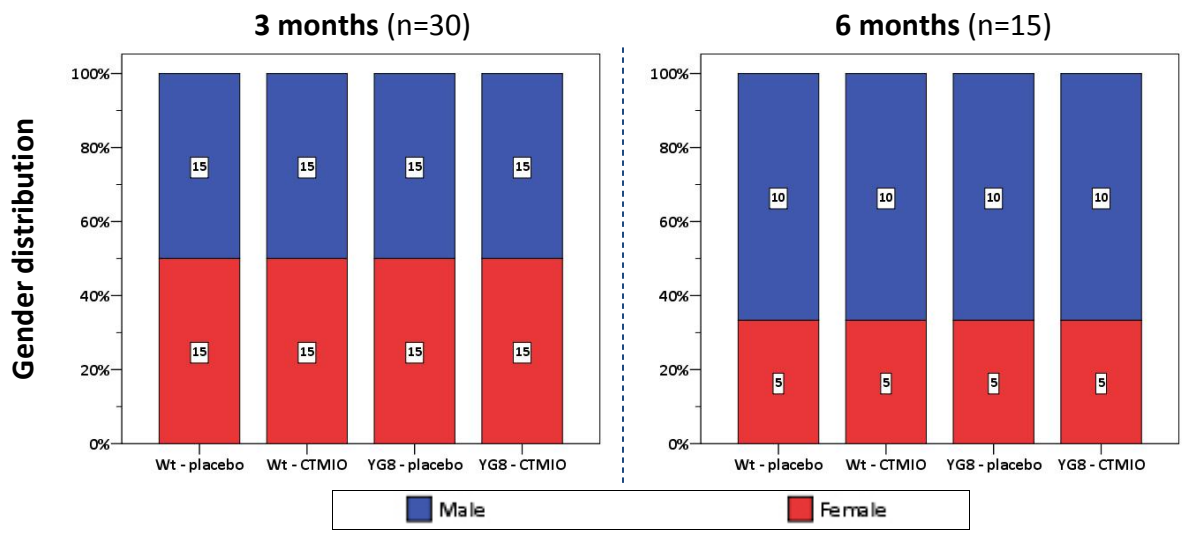

Figure 4.5 – Gender distribution of mice used in the CTMIO studies.

All mice in the different study groups started off with similar weight levels (Figure B.1), and although they all constantly gained weight throughout the study, YG8 mice seem to have gained relatively more than Wt (Figure 4.6 and Figure B.2). This was particularly noticeable at the end of the 6 months study, where, on average, Wt mice had increased their weight by 40% while YG8 mice showed a 52% increase. In fact, 2-way mixed ANOVA for repeated measures confirmed that not only the age of the mice (timepoint) had a significant effect on the weight gain, but also the genotype (Table 4.5). It was also noticeable that throughout the study all CTMIO-taking mice seem to have gained more weight when compared to placebo-taking mice of the same genotypic background. However, this was generally statistically non-significant (Table 4.5).

Regarding rotarod analysis, mice from all study groups showed similar average performance levels at the start of the study (Figure B.3). However, a considerable variability of performance levels were observed within all study groups, with values regularly ranging from approximately 100s to the test maximum of 400s (Figure B.3). As the study progressed, the number of highly performing mice seems to have reduced, but at the end of the 6

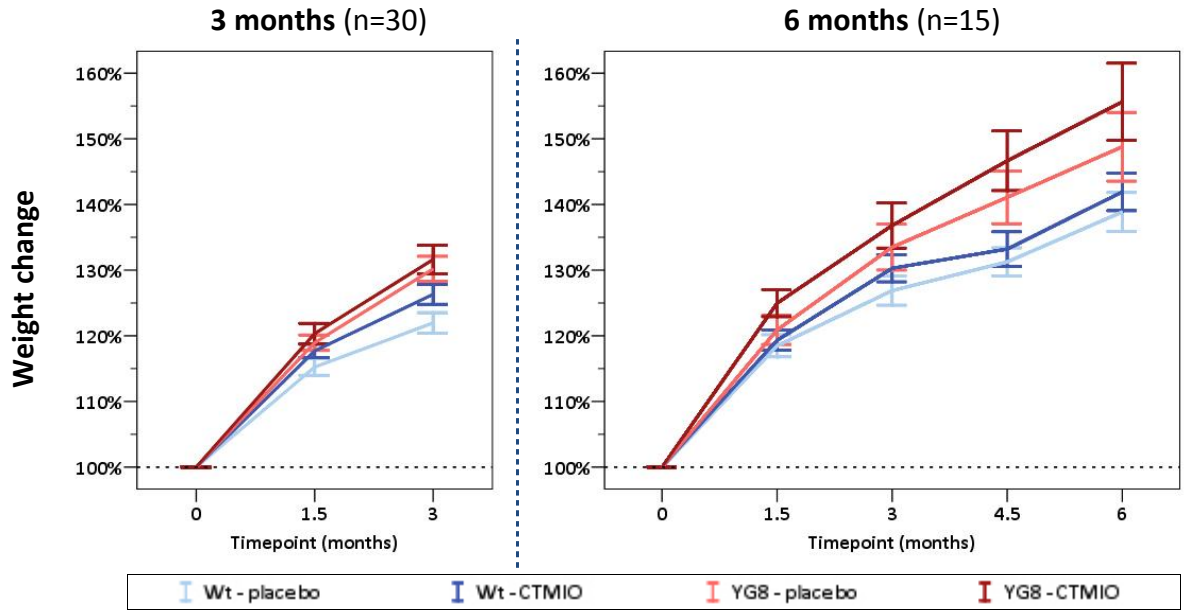

Figure 4.6 – Weight gain/loss during the CTMIO studies. (error bars: +/- 1 SE)

Table 4.5 – ANOVA associated *p*-values of timepoint, genotype and drug treatment effect on the various functional measurements during the CTMIO studies.

		ANOVA *p*-values			
		3months (n=30)		**6 months** (n=15)	
Treatment effect on	**Genotype**	**Timepoint**	**Timepoint * Treatment**	**Timepoint**	**Timepoint * Treatment**
Weight	Wt	<0.001	0.042	<0.001	0.655
	YG8	<0.001	0.763	<0.001	0.658
Rotarod performance	Wt	0.129	0.113	<0.001	0.252
	YG8	<0.001	0.519	<0.001	0.272
Locomotor activity	Wt	0.001	0.219	<0.001	0.060
	YG8	<0.001	0.470	<0.001	0.255
		3months (n=30)		**6 months** (n=15)	
Genotype effect on	**Treatment**	**Timepoint**	**Timepoint * Genotype**	**Timepoint**	**Timepoint * Genotype**
Weight	Placebo	<0.001	<0.001	<0.001	0.015
	CTMIO	<0.001	0.039	<0.001	0.005
Rotarod performance	Placebo	<0.001	0.584	<0.001	0.479
	CTMIO	0.002	0.040	<0.001	0.046
Locomotor activity	Placebo	0.001	0.679	<0.001	0.022
	CTMIO	<0.001	0.056	<0.001	0.943

months study these were still present, particularly in YG8 study groups (Figure B.3). Regarding individual changes in performance these were also relatively normally distributed (Figure B.4). Overall, although rotarod performance levels were maintained for the first 1.5 months, they significantly declined after that (Figure 4.7 and Table 4.5). Final drops of approximately 14% and 28% were respectively observed in Wt placebo- and CTMIO-taking mice, while a 30% and 43% reduction was observed in YG8 placebo- and CTMIO-taking mice, respectively (Figure 4.7). Therefore, it appears that the YG8 mice demostrated greater declines in rotarod performance when compared to the Wt mice. In fact, this was found to be statistically significant when comparing Wt and YG8 CTMIO-taking mice (Table 4.5). Additionally, it seems that the CTMIO treatment is having a detrimental effect on rotarod performance: both Wt and YG8 CTMIO-taking mice showed stronger decreases in rotarod performance when compared to the respective placebo-taking mice (Figure 4.7). However, this was not found to be statistically significant (Table 4.5).

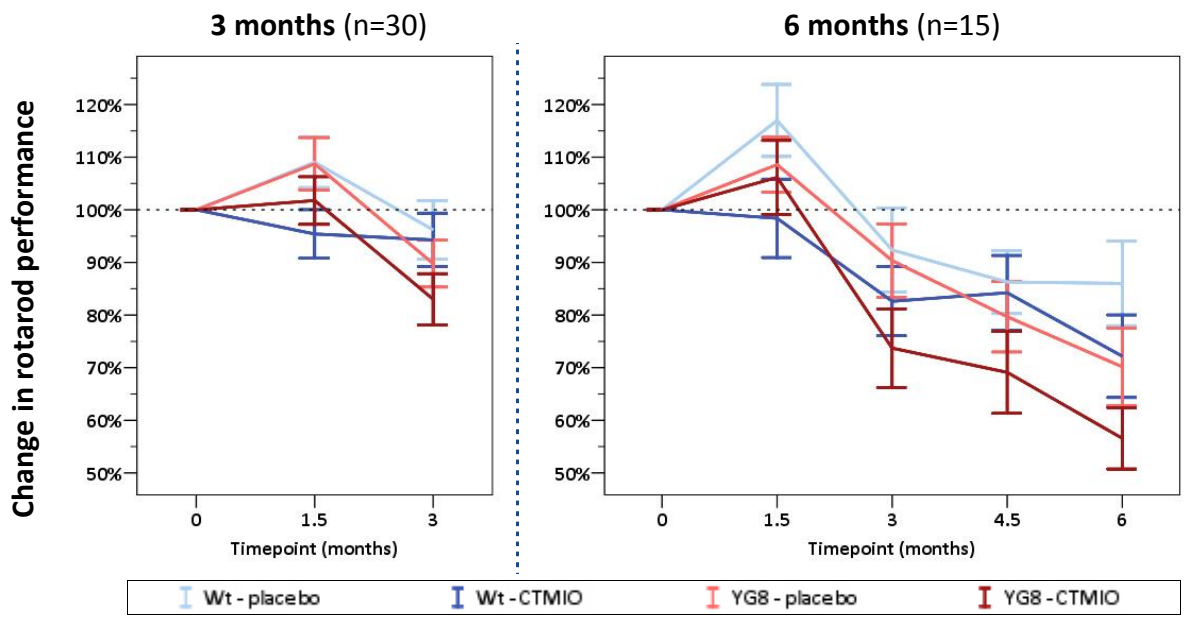

Figure 4.7 – Rotarod performance change during the CTMIO studies. (error bars: +/- 1 SE)

Regarding locomotor activity, with the exception of two CTMIO-taking Wt mice which were clearly hyperactive (regularly covering >20 squares in 30s), the absolute values were normally distributed, regularly ranging from 0-15 squares (Figure B.5). However, when a change in activity levels was computed, much greater levels of variability were observed: some mice from the same study groups more than doubled their activity while others showed drastic drops in activity (Figure B.6). Nevertheless, activity levels of all study groups generally decreased throughout the study. Although the progress of locomotor activity performance throughout the study was found to be significantly different between Wt and YG8 placebo-taking mice (Table 4.5), both study groups completed the 6 months study with similar final average levels: 51% and 49% reduction in locomotor activity, respectively (Figure 4.8). Additionally, CTMIO treatment slowed the decline in locomotor activity over the 6 months study: 38% and 35% reduction in final average locomotor activity levels of Wt and YG8 CTMIO-taking mice, respectively (Figure 4.8). However, this was not found to be statistically significant (Table 4.5).

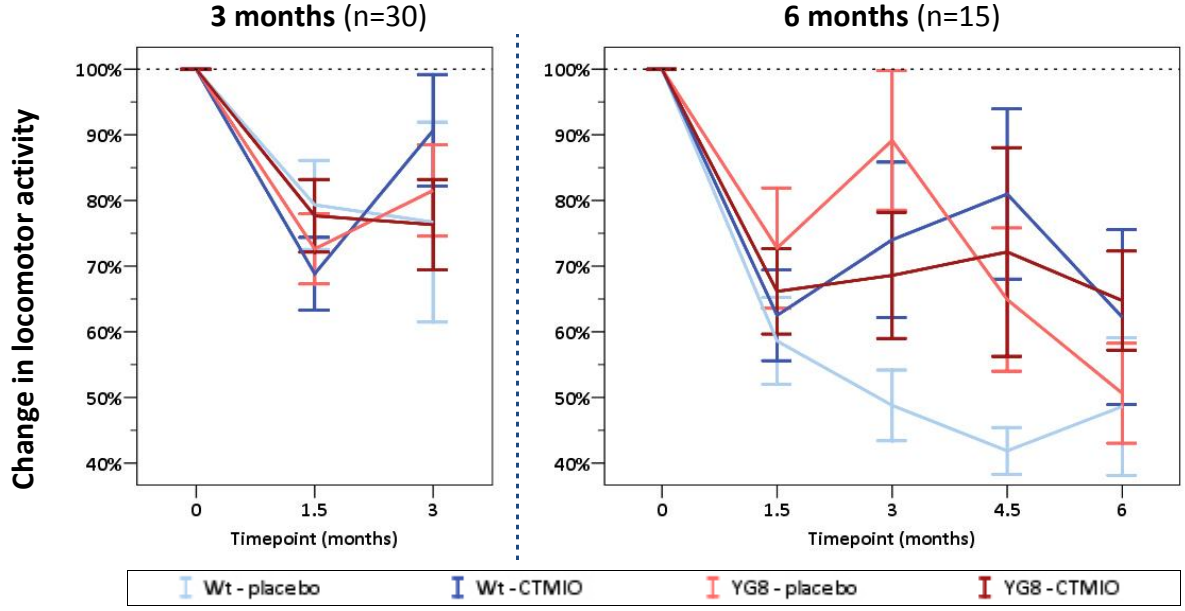

Figure 4.8 – Change in locomotor activity during the CTMIO studies. (error bars: +/- 1 SE)

4.4.2 – Oxyblot analysis

The levels of protein oxidation were determined in the brain of Wt and YG8 rescue mice from the 3 and 6 months CTMIO studies (n=6). Four oxyblots, each containing all samples investigated, were quantified by densitometry (Figure B.7), with similar results between them. Combined analysis of all oxyblots revealed no great differences in the average levels of protein oxidation between the 3 and 6 months duration studies. Although average protein oxidation levels in YG8 brains seem to be generally higher than in Wt (Figure 4.9), these were not found to be statistically significant (Table 4.6). CTMIO treatment seems to have further increased protein oxidation levels in the brain of both Wt and YG8 rescue mice, even elevating the Wt levels to those observed in YG8 mice (Figure 4.9). In fact, the treatment effect was found to be statistically significant in Wt mice from the 3 months study and in YG8 rescue mice from the 6 months study (Table 4.6).

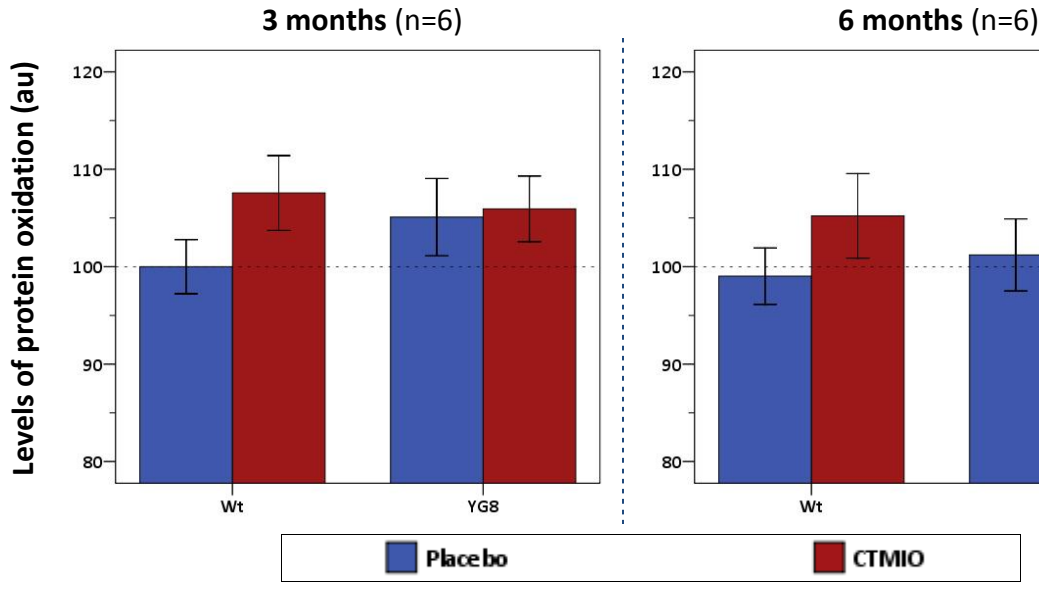

Figure 4.9 – Levels of protein oxidation in the brain of mice from the CTMIO studies, as determined by Oxyblot analysis. (error bars: +/- 1 SE)

Table 4.6 – Independent samples *t*-test associated *p*-values of treatment and genotype effect on brain levels of protein oxidation during the CTMIO studies.

Treatment effect		
Genotype	***p*-value** (n=6)	
	3 months	**6 months**
Wt	0.032	0.100
YG8	0.747	0.023

Genotype effect		
Treatment	***p*-value** (n=6)	
	3 months	**6 months**
placebo	0.092	0.343
CBD	0.585	0.525

4.4.3 – Histological analysis

Histological analysis was performed by means of H&E staining of lumbar vertebral column sections (as performed for the cannabinoid studies – Figure 3.11 and Figure 3.12) from Wt (placebo) and YG8 rescue (placebo and CTMIO) mice (n=2). The levels of DRG neurodegeneration were determined by counting the number of neuronal cell bodies displaying vacuoles (Figure 3.12). All of the mice investigated were from the 6 months study and were 8 to 8.5 months old.

Analysis of distal sections of the lumbar vertebrae (VL_{3+4}) consistently revealed higher levels of neurodegeneration when compared to the proximal lumbar vertebrae (VL_{1+2}) in all mice analysed (Figure 4.10). CTMIO treatment seems to have induced higher levels of DRG neurodegeneration in YG8 mice: CTMIO-treated YG8 mice showed 3x (VL_{1+2}) and 2.5x (VL_{3+4}) the number of DRG cell bodies with vacuoles compared with placebo YG8 mice (Figure 4.10).

Relatively high levels of DRG neurodegeneration were also detected in Wt placebo-treated mice (Figure 4.10). These levels were similar to the ones observed in YG8 CTMIO-treated mice.

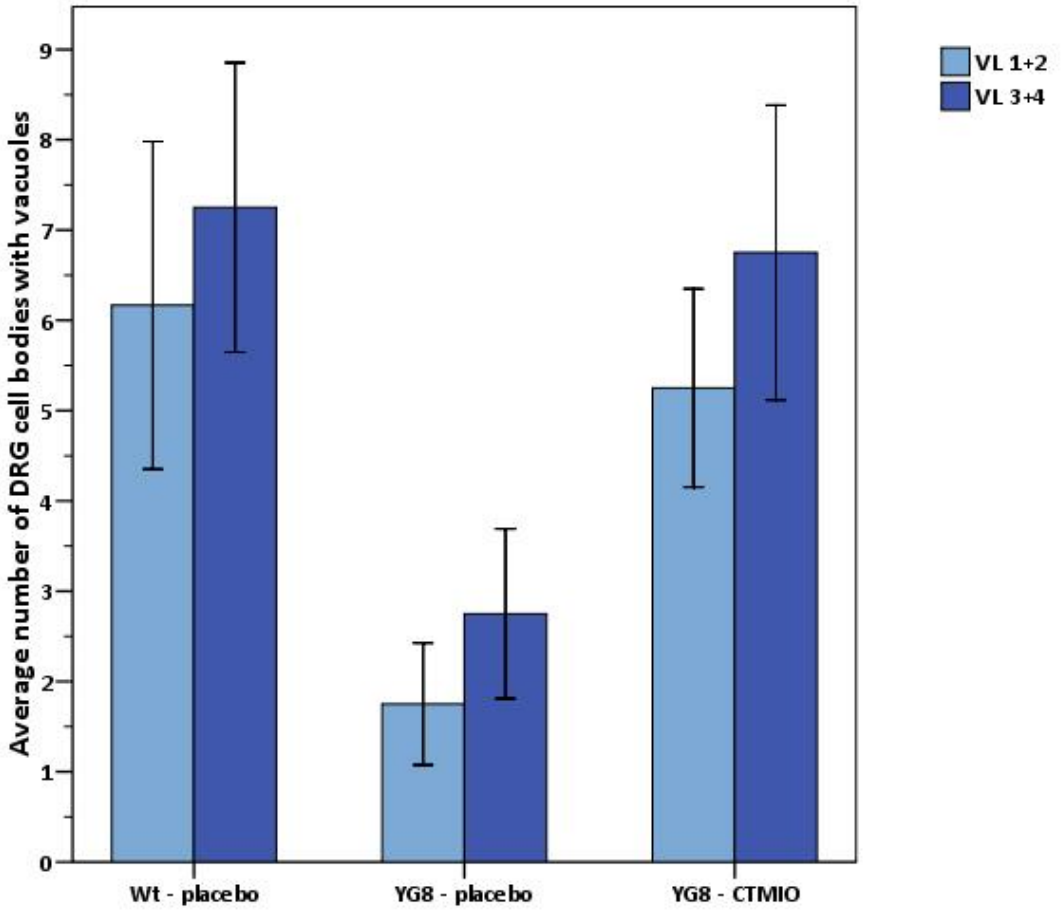

Figure 4.10 – Levels of DRG neurodegeneration following the 6 months CTMIO treatment.
(n=2; error bars: +/- 1 SE)

4.5 – Discussion

The reported antioxidant and neuroprotective effects of the isoindoline nitroxide CTMIO displayed in A-T cell and mouse models (Gueven *et al.* 2006) suggested that such compound could possibly be of therapeutic use to FRDA patients. Therefore, the effect of CTMIO on FRDA was investigated by performing drug studies on Wt and YG8 rescue mice. These studies consisted of administering 40µM CTMIO (or placebo) *ad libitum* in drinking water for a period of 3 and 6 months. This was the same CTMIO concentration as originally described by Gueven *et al.* (2006). Various functional studies were routinely performed throughout the treatment period, such as: weight monitoring, assessment of rotarod performance and locomotor activity.

Analysis of the data revealed that CTMIO treatment produced an increased weight gain at the same time as having a detrimental effect on rotarod performances. On the other hand, CTMIO treatment slowed the decline in average locomotor activity levels throughout the study. These data may seem contradictory, but such effects were statistically non-significant. In fact, although a considerable number of mice were investigated (n=30 and n=15 in 3 and 6 months studies respectively), statistical analysis of functional data seems to be limited by the mild severity of the FRDA-associated phenotype displayed by YG8 rescue mice.

The antioxidant properties of CTMIO were further investigated by performing oxyblot analysis on brain samples of treated Wt and YG8 mice. This analysis confirmed marginally elevated protein oxidation levels in YG8 mice, when compared to Wt, although not statistically significant. CTMIO treatment seems to have further increased these levels. In fact, this effect was determined to be of statistical significance in both Wt (3 months) and YG8 (6 months) study groups. This finding not only seems to negate the antioxidant

properties of CTMIO (at least in brain tissue), but rather seems to suggest a detrimental effect as far as protection from oxidative stress in the brain is concerned. Nevertheless, the lack of any significant difference between Wt and YG8 mice and the fact that the degree of variability between the study groups was minimal (<9%), suggests that any findings should be interpreted with caution.

Histological analysis of DRG from YG8 mice confirmed the FRDA-like "dying back" effect, demonstrated by the higher levels of neurodegeneration present in DRG from distal lumbar vertebrae. CTMIO treatment seems to have aggravated the levels of DRG neurodegeneration in YG8 mice. Interestingly, Wt mice (placebo) displayed previously unreported (Al-Mahdawi *et al.* 2006) high levels of DRG degeneration. Therefore, the presence of vacuoles in DRG cell bodies of YG8 mice as an FRDA-associated pathological phenotypic trait must now be re-evaluated.

Additionally, histological and immunohistochemical analysis was performed by Dr John Luff and Dr Nuri Gueven from the Queensland Institute of Medical Research in Australia, investigating levels of: nitrotyrosine (NO-dependent oxidative stress marker), 4HNE (lipid peroxidation marker), p53 (tumour suppressor gene), ATM S1981 (protein phosphorylation marker), 8oxoG (DNA damage marker), Fe deposits, and cardiac hypertrophy. However, no significant differences were detected between Wt and YG8 mice, and thus no CTMIO-associated improvements could be measured (N. Gueven, personal communication).

In summary, based on rotarod performance studies, oxyblot and DRG histology analysis, it seems that CTMIO may have a more damaging than neuroprotective effect for FRDA mice. However, any conclusive interpretations from this study, concerning the use of CTMIO in FRDA therapy, are considerably restricted by the lack of a strong demarcation between Wt and YG8 mice in functional, biochemical and histological terms. As a

consequence, the potential beneficial or detrimental effects of CTMIO may go by unnoticed. In fact, the antioxidant and neuroprotective effects of CTMIO were originally reported in *Atm*$^{-/-}$ mice exhibiting a severe phenotype such as life expectancy <5 months (Gueven *et al.* 2006).

Therefore, based on the findings hereby reported, it is not possible to promote or refute the use of CTMIO as therapeutic agent for FRDA patients.

Consequently, future investigations into the potential therapeutic effect of CTMIO for FRDA should, in a first instance, rely on the use of cell lines derived from FRDA patients. Only then, assuming promising results, should investigations be followed *in vivo*, making use of more severely affected FRDA mice. This may consist of performing studies that either use the current FRDA model, but with mice that are much older and displaying a potentially more significant phenotype, or else use a model with an earlier phenotype, as yet to be developed.

Chapter 5 – HDACi 106 therapeutic testing in FRDA mice

5.1 – Introduction

DNA methylation at CpG dinucleotides and histone modifications control accessibility of chromatin to the core transcriptional machinery and play an essential role in determining the activation state of genes. An array of post-translational histone modifications are known to occur at the N-termini of histone polypeptides, also known as histone tails. To date, more than 60 different modifications have been detected and these include acetylation, methylation, ubiquitylation, phosphorylation, and sumoylation (Table 5.1), all of which can serve as epigenetic tags (reviewed by Kouzarides 2007). Although most of these modifications remain poorly understood, there has been great progress in recent years, particularly in the understanding of methylation and acetylation roles in transcriptional regulation. In addition to roles in transcriptional regulation, histone modifications have been implicated in DNA replication, condensation and repair (Kouzarides 2007).

Table 5.1 – Different classes of modifications identified on histones (Kouzarides 2007)

Chromatin Modifications	**Residues Modified**	**Functions Regulated** *
Acetylation	**K**-ac	Trans, Rep, Repli, Cond
Methylation (lysines)	**K**-me1 **K**-me2 **K**-me3	Trans, Rep
Methylation (arginines)	**R**-me1 **R**-me2a **R**-me2s	Trans
Phosphorylation	**S**-ph **T**-ph	Trans, Rep, Cond
Ubiquitylation	**K**-ub	Trans, Rep
Sumoylation	**K**-su	Trans
ADP ribosylation	**E**-ar	Trans
Deimination	**R > Cit**	Trans
Proline Isomerization	**P-cis > P-trans**	Trans

* – Trans = Transcription, Rep = Repair, Repli = Replication, Cond = Condensation.

5.1.1 – Histone modifications and transcriptional regulation

Histone modifications primarily regulate gene expression in two mechanistic ways. Firstly, they regulate chromatin structure, making genetic loci more or less accessible to the transcriptional machinery. Secondly, they serve a signalling role by integrating responses to multiple biochemical signalling cascades and recruit or repel the transcriptional machinery and chromatin remodelling complexes (Kouzarides 2007).

It is generally accepted that histone modifications determine higher-order chromatin structure by affecting the contact between different histones in adjacent nucleosomes or the interaction of histones with DNA. Of all the known histone modifications, acetylation has the most potential to unfold chromatin since it neutralizes the basic charge of the lysine (Abel and Zukin 2008). This function is not easy to observe *in vivo*, but biophysical analysis indicates that inter-nucleosomal contacts are important for stabilization of higher-order chromatin structure (Abel and Zukin 2008). Thus, any alteration in histone charge will undoubtedly have structural consequences for the chromatin architecture.

Histone acetylation is catalysed by transcriptional coactivators such as CREB-binding protein, which possess histone acetyltransferase (HAT) activity (Lee and Workman 2007). Specificity of gene regulation is achieved by the recruitment of HATs by transcription factors to specific genetic loci, where they locally modify histones. Importantly, HATs interact with a large number of transcription factors and thus serve as crucial hubs, integrating the activity of multiple signalling cascades (Abel and Zukin 2008).

The effects of HATs can be reversed by histone deacetylases (HDAC), which remove acetyl groups from lysine residues in the histone tails (Lee and Workman 2007). Deacetylation of histone proteins shifts the balance toward chromatin condensation and thereby silences gene expression. Altogether, mammalian HDACs fall into four main classes

(I–IV), with class I and class II HDACs receiving the most attention in the nervous system (Carey and La Thangue 2006). Class I HDACs (HDACs 1, 2, 3, and 8) are constitutively nuclear proteins and are widely expressed, while class II HDACs (HDACs 4, 5, 6, 7, 9, and 10) are expressed in a tissue- and cell-specific manner, and are regulated, at least in part, by shuttling between the nucleus and cytoplasm (Bolden *et al.* 2006). Sequence specificity of HDAC action is acquired by recruitment of HDACs to specific genetic loci by repressors, corepressors, and methyl-DNA-binding proteins (Abel and Zukin 2008).

5.1.2 – Histone modifications in FRDA

Recent findings consensually implicate chromatin modifications in the aetiology of FRDA (Herman *et al.* 2006; Greene *et al.* 2007; Al-Mahdawi *et al.* 2008). Herman *et al.* (2006) originally investigated the histone acetylation state of the *FXN* gene in a lymphoblastoid cell line derived from a FRDA patient ($GAA_{650/1030}$) by ChIP, and reported significantly lower levels of histone acetylation in H3K9, H3K14, H4K5, H4K8, H4K12 and H4K16 surrounding the GAA repeat, when compared to a normal cell line (Figure 5.1a). No significant difference was observed on the *FXN* promoter region. Additionally, the levels of H3K9 mono-, di- and trimethylation (me3) for the region upstream of the GAA repeat were also reported to be significantly higher in the FRDA cell line, particularly those of H3K9 trimethylation (Figure 5.1b). Similarly, Greene *et al*. (2007) reported significantly elevated levels of H3K9 dimethylation upstream of the GAA repeat in lymphoblasts from four FRDA patients, when compared to those of unaffected individuals.

Investigation of H3 and H4 acetylation and H3K9 methylation modifications was later extended by Al-Mahdawi *et al.* (2008) by ChIP analysis (in the same *FXN* regions investigated by Herman *et al.* 2006) in autopsy brain tissues from two FRDA patients and two unaffected

individuals (Figure 1.12). Overall decreased H3ac and H4ac was confirmed in FRDA brain tissue, particularly in the downstream GAA region. All of the six acetylated histone residues examined (H3: K9, K14; and H4: K5, K8, K12, K16) showed a GAA-induced gradient of comparative acetylation that is highest in the *FXN* 5'UTR and lowest in the downstream GAA region, with the single most altered residue being H3K9. Interestingly, H3K9 also showed consistently increased levels of di- and trimethylation in all three of the *FXN* regions (Al-Mahdawi *et al.* 2008).

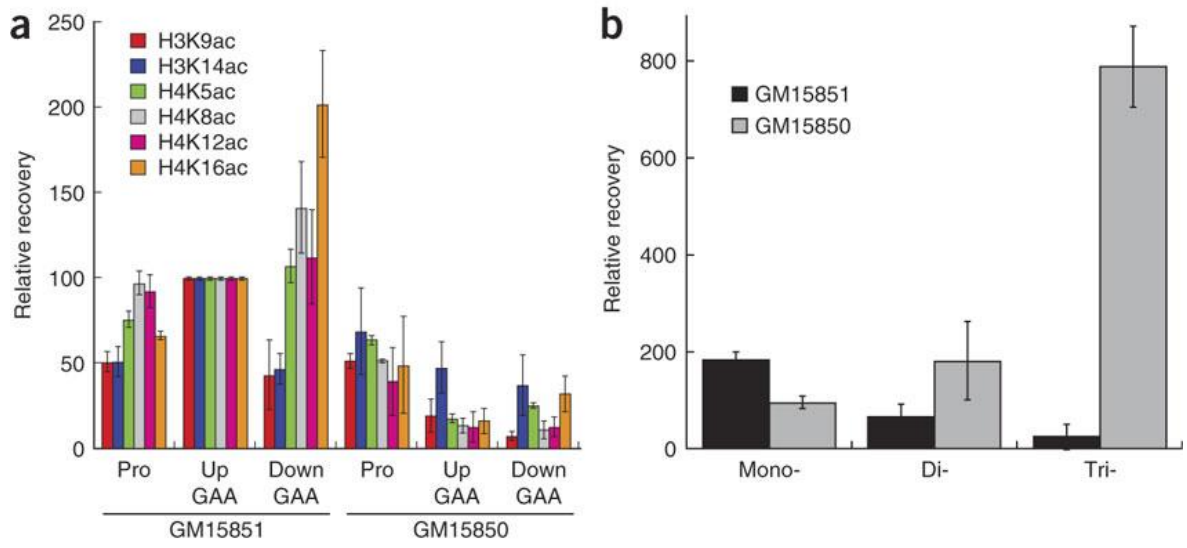

Figure 5.1 – Investigation of histone modifications in the *FXN* gene by ChIP analysis on a FRDA (GM15850) versus a normal lymphoblastoid cell line (GM15851). In FRDA, (**a**) histone acetylation levels at specified lysine residues are generally lower immediately upstream and downstream of the GAA repeat, (**b**) while levels of H3K9 methylation are significantly higher upstream of the GAA., when compared to the normal cell line (Herman *et al.* 2006).

5.1.3 – Use of HDAC inhibitors as therapy for FRDA

Considering the recent findings regarding an altered histone acetylation/methylation profile in FRDA, which resulted in a heterochromatin-mediated silencing effect of the *FXN* gene, it was postulated that the reversal/inhibition of these histone modifications could represent a potential therapeutic route for FRDA (Figure 5.2) (Herman *et al.* 2006).

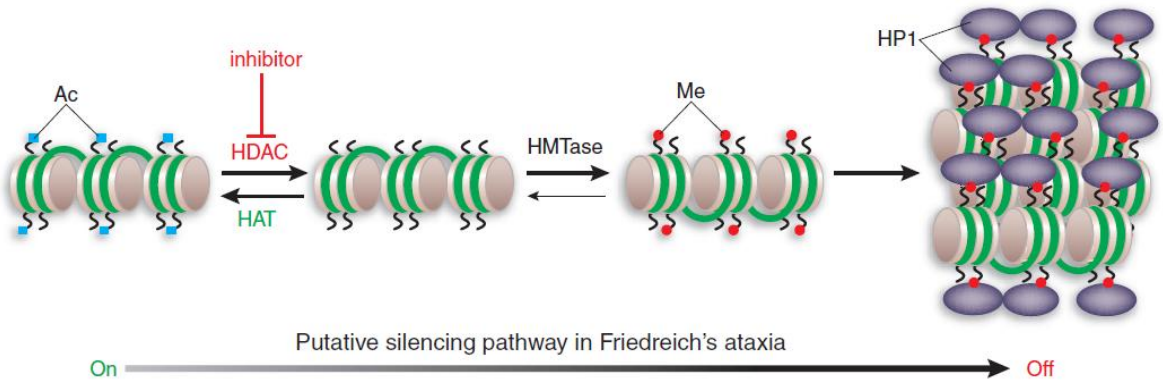

Figure 5.2 – HDACi therapy may reverse the heterochromatin-mediated silencing pathway in FRDA (Festenstein 2006).

Unlike HATs, HDACs have a rich structural diversity, which confers diversity of function and renders HDACs promising targets for drug discovery and therapeutic intervention.

In recent years there has been great activity in the development of new HDAC inhibitors (HDACi) (Carey and La Thangue 2006). HDACi can be classified into four main chemical families, the short-chain fatty acids (e.g. sodium butyrate, phenylbutyrate, and valproic acid), the hydroxamic acids (e.g. trichostatin A and suberoylanilide hydroxamic acid (SAHA)), the epoxyketones (e.g. trapoxin), and the benzamides (Abel and Zukin 2008). Of these, the most widely studied are sodium butyrate, phenylbutyrate, trichostatin A, and SAHA.

Initial studies linked HDACs to a wide variety of human cancers and in some cases HDACi treatment was successfully shown to have potent anticancer effects, with remarkable tumour specificity (Carey and La Thangue 2006; Minucci and Pelicci 2006). Inhibitors of class I and II HDACs are currently in phase I/II clinical trials for cancer therapy and potentially cancer prevention (Kuo *et al.* 2008; Molife *et al.* 2009).

Additionally, recent work has revealed that inhibitors of class I and II HDACs represent novel therapeutic approaches to treat neurodegenerative disorders, depression and anxiety, and the cognitive deficits that accompany many neurodevelopmental disorders (reviewed by Abel and Zukin 2008). This therapeutic potential in neurodegenerative disorders was initially revealed in Huntington disease (HD), where HDACi therapy was shown to ameliorate the characteristic cognitive and motor deficits (Ferrante *et al.* 2003; Hockly *et al.* 2003).

The potential of HDACi use in FRDA therapy was initially investigated by monitoring the effects of a range of commercial HDACi on the levels of histone acetylation and *FXN* transcription in a FRDA lymphoid cell line (Herman *et al.* 2006). This study showed that, of the tested compounds, the benzamide-type SAHA derivative BML-210 was the only HDACi to significantly increase (~2-fold) the level of *FXN* mRNA in the FRDA cell line (Figure 5.3b), even though other HDACi produced much higher levels of total acetylated histone (Figure 5.3a).

In this same study, a series of BML-210-derived HDACi were also described, with one compound in particular – 4b – showing great promise as a therapeutic agent for FRDA (Herman *et al.* 2006). HDACi 4b was shown to successfully increase the acetylation levels of H3K14, H4K5 and H4K12 in the GAA upstream region of *FXN*. Additionally, it significantly increased (~2.5-fold) the *FXN* mRNA levels in primary lymphocytes derived from individual with FRDA, to approximately 80% of that in unaffected individuals and to at least those of carriers (Figure 5.4), without apparent toxicity (Herman *et al.* 2006).

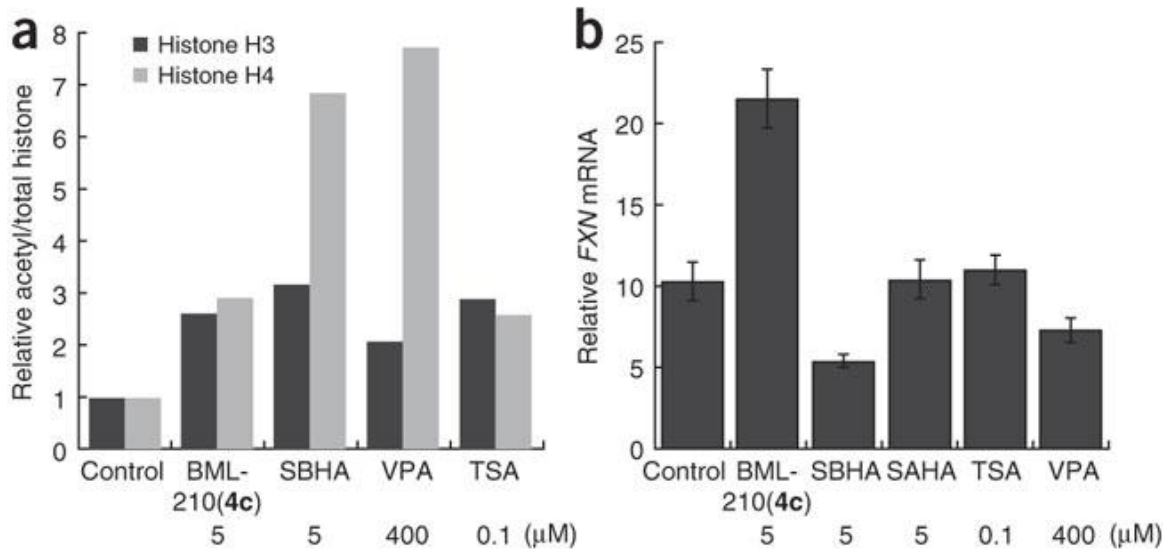

Figure 5.3 – Effects of commercial HDACi in a FRDA lymphoid cell line on: (**a**) the levels of H3 and H4 acetylation and (**b**) *FXN* mRNA levels (Herman *et al.* 2006). Compounds used: BML-210 (SAHA derivative), SBHA (suberoyl bis-hydroxamic acid), SAHA (suberoylanilide hydroxamic acid), TSA (trichostatin A), and VPA (valproic acid).

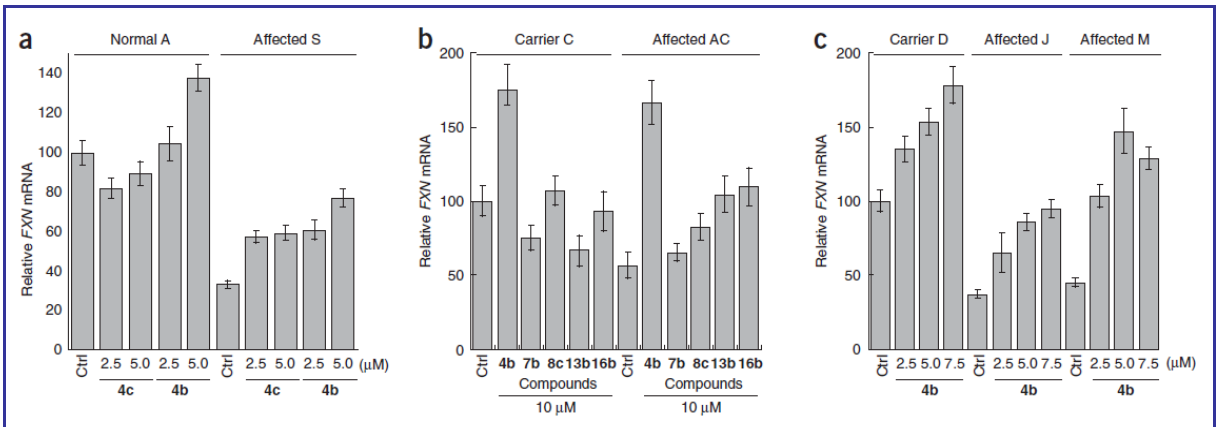

Figure 5.4 – HDACi increase *FXN* mRNA in primary lymphocytes from individuals with FRDA (Herman *et al.* 2006).

More recently, with the further development of a safe and effective compound for FRDA therapy in mind, a derivative of 4b, named 106 (Figure 5.5), was generated by RepliGen Corporation (Waltham, USA).

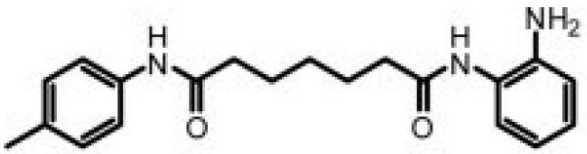

N^1-(2-aminophenyl)-N^7-*p*-tolylheptanediamide

Figure 5.5 – Chemical structure of HDACi 106 (Chou *et al.* 2008).

Recent studies with 106 confirmed the induced hyperacetylation of H3 (K9 and K14) and up-regulation of frataxin protein in FRDA lymphoblast cell cultures (Chou *et al.* 2008). In this study the duration of effect after removal of 106 from culture was also investigated, revealing that hyperacetylated levels of H3 do not fully return to basal levels until 6-7h after the removal of the inhibitor. Regarding the frataxin protein levels, although a 2-fold increase was initially observed after 24h of treatment, a far more significant increase in frataxin levels was observed 1-2h after removal of 106 (Figure 5.6).

Further investigations on 106 revealed that the causal increased levels of acetylated histones in the *FXN* gene and the increased frataxin expression result from a slow and strong inhibition of class I HDACs (HDAC1, 2, and 3), particularly of HDAC3 (Chou *et al.* 2008).

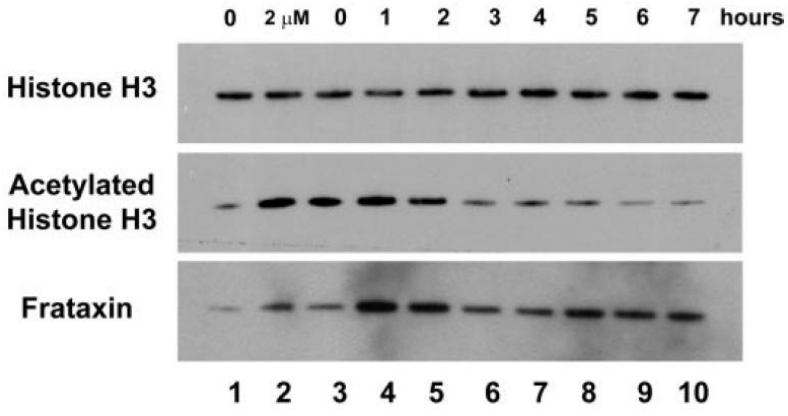

Figure 5.6 – HDACi 106 prolongs H3 acetylation and increases frataxin protein in FRDA lymphoblasts, as determined by Western blotting. GM15850 FRDA lymphoblast cells were either untreated (*lane 1*, marked 0 at top) or treated with 106 at 2 μM concentration for 24h (*lane 2*, marked 2μM at *top*), and then washed to remove the inhibitors. Cells were harvested at the indicated times (*lanes 3–10*, 0–7h) (Chou *et al.* 2008).

5.2 – Aim of study

Along with histone hypoacetylation, trimethylation of H3K9 is a recognised hallmark of heterochromatin. Thus, the reported histone modification states observed in pathology-associated *FXN* alleles are consistent with a chromatin-mediated mechanism as the cause of gene silencing in FRDA.

The *FXN* YAC transgenic mouse model described by Al-Mahdawi *et al*. (2008) shows FRDA patient-comparable epigenetic changes, including an altered DNA methylation profile, decreased H3K9 acetylation and increased in H3K9 methylation at the *FXN* transgenic locus.

The recently described series of benzamide-type, pimelic diphenylamide HDACi shows great promise as therapeutics for FRDA, particularly compound 106, which successfully increases levels of histone acetylation at the *FXN* gene and significantly increases levels of frataxin mRNA and protein (Herman *et al.* 2006; Chou *et al.* 2008).

For that reason, the aim of this research project is to examine the effects of 106 in FRDA by performing drug trials on the *FXN* YAC GAA transgenic mice available.

5.3 – Materials and methods

5.3.1 – HDACi 106 origin and drug preparation

The HDACi 106 was synthesised and made available to us by RepliGen Corporation. The drug was provided to us in a solid form as an HCl salt and was stored at 4°C. The different diluent solutions were also prepared and provided by RepliGen. Different HDACi 106 formulations were prepared according to the administration method.

Formulation A: 330mg of HDACi 106 was initially completely resuspended in 3 ml of diluent A (80% PEG400, 0.1M Na-acetate pH5.2), followed by 7ml of diluent B (40% HP-β-CD, 0.14M Na-acetate pH5.2) resulting in a 30mg/ml HDACi 106 solution. A placebo solution (24%PEG400, 28% HP-β-CD, 0.13M Na-acetate pH5.2) was prepared by mixing 3 parts diluent A with 7 parts diluent B. The drug/placebo solution was stored at 4°C.

Formulation B: 330mg of HDACi 106 was initially completely resuspended in 1 ml of DMSO (pre-warmed to 37°C), followed by 19ml of diluent C (40% HP-β-CD, 0.1M Na-acetate pH5.2)(pre-warmed to 37°C) resulting in a 15mg/ml HDACi 106 stock solution which was stored at 4°C. This stock drug solution was then diluted 1:15 in drinking tap water, resulting in a 1mg/ml HDACi 106 solution. A placebo solution (0.33% DMSO, 2.5% HP-β-CD, 6mM Na-acetate pH5.2) was prepared by mixing 1 parts DMSO with 19 parts diluent C, followed by 1:15 dilution in drinking tap water.

Formulation C: 330mg of HDACi 106 was initially completely resuspended in 0.25 ml of DMSO (pre-warmed to 37°C), followed by 9.75ml of diluent C (40% HP-β-CD, 0.1M Na-acetate pH5.2)(pre-warmed to 55°C) resulting in a 30mg/ml HDACi 106 solution which was stored at 4°C. A placebo solution (2.5% DMSO, 39% HP-β-CD, 0.1M Na-acetate pH5.2) was prepared by mixing 1 part DMSO with 39 parts diluent C.

5.3.2 – Study design: drug administration and sample collection

Pre-studies

Initial short-term pre-studies were performed on the YG8 mouse line, exploring 2 different delivery routes: sub-cutaneous injection and oral gavage. Mice subjected to this treatment were 3-5 months old and treatments consisted of 3 consecutive daily doses of HDACi 106 formulation A (30mg/ml) by either: oral gavage (150mg/kg) or sub-cutaneous (subQ) injection (150mg/kg and 300mg/kg). Regarding the placebo control mice, a corresponding volume of formulation A placebo solution was administered. Samples were collected for molecular biology/biochemistry analysis at distinct timepoints for each HDACi 106 treatment plan: 4h and 24h after the last dose (Table 5.2).

Table 5.2 – HDACi 106 pre study details including the number of mice used in each group

	Sub cutaneous administration		**Oral administration (gavage)**		
	150mg/kg		**150mg/kg**		**300mg/kg**
	4h*	**24h***	**4h***	**24h***	**24h***
Placebo	6	6	5	5	–
HDACi 106	6	6	5	5	3

* - time of study termination after last dose.

Long-term study – oral administration

A long-term study was performed on the YG8 line with 15 mice in each drug/placebo group. Mice subjected to this treatment were 4-5 months old and the treatment consisted of continuous *ad libitum* administration of HDACi 106 formulation B (1mg/ml), as replacement to normal drinking water, for 3 months (Table 5.3). Regarding the placebo control mice, formulation B placebo solution was administered in the same way. After the treatment

period was completed, a proportion of the mice were immediately culled and sampled for molecular biology/biochemistry analysis (8 mice per group) and for histology analysis (2 mice per group). The remaining mice (5 mice per group) were kept alive for an additional month with normal drinking water.

Long-term study – sub-cutaneous administration

A long-term study was performed on the YG8 line with 15 mice in each drug/placebo group. Mice subjected to this treatment were approximately 4 months old. The treatment consisted of continuous sub-cutaneous administration of 150mg/kg HDACi 106 formulation C (30mg/ml), 3x per week (i.e. Monday, Wednesday and Friday), for 4.5 months (Table 5.3). Regarding the placebo control mice, a corresponding volume of formulation C placebo solution was administered. After the treatment period was completed, mice were culled and sampled at distinct timepoints: 4h, 24h and 1 month after the last dose. Mice were sampled for molecular biology/biochemistry and histological analysis, respectively 4 and 1 mice from each distinct group.

Table 5.3 – HDACi 106 long-term study details including the number of mice used per group

	Sub cutaneous administration			**Oral administration (*ad libitum* in drinking water)**	
	150mg/kg 4.5 month treatment			**150mg/kg 3 month treatment**	
	4h*	**24h***	**1 month***	**0h***	**1 month***
Placebo	5	5	5	10	5
HDACi 106	5	5	5	8	5

* - time of study termination after last dose.

5.3.3 – Functional studies during drug treatments

Weight, rotarod performance and locomotor activity measurements (only performed for the long-term studies) were taken just before the start of the drug treatments and repeated thereafter until the completion of the treatment every 1-1.5 months.

5.3.4 – Investigation of frataxin expression

FXN mRNA expression investigated by relative Q-RT-PCR

The *FXN* levels were determined by relative Q-RT-PCR amplification using SYBR Green in a microplate-based real-time PCR system (ABI Prism 7900HT, Applied Biosystems) as previously described. Relative Q-RT-PCR analysis was performed using mRNA-specific primers for *FXN* and for *Gapdh* (endogenous control) (Table 2.2). Relative quantification values were determined by the $2^{-\Delta\Delta Ct}$ method using SDS 2.1 software (Applied Biosystems).

Table 5.4 – Number of brain samples investigated for *FXN* mRNA expression by Q-RT-PCR

	Pre-studies					Long-term studies				
	Oral			SubQ		Oral		SubQ		
	4h*	24h*	24h*#	4h*	24h*	0h*	1M*	4h*	24h*	1M*
Placebo	5	5	–	6	6	4	4	4	4	4
HDACi 106	5	5	3	6	6	4	4	4	4	4

* - time of study termination after last dose; # - [300mg/kg]

Frataxin protein expression investigated by Western blotting

The levels of frataxin protein were determined in brain samples from mice submitted to both short- and long-term HDACi 106 studies by Western blot analysis (Table 5.5), as

previously described. Frataxin levels were detected with rabbit anti-mature frataxin antibody (G. Isaya, Mayo Clinic) and were normalised to the levels of tubulin, detected by using rabbit anti-tubulin (Sigma).

Table 5.5 – Number of brain samples investigated for frataxin expression by Western blot

	Pre-studies		Long-term studies				
	SubQ		Oral		SubQ		
	4h*	24h*	0h*	1M*	4h*	24h*	1M*
Placebo	4	4	4	4	4	4	4
HDACi 106	4	4	4	4	4	4	4

* - time of study termination after last dose

5.3.5 – Investigation of histone modifications following drug treatment

The effect of HDACi 106 treatment on histone acetylation levels, particularly H3ac and H4ac, was investigated on brain samples from the short- and long-term studies by Western blot analysis (Table 5.6), as previously described. H3ac and H4ac levels were detected with rabbit anti-H3ac and anti-H4ac antibodies (Upstate) and were normalised to the levels of tubulin, detected by using rabbit anti-tubulin (Sigma).

Table 5.6 – Number of brain samples investigated for histone modifications by Western blot

	Pre-studies		Long-term studies				
	SubQ		Oral		SubQ		
	4h*	24h*	0h*	1M*	4h*	24h*	1M*
Placebo	4	4	4	4	4	4	4
HDACi 106	4	4	4	4	4	4	4

* - time of study termination after last dose.

5.3.6 – Histological analysis

Brain and DRG paraffin embedded sections were analysed by standard H&E histology (Table 5.7). This investigation was performed on the long-term studies and only for the mice culled immediately after the end of treatment.

Table 5.7 – Number of DRG samples from long-term studies investigated by H&E histology

	SubQ	Oral
Placebo	2	2
HDACi 106	2	2

5.4 – Results

5.4.1 – Preliminary short-term HDACi 106 studies

Short-term preliminary studies investigating the effect of HDACi 106 on FRDA were performed on a small number of YG8 rescue mice (n=3-6, Table 5.2). Mice subjected to this treatment were 3-5 months old and treatments consisted of 3 consecutive daily doses of 106 by either: oral gavage (150mg/kg) or sub-cutaneous (subQ) injection (150mg/kg and 300mg/kg). Samples were collected for analysis 4h and 24h after the last dose. Treatment with the lower dose of 106 (150mg/kg) did not produce any explicit toxicity, but the higher dose (300mg/kg) displayed severe signs of toxicity with 5 out of 8 treated mice dying.

Treatment with 106 (150mg/kg) reduced by approximately half the relative *FXN* mRNA levels in the brain of YG8 mice, 4h after the last dose (Figure 5.7). However, after 24h these levels were increased by approximately 20% when compared with placebo samples (Figure 5.7). These results were obtained with both oral and sub-cutaneous drug administration. Treatment with 106 (300mg/kg) reduced the relative *FXN* mRNA levels to 80% of those observed in placebo brain samples, 24h after the last dose (Figure 5.7).

Sub-cutaneous treatment with 106 (150mg/kg) reduced the relative levels of frataxin protein in the brain of YG8 mice to approximately 80% of those observed in placebo brain samples, 4h after the last dose (Figure 5.8). These levels were increased 24h after the final dose (approximately 20% higher than placebo) (Figure 5.8).

Additionally, sub-cutaneous treatment with 106 (150mg/kg) increased the total levels of H3 and H4 acetylation in the brain of YG8 mice by approximately 30%, 4h after the last dose, when compared with placebo samples (Figure 5.9). The levels of H3 acetylation remained increased 24h after the final dose (10% higher than placebo), while H4 acetylation levels returned to normal placebo levels (Figure 5.9).

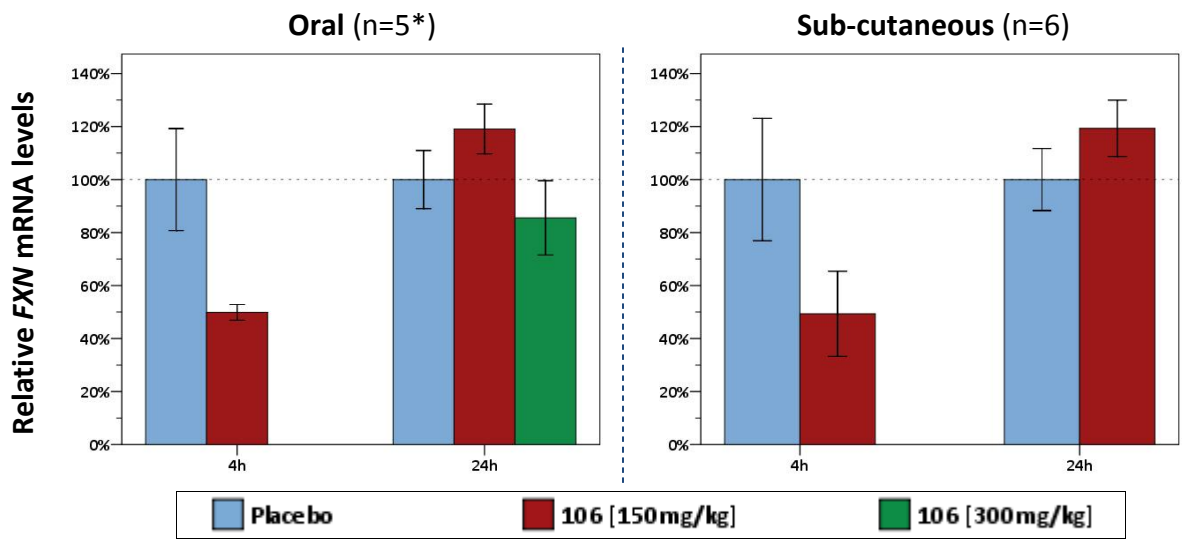

Figure 5.7 – Relative *FXN* mRNA levels in YG8 mouse brain following treatment with 106, as determined by Q-RT-PCR. (* - n= 3 for [300mg/kg]; error bars: +/- 1 SE)

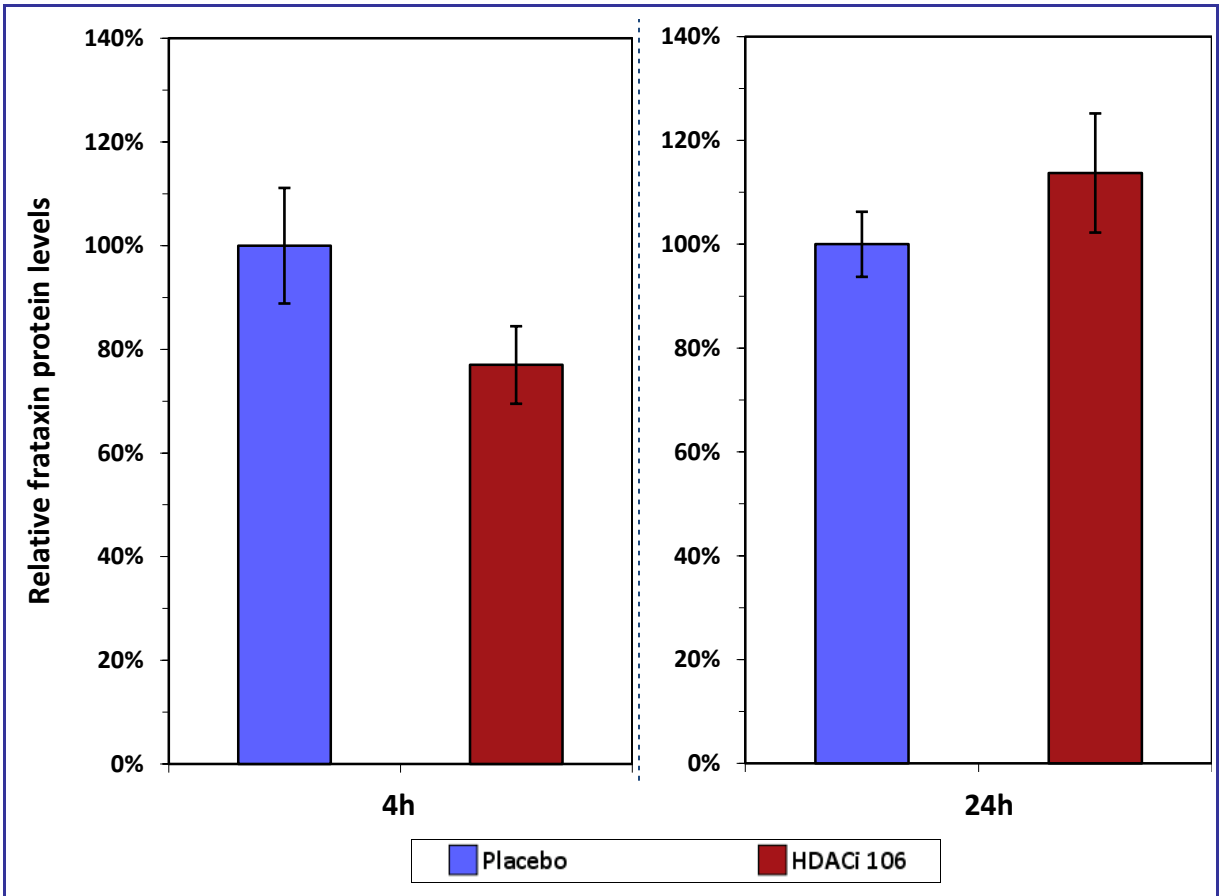

Figure 5.8 – Relative frataxin protein levels in YG8 mouse brain following treatment with 106 [150mg/kg] (sub-cutaneous administration), as determined by Western blot analysis. (n=4; error bars: +/- 1 SE)

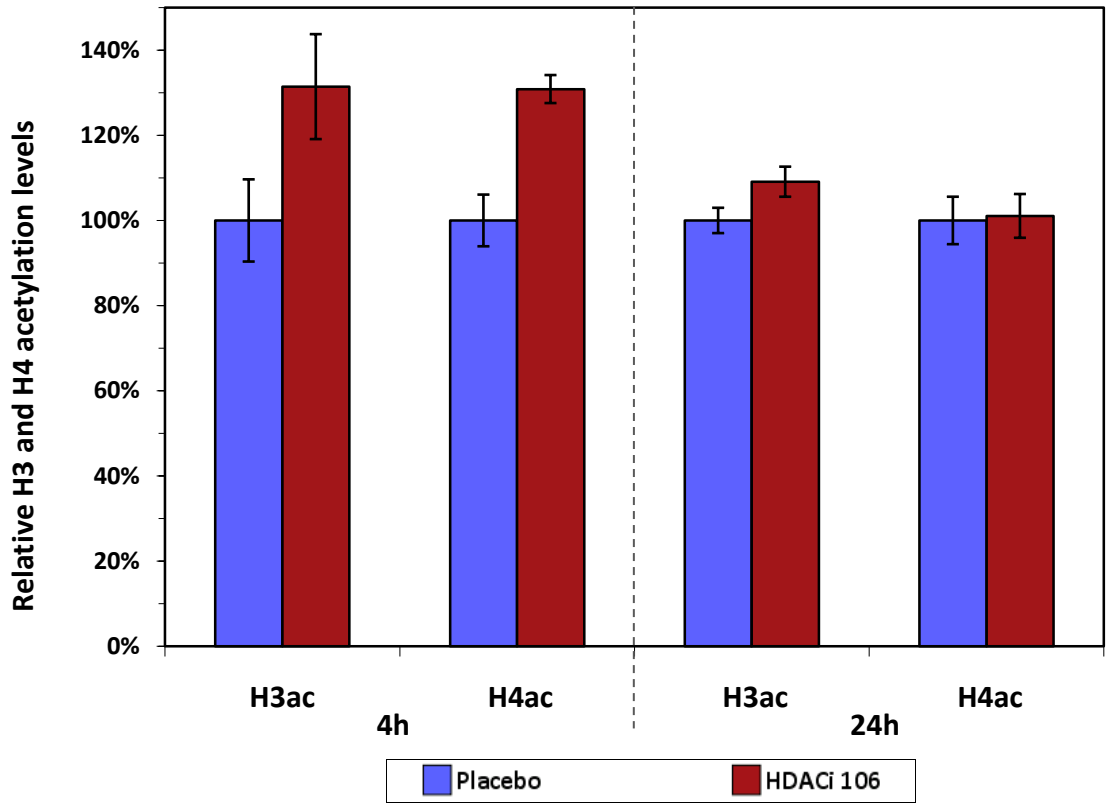

Figure 5.9 – Relative H3 and H4 acetylation levels in YG8 mouse brain following treatment with 106 [150mg/kg] (sub-cutaneous administration), as determined by Western blotting. (n=4; error bars: +/- 1 SE)

5.4.2 – Long-term HDACi 106 studies

The effect of HDACi 106 on FRDA was subsequently investigated by performing long-term studies on YG8 rescue mice (n=15). HDACi 106 (150mg/kg) was administered on a continuous base, either orally (*ad libitum*, as replacement to normal drinking water) or sub-cutaneously, for periods of 3 and 4.5 months respectively (Table 5.3).

Placebo and drug-taking mice from both studies were relatively matched for age, at approximately 4.7 and 3.8 months of age at the start of the oral and sub-cutaneous studies, respectively (Figure 5.10). In both studies, approximately two thirds of the treated animals were females (Figure 5.11).

The duration of effect was investigated in both studies by keeping a proportion of the treated animals (n=5) for an additional period of 1 month on drinking water only, following the last dose. These animals were either all females or all males in the oral and sub-cutaneous studies, respectively (Figure 5.11).

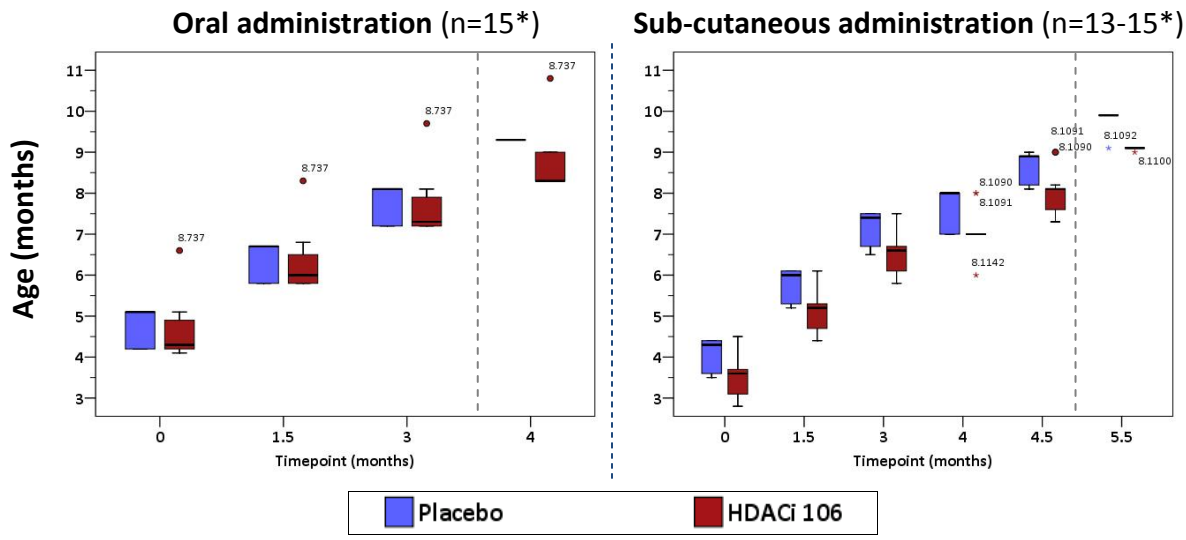

Figure 5.10 – Age distribution of mice used in the long-term HDACi 106 studies. Vertical dashed line represents the end of drug treatment. * - n=5 for duration of effect studies.

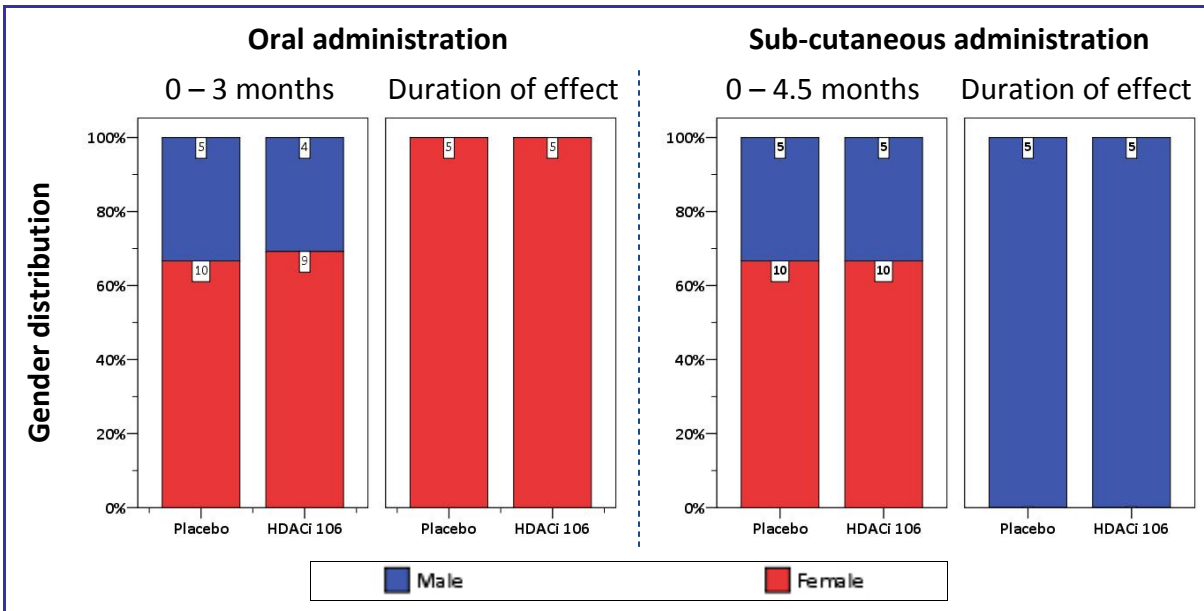

Figure 5.11 – Gender distribution of mice used in the long-term HDACi 106 studies.

Functional studies

Sub-cutaneous administration of 106 did not produce overt toxicity, but two deaths (out of 15) were observed within the first 1.5 months of the 106 oral administration study.

At the start of both 106 studies, placebo and drug-taking mice showed similar weight distributions (Figure C.1), which significantly increased throughout the studies (Table 5.8). Both 106 treatments significantly slowed the natural weight gain (Figure 5.12 and Table 5.8), which resumed after treatment withdrawal (Figure 5.13).

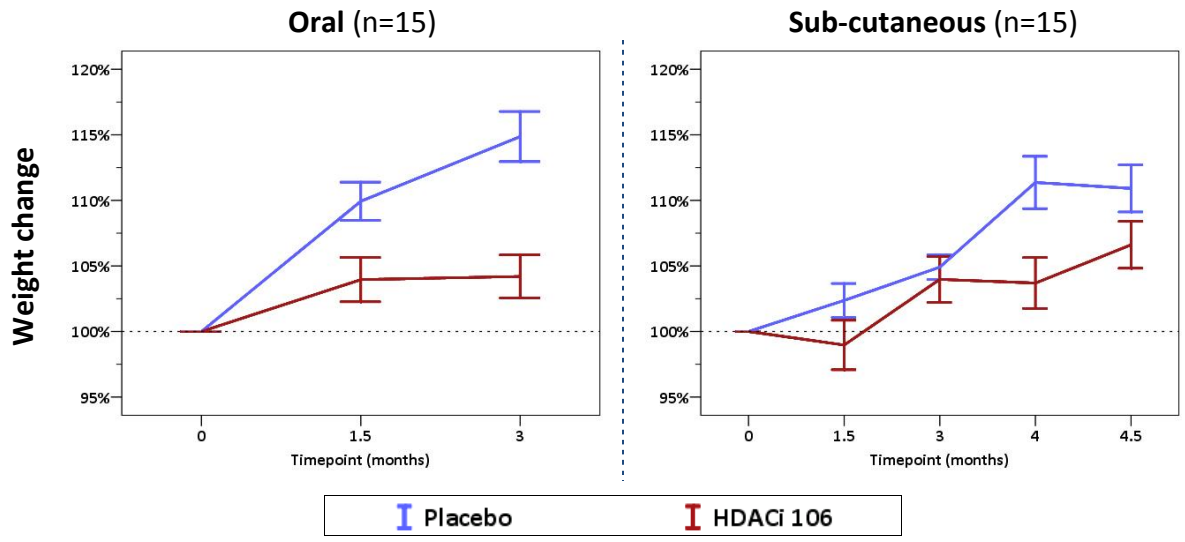

Figure 5.12 – Weight gain/loss during the HDACi 106 studies. (error bars: +/- 1 SE)

Table 5.8 – ANOVA associated *p*-values of timepoint and drug treatment effect on the various functional measurements during the oral and sub-cutaneous HDACi 106 studies.

	ANOVA *p*-values (n=12-15)			
	Oral administration		**Sub-cutaneous administration**	
Treatment effect on	**Timepoint**	**Timepoint * Treatment**	**Timepoint**	**Timepoint * Treatment**
Weight	<0.001	<0.001	<0.001	0.002
Rotarod performance	0.003	0.146	0.001	0.080
Locomotor activity	<0.001	0.332	<0.001	0.661

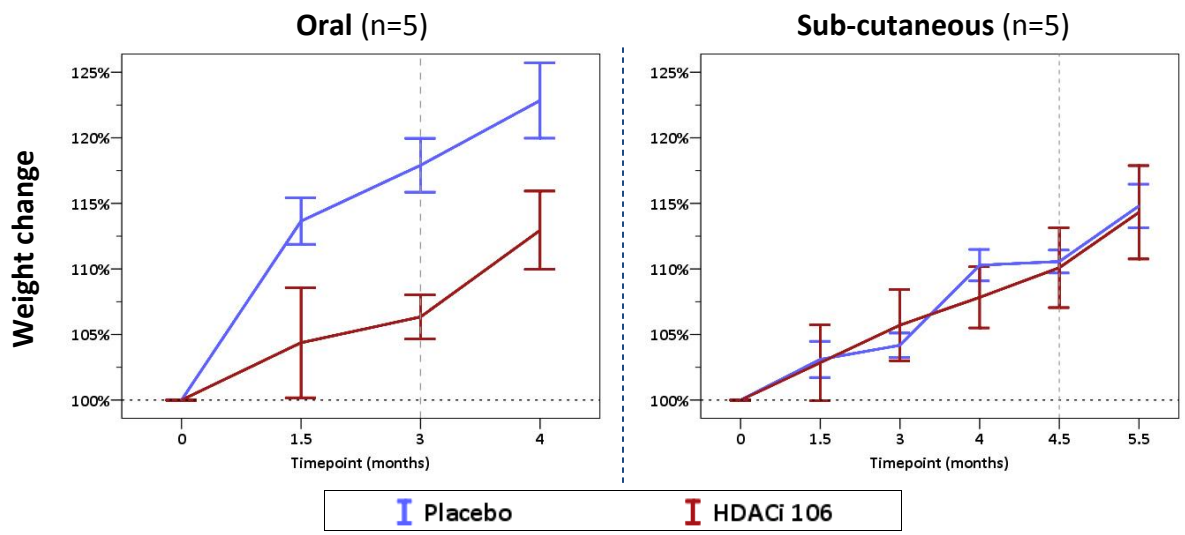

Figure 5.13 – Duration of effect on weight gain/loss during the HDACi 106 studies. (vertical dashed line represents last dose; error bars: +/- 1 SE)

Regarding rotarod analysis, placebo and drug-taking mice from both studies showed similar average performance levels at the start of the study (Figure C.3). No evident drug effect was detected when 106 was orally administered, but average performance levels of 106-taking mice were higher at treatment completion, when compared to placebo (Figure 5.14). Sub-cutaneous administration had a positive effect on rotarod performance, with 106-taking mice regularly displaying improved changes in performance throughout the study (Figure 5.14). However, the effect of 106 was not significant for either of the two studies (Table 5.8). Withdrawal of the drug treatment, for a period of 1 month, did not produce noticeable changes in rotarod performance in either study (Figure 5.15).

Regarding locomotor activity, with the exception of a single mouse which showed relatively higher than average levels, the absolute values were normally distributed, regularly ranging from 0-15 squares (Figure C.5). However, when the change in activity levels was analysed, much greater levels of variability were observed: some mice from the same study groups almost doubled their activity while others showed drastic drops in activity (Figure C.6). Nevertheless, activity levels of all study groups generally decreased throughout

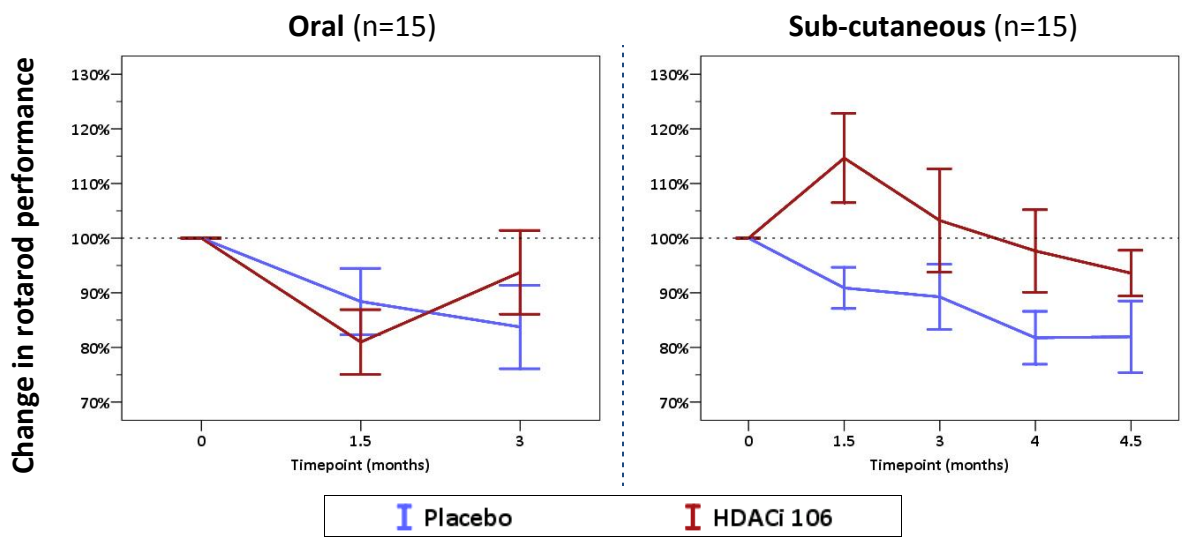

Figure 5.14 – Rotarod performance change during the HDACi 106 studies. (error bars: +/- 1 SE)

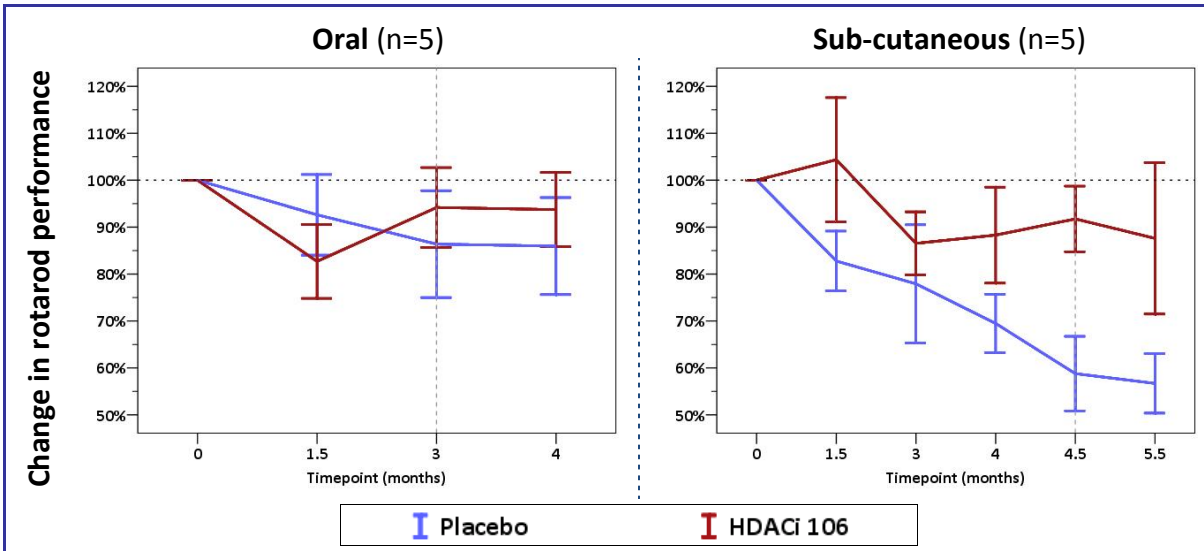

Figure 5.15 – Duration of effect on rotarod performance during the HDACi 106 studies. (vertical dashed line represents last dose; error bars: +/- 1 SE)

the study. Oral administration of 106 slowed the decline of locomotor activity (Figure 5.16). However, sub-cutaneous administration of 106 had the opposite effect, further decreasing the average levels of locomotor activity, when compared to placebo levels (Figure 5.16). Nevertheless, the effect of 106 on locomotor activity was not statistically significant in either study (Table 5.8). After drug treatment withdrawal for a period of 1 month, the 106 orally-treated mice retained their activity levels, as opposed to the corresponding placebo mice,

which showed a strong drop in activity (Figure 5.17). Sub-cutaneously treated mice, which showed reduced locomotor activity levels throughout the study, ultimately displayed a strong increase in these levels 1 month after the treatment withdrawal (Figure 5.17). At this stage, these levels were even higher than those of placebo mice.

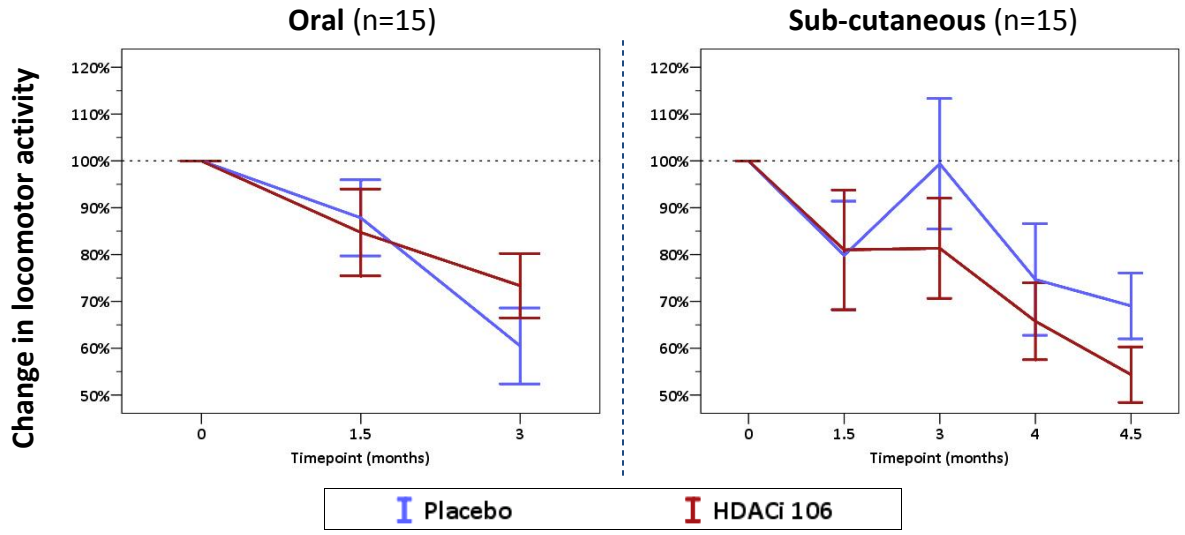

Figure 5.16 – Change in locomotor activity during the HDACi 106 studies. (error bars: +/- 1 SE)

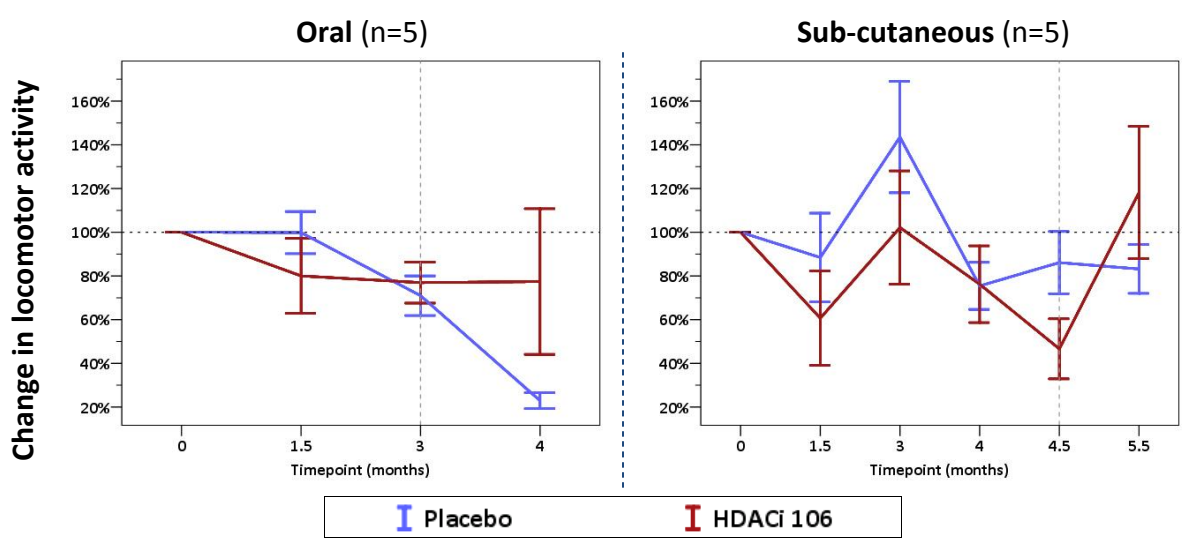

Figure 5.17 – Duration of effect on locomotor activity during the HDACi 106 studies. (vertical dashed line represents last dose; error bars: +/- 1 SE)

Investigation of frataxin expression

Continuous oral administration of 106 for a period of 3 months resulted in increased *FXN* mRNA levels in the brain of YG8 mice (Figure 5.18). These levels were 20% higher than placebo levels (p=0.029; Table 5.9). However, 1 month after treatment withdrawal, these levels had dropped to 68% of those observed in placebo brain (Figure 5.18). Sub-cutaneous administration of 106 for a period of 4.5 months resulted, at an initial stage (4h after last dose), in significantly decreased *FXN* mRNA levels (77% of placebo, p=0.014), followed by significantly increased levels 24h after the last dose (30% higher than placebo, p=0.014) (Figure 5.18 and Table 5.9). These levels remained increased in the brain of sub-cutaneously treated YG8 mice 1 month after treatment withdrawal (19% higher than placebo) (Figure 5.18).

Oral administration of 106 had a similar effect on the frataxin protein levels to the findings for *FXN* mRNA levels: significantly increased levels of frataxin were detected in the brain of YG8 mice immediately after treatment (23% higher than placebo, p=0.029), followed by decreased levels 1 month after treatment withdrawal (79% of placebo) (Figure 5.19 and Table 5.9). Regarding the sub-cutaneous treatment, increased frataxin protein levels were determined 4h after the last dose (41% higher than placebo) (Figure 5.19). However, 24h after the final dose these levels were approximately the same for 106- and placebo-treated mice (Figure 5.19). Finally, the levels of frataxin protein were significantly increased 1 month after the last sub-cutaneous dose (70% higher than placebo, p=0.014) (Figure 5.19 and Table 5.9), suggesting a compensatory effect to potential 106-induced inhibition of frataxin expression throughout the study.

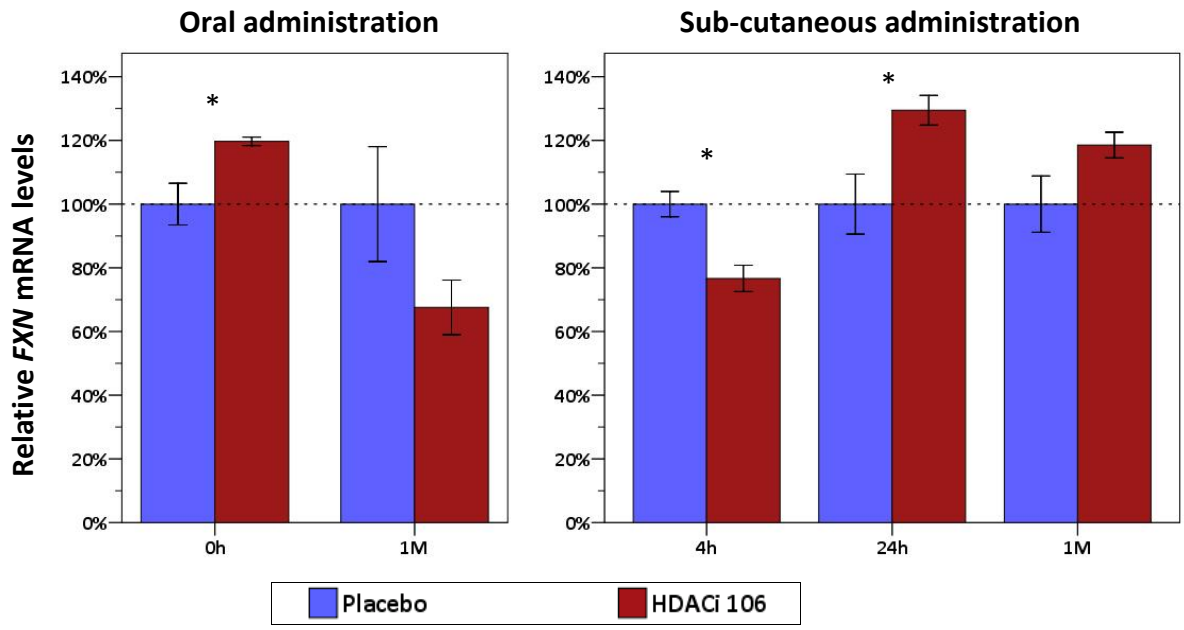

Figure 5.18 – Relative *FXN* mRNA levels in YG8 mouse brain following long-term treatment with 106, as determined by Q-RT-PCR. 0h, 4h, 24h and 1M indicate the time of sample collection, after the last dose. (n=4; * p<0.05; error bars: +/- 1 SE)

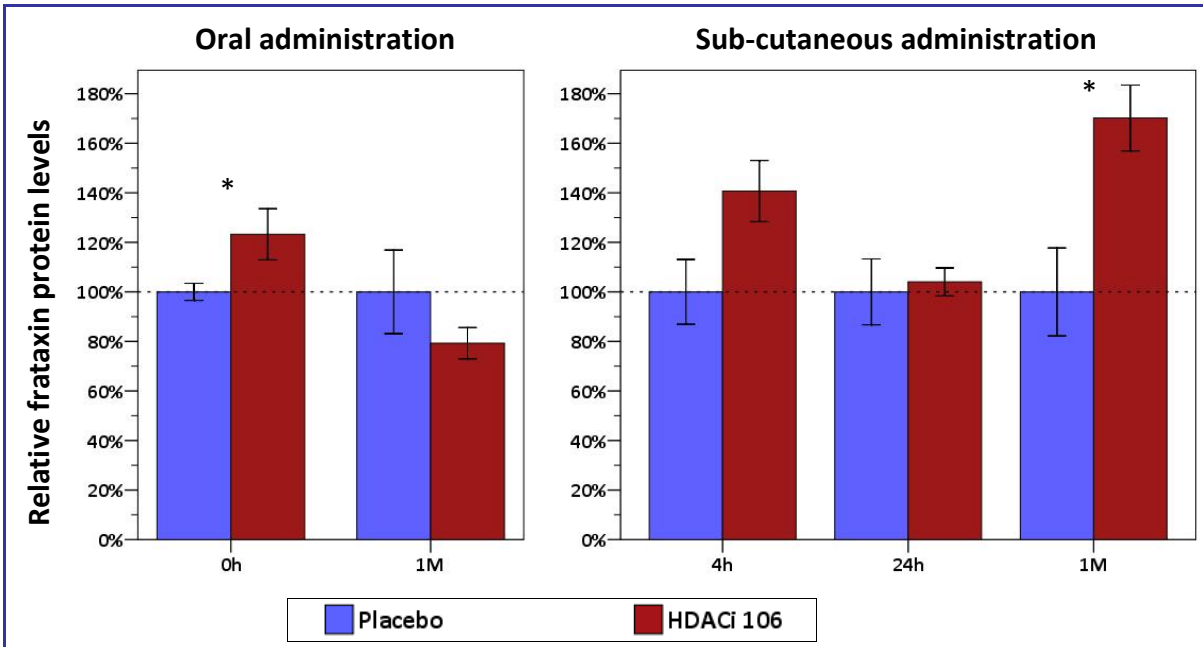

Figure 5.19 – Relative frataxin protein levels in YG8 mouse brain following long-term treatment with 106, as determined by Western blot analysis. 0h, 4h, 24h and 1M indicate the time of sample collection, after the last dose. (n=4; * p<0.05; error bars: +/- 1 SE)

Table 5.9 – Non-parametric test associated *p*-values of HDACi 106 treatment effect on frataxin expression and H3/H4 acetylation levels during the oral and sub-cutaneous studies.

	Mann-Whitney test *p*-values (n=4)				
	Oral administration		**Sub-cutaneous administration**		
Treatment effect on	**0h**	**1M**	**4h**	**24h**	**1M**
FXN mRNA levels	0.029	0.171	0.014	0.014	0.057
Frataxin protein levels	0.029	0.171	0.057	0.443	0.014
H3 acetylation levels	0.171	0.014	0.014	0.443	0.557
H4 acetylation levels	0.443	0.171	0.057	0.029	0.029

Investigation of histone modifications following drug treatment

Oral administration of 106 caused slightly increased levels of total H3 acetylation in the brain of YG8 treated mice (10% higher than placebo). These levels were even higher 1 month after treatment withdrawal (41% higher than placebo, p=0.014) (Figure 5.20 and Table 5.9). At an initial stage (4h after last dose), sub-cutaneous administration of 106 seems to have significantly increased the levels of H3 acetylation in the brain of treated mice (28% higher than placebo, p=0.014). However, 24h after the last dose and 1month following treatment withdrawal no significant changes in H3 acetylation levels were detected (97% of placebo and 5% higher than placebo, respectively) (Figure 5.20 and Table 5.9).

Regarding total H4 acetylation levels, these were initially unchanged (0h), but 1 month after treatment withdrawal a 16% increase was detected in the brain of orally treated mice (Figure 5.21). When 106 was administered sub-cutaneously, H4 acetylation levels were initially increased in the brain of treated mice: 29% and 37% (p=0.029) higher than placebo levels 4h and 24h after the last 106 dose respectively (Figure 5.21 and Table 5.9). However, these levels were significantly decreased 1 month after treatment withdrawal (56% of

placebo, p=0.029) (Figure 5.21 and Table 5.9), suggesting a 106 duration of effect for less than 1 month.

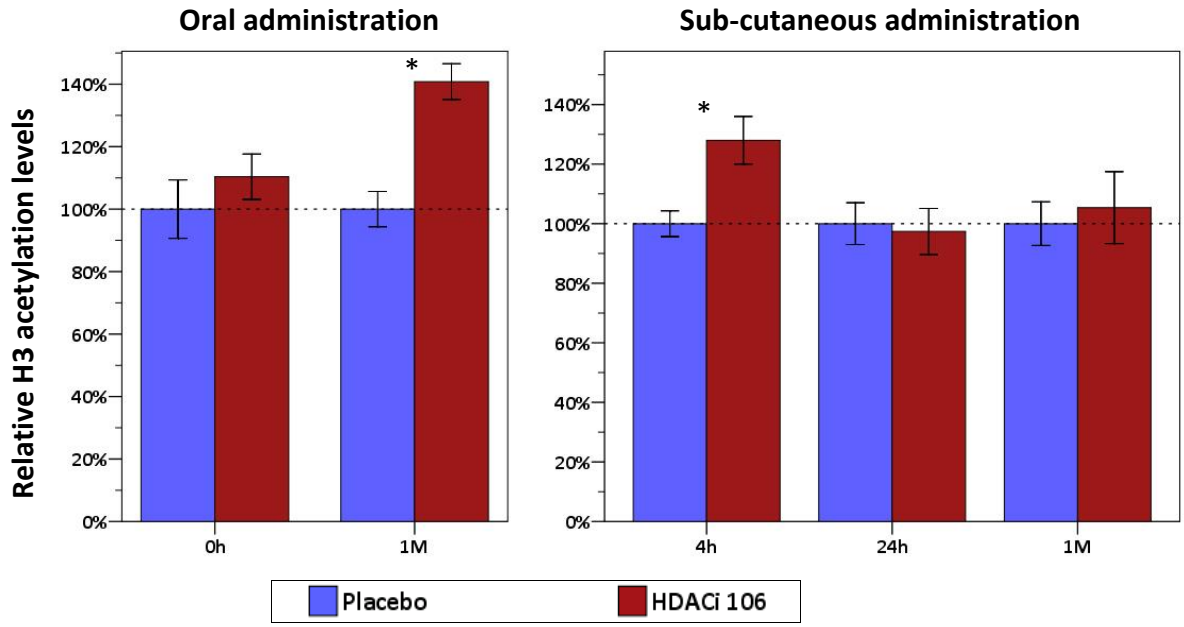

Figure 5.20 – Relative H3 acetylation levels in YG8 mouse brain following long-term treatment with 106, as determined by Western blot analysis. 0h, 4h, 24h and 1M indicate the time of sample collection, after the last dose. (n=4; * p<0.05; error bars: +/- 1 SE)

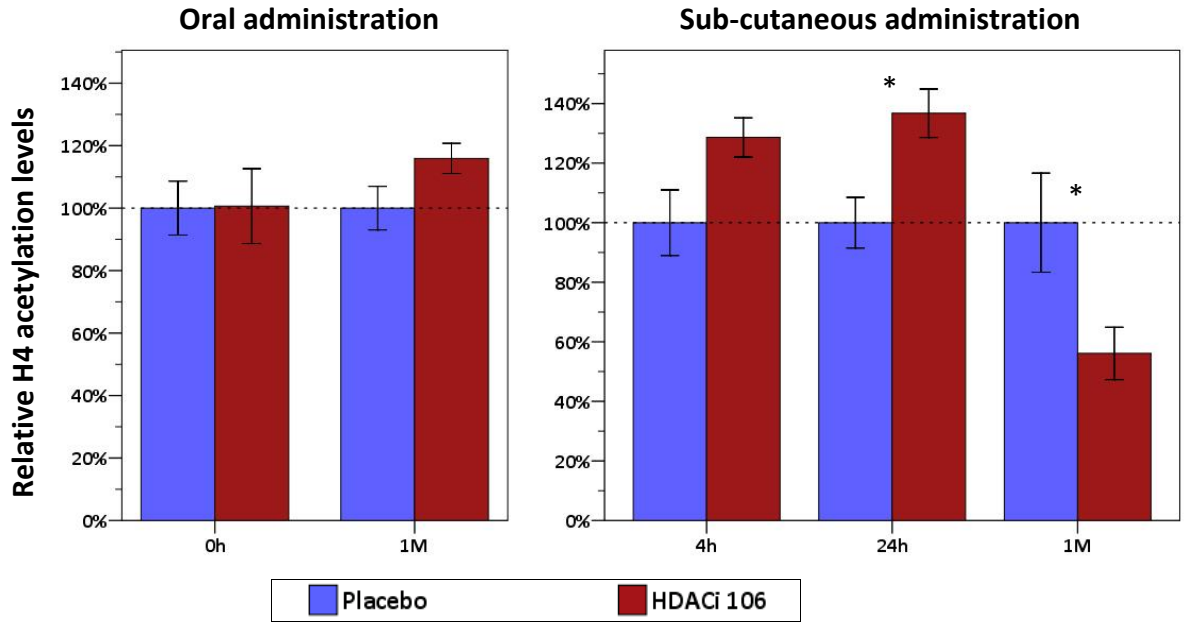

Figure 5.21 – Relative H4 acetylation levels in YG8 mouse brain following long-term treatment with 106, as determined by Western blot analysis. 0h, 4h, 24h and 1M indicate the time of sample collection, after the last dose. (n=4; * p<0.05; error bars: +/- 1 SE)

Histological analysis

Histological analysis was performed by means of H&E staining of lumbar vertebral column sections (Figure 3.11 and Figure 3.12). The levels of DRG neurodegeneration were determined by counting the number of cell bodies displaying vacuoles (Figure 3.12). A total of 2 mice were investigated from each study group of both 106 studies. The average age of the mice was 8 months old.

In general, very low levels of DRG neurodegeneration were detected in all investigated animals, with the average number of DRG neuronal cells displaying vacuoles being lower than 1 on most of the analysed samples (Figure 5.22). Analysis of DRG sections from the distal lumbar region (VL_{3+4}) revealed slightly higher levels of neurodegeneration (when compared to VL_{1+2}), with the exception of sub-cutaneously placebo-treated mice (Figure 5.22). Regarding a potential drug effect, 106 orally treated mice showed lower levels than placebo-treated mice. As far as the sub-cutaneous study is concerned, no discernible effect was detected (Figure 5.22).

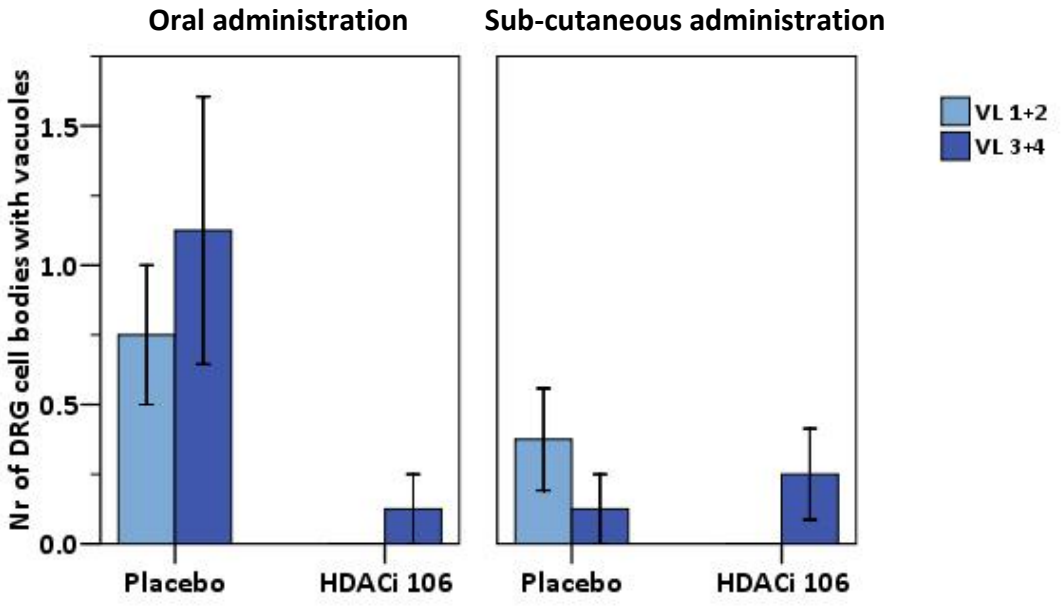

Figure 5.22 – Levels of DRG neurodegeneration following the HDACi 106 treatments.
(n=2; error bars: +/- 1 SE)

5.5 – Discussion

It is currently generally accepted that FRDA may be caused by a heterochromatin-mediated silencing effect of the *FXN* gene (Festenstein 2006). This phenomenon is characterized by a differential DNA methylation profile accompanied by decreased histone acetylation (H3K9, H3K14, H4K5, H4K8, H4K12 and H4K16) and increased H3K9 trimethylation flanking the GAA repeat (Herman *et al.* 2006; Greene *et al.* 2007; Al-Mahdawi *et al.* 2008).

Herman *et al.* (2006) originally described the use of a particular class of HDACi in order to target such chromatin modifications. In fact, treatment of FRDA patient lymphocytes with a particular HDACi (4b) successfully increased the levels of acetylation at H3K14, H4K5 and H4K12 surrounding the GAA repeat. In turn, this resulted in 2.5 to 3-fold increases in *FXN* mRNA levels (Herman *et al.* 2006).

The fact that the *FXN* YAC GAA mouse model described by Al-Mahdawi *et al*. (2008) exhibits epigenetic modifications similar to the ones observed in FRDA patients suggested that such mice would be ideal for the *in vivo* investigation of such HDACi-based therapeutic approaches for FRDA.

Therefore, preliminary short studies were performed by administering 3 consecutive daily doses of HDACi 106 (4b derivative) to YG8 rescue mice. While oral and sub-cutaneous administration of 150mg/kg 106 showed no signs of toxicity whatsoever, oral administration of 300mg/kg 106 resulted in a very high death rate (5 in 8 treated mice). This suggested that special considerations should be taken in the monitoring of potential adverse events, rather than simply investigating the drug's efficiency in modifying histone acetylation levels and regulating frataxin expression.

Oral and sub-cutaneous administration of 150mg/kg 106 had similar effects on frataxin expression. The levels of both *FXN* mRNA and frataxin protein were initially reduced (4h after dose) in the brain of YG8 rescue mice, but afterwards (24h after last dose) increased levels were detected, when compared to placebo. Curiously, this initial frataxin reduction was associated with considerably increased total levels of both H3 and H4 acetylation in the brain of YG8 mice. Then 24h after dosing, when the frataxin levels were increased, histone acetylation levels were reduced to either marginally increased (H3ac) or normal (H4ac) levels. However, the histone acetylation levels that were measured are general and not specific for the *FXN* locus. Therefore, histone acetylation at the *FXN* locus may in fact be decreased. This could be investigated by future ChIP experiments.

Nonetheless, these preliminary studies indicate that 106 successfully crossed the blood-brain barrier, caused global H3 and H4 acetylation changes in the brain and eventually increased frataxin expression levels in FRDA-associated *FXN* alleles. However, the results also suggested that an initial frataxin inhibitory mechanism must be activated soon after 106 dosing.

Following from these encouraging findings, long-term studies were performed in order to investigate the effect of extended oral and sub-cutaneous administration of 150mg/kg 106. Sub-cutaneous administration produced no overt toxicity, but two deaths (out of 15) were observed when the drug was administered *ad libitum* in drinking water. It is possible that this was a result of drug toxicity, since no deaths were observed in the placebo group. However, before dying, these mice refused to drink either the 106 or the placebo solution, but would happily drink plain water. Therefore, the implication is that these mice probably died of dehydration due to the use of an unacceptable drug vehicle, which should not be used for *ad libitum* oral therapy in future.

Weight gain in 106 treated mice was significantly decreased throughout both studies when compared to placebo. Additionally, sub-cutaneously treated mice showed improved rotarod performance levels, suggesting a potentially neuroprotective effect of the drug. However, such improvement was not statistically significant. In fact, no statistically significant improvements were observed for either the rotarod performance or locomotor activity studies. This lack of statistical significance does not negate the therapeutic ability of 106 for FRDA, and is probably explained by the mild severity of the FRDA-associated phenotype displayed by YG8 rescue mice.

Additionally, the neuroprotective potential of extended 106 administration was also investigated by histological analysis of lumbar DRG. However, the observed levels of DRG neurodegeneration in treated and untreated mice were so insignificant that it would be inappropriate to make any interpretation. Consequently, as previously mentioned in Chapter 4, this implies that the presence of vacuoles in DRG cell bodies of YG8 mice as an FRDA-associated pathological phenotypic trait needs to be re-evaluated.

Regarding frataxin expression levels, these were only investigated in brain samples and different results were obtained with oral and sub-cutaneous 106 administration. Oral administration resulted in significantly increased levels (approximately 20% higher) of both *FXN* mRNA and frataxin protein levels immediately after treatment termination. This suggested that 106 treated YG8 mice were regularly expressing 20% more frataxin in the brain throughout the 3 months treatment period.

Regular sub-cutaneous administration of 106 over a period of 4.5 months had a similar effect on frataxin mRNA expression levels as initially observed in the short-term preliminary studies: the levels of *FXN* mRNA were initially (4h) significantly decreased but then significantly increased 24h after the last dose (30% increase). However, long-term treatment

did not cause a reduction of frataxin protein levels shortly after dosing, as opposed to what had been observed in the pre-studies. In fact, 4h after sub-cutaneous dosing the levels of frataxin protein were increased by 40%. This was probably residual frataxin found at higher levels due to the increased expression resultant from the previous dose. However, the reduced levels of *FXN* mRNA transcription observed shortly after dosing seem to have had an effect on protein levels 24h later, where frataxin levels had reduced to normal values.

As previously mentioned for the preliminary studies, this negative effect on *FXN* transcription shortly after 106 administration may be caused by an inhibitory mechanism that is triggered by the sudden increase in the drug concentration present in the organism. This yet to be investigated mechanism seems to be related to the significantly increased levels of total H3 acetylation initially found in the brain 4h after dosing. This theory gains strength from the fact that 24h later, when *FXN* mRNA levels were found significantly increased, the level of total H3ac had decreased to normal levels.

A possible explanation for this phenomenon may be linked to the specificity and different mechanisms of HDAC inhibition exhibited by 106. Recent investigations suggest that 106 has a slow and strong inhibition of class I HDACs (HDAC1, 2, and 3), but particularly of HDAC3 (Chou *et al.* 2008). Therefore, it is possible that 106 may initially inhibit the different class I HDACs, but later exhibits its preferential affinity to HDAC3. At first, this could translate into increased global H3ac and H4ac, later followed by more localised histone modifications. These initially increased total levels of H3ac and H4ac could simultaneously increase the expression of multiple genes, therefore potentially overstretching the transcription machinery. Alternatively, generalised increased H3ac and H4ac levels could be responsible for the up-regulation of an, as yet unknown, *FXN* negative regulator. In support of such hypotheses, recent reports have indeed described HDACi-induced down-regulation

of specific genes within a global increase in histone acetylation levels (Reid *et al.* 2005; Rada-Iglesias *et al.* 2007).

This aspect of 106 treatment needs to be further investigated since a momentary reduction in frataxin levels could have detrimental effects that may ultimately overpower any therapeutic effect caused by a subsequent rise in frataxin.

Treatment withdrawal had contrasting effects between the oral and the sub-cutaneous treatments. A detrimental effect was observed 1 month after oral administration was interrupted since both frataxin mRNA and protein levels were considerably reduced. On the other hand, the levels of *FXN* mRNA were still increased by approximately 20% 1 month after the last sub-cutaneous 106 injection, and most surprisingly, frataxin protein levels were 70% higher than in placebo. Again, these contrasting results seem to be associated with the levels of total H3ac and H4ac. While 1 month after interruption of oral treatment the reduced frataxin levels were accompanied by increased total histone acetylation (particularly H3ac), the significantly increased levels of frataxin 1 month after sub-cutaneous treatment interruption were associated with normal levels of total H3ac and significantly reduced total H4ac levels (approximately 50%).

The reason for these opposing treatment interruption reactions could be related to the fact that during the oral treatment 106 was being administered in a much more constant fashion than when sub-cutaneously injected: when administered via drinking water the levels of 106 should have always been found in the organism at a steady concentration, while when sub-cutaneously injected the mice experienced cycles of high 106 concentration, peaking immediately after dosing, followed by a gradual concentration decrease. Hypothetically, the constant exposure to 106 in the 3 months oral study could have induced a drug dependence, particularly in the CNS, and following interruption of treatment a

withdrawal effect occurred, which was still evident 1 month later. On the other hand, the concentration fluctuation of 106 throughout the study associated with sub-cutaneous administration could have allowed for plasticity to be retained.

In summary, although sub-cutaneous 106 administration could momentarily result in the higher levels of frataxin expression, oral administration of 106 seems to have had a more consistent effect on brain frataxin levels, regularly increasing them by 20%. Additionally, total H3ac and H4ac changes were detected, suggesting that 106 may mediate its effect on frataxin expression by modulating acetylation levels of H3 and H4. However, since the analysis performed only investigated total H3ac and H4ac levels, it is inappropriate to assert that 106 facilitated *FXN* expression by specifically targeting H3 and H4 residues in FRDA-associated *FXN* alleles. Therefore, further investigation should be performed to characterize the histone modifications in the *FXN* gene following extended 106 treatment. To begin with, ChIP analysis using antibodies specific for individual histone modifications (eg. H3K9ac, H4K12ac and H3K9me3) should be performed. Additional analysis of DNA methylation alterations should also be carried out either by “bisulfite sequencing” or “methylscreen” approaches.

Nevertheless, a recently reported *in vivo* study where 150mg/kg 106 was sub-cutaneously administered to KIKI FRDA mice (both alleles of *Fxn* gene contain GAA_{230} inserted in intron 1) for 3 consecutive days confirmed the ability of 106 to specifically increase the acetylation levels at H3K14, H4K5, H4K8 and H4K16 in a region just upstream of the GAA repeat (Rai *et al.* 2008). This study also reported increased frataxin protein levels in the brain and elevated *FXN* mRNA levels in the brain, cerebellum and heart of treated KIKI mice, concurring with the results obtained with the YG8 rescue mice.

Despite the encouraging potential of 106 to successfully increase frataxin expression it is of major importance to determine the specificity of HDACi to the *FXN* gene. Recent investigations have determined that 106 has a slow and strong inhibitory effect on class I HDACs, particularly on HDAC3 (Chou *et al.* 2008). Nevertheless, it is possible that specifically inhibiting HDAC3 may have significant effects on the expression of genes other than *FXN*, which in turn could have a potentially negative outcome. For that reason, it seems critical to perform microarray analysis of treated samples.

Additionally, some considerations should be taken into account for future studies with 106. For instance, administration of lower 106 doses should be experimented in an attempt to avoid the negative effect on frataxin expression observed shortly after sub-cutaneous administration of 150mg/kg 106. To compensate for this reduction, maybe more frequent dosing should be performed. Alternatively, taking into the account that the effect of 106 was at its peak 1 month after the last dose, more widespread dosing sessions may be more beneficial. On the other hand, in an attempt to circumvent the initial negative effect of 106, further drug development should also be considered. As far as this is concerned, particular attention should therefore be directed at developing a slow-releasing formulation.

In reality, novel formulations of 106 are currently being developed in order to potentially improve specificity and potency (Hu *et al.* 2009). As a result, a derivative of 106 (HDACi 136) has been recently generated. HDACi 136 is currently being investigated in Wt and YG8 rescue mice (C. Sandi, personal communication).

Finally, the fact that the GAA tract is capable of solely inducing the FRDA-associated epigenetic modifications (Saveliev *et al.* 2003; Rai *et al.* 2008; Soragni *et al.* 2008) suggests that for future *in vivo* studies the use of a model containing larger GAA repeats is of paramount importance.

Chapter 6 – Analysis of CTCF binding to the *FXN* gene in FRDA

6.1 – Introduction

Recent advances in studying long-range chromatin interactions have shifted focus from the transcriptional regulation by nearby regulatory elements to recognition of the role of higher-order chromatin organization within the nucleus. These advances have also suggested that CCCTC-binding factor (CTCF), a known chromatin insulator protein, may play a central role in mediating long-range chromatin interactions, directing DNA segments into transcription factories and/or facilitating interactions with other DNA regions (Filippova 2008). Several models that describe possible mechanisms for multiple functions of CTCF in establishment and maintenance of epigenetic programs are now emerging.

Epigenetics plays an important role in normal development and disease. CTCF involvement in multiple aspects of epigenetic regulation, including regulation of genomic imprinting and X-chromosome inactivation, has been well established (Reik 2007). Emerging evidence also points to the role of CTCF deregulation in the epigenetic imbalance in cancer (Recillas-Targa *et al.* 2006). More recently, CTCF was found to play a role in regulation of noncoding transcription and establishing local chromatin structure at the repetitive elements in mammalian genomes (Cho and Tapscott 2007; Libby *et al.* 2008), suggesting a new epigenetic basis for several repeat-associated genetic disorders, including FRDA.

6.1.1 – CTCF, the multivalent factor

CTCF is a widely expressed 11-zinc finger (ZF) nuclear protein originally identified as a transcription factor that binds to the avian and mammalian *MYC* promoters (Lobanenkov *et al.* 1990). The 11-ZF DNA-binding domain of CTCF consists of 10 C_2H_2 type of ZFs and 1 C_2HC ZF (Ohlsson *et al.* 2001) (Figure 6.1). CTCF was initially called the *multivalent* factor due to its

ability to bind to diverse and unusually long DNA sequences (~50bp) by using different combinations of its individual ZFs (Filippova *et al.* 1996).

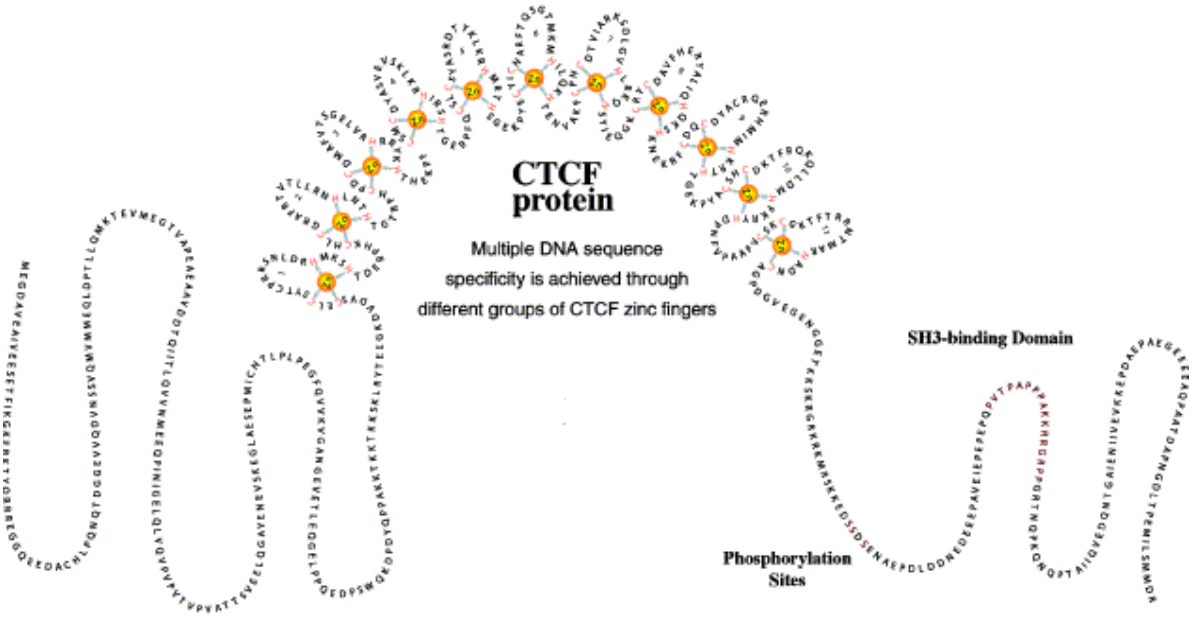

Figure 6.1 – Structural features of CTCF. This schematic illustrates the molecular basis for the *multivalent* DNA-sequence specificity mediated by different sets of ZFs. The complete amino acid sequence of the wild-type human CTCF protein is schematically drawn to show the DNA binding domain composed of 10 C_2H_2-class and 1 C_2HC-class Zn fingers. Functionally significant sites for CKII phosphorylation and a putative SH3-binding motif are also depicted (Klenova *et al.* 2002).

CTCF is remarkably evolutionarily conserved among vertebrates, exhibiting 100% identity of amino acid sequences within the 11-ZF DNA-binding domains of avian and human CTCF proteins (Filippova *et al.* 1996; Burke *et al.* 2002). However, despite this strict evolutionary conservation, there appears to be considerable flexibility inherent in the CTCF DNA-binding domain, enabling it to bind to evolutionarily divergent target sequences (Filippova *et al.* 1996).

CTCF has been shown to function both as a classical transcription factor (Klenova *et al.* 1993; Filippova *et al.* 1996; Vostrov and Quitschke 1997) and as a chromatin insulator that

does not directly regulate gene expression, but instead blocks functional communication between a promoter and surrounding enhancers and/or silencers (Bell *et al.* 1999; Bell and Felsenfeld 2000; Hark *et al.* 2000; Kanduri *et al.* 2000) (Figure 6.2).

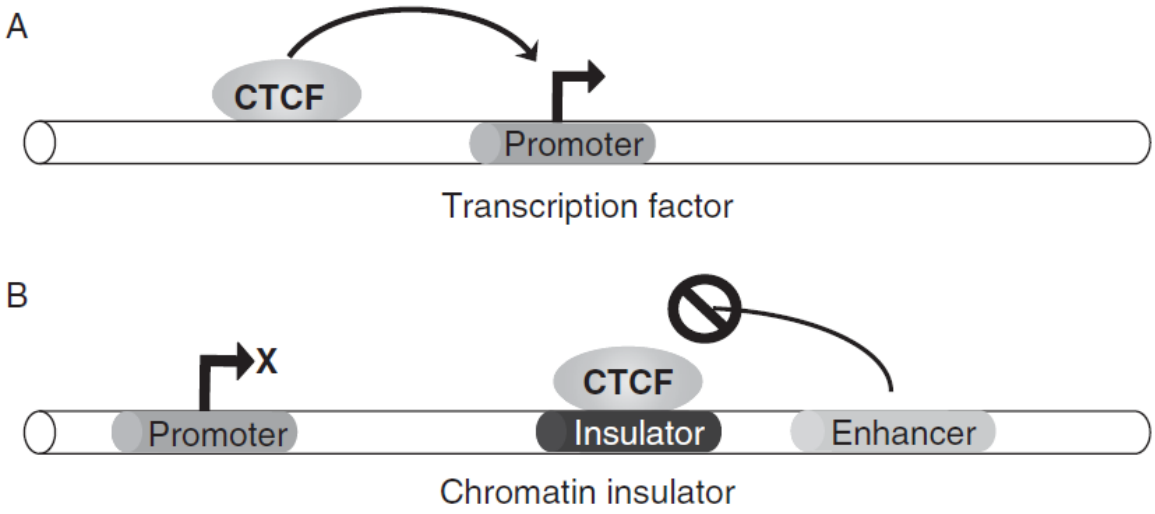

Figure 6.2 – Multiple functions of CTCF in gene regulation are thought to be at least partly mediated by the multiple sequence specificity of CTCF (Filippova 2008). (**A**) For a subset of CTCF target sites, CTCF was shown to function as a classical transcription factor that activates or represses transcription of its target genes. (**B**) CTCF also binds to all known vertebrate insulators and functions as a chromatin insulator protein that does not directly affect transcription but instead prevents interaction between a promoter and nearby enhancers or silencers, thereby preventing inappropriate activation or silencing of the genes and establishing independently regulated chromatin domains.

In this latter case, CTCF functions as a chromatin insulator protein that binds all known vertebrate insulators and prevents inappropriate activation or silencing of genes by neighbouring regulatory elements, thereby establishing independently regulated chromatin domains. Initially, the CTCF-mediated insulator was characterized at the chicken β-globin locus (Bell *et al.* 1999). Enhancer blocking activity of the CTCF site within the HS4 insulator at this locus was found to be separable from the barrier function responsible for the prevention of heterochromatin spreading (Recillas-Targa *et al.* 2002; West *et al.* 2002). Later, CTCF was found to bind to a differentially methylated region (DMR) upstream of the *H19*

gene and mediate insulator activity by blocking access of *Igf2* to an enhancer shared with *H19*, resulting in the lack of *Igf2* expression from the maternal allele (Bell and Felsenfeld 2000; Hark *et al.* 2000; Kanduri *et al.* 2000). These studies also showed that CpG methylation inhibits CTCF binding and allows *Igf2* expression from the paternal allele. Therefore, differential methylation of CTCF-binding sites in the *Igf2*/*H19* locus likely accounts for the parent of origin-specific imprinting that occurs at this locus.

Remarkably, in addition to the fact that DNA methylation prevents CTCF binding, CTCF was also shown to prevent spreading of DNA methylation and play a critical role in maintaining methylation-free zones (Schoenherr *et al.* 2003; Fedoriw *et al.* 2004; Lewis and Murrell 2004; Pant *et al.* 2004; Filippova *et al.* 2005; Engel *et al.* 2006). Taken together these data suggested a dual function for CTCF insulators that, in addition to enhancer blocking, prevents spreading of methylation and therefore protects nearby promoters from epigenetic silencing (Figure 6.3).

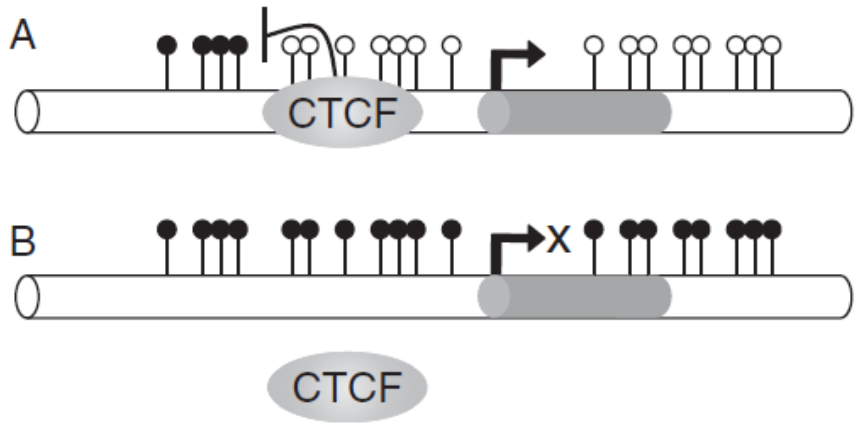

Figure 6.3 – CTCF binding prevents CpG methylation, and CpG methylation prevents CTCF binding (Filippova 2008). (**A**) CTCF was shown to prevent spreading of CpG methylation and maintain methylation-free zones suggesting a dual function for CTCF insulators that, in addition to enhancer blocking, protect nearby promoters from silencing by keeping them free of DNA methylation. (**B**) CpG methylation prevents CTCF binding to CpG-containing CTCF target sites. Black circles depict methylated CpGs, and open circles, unmethylated CpGs.

6.1.2 – CTCF function and repetitive elements

Chromatin organization of repetitive elements

Recent evidence suggests that CTCF may play a role in the regulation of noncoding transcription and establishing local chromatin structure at several disease-associated repeat loci. This suggests that the expansion of repeats may interfere with a normal function of CTCF at these loci and therefore providing a new epigenetic basis for several repeat-associated genetic disorders (Filippova *et al.* 2001; Cho *et al.* 2005).

Epigenetic profiling of repetitive elements in mammalian genome revealed strong correlation between tandem repeats, bidirectional transcription of noncoding RNAs, histone H3 lysine 9 methylation, and DNA methylation, suggesting that tandem repeats and double-stranded RNA (dsRNA) may play a role of primary triggers for stable repeat-associated repressive chromatin imprints (Martens *et al.* 2005). According to the current model of heterochromatin formation at repetitive elements, bidirectional transcription across repeats would induce formation of dsRNA, which in turn would result in recruitment of repressive chromatin modifications and DNA methylation to the repeat locus (Martens *et al.* 2005; Talbert and Henikoff 2006).

The role for CTCF insulators in establishing the local chromatin structure at repetitive elements was initially revealed by studies at the myotonic dystrophy type 1 (DM1) locus (Filippova *et al.* 2001; Cho *et al.* 2005). DM1 is a dominantly inherited disease caused by a CTG expansion in the 3'UTR of the *DMPK* gene (Otten and Tapscott 1995). CTCF-binding sites were found to flank the CTG repeat and form a methylation-sensitive chromatin insulator at the DM1 locus (Filippova *et al.* 2001). Further analysis demonstrated that the CTG repeat on the wild-type allele is characterized by localized repressive histone modifications that are restricted to a CTG-containing nucleosome flanked by CTCF sites and surrounded by active

chromatin. Mutations of CTCF-binding sites (inhibiting CTCF binding) led to the spreading of these repressive modifications. Consistently, the expanded allele in congenital DM1 was associated with the loss of CTCF binding, spread of heterochromatin, and regional CpG methylation (Cho *et al.* 2005).

In agreement with the current model for the role of bidirectional RNA transcripts in heterochromatin formation at repetitive elements, an antisense transcript overlapping the CTG repeats at the DM1 locus was characterized and shown to be processed into small (~21-nucleotide) RNA fragments. CTCF restricted the extent of the antisense transcript at the CTG repeat and prevented spreading of the repressive chromatin marks recruited to the locus, possibly due to siRNA-mediated transcriptional repression (Cho *et al.* 2005) (Figure 6.4).

Consistent with this model, the function of CTCF in regulation of noncoding transcripts has been proposed in the context of CTCF interaction with the largest subunit of RNA polymerase II, an essential component of the transcriptional machinery (Chernukhin *et al.* 2007). In addition, it was demonstrated that a single CTCF target site can initiate transcription of the reporter gene (Chernukhin *et al.* 2007). This raises an attractive possibility of the dual role for CTCF sites surrounding repeats to both trigger heterochromatin formation, through the ability to initiate bidirectional transcription at repetitive elements, and to prevent its spreading by limiting the extent of the transcripts by stalling RNA polymerase II (Filippova 2008).

Besides DM1, CTCF sites have already been identified flanking trinucleotide repeats at other disease-associated loci, including: Huntington disease (HD); spinocerebellar ataxia (SCA) types 2, 7 and 8; dentatorubral-pallidoluysian atrophy (DRPLA); and fragile X mental retardation (Filippova *et al.* 2001; Ladd *et al.* 2007; Libby *et al.* 2008), suggesting a

widespread function for CTCF in regulation of noncoding transcription and establishing local chromatin structure at multiple repeat-associated loci in the genome.

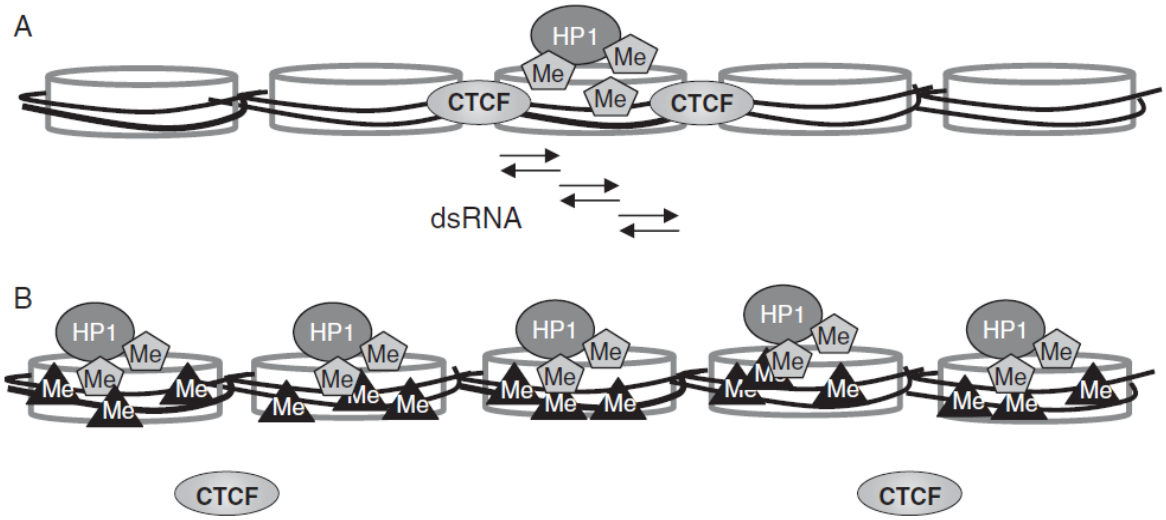

Figure 6.4 – CTCF role in establishing local heterochromatin structure at repetitive elements (Filippova 2008). (**A**) CTCF insulators flank repetitive elements in the genome. CTCF restricts the extent of the bidirectional transcript across repeats and prevents spreading of the repressive chromatin marks recruited to the locus, due to dsRNA-mediated transcriptional repression (Cho *et al.* 2005). (**B**) Loss of CTCF binding is associated with the spread of heterochromatin and regional CpG methylation (Cho *et al.* 2005). In the model for dsRNA-mediated heterochromatin formation at repetitive sequences, bidirectional transcription across repeats forms dsRNA, which in turn recruits histone methyltransferases to methylate H3K9 (gray pentagons), providing a binding site for the heterochromatin protein HP1. HP1 binding further promotes heterochromatin formation through recruitment of DNA methyltransferases, leading to methylation of CpG dinucleotides (black triangles) (Martens *et al.* 2005; Talbert and Henikoff 2006).

CTCF and trinucleotide repeat instability

CTCF binding has recently been implicated in the regulation of genetic repeat stability. Transgenic mice, carrying SCA7 genomic fragments with CTCF-binding site mutations, were used to demonstrate that the loss of CTCF at the binding sites flanking the CAG repeat promotes triplet repeat instability, both in the germ line and in somatic tissues. Similarly, CpG methylation of CTCF-binding sites produces a comparable outcome (Libby *et al.* 2008).

These findings suggest that CTCF is a *trans*-acting factor that specifically interacts in a methylation-dependent manner with the adjacent *cis*-environment to prevent hyper-expansion of disease length CAG repeats. Acquisition of CTCF-binding sites at mutational hot spots may therefore represent an evolutionary strategy for insulating noxious DNA sequences (Libby *et al.* 2008).

6.2 – Aim of study

CTCF binding to the *FXN* gene in FRDA is yet to be investigated. Nevertheless, there are various reasons that suggest that CTCF may play a role on the development of FRDA:

FRDA is a neurodegenerative disorder caused by the hyperexpansion of a GAA repeat within intron 1 of the *FXN* gene, leading to a genetic silencing effect, and culminating in reduced levels of the mitochondrial protein frataxin (Pandolfo 2002b). CTCF has been reported to regulate gene expression either by functioning as a transcription factor or as a chromatin insulator (Bell and Felsenfeld 2000; Filippova *et al.* 2001).

Recent studies suggest that the silencing effect in FRDA may be via a heterochromatin-mediated effect (Saveliev *et al.* 2003). Heterochromatin hallmarks such as reduced levels of histone H3 and H4 acetylation, accompanied by increased H3K9 trimethylation, are particularly noticeable in FRDA immediately upstream and downstream of the expanded GAA repeat tract (Herman *et al.* 2006; Al-Mahdawi *et al.* 2008). CTCF has been identified flanking trinucleotide repeats at various disease-associated loci, constraining the heterochromatic region to the repetitive element, thereby preventing the spreading of these repressive modifications (Filippova *et al.* 2001; Cho *et al.* 2005).

Additionally, CTCF has been specifically implicated in the regulation of CAG repeat instability in SCA7 (Libby *et al.* 2008). FRDA is also characterized by GAA somatic and intergenerational instability. This instability is positively correlated with the size of the repeat (Sharma *et al.* 2002).

The frequent distribution of CTCF-binding sites throughout the genome (Kim *et al.* 2007), as well as the multiple functions of CTCF described above, suggest that CTCF may indeed play a role on the development of FRDA. For that reason the aim of this study is to investigate such relationship.

6.3 – Materials and methods

6.3.1 – Identification of potential CTCF-binding sites in the *FXN* gene

In silico screening

A 40kb region spanning in entirety the *FXN* gene (chromosome 9: 71,649,744bp to 71,689,537bp) (NCBI 2009), was initially screened for potential CTCF-binding sites using a bioinformatics web tool designed by Klenova and colleagues at the University of Essex, available from <http://www.essex.ac.uk/bs/molonc/spa.htm> (Klenova 2007).

Subsequently, following the publication of a CTCF-binding site database (CTCFBSDB) – a collection of experimentally identified and computationally predicted CTCF-binding sites (Bao *et al.* 2008) – a larger region (140kb; chromosome 9: 71,610,181bp to 71,750,180bp) (NCBI 2009), comprising the whole *FXN* gene and including approximately 40kb upstream and 60kb downstream of the gene, was also investigated for potential CTCF-binding sites.

6.3.2 – Confirmation of CTCF-binding sites in the *FXN* gene

Electrophoretic mobility shift assay (EMSA)

a) Non-radioactive approach using EMSA kit (Invitrogen):

PCR products were generated for 2 regions in the imprinted maternally expressed gene *H19* (chromosome 11): H19 and H19neg (see Table 2.3 for primers used). The former region had been shown to contain high levels of CTCF bound to it, while the latter did not show any CTCF binding ability (Burke *et al.* 2005). The PCR products were gel-purified using a Geneclean III kit (Bio 101). Binding reactions were performed by incubating 100ng of geneclean PCR product with 10µg of HELA cells nuclear extract (Upstate) in a final volume of 10µl, at room temperature, for 1 hour. For supershift analysis 1µl of anti-CTCF antibody

(Upstate) was added to the respective reaction. Samples were then separated by 5% nondenaturing PAGE run in 0.5x TBE buffer at 50V. The PAGE gels were stained for DNA with SYBR Green and subsequently stained for protein with SYPRO Ruby. Visualization and documentation of both stains was performed using a UV-lighted gel documentation cabinet (Alpha Innotech).

b) EMSA using γ-^{32}P end-labelled DNA probes and nuclear extracts:

H19 and H19neg gene-cleaned PCR products were prepared as described above and then γ-^{32}P end-labelled using T4 polynucleotide kinase (Invitrogen) and γ-^{32}P ATP (PerkinElmer). Unincorporated radionucleotides were removed using a MicroSpin S-200 HR column (Amersham Biosciences). The labelled PCR products were then added to 10µg of nuclear extract from normal human cerebellum tissue, in the presence of 1µg of double-stranded competitor DNA poly(dI-dC) (Sigma Aldrich) in a phosphate-buffered saline (PBS)-based buffer containing standard PBS with 5mM $MgCl_2$, 0.1mM $ZnSO_4$, 1mM dithiothreitol, 0.1% Nonidet P-40, and 10% glycerol (Filippova *et al.* 1996). For supershift analysis 1µl of anti-CTCF antibody (Upstate) was added to the respective reaction, and this was replaced with equal amounts of either pre-immune serum or anti-H3ac antibody (Upstate) as controls for the supershift analysis. Reaction mixtures with a final volume of 10µl were incubated for 30min at room temperature and then analyzed by 5% nondenaturing PAGE run in 0.5x TBE buffer at 100V. Amersham Hyperfilm ECL films (GE Healthcare) were exposed to the vacuum-dried gels and hand-developed using X-OMAT developer and fixer (Kodak).

c) EMSA using γ-^{32}P end-labelled DNA probes and full-length recombinant CTCF:

PCR products were generated for 3 potential CTCF-binding regions identified in *FXN*: 5'UTR; upstream; and downstream of GAA (see Table 2.3 for primer used). PCR products of the DM1 CTCF-binding sites 1 and 3 described by Filippova (Filippova *et al.* 2001) were

respectively used as positive and negative control regions (see Table 2.3 for primer used). The PCR products were gel-purified using a Geneclean III kit (BIO 101) and then γ-^{32}P end-labelled using T4 polynucleotide kinase (Invitrogen) and γ-^{32}P ATP (PerkinElmer). Unincorporated radionucleotides were removed using a MicroSpin S-200 HR column (Amersham Biosciences). The labelled PCR products were then added to 0.2µg of CTFC full-length recombinant protein (Abnova) in the presence of 1µg of double-stranded competitor DNA poly(dI-dC) (Sigma Aldrich) in a PBS-based buffer containing 5mM $MgCl_2$, 0.1mM $ZnSO_4$, 1mM dithiothreitol, 0.1% Nonidet P-40, and 10% glycerol (Filippova *et al.* 1996). Reaction mixtures with a final volume of 10µl were incubated for 30min at room temperature and then analyzed by 5% nondenaturing PAGE run in 0.5x TBE buffer at 100V. Amersham Hyperfilm ECL films (GE Healthcare) were exposed to the vacuum-dried gels and hand-developed using X-OMAT developer and fixer (Kodak).

6.3.3 – Determination of CTCF levels in the *FXN* gene

Optimization of DNA shearing method using Southern blot analysis

This experiment was designed in order to determine the best method of shearing the DNA for chromatin immunoprecipitation (ChIP) analysis of CTCF levels in the *FXN* gene. Specifically, two previously described DNA fractionation methods for ChIP analysis were compared: restriction enzyme digestion (Kang *et al.* 2002) and sonication (Al-Mahdawi *et al.* 2008). Consequently, this experiment consisted of 5 different sample preparations, each one starting with 30mg of human normal cerebellum homogenised in cold PBS, in a final volume of 1ml:

1 – Standard DNA extraction and *Bcc*I restriction digestion

The cells were pelleted by centrifugation at 13K rpm and digested with 0.5mg Proteinase K in 400µl of tail digestion buffer, at 65°C overnight. The DNA was then extracted using the phenol/chloroform method, followed by ethanol precipitation, and finally resuspended in TE buffer. 10µg of DNA was then digested with 20U of *Bcc*I (New England Biolabs) in the presence of BSA in a final volume of 10µl, at 37°C overnight.

2 – Simulation of ChIP experiment with no DNA shearing

DNA-bound proteins were cross-linked to the DNA after incubation at room temperature for 20min in 1% formaldehyde (Sigma Aldrich). The cross-linking reaction was stopped by adding glycine to 125mM and incubating for 5min at room temperature. The cells were pelleted by centrifugation for 5min at 13K rpm, 4°C, and washed 2x with 500µl cold PBS. The cells were lysed in the presence of protease inhibitors (Roche) in 250µl of cell lysis buffer, for 10min on ice. The nuclei were pelleted by centrifugation for 5min at 5K rpm, 4°C. The pelleted nuclei were then lysed in the presence of protease inhibitors in 100µl of nuclei lysis buffer, for 10min on ice. The cell debris was removed by centrifugation for 30min at 13K rpm, 4°C, the DNA collected as the supernatant phase and stored at -20°C.

3 – Simulation of ChIP experiment with DNA restriction digestion – pre-nuclei lysis

DNA-bound proteins were cross-linked to the DNA after incubation at room temperature for 20min in 1% formaldehyde (Sigma Aldrich). The cross-linking reaction was stopped by adding glycine to 125mM and incubating for 5min at room temperature. The cells were pelleted by centrifugation for 5min at 13K rpm, 4°C, and washed 2x with 500µl cold PBS. The cells were lysed in the presence of protease inhibitors (Roche) in 250µl of cell lysis buffer, for 10min on ice. The nuclei were pelleted by centrifugation for 5min at 5K rpm, 4°C, and washed 2x with 1x restriction digest buffer (New England Biolabs). The pelleted nuclei were digested with 100U of *Bcc*I (New England Biolabs) in the presence of BSA and

protease inhibitors, in a final volume of 100µl, at 37°C overnight. The nuclei were re-pelleted as described before, and lysed in the presence of protease inhibitors in 100µl of nuclei lysis buffer, for 10min on ice. The cell debris was removed by centrifugation for 30min at 13K rpm, 4°C, and the DNA collected as the supernatant phase.

4 – Simulation of ChIP experiment with DNA restriction digestion – post-nuclei lysis

DNA-bound proteins were cross-linked to the DNA after incubation at room temperature for 20min in 1% formaldehyde (Sigma Aldrich). The cross-linking reaction was stopped by adding glycine to 125mM and incubating for 5min at room temperature. The cells were pelleted by centrifugation for 5min at 13K rpm, 4°C, and washed 2x with 500µl cold PBS. The cells were lysed in the presence of protease inhibitors (Roche) in 250µl of cell lysis buffer, for 10min on ice. The nuclei were pelleted by centrifugation for 5min at 5K rpm, 4°C. The pelleted nuclei were then lysed in the presence of protease inhibitors in 100µl of nuclei lysis buffer, for 10min on ice. The cell debris was removed by centrifugation for 30min at 13K rpm, 4°C, and the DNA collected as the supernatant phase. The DNA was ethanol precipitated, resuspended in TE buffer and digested with 100U of *Bcc*I (New England Biolabs) in the presence of BSA and protease inhibitors, in a final volume of 100µl, at 37°C overnight.

5 – Simulation of ChIP experiment with DNA shearing by sonication

DNA-bound proteins were cross-linked to the DNA after incubation at room temperature for 20min in 1% formaldehyde (Sigma Aldrich). The cross-linking reaction was stopped by adding glycine to 125mM and incubating for 5min at room temperature. The cells were pelleted by centrifugation for 5min at 13K rpm, 4°C, and washed 2x with 500µl cold PBS. The cells were lysed in the presence of protease inhibitors (Roche) in 250µl of cell lysis buffer, for 10min on ice. The nuclei were pelleted by centrifugation for 5min at 5K rpm, 4°C. The pelleted nuclei were then lysed in the presence of protease inhibitors in 100µl of

nuclei lysis buffer, for 10min on ice. The DNA was then sheared by sonicating 5x for 10 seconds at 21-22db using a sonicator (Soniprep 150). The cell debris was removed by centrifugation for 30min at 13K rpm, 4°C, the DNA collected as the supernatant phase and stored at -20°C.

TE buffer was added to the cross-linked samples (2-5) to a final volume of 250µl and each sample was then split in 3 (A - 50µl, B and C - 100µl):

A – The sample was stored at -20°C;

B – Cross-linking was reversed by adding 200µl of ChIP elution buffer and 0.5mg Proteinase K, at 37°C for 30min, followed by 65°C overnight;

C – The sample was ethanol precipitated and the pellet resuspended in 300µl TE buffer. Cross-linking was reversed as described above.

The DNA was then extracted using the phenol/chloroform method, followed by ethanol precipitation, and finally resuspended in TE buffer. Approximately 10µg of each sample was separated on a 1% agarose 1x TBE midi-gel for Southern blot analysis (see detailed method in Chapter 2). The DNA was then transferred to a Hybond N+ membrane (Amersham Biosciences) in 0.4M NaOH, overnight. The blot was then washed twice in 3x SSC and pre-hybridised in 10ml pre-warmed (65°C) Church buffer, at 65°C for ≥1hr, with gentle rotation. A radiolabelled probe was prepared by generating an 186bp PCR product for the potential CTCF-binding region identified in the 5'UTR of *FXN* (see Table 2.3 for primers used). The PCR product was gel-purified using a Geneclean III kit (BIO 101) and then labelled with ^{32}P using the Klenow fragment-based RadPrime DNA labelling system (Invitrogen) and α-^{32}P dCTP (PerkinElmer). Unincorporated radionucleotides were removed using a MicroSpin S-200 HR column (Amersham Biosciences). The Probe was heat-denatured at 98°C for 10min,

followed by a 5min incubation on ice, and then added to 10ml of prewarmed (65°C) Church buffer. Hybridisation was achieved by adding the probe solution to the blot, followed by incubation at 65°C overnight. Amersham Hyperfilm ECL films (GE Healthcare) were then exposed to the stringency washed blot and hand-developed using X-OMAT developer and fixer (Kodak).

Determination of CTCF levels in the *FXN* gene using ChIP analysis

The CTCF levels were investigated at three potential CTCF-binding regions identified in the *FXN* gene: 5'UTR, upstream and downstream of GAA, using normal and FRDA samples from human cerebellum. This procedure was adapted from a method previously used to investigate histone modifications by ChIP (Al-Mahdawi *et al.* 2008). CTCF ChIP was performed exactly as described in Chapter 2 and relied on the use of an anti-CTCF antibody (Upstate).

Relative Q-PCR amplification was carried out with SYBR Green (Applied Biosystems) in an ABI Prism 7900HT real-time PCR instrument (Applied Biosystems) as described in Chapter 2. Reactions were carried out in triplicates, in a final volume of 20µl containing 12.5pmol of each of the respective forward and reverse primers (see Table 2.3 for primers used). Relative quantification CTCF values were normalised to input and minus antibody samples, and finally determined in relation to a previously described CTCF-binding control region in the human *H19* gene (Burke *et al.* 2005).

6.4 – Results

6.4.1 – Identification of potential CTCF-binding sites in the *FXN* gene

In silico screening of a 40kb region spanning in entirety the *FXN* gene using a bioinformatics web tool designed by Klenova and colleagues at the University of Essex (Klenova 2007) produced a relatively large number of potential CTCF-binding sites, with a total of 15 and 12 sense and anti-sense sites respectively (Table 6.1 and Figure 6.5). All sites identified were found in non-coding regions.

Table 6.1 – List of potential CTCF-binding sites identified in the *FXN* gene using a bioinformatics tool designed by Klenova and colleagues, University of Essex (Klenova 2007).

		***FXN* gene**												
	5'	**5' UTR**	**Exon 1**	**Intron 1**	**Exon 2**	**Intron 2**	**Exon 3**	**Intron 3**	**Exon 4**	**Intron 4**	**Exon 5**	**3' UTR**	**3'**	**Total**
Sense	1	1	0	4	0	1	0	2	0	6	0	0	0	15
Anti-sense	0	1	0	3	0	1	0	2	0	4	0	0	1	12
Total	1	2	0	7	0	2	0	4	0	10	0	0	1	27

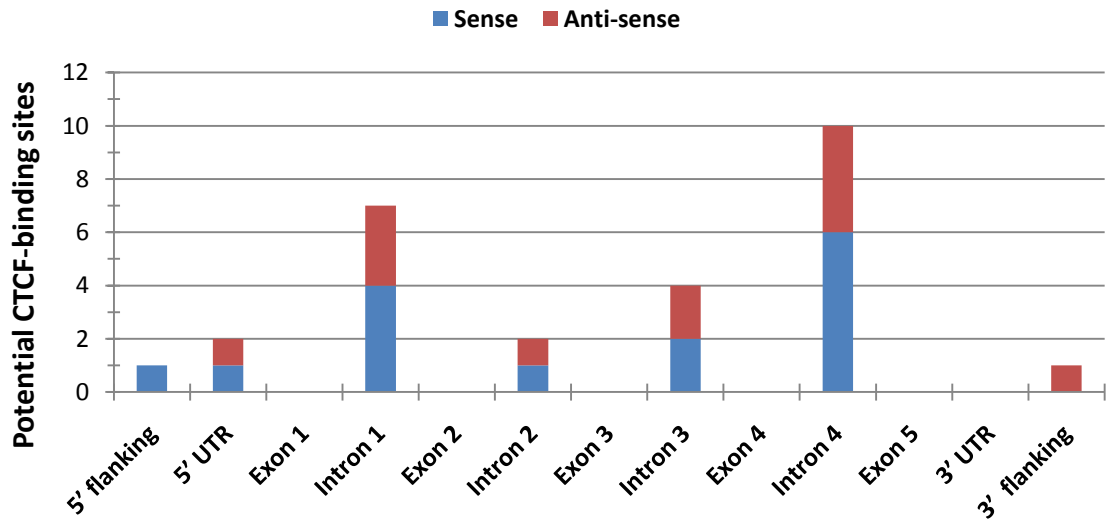

Figure 6.5 – Distribution of potential CTCF-binding sites identified in the *FXN* gene.

Particular interest was devoted towards 4 of the potential CTCF-binding sites in 3 regions of the *FXN* gene because of their location and therefore potential involvement in GAA repeat dynamics and the regulation of transcription: 1 sense and 1 anti-sense site in the 5'UTR; 1 sense site upstream of the GAA repeat; and 1 anti-sense site downstream of the GAA repeat (Figure 6.6).

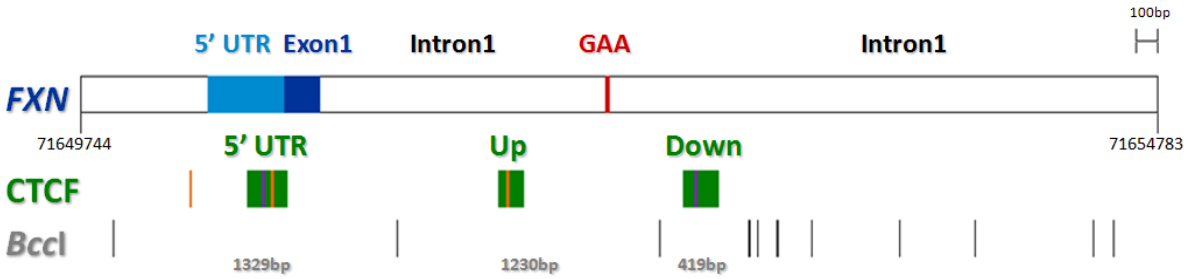

Figure 6.6 – Schematic representation of the potential CTCF-binding sites in the *FXN* gene. **Orange** bands represent sense CTCF-binding sites and **purple** bands represent anti-sense sites. The 3 **green** bands represent the regions investigated by CTCF ChIP analysis: 5'UTR, upstream and downstream of the GAA repeat. **Dark grey** bands represent the *Bcc*I restriction sites generating different sized fragments for the 3 regions investigated for CTCF: 1329bp, 1230bp and 419bp for 5'UTR, upstream and downstream of the GAA repeat, respectively.

6.4.2 – Determination of CTCF levels in the *FXN* gene using ChIP analysis

CTCF ChIP analysis was performed on the 3 regions of interest using 3 normal (JM, 62341 and 62395) and 3 FRDA (HK, MS and CA) cerebellum samples. All 3 FRDA samples were homozygous for expanded GAA repeats, with sizes of 750/650, 700/700 and 750/550 respectively. ChIP analysis revealed that immunoprecipitation with anti-CTCF antibody generally produced higher levels of chromatin at all genetic regions investigated when compared with the samples precipitated with IgG (minus antibody sample: "-ab"), with the exception of the upstream and downstream regions of one cerebellum sample (MS) (Figure D.1).

CTCF enrichment was determined by subtracting the respective minus antibody samples from the CTCF-precipitated samples, followed by normalisation to the input sample. Overall, less CTCF enrichment was detected for all *FXN* regions when compared to the *H19* CTCF-positive region: in normal cerebellum samples the enrichment levels in the 5'UTR, upstream and downstream of the GAA repeat regions were 82%, 54% and 43% of *H19* enrichment levels, respectively (Figure D.2). Although the levels of chromatin enrichment around the GAA repeat are lower than in the 5'UTR, this difference not statistically significant (Table 6.2).

Table 6.2 – Independent samples *t*-test associated *p*-values of chromatin enrichment levels following CTCF ChIP between the 3 different regions in the *FXN* gene, determined separately for normal and FRDA samples.

	***FXN* region**	***p*-value**
Normal	5'UTR vs Up	0.389
	5'UTR vs Down	0.228
	Up vs Down	0.454
FRDA	5'UTR vs Up	0.265
	5'UTR vs Down	0.087
	Up vs Down	0.452

Normal, n=4; FRDA, n=6;

Decreased CTCF levels in FRDA-associated *FXN* gene

Subsequently, relative CTCF levels were determined by normalising the CTCF-precipitated values to the respective input and minus antibody samples, and finally standardizing with the *H19* CTCF-positive region values. In general, lower relative CTCF binding was identified for the 3 *FXN* regions investigated in FRDA-patient cerebellum when compared to those from normal individuals: 75%, 47% and 49% of normal values in the

5'UTR, upstream and downstream of GAA regions, respectively (Figure 6.7 and Figure D.3). However, upon statistical analysis, the lower FRDA-associated CTCF levels were not found to be significantly different from the normal-associated levels (Table 6.3).

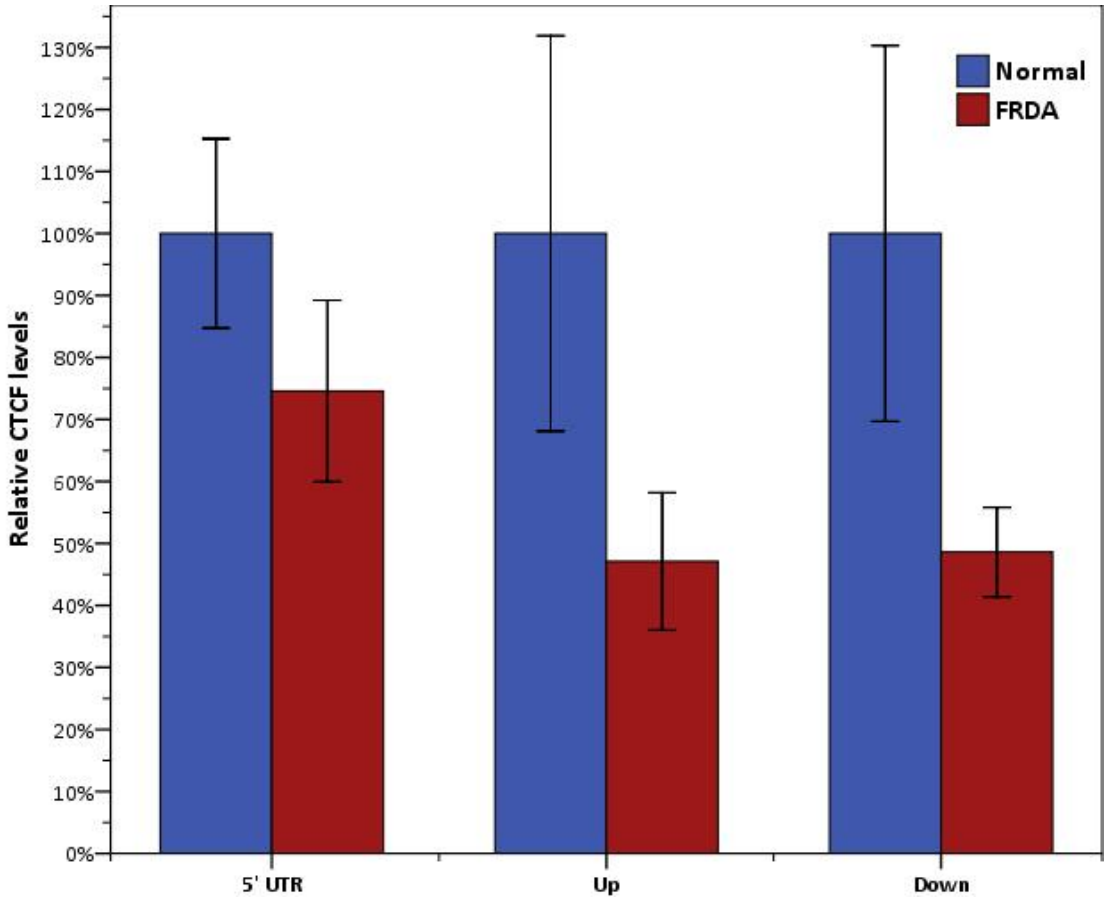

Figure 6.7 – Relative CTCF levels determined in the *FXN* gene of normal and FRDA cerebellum samples. CTCF levels were normalised to input and minus antibody samples, and finally determined in relation to a previously described CTCF-binding control region in the human *H19* gene. (Normal, n=4; FRDA, n=6; error bars: +/- 1 SE)

Table 6.3 – Independent samples *t*-test associated *p*-values of relative CTCF levels in the *FXN* gene of normal vs FRDA patients.

***FXN* region**	***p*-value**
5'UTR	0.279
Upstream of GAA	0.103
Downstream of GAA	0.079

Normal, n=4; FRDA, n=6;

6.4.3 – Confirmation of CTCF-binding sites in the *FXN* gene by EMSA

An initial investigation into the ability of CTCF to bind to the investigated regions of the *FXN* gene consisted on a non-radioactive EMSA approach. However, the fact that nuclear extracts were used rather than purified CTCF made the interpretation of results very difficult and ultimately, unreliable. A second approach consisted of using γ-^{32}P end-labelled DNA probes and nuclear extracts. However, supershift analysis was inconclusive.

Eventually, EMSA was performed using γ-^{32}P end-labelled DNA probes and full-length recombinant CTCF. This proved to be a much more convincing approach, since any shift observed could only represent an interaction between the DNA probe of interest and CTCF. To begin with, the validity of the technique was confirmed by replicating previously described results (Figure 6.8), which reported the DM1 CTCF-binding sites 1 and 3 as CTCF positive- and negative-binding regions, respectively (Filippova *et al.* 2001).

CTCF binds to the 5'UTR region of the *FXN* gene

EMSA analysis using γ-^{32}P end-labelled DNA probes and full-length recombinant CTCF confirmed that CTCF can recognise and bind to the 5'UTR region of the *FXN* gene, but not to the investigated regions upstream and downstream of the GAA repeat in intron 1 (Figure 6.8). This was demonstrated by the ability of CTCF to form (or not) a high molecular weight complex with the DNA probe, therefore shifting the radioactive signal.

Subsequently to all practical investigations, and following the publication of a CTCF-binding site database (CTCFBSDB) (Bao *et al.* 2008), the *FXN* gene was reinvestigated for the presence of CTCF-binding sites. CTCFBSDB consists of a collection of experimentally identified and computationally predicted CTCF-binding sites and screening of a larger region

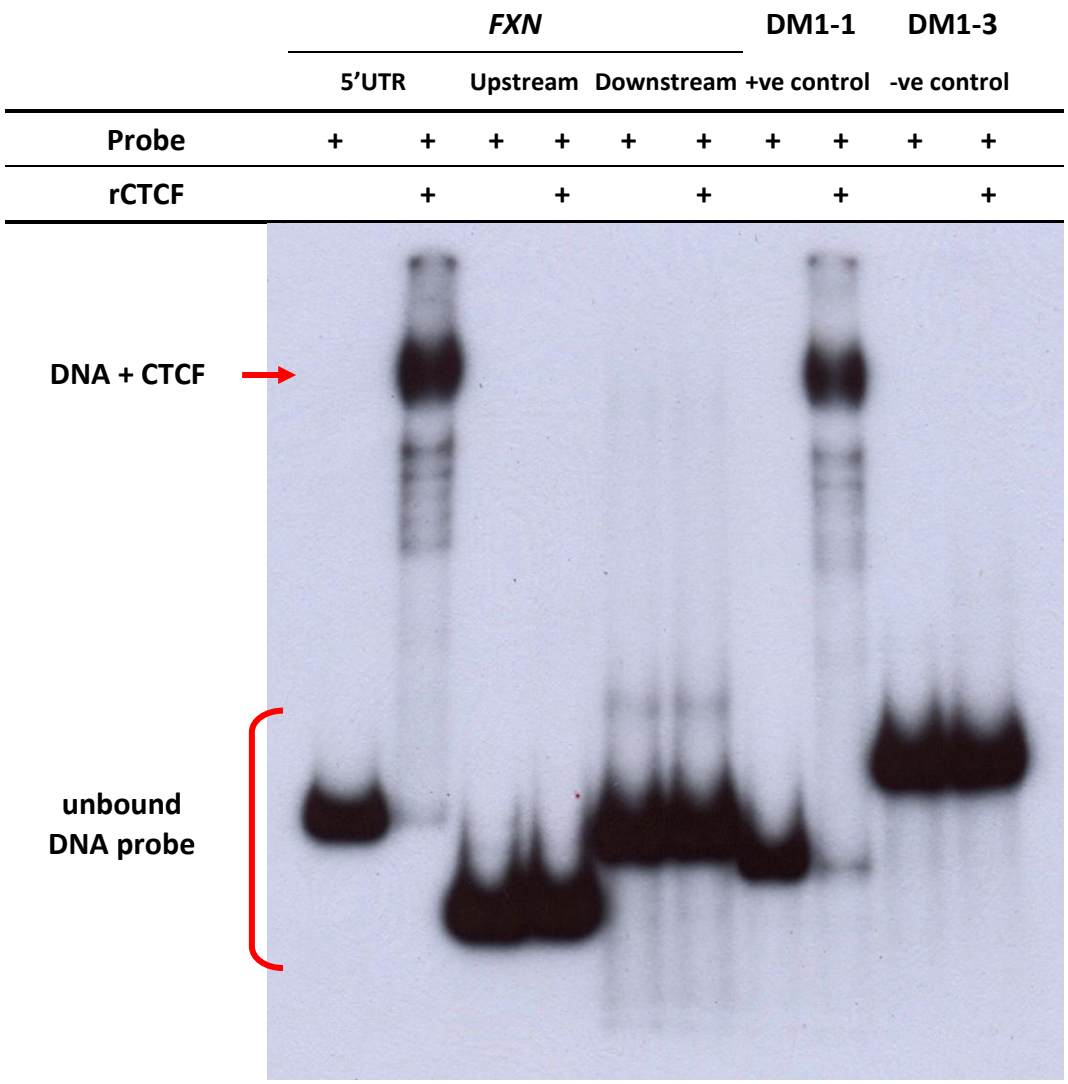

Figure 6.8 – Confirmation of CTCF-binding sites in the *FXN* gene by EMSA. γ-^{32}P end-labelled DNA probes separated by PAGE in the presence or absence of full-length recombinant CTFC protein.

comprising the whole *FXN* gene and including approximately 40kb upstream and 60kb downstream of the gene, revealed five different sites originally identified by high-throughput ChIP-chip analysis: 2 sites in the 5' flanking region, 2 sites in the 5'UTR, and 1 site in the 3' flanking region of the *FXN* gene (Figure 6.9). *In silico* prediction of CTCF-binding motifs in the same region using the CTCFBSDB tool resulted in a single site being identified in intron 3 of the *FXN* gene. Further analysis of the 5'UTR sites identified by ChIP-chip analysis confirmed that both overlap with the 5'UTR region hereby investigated by EMSA and ChIP analysis.

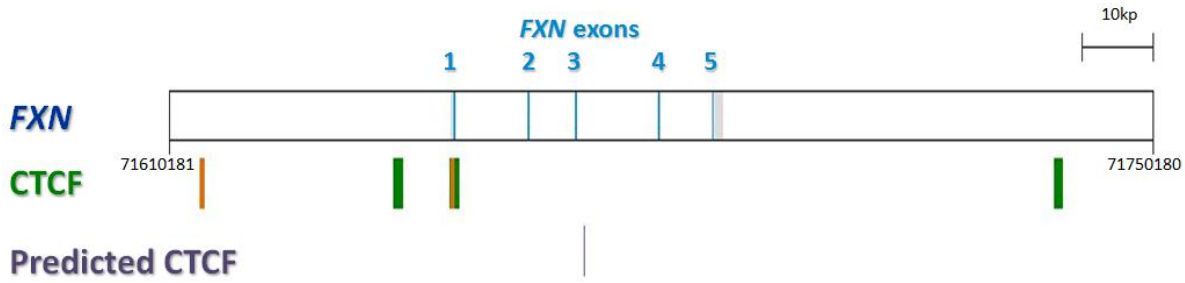

Figure 6.9 – Schematic representation of the CTCFBSDB-identified sites in the *FXN* gene (Bao *et al.* 2008). **Orange** and **green** bands represent the CTCF-binding sites experimentally identified by 2 independent high-throughput ChIP-chip analysis. The **purple** band represents the *in silico*-predicted CTCF-binding site.

6.5 – Discussion

The reported ability of CTCF to regulate gene expression, constrain heterochromatin regions, and influence trinucleotide repeat instability suggested that CTCF could play a role in the development of FRDA.

To date, no FRDA research concerning CTCF has been reported. For that reason, an initial step consisted on identifying potential CTCF-binding sites in the *FXN* gene. This was initially addressed by performing an *in silico* screen of the entire *FXN* gene relying on previously identified CTCF motifs. However, this approach seems to have produced an unrealistically high number of sites (a total of 27 in a 40kb region) since, for example, genome-wide mapping of CTCF-binding sites using a ChIP-chip approach has previously shown that CTCF-rich genomic regions never exceeded a density of 60 sites per 2Mb, in the human chromosome 11 (Kim *et al.* 2007). According to this, a 40kb region should not normally contain more than one single CTCF-binding site, let alone 27.

In fact, the effort to computationally identify potential insulators in the human genome is still hampered by an incomplete understanding of the DNA-recognition sequence of CTCF, with CTCF-binding sites identified so far exhibiting extensive sequence variation and lacking specificity for genome-wide prediction of CTCF binding (Ohlsson *et al.* 2001).

Looking at the results obtained from this screen, it may seem interesting that all sites identified locate to noncoding regions. However, the coding fraction only counted for 1.6% of the whole 40kb region analysed. The previously mentioned genome-wide mapping of CTCF-binding sites study has reported that CTCF-binding sites are generally very far from promoters (average distance of 48kb), with nearly half (46%) of the CTCF-binding sites being located in the intergenic regions, 20% near transcription start sites, and 22% and 12% in intronic and exonic regions, respectively (Kim *et al.* 2007).

Nevertheless, considering the reported ability of CTCF to function as a transcription factor and in view of the situation described at the locus of various trinucleotide repeat-associated disorders, where CTCF-binding sites were identified flanking the repeat regions, particular attention was devoted to the potential binding sites identified in 3 regions of the *FXN* gene: 5'UTR, upstream and downstream of the GAA repeat.

Preliminary CTCF ChIP analysis of 3 normal and 3 FRDA patients' cerebellum samples indicated that in FRDA lower levels of CTCF are found in these 3 regions of the *FXN* gene. In fact, although not statistically significant, the determined CTCF levels in FRDA were only 75%, 47% and 49% of normal levels in the 5'UTR, upstream and downstream of GAA regions, respectively (Figure 6.7).

These findings agree with the proposed hypothesis of CTCF's involvement in FRDA. As previously mentioned, CTCF has the ability to directly regulate the expression in *cis* by behaving as a transcription factor (Filippova *et al.* 1996). Although, the regulation of the *FXN* gene is still poorly understood, with no conclusive promoter region nor associated transcription factors identified to date (Greene *et al.* 2007), the lower levels of CTCF observed in the 5'UTR could possibly (and probably only partially) explain the reduced expression of the *FXN* gene observed in FRDA.

Additionally, the apparent loss of CTCF surrounding the GAA repeat could possibly also contribute to this by failing to constrain the heterochromatic region to the repetitive element. In fact, this spreading of heterochromatin has been previously described in FRDA-associated *FXN* genes, with higher levels of DNA methylation and heterochromatin-characteristic histone modifications being observed in the region upstream of the GAA and even reaching the 5'UTR region of the *FXN* gene (Greene *et al.* 2007; Al-Mahdawi *et al.* 2008).

On a separate note, the lower levels of CTCF surrounding the GAA repeat of FRDA patients may be linked to the increased FRDA-associated GAA repeat instability. As previously mentioned, the loss of the CTCF-binding sites flanking the CAG repeat at the SCA7 locus has induced a significant increase in triplet repeat instability (Libby *et al.* 2008). For that reason, these findings suggest that a similar effect may be occurring at the FRDA locus.

In line with reduced binding of CTCF in the *FXN* gene of FRDA patients, there have been recent descriptions of novel noncoding antisense transcripts that show increased expression in FRDA alleles (K. Usdin and S. Bidichandani, personal communications). As previously mentioned, CTCF has been shown to restrict the extent of an antisense transcript at the DM1 locus (Cho *et al.* 2005). It is generally accepted that expression of noncoding antisense transcripts may have a siRNA-mediated transcription repressive effect. As a result, it seems logical to consider that the loss of CTCF at the FRDA locus may also result in increased levels of antisense transcription, which additionally implicates CTCF in the regulation of *FXN* expression.

Although such interpretations of the ChIP results may seem plausible and in line of what was initially hypothesised, they do not concur with subsequent EMSA analysis that was performed to confirm the ability of CTCF to bind to the 3 investigated *FXN* regions. This analysis revealed that CTCF can form a complex with the 5'UTR region, but not with the regions upstream and downstream of the GAA repeat (Figure 6.8).

This finding is somehow contradictory to what was originally observed by ChIP analysis, where immunoprecipitation with anti-CTCF antibody generally produced higher levels of chromatin at all genetic regions investigated when compared with the samples simply precipitated with IgG (Figure D.1), therefore suggesting the presence of CTCF in such regions.

However, it is also true that the level of chromatin enrichment caused by CTCF immunoprecipitation was higher at the 5'UTR than in the GAA-flanking regions, with the downstream region showing the lowest level of enrichment (Figure D.2), although this difference was statistically non significant (Table 6.2).

A possible explanation for the discrepancy between ChIP and EMSA data is that, since the sites investigated are relatively close together (992bp between 5'UTR and GAA upstream regions; and 1856bp between 5'UTR and GAA downstream regions), perhaps the method used to fractionate the chromatin was ineffective at generating sufficiently distinct fragments for each of the regions investigated. In the event of this being true, Q-PCR quantification of upstream and downstream regions could actually represent chromatin fragments that were only immunoprecipitated with anti-CTCF because they were too large and also contained the CTCF-binding site in the 5'UTR region.

In fact, this hypothesis gained strength when Southern blot analysis of sonicated CTCF ChIP samples (following reversal of cross-linking), using a probe specific for the 5'UTR region, revealed the presence of some chromatin fragments just exceeding 2kb.

To address this issue, a restriction digestion-based approach was designed, relying on the ability of *Bcc*I to specifically cut the chromatin at sites between the *FXN* regions investigated (Figure 6.6). Although *Bcc*I restriction digestion of purified DNA confirmed the ability to generate distinct chromatin fragments for each of the *FXN* regions of interest, simulation of a ChIP experiment with *Bcc*I restriction digestion was unsuccessful.

Therefore, in future CTCF ChIP experiments, extra attention must be devoted to the sonication methodology in order to ensure appropriate chromatin fractionation. This assessment must be made after cross-linking reversal.

Subsequent to all practical investigations, and following the publication of a genome-wide CTCF-binding site database (Bao *et al.* 2008), the FRDA locus was reinvestigated for the presence of CTCF. This database reported a total of four distinct experimentally determined CTCF-binding sites: 2 sites upstream, 1 site in the 5'UTR, and 1 site downstream of the *FXN* gene (Figure 6.9). Detailed analysis of this 5'UTR site (identified by ChIP-chip analysis) established that this is the same region hereby investigated by ChIP and confirmed by EMSA. However, this database showed no records of any sites identified nearby the GAA repeat, suggesting that indeed they do not exist.

Finally, despite the scenario of events concerning the presence of CTCF around the GAA repeat appearing to be inconclusive at this stage, the existence of a CTCF-binding site at the 5'UTR of the *FXN* gene does seem conclusive. Additionally, although no statistically significance was observed, it seems that there is a loss of CTCF in this site in FRDA. Therefore, it is reasonable to suggest that CTCF may play a role in the silencing mechanism associated with FRDA.

Chapter 7 – General discussion and conclusion

Friedreich ataxia is an autosomal-recessive, neurodegenerative disease that primarily affects the nervous system and heart. It is a severely debilitating disease that has a major influence on the lives of affected individuals. Disappointingly, there currently is no effective therapy for FRDA, and the development of a suitable treatment has been strongly hampered by an incomplete understanding of FRDA pathogenesis.

FRDA is mainly caused by a GAA repeat hyper-expansion in intron 1 of the *FXN* gene, which results in decreased levels of the mitochondrial protein frataxin being expressed. It is accepted that, via a mechanism yet to be fully understood, such frataxin deficiency results at a first instance in a flawed ability to deal with oxidative stress (Chantrel-Groussard *et al.* 2001). The antioxidant properties of coenzyme Q10, vitamin E and idebenone suggested a potential role for these agents in FRDA therapy. Although recent clinical trials in FRDA patients with such agents confirmed improved cardiac function, no significant neuroprotective effects were detected (reviewed by Schulz *et al.* 2009).

Antioxidant therapy investigated in the *FXN* YAC GAA mouse model

The reported antioxidant and neuroprotective properties of the cannabinoids CBD and THC (Hampson *et al.* 1998) and the isoindoline nitroxide CTMIO (Gueven *et al.* 2006) suggested a potential use for FRDA therapy. For that reason, *in vivo* drug trials were performed on the YG8 and YG22 *FXN* YAC GAA transgenic mouse models (Al-Mahdawi *et al.* 2006). CBD treatment provided a small protection against oxidative stress and marginally improved rotarod performance. On the other hand, treatment with CBD:THC and CTMIO produced small detrimental effects on rotarod performance, locomotor activity and protein oxidation levels. Additionally, no neuroprotective effect in the DRG was detected with either treatment.

However, these findings lack statistical significance. This may be due to the mildness of the FRDA-associated phenotype displayed by the current *FXN* YAC GAA-containing mice and the lack of a strong demarcation between Wt and FRDA mice, despite the initial reported differences (Al-Mahdawi *et al.* 2006). In fact, in all studies performed (functional, biochemical and histological) no significant difference was observed between the FRDA and Wt mice. This could be a result of the relatively small GAA repeat currently found in the *FXN* YAC GAA mouse models (maximum size of GAA_{230}), together with changes in the transgenic *FXN* locus and the genetic background of the mice throughout many generations of breeding. With this in mind, it should be noted that the initial report by Al-Mahdawi *et al.* (2006) used Wt littermates of predominantly, but not exclusively, C57BL6 background, whereas the Wt controls in the present studies were unrelated 100% C57BL6 mice.

On the other hand, the lack of significant difference may be linked to technical aspects associated with the methodology used. For example, a wide variability in rotarod performance was observed between mice from the same study groups. The reliability of this technique could possibly be improved by distributing more measuring points throughout the studies. Additionally, alternative functional studies should be considered, such as beam walking assays. In fact, the improved sensitivity of beam walking over rotarod in determining motor coordination deficits has been reported (Stanley *et al.* 2005). Regarding locomotor activity monitoring, new methodology is also available which could provide a greater insight into the FRDA mouse model phenotype. An example of this consists of an open field activity monitoring system equipped with laser beams that automatically and accurately tracks the behaviour of the mouse, monitoring values such as ambulatory distance, velocity, vertical movements and stereotypic actions. In fact, locomotor characterization of the *FXN* YAC GAA

mouse model is currently being performed using such methodology (C. Sandi, personal communication).

Nonetheless, the development of more severely-affected GAA FRDA mice is crucial for future investigations. Potentially, this could be achieved by crossing the currently available *FXN* YAC GAA mice with either different genetic background mice (Lloret *et al.* 2006), mismatch repair deficient mice (van den Broek *et al.* 2002; Gomes-Pereira *et al.* 2007; Kovtun *et al.* 2007), or DNA methyltransferase deficient mice (Dion *et al.* 2008) in an attempt to promote GAA instability and therefore obtain *FXN* YAC mice with increased GAA repeat tracts. Such strategies are currently being followed with both YG8 and YG22 lines of *FXN* YAC GAA mouse model (M. Pook, personal communication). Alternatively, a recently generated *FXN* BAC transgenic mouse model that contains an expanded GAA tract (approximately 500 repeats) could be of use. However, to date no GAA repeat instability and no FRDA-like phenotype has been detected in such mice, most likely due to an interrupted GAA tract (J. Sarsero, personal communication).

In summary, the results obtained suggest minimal or no therapeutic potential of CBD, THC and CTMIO for FRDA. Any future investigations into the potential therapeutic effect of CBD, THC and CTMIO for FRDA should initially rely on *in vitro* studies, using for example FRDA patient-derived cell lines. Only then, assuming promising results, should investigations be followed *in vivo*, preferably making use of a more severely affected FRDA model yet to be developed.

Antioxidants have been used as the first line of attack in FRDA therapy because such drug compounds are already widely available and have been shown to be safe. However, the use of antioxidants for FRDA therapy is unlikely to be the most effective strategy since it only

addresses one of the pathological endpoints, rather than targeting the primary molecular defect, which is frataxin deficiency.

HDACi therapy investigated in the *FXN* YAC GAA mouse model

More recently, new strategies focusing on increasing frataxin expression have been considered for the therapy of FRDA. One strategy is the use of cellular models for high-throughput screening of small molecules to identify compounds that can increase frataxin expression by undetermined mechanisms (Sarsero *et al.* 2003; Calmels *et al.* 2009).

Another strategy takes into account the heterochromatin-mediated silencing effect of the *FXN* gene in FRDA (Saveliev *et al.* 2003; Herman *et al.* 2006). Expanded GAA tracts have been shown to induce heterochromatin-associated histone modifications such as decreased H3ac and H4ac as well as increased H3K9me3, accompanied by a differential DNA methylation profile in the surrounding genomic regions (Herman *et al.* 2006; Greene *et al.* 2007; Al-Mahdawi *et al.* 2008). Therefore, reversing such modifications should render the potential to increase frataxin expression in FRDA-associated *FXN* alleles.

Herman *et al.* (2006) have recently described a class of benzamide-type HDACi that seems to specifically inhibit these FRDA-associated histone modifications and as a result successfully increased frataxin expression in FRDA patient-derived lymphocytes. In fact, one such HDACi – 4b – successfully increased the acetylation levels of H3K14, H4K5 and H4K12 in the GAA upstream region of *FXN* and significantly increased the *FXN* mRNA levels, to approximately 80% of that in unaffected individuals (Herman *et al.* 2006).

However, such encouraging results call for *in vivo* confirmation. For that reason, the effects of HDACi 106, an improved derivative of 4b, were investigated by performing long-term drug trials on the available *FXN* YAC GAA model (Al-Mahdawi *et al.* 2006). Two distinct

delivery routes were investigated for 106: oral *ad libitum* administration in drinking water and sub-cutaneous injections.

With the exception of sub-cutaneously treated mice, which showed a mild improvement in rotarod performance, prolonged treatment with 150mg/kg 106 produced no observable effects on the functional parameters investigated, similarly to the previous cannabinoid and CTMIO studies. Again, this lack of significance may be due to the mildness of the phenotype observed in the *FXN* YAC GAA mice (Al-Mahdawi *et al.* 2006).

However, while the functional phenotype displayed by these mice is very mild, the FRDA-associated epigenetic changes in the *FXN* transgene are rather obvious (Al-Mahdawi *et al.* 2008), allowing for further investigation of the effect of 106 in terms of its ability to target histone modifications and ultimately up-regulate frataxin expression.

Significant changes in global H3ac and H4ac levels were detected in the brain following oral and sub-cutaneous treatments with 150mg/kg 106, indicating that the drug is capable of crossing the blood-brain barrier. Additionally, the ability of 106 to increase frataxin expression was confirmed in the brain of *FXN* YAC GAA mice. The levels of *FXN* mRNA and frataxin proteins were significantly increased by 20% in the brain of orally treated mice, and sub-cutaneous administration resulted in a 30% increase of *FXN* mRNA levels 24h after dosing. Cessation of sub-cutaneous 106 treatment for a period of 1 month produced exciting results, exemplified by a 70% increase in frataxin protein levels in the brain and suggesting a long-term duration of effect for 106.

However, sub-cutaneous administration of 150mg/kg 106 produced an initial frataxin inhibitory effect 4h after dosing. This negative effect on *FXN* transcription shortly after 106 sub-cutaneous administration, caused by some yet to be understood inhibitory mechanism, appears to be related to the considerably increased levels of global H3ac and H4ac initially

found in the brain soon after dosing. This may be partly explained by the fact that although 106 preferentially inhibits HDAC3, it is capable of inhibiting other class I HDACs (Chou *et al.* 2008). This raises the concern that 106 may be at some point affecting the regulation of various genes other than *FXN*. To address this issue, microarray investigation should be followed on brain samples following 106 treatment.

Additionally, the fact that only global levels of H3ac and H4ac were determined in these studies makes it difficult to interpret the 106 effect in terms of the mechanism of *FXN* up-regulation. For this reason, it is of paramount importance to further investigate the effect of 106 at the *FXN* locus by ChIP analysis. Additionally, the DNA methylation profile at the *FXN* locus following treatment with 106 should also be analysed by either bisulfite sequencing or methylscreen techniques.

Recently, a short-term *in vivo* study also reported the ability of 106 to significantly increase the expression of frataxin in the brain (among other tissues) of KIKI mice, by specifically increasing H3ac and H4ac at particular residues in a region just upstream of the GAA repeat (Rai *et al.* 2008).

Overall, the potential of 106 to increase frataxin expression in the brain of *FXN* YAC GAA treated mice has been confirmed, but at the same this raised concerns regarding dosing. In an attempt to overcome this issue, ongoing investigations are focusing on the effect of a 106 derivative – 136 – which is being administered to *FXN* YAC GAA mice at a lower concentration, but with more regular dosing.

Additionally, both *in vivo* studies performed so far have only confirmed 106 up-regulation of frataxin in the presence of relatively small GAA repeat tracts (maximum of 230), and although *in vitro* studies suggest that 106 can indeed up-regulate frataxin in the presence of larger GAA expansions (maximum of 650) (Herman *et al.* 2006) it is still

necessary to investigate the potential of 106 in much larger GAA-containing FRDA models *in vivo*. As previously discussed, such models could arise from breeding the current *FXN* YAC GAA model against a variety of genetic backgrounds or DNA repair deficient mice, consequently resulting in spontaneous GAA expansions. Alternatively, the *FXN* BAC GAA (interrupted GAA_{500} tract) model could be used (J. Sarsero, personal communication). However, an FRDA-associated epigenetic phenotype is yet to be described in these mice.

Promising alternative therapeutic strategies

HDACi-based treatment, in particular the benzamide group of HDACi described above, is currently the most promising therapy for FRDA. Nevertheless, a variety of additional compounds have the potential to be of therapeutic use for FRDA and should therefore be further investigated.

Biacsi *et al*. (2008) have recently described the use of SIRT1 (class III HDAC) inhibitors such as splitomicin to alleviate the heterochromatin-mediated silencing effect present at the Fragile X locus. Sirtinol is another SIRT1 inhibitor (Ota *et al.* 2006) and therefore should similarly hold the potential to target repressive histone modifications.

Taking into account the increased levels of DNA methylation observed in the 5'UTR and upstream of GAA repeat regions of FRDA-associated *FXN* alleles (Greene *et al.* 2007; Al-Mahdawi *et al.* 2008), suggests the potential use of DNA de-methylating agents such as zebularine (Yoo *et al.* 2004) and 5-AzaC (Baylin 2004) in FRDA therapy. However, the use of such drugs may be limited due to their exclusive action on dividing cells and their high levels of cytotoxicity.

A small molecule compound DB221 has been shown to interact with expanded GAA repeat tracts and potentially facilitate *FXN* expression in FRDA (D. Boykin, Georgia State

University, personal communication). However, such compounds are in very early stages of development and will require many future studies to determine efficacy and toxicity.

Additionally, the antioxidant agent resveratrol has been shown to up-regulate frataxin, as determined by high throughput cellular screening assays (J. Sarsero, personal communication). The combination of antioxidant properties with the ability to increase frataxin levels could prove doubly beneficical for FRDA therapy.

The therapeutic potentials of the compounds mentioned above are currently being investigated *in vitro* and in the eventuality of promising findings, research will be followed in the *FXN* YAC GAA mouse model (C. Sandi and M. Pook, personal communications).

Further epigenetic characterization in FRDA

Although great progress has been made into the understanding of molecular mechanisms involved in FRDA, significant aspects remain to be fully clarified, particularly those concerning the regulation of the *FXN* gene and the dynamics of GAA repeat tracts at the FRDA locus.

In an attempt to partially address this, investigations were performed as part of this thesis to ascertain the potential involvement of the DNA insulator protein CTCF in FRDA. CTCF has been reported to regulate gene expression either by functioning as a transcription factor or as a chromatin insulator (Bell and Felsenfeld 2000; Filippova *et al.* 2001). Additionally, CTCF has been identified flanking trinucleotide repeats at various disease-associated loci, constraining the heterochromatic region to the repetitive element, thereby preventing the spreading of these repressive modifications (Filippova *et al.* 2001; Cho *et al.* 2005). Moreover, CTCF has been specifically implicated in the regulation of CAG repeat instability in SCA7 (Libby *et al.* 2008).

Investigation of computationally predicted CTCF-binding sites in 3 regions of the *FXN* gene of particular interest – 5'UTR, GAA upstream and GAA downstream – was performed in normal and FRDA patient cerebellum samples. ChIP analysis of CTCF binding to the *FXN* gene revealed FRDA-associated lower levels of CTCF in all 3 of the investigated regions at the *FXN* gene.

As previously mentioned, the regulation of the *FXN* gene is still poorly understood, with no conclusive promoter region nor associated transcription factors identified to date (Greene *et al.* 2007). However, the reported ability of CTCF to regulate gene expression combined with the finding of lower levels of CTCF at the 5'UTR of *FXN* in FRDA, suggests that CTCF may indeed play a role in the regulation of frataxin expression in *cis*.

Additionally, Rothe (2008) has recently described a RNA pol II transcriptional pausing site in exon 1 of FRDA-associated *FXN* alleles, supporting the idea of deficient transcription elongation as the cause for frataxin deficiency. Rather interestingly, this study also reported the presence of CTCF at this pausing site. Although, the possibility that this pausing site corresponds to the 5'UTR region herein investigated for CTCF still needs to be ascertained, it seems likely that they are indeed the same CTCF-binding region. Therefore it is logical to suggest that CTCF may play a role in facilitating transcript elongation at this site and the decreased levels of CTCF found in the 5'UTR of FRDA-associated *FXN* alleles may be responsible for the reported RNA pol II transcriptional pausing.

Recent descriptions of novel noncoding antisense transcripts at the *FXN* gene that show increased expression in FRDA *FXN* alleles (K. Usdin and S. Bidichandani, personal communications) further concurs with the involvement of CTCF in the regulation of frataxin expression. CTCF has been shown to restrict the extent of an antisense transcript at the DM1 locus (Cho *et al.* 2005) and since it is generally accepted that expression of noncoding

antisense transcripts may have a siRNA-mediated transcription repressive effect, it is possible that the loss of CTCF at the FRDA locus may be a causal element of such increased levels of antisense transcription, which may consequently down-regulate *FXN* expression.

Moreover, the observed lower levels of CTCF around expanded GAA repeat tracts in *FXN*, combined with the heterochromatin-associated histone modifications observed in FRDA-associated *FXN* alleles, further adds to the involvement of CTCF in *FXN* regulation. CTCF is responsible for constraining the spread of heterochromatin from repetitive elements (Filippova *et al.* 2001), suggesting that loss of CTCF may be responsible for the observed spreading of heterochromatin into the GAA upstream and 5'UTR regions of FRDA *FXN* genes (Al-Mahdawi *et al.* 2008).

In a related manner, the reduced levels of CTCF surrounding the expanded GAA repeat tracts in *FXN* may also be responsible for the increased GAA repeat instability observed in FRDA-associated *FXN* alleles. Conversely, expanded GAA repeats and associated heterochromatin formation may result in reduced levels of CTCF binding. Further studies will be required to determine the order of such events.

As part of this thesis, EMSA analysis of the 3 *FXN* regions confirmed the ability of CTCF to bind the 5'UTR, but not to the regions surrounding the GAA repeat. However, this finding contradicted the ChIP data, suggesting that the DNA fragmentation methodology used for the ChIP may not have been optimal. Therefore, future investigations should be undertaken to address this issue. Additionally, the differences in CTCF levels between normal and FRDA patient cerebellum samples were not statistically significant. Therefore, additional investigation needs to be performed to confirm the significance of the findings. It would similarly be interesting to investigate the binding of CTCF in the *FXN* YAC GAA model of FRDA.

In conclusion, further CTCF investigation is required to ascertain if the observed lower levels of CTCF in FRDA-associated *FXN* genes are indeed a causal element of the molecular mechanism of FRDA, or if this is actually a consequence of the epigenetic modifications that may prevent accessibility of CTCF to its binding sites.

Summary

Since the identification of *FXN* as the FRDA gene in 1996, extensive research has progressed the understanding of this disorder to the extent that many clinical trials of antioxidants and iron-chelators are currently underway, and several other potential therapies are being investigated at a pre-clinical level.

The mouse model therapeutic studies using cannabinoids and CTMIO carried out as part of this thesis do not promote the use of these compounds in future clinical trials. However, the most promising small molecule therapy for FRDA at the moment is actually the use of HDACi to induce increased frataxin expression, and the HDACi 106 mouse model therapeutic studies reported within this thesis provide supportive evidence that the benzamide group of HDACi should definitely be pursued as a potential FRDA therapy.

Further investigations into the FRDA molecular disease mechanisms, such as the CTCF studies within this thesis, the development of more severe FRDA mouse models and the development of new small molecule drug compounds, will hopefully all culminate in the identification of an effective FRDA therapy in the near future.

List of references

Abel T and Zukin RS (2008) Epigenetic targets of HDAC inhibition in neurodegenerative and psychiatric disorders. *Curr Opin Pharmacol*, **8** (1): 57-64.

Acquaviva F, Castaldo I, Filla A, Giacchetti M, Marmolino D *et al.* (2008) Recombinant human erythropoietin increases frataxin protein expression without increasing mRNA expression. *Cerebellum*, **7** (3): 360-5.

Al-Mahdawi S, Pinto RM, Ismail O, Varshney D, Lymperi S *et al.* (2008) The Friedreich ataxia GAA repeat expansion mutation induces comparable epigenetic changes in human and transgenic mouse brain and heart tissues. *Hum Mol Genet*, **17** (5): 735-46.

Al-Mahdawi S, Pinto RM, Ruddle P, Carroll C, Webster Z *et al.* (2004) GAA repeat instability in Friedreich ataxia YAC transgenic mice. *Genomics*, **84** (2): 301-10.

Al-Mahdawi S, Pinto RM, Varshney D, Lawrence L, Lowrie MB *et al.* (2006) GAA repeat expansion mutation mouse models of Friedreich ataxia exhibit oxidative stress leading to progressive neuronal and cardiac pathology. *Genomics*, **88** (5): 580-90.

Ashton CH (1997) *Therapeutic uses of cannabis*, British Medical Association, London, Harwood Academic Publishers.

Bao L, Zhou M and Cui Y (2008) CTCFBSDB: a CTCF-binding site database for characterization of vertebrate genomic insulators. *Nucleic Acids Res*, **36** (Database issue): D83-7.

Barlow C, Hirotsune S, Paylor R, Liyanage M, Eckhaus M *et al.* (1996) Atm-deficient mice: a paradigm of ataxia telangiectasia. *Cell*, **86** (1): 159-71.

Baylin SB (2004) Reversal of gene silencing as a therapeutic target for cancer--roles for DNA methylation and its interdigitation with chromatin. *Novartis Found Symp*, **259**: 226-33; discussion 234-7, 285-8.

Begg M, Mo FM, Offertaler L, Batkai S, Pacher P *et al.* (2003) G protein-coupled endothelial receptor for atypical cannabinoid ligands modulates a Ca2+-dependent K+ current. *J Biol Chem*, **278** (46): 46188-94.

Begg M, Pacher P, Batkai S, Osei-Hyiaman D, Offertaler L *et al.* (2005) Evidence for novel cannabinoid receptors. *Pharmacol Ther*, **106** (2): 133-45.

Bell AC and Felsenfeld G (2000) Methylation of a CTCF-dependent boundary controls imprinted expression of the Igf2 gene. *Nature*, **405** (6785): 482-5.

Bell AC, West AG and Felsenfeld G (1999) The protein CTCF is required for the enhancer blocking activity of vertebrate insulators. *Cell*, **98** (3): 387-96.

Berciano J, Mateo I, De Pablos C, Polo JM and Combarros O (2002) Friedreich ataxia with minimal GAA expansion presenting as adult-onset spastic ataxia. *J Neurol Sci*, **194** (1): 75-82.

Biacsi R, Kumari D and Usdin K (2008) SIRT1 inhibition alleviates gene silencing in Fragile X mental retardation syndrome. *PLoS Genet*, **4** (3): e1000017.

Bisogno T, Hanus L, De Petrocellis L, Tchilibon S, Ponde DE *et al.* (2001) Molecular targets for cannabidiol and its synthetic analogues: effect on vanilloid VR1 receptors and on the cellular uptake and enzymatic hydrolysis of anandamide. *Br J Pharmacol*, **134** (4): 845-52.

Bolden JE, Peart MJ and Johnstone RW (2006) Anticancer activities of histone deacetylase inhibitors. *Nat Rev Drug Discov*, **5** (9): 769-84.

Bontekoe CJ, Bakker CE, Nieuwenhuizen IM, van der Linde H, Lans H *et al.* (2001) Instability of a (CGG)98 repeat in the Fmr1 promoter. *Hum Mol Genet*, **10** (16): 1693-9.

Bottle SE, Gillies DG, Hughes DL, Micallef AS, Smirnov AI *et al.* (2000) Synthesis, single crystal X-ray structure and W-band (95 GHz) EPR spectroscopy of a new anionic isoindoline aminoxyl: synthesis and characterisation of some derivatives. *J Chem Soc, Perkin Trans*, **2** (7): 1285-91.

Bouaboula M, Dussossoy D and Casellas P (1999) Regulation of peripheral cannabinoid receptor CB2 phosphorylation by the inverse agonist SR 144528. Implications for receptor biological responses. *J Biol Chem*, **274** (29): 20397-405.

Bradley JL, Blake JC, Chamberlain S, Thomas PK, Cooper JM *et al.* (2000) Clinical, biochemical and molecular genetic correlations in Friedreich's ataxia. *Hum Mol Genet*, **9** (2): 275-82.

Branda SS, Cavadini P, Adamec J, Kalousek F, Taroni F *et al.* (1999a) Yeast and human frataxin are processed to mature form in two sequential steps by the mitochondrial processing peptidase. *J Biol Chem*, **274** (32): 22763-9.

Branda SS, Yang ZY, Chew A and Isaya G (1999b) Mitochondrial intermediate peptidase and the yeast frataxin homolog together maintain mitochondrial iron homeostasis in Saccharomyces cerevisiae. *Hum Mol Genet*, **8** (6): 1099-110.

Brotchie JM (2003) CB1 cannabinoid receptor signalling in Parkinson's disease. *Curr Opin Pharmacol*, **3** (1): 54-61.

Burke LJ, Zhang R, Bartkuhn M, Tiwari VK, Tavoosidana G *et al.* (2005) CTCF binding and higher order chromatin structure of the H19 locus are maintained in mitotic chromatin. *EMBO J*, **24** (18): 3291-300.

Burke LJ, Zhang R, Lutz M and Renkawitz R (2002) The thyroid hormone receptor and the insulator protein CTCF: two different factors with overlapping functions. *J Steroid Biochem Mol Biol*, **83** (1-5): 49-57.

Burnett R, Melander C, Puckett JW, Son LS, Wells RD *et al.* (2006) DNA sequence-specific polyamides alleviate transcription inhibition associated with long GAA.TTC repeats in Friedreich's ataxia. *Proc Natl Acad Sci U S A*, **103** (31): 11497-502.

Buyse G, Mertens L, Di Salvo G, Matthijs I, Weidemann F *et al.* (2003) Idebenone treatment in Friedreich's ataxia: neurological, cardiac, and biochemical monitoring. *Neurology*, **60** (10): 1679-81.

Calmels N, Seznec H, Villa P, Reutenauer L, Hibert M *et al.* (2009) Limitations in a frataxin knockdown cell model for Friedreich ataxia in a high-throughput drug screen. *BMC Neurol*, **9**: 46.

Campuzano V, Montermini L, Lutz Y, Cova L, Hindelang C *et al.* (1997) Frataxin is reduced in Friedreich ataxia patients and is associated with mitochondrial membranes. *Hum Mol Genet*, **6** (11): 1771-80.

Campuzano V, Montermini L, Molto MD, Pianese L, Cossee M *et al.* (1996) Friedreich's ataxia: autosomal recessive disease caused by an intronic GAA triplet repeat expansion. *Science*, **271** (5254): 1423-7.

Carey N and La Thangue NB (2006) Histone deacetylase inhibitors: gathering pace. *Curr Opin Pharmacol*, **6** (4): 369-75.

Cavadini P, Gellera C, Patel PI and Isaya G (2000) Human frataxin maintains mitochondrial iron homeostasis in Saccharomyces cerevisiae. *Hum Mol Genet*, **9** (17): 2523-30.

Cavadini P, O'Neill HA, Benada O and Isaya G (2002) Assembly and iron-binding properties of human frataxin, the protein deficient in Friedreich ataxia. *Hum Mol Genet*, **11** (3): 217-27.

Cerami A, Brines M, Ghezzi P, Cerami C and Itri LM (2002) Neuroprotective properties of epoetin alfa. *Nephrol Dial Transplant*, **17 Suppl 1**: 8-12.

Chamberlain S, Shaw J, Rowland A, Wallis J, South S *et al.* (1988) Mapping of mutation causing Friedreich's ataxia to human chromosome 9. *Nature*, **334** (6179): 248-50.

Chantrel-Groussard K, Geromel V, Puccio H, Koenig M, Munnich A *et al.* (2001) Disabled early recruitment of antioxidant defenses in Friedreich's ataxia. *Hum Mol Genet*, **10** (19): 2061-7.

Chen P, Peng C, Luff J, Spring K, Watters D *et al.* (2003) Oxidative stress is responsible for deficient survival and dendritogenesis in purkinje neurons from ataxia-telangiectasia mutated mutant mice. *J Neurosci*, **23** (36): 11453-60.

Chernukhin I, Shamsuddin S, Kang SY, Bergstrom R, Kwon YW *et al.* (2007) CTCF interacts with and recruits the largest subunit of RNA polymerase II to CTCF target sites genome-wide. *Mol Cell Biol*, **27** (5): 1631-48.

Cho DH and Tapscott SJ (2007) Myotonic dystrophy: emerging mechanisms for DM1 and DM2. *Biochim Biophys Acta*, **1772** (2): 195-204.

Cho DH, Thienes CP, Mahoney SE, Analau E, Filippova GN *et al.* (2005) Antisense transcription and heterochromatin at the DM1 CTG repeats are constrained by CTCF. *Mol Cell*, **20** (3): 483-9.

Chou CJ, Herman D and Gottesfeld JM (2008) Pimelic diphenylamide 106 is a slow, tight-binding inhibitor of class I histone deacetylases. *J Biol Chem*, **283** (51): 35402-9.

Clark RM, De Biase I, Malykhina AP, Al-Mahdawi S, Pook M *et al.* (2006) The GAA triplet-repeat is unstable in the context of the human *FXN* locus and displays age-dependent expansions in cerebellum and DRG in a transgenic mouse model. *Hum Genet*: (in Press).

Consroe P (1998) Brain cannabinoid systems as targets for the therapy of neurological disorders. *Neurobiol Dis*, **5** (6 Pt B): 534-51.

Consroe P, Laguna J, Allender J, Snider S, Stern L *et al.* (1991) Controlled clinical trial of cannabidiol in Huntington's disease. *Pharmacol Biochem Behav*, **40** (3): 701-8.

Coppola G, Choi SH, Santos MM, Miranda CJ, Tentler D *et al.* (2006) Gene expression profiling in frataxin deficient mice: microarray evidence for significant expression changes without detectable neurodegeneration. *Neurobiol Dis*, **22** (2): 302-11.

Corsi B, Cozzi A, Arosio P, Drysdale J, Santambrogio P *et al.* (2002) Human mitochondrial ferritin expressed in HeLa cells incorporates iron and affects cellular iron metabolism. *J Biol Chem*, **277** (25): 22430-7.

Cossee M, Puccio H, Gansmuller A, Koutnikova H, Dierich A *et al.* (2000) Inactivation of the Friedreich ataxia mouse gene leads to early embryonic lethality without iron accumulation. *Hum Mol Genet*, **9** (8): 1219-26.

Cossee M, Schmitt M, Campuzano V, Reutenauer L, Moutou C *et al.* (1997) Evolution of the Friedreich's ataxia trinucleotide repeat expansion: founder effect and premutations. *Proc Natl Acad Sci U S A*, **94** (14): 7452-7.

Costa B, Colleoni M, Conti S, Parolaro D, Franke C *et al.* (2004) Oral anti-inflammatory activity of cannabidiol, a non-psychoactive constituent of cannabis, in acute carrageenan-induced inflammation in the rat paw. *Naunyn Schmiedebergs Arch Pharmacol*, **369** (3): 294-9.

Cunha JM, Carlini EA, Pereira AE, Ramos OL, Pimentel C *et al.* (1980) Chronic administration of cannabidiol to healthy volunteers and epileptic patients. *Pharmacology*, **21** (3): 175-85.

Damiani E, Kalinska B, Canapa A, Canestrari S, Wozniak M *et al.* (2000) The effects of nitroxide radicals on oxidative DNA damage. *Free Radic Biol Med*, **28** (8): 1257-65.

De Biase I, Rasmussen A, Endres D, Al-Mahdawi S, Monticelli A *et al.* (2007a) Progressive GAA expansions in dorsal root ganglia of Friedreich's ataxia patients. *Ann Neurol*, **61** (1): 55-60.

De Biase I, Rasmussen A, Monticelli A, Al-Mahdawi S, Pook M *et al.* (2007b) Somatic instability of the expanded GAA triplet-repeat sequence in Friedreich ataxia progresses throughout life. *Genomics*, **90** (1): 1-5.

de Francisco AL, Fernandez Fresnedo G, Rodrigo E, Pinera C, Heras M *et al.* (2002) Past, present and future of erythropoietin use in the elderly. *Int Urol Nephrol*, **33** (1): 187-93.

De Michele G, Cavalcanti F, Criscuolo C, Pianese L, Monticelli A *et al.* (1998) Parental gender, age at birth and expansion length influence GAA repeat intergenerational instability in the

X25 gene: pedigree studies and analysis of sperm from patients with Friedreich's ataxia. *Hum Mol Genet*, **7** (12): 1901-6.

de Wind N, Dekker M, Berns A, Radman M and te Riele H (1995) Inactivation of the mouse Msh2 gene results in mismatch repair deficiency, methylation tolerance, hyperrecombination, and predisposition to cancer. *Cell*, **82** (2): 321-30.

Delatycki MB, Williamson R and Forrest SM (2000) Friedreich ataxia: an overview. *J Med Genet*, **37** (1): 1-8.

Devane WA, Dysarz FA, 3rd, Johnson MR, Melvin LS and Howlett AC (1988) Determination and characterization of a cannabinoid receptor in rat brain. *Mol Pharmacol*, **34** (5): 605-13.

Devane WA, Hanus L, Breuer A, Pertwee RG, Stevenson LA *et al.* (1992) Isolation and structure of a brain constituent that binds to the cannabinoid receptor. *Science*, **258** (5090): 1946-9.

Dewey WL (1986) Cannabinoid pharmacology. *Pharmacol Rev*, **38** (2): 151-78.

Dion V, Lin Y, Hubert L, Jr., Waterland RA and Wilson JH (2008) Dnmt1 deficiency promotes CAG repeat expansion in the mouse germline. *Hum Mol Genet*, **17** (9): 1306-17.

Durr A, Cossee M, Agid Y, Campuzano V, Mignard C *et al.* (1996) Clinical and genetic abnormalities in patients with Friedreich's ataxia. *N Engl J Med*, **335** (16): 1169-75.

El-Remessy AB, Khalil IE, Matragoon S, Abou-Mohamed G, Tsai NJ *et al.* (2003) Neuroprotective effect of (-)Delta9-tetrahydrocannabinol and cannabidiol in N-methyl-D-aspartate-induced retinal neurotoxicity: involvement of peroxynitrite. *Am J Pathol*, **163** (5): 1997-2008.

Elgin SC and Grewal SI (2003) Heterochromatin: silence is golden. *Curr Biol*, **13** (23): R895-8.

Engel N, Thorvaldsen JL and Bartolomei MS (2006) CTCF binding sites promote transcription initiation and prevent DNA methylation on the maternal allele at the imprinted H19/Igf2 locus. *Hum Mol Genet*, **15** (19): 2945-54.

Ensembl (2006) *Human ContigView*. Accessed October, 2006, from <http://www.ensembl.org/>.

Erbayraktar S, Yilmaz O, Gokmen N and Brines M (2003) Erythropoietin is a multifunctional tissue-protective cytokine. *Curr Hematol Rep*, **2** (6): 465-70.

Fedoriw AM, Stein P, Svoboda P, Schultz RM and Bartolomei MS (2004) Transgenic RNAi reveals essential function for CTCF in H19 gene imprinting. *Science*, **303** (5655): 238-40.

Ferrante RJ, Kubilus JK, Lee J, Ryu H, Beesen A *et al.* (2003) Histone deacetylase inhibition by sodium butyrate chemotherapy ameliorates the neurodegenerative phenotype in Huntington's disease mice. *J Neurosci*, **23** (28): 9418-27.

Festenstein R (2006) Breaking the silence in Friedreich's ataxia. *Nat Chem Biol*, **2** (10): 512-3.

Filippova GN (2008) Genetics and epigenetics of the multifunctional protein CTCF. *Curr Top Dev Biol*, **80**: 337-60.

Filippova GN, Cheng MK, Moore JM, Truong JP, Hu YJ *et al.* (2005) Boundaries between chromosomal domains of X inactivation and escape bind CTCF and lack CpG methylation during early development. *Dev Cell*, **8** (1): 31-42.

Filippova GN, Fagerlie S, Klenova EM, Myers C, Dehner Y *et al.* (1996) An exceptionally conserved transcriptional repressor, CTCF, employs different combinations of zinc fingers to bind diverged promoter sequences of avian and mammalian c-myc oncogenes. *Mol Cell Biol*, **16** (6): 2802-13.

Filippova GN, Thienes CP, Penn BH, Cho DH, Hu YJ *et al.* (2001) CTCF-binding sites flank CTG/CAG repeats and form a methylation-sensitive insulator at the DM1 locus. *Nat Genet*, **28** (4): 335-43.

Filla A, De Michele G, Cavalcanti F, Pianese L, Monticelli A *et al.* (1996) The relationship between trinucleotide (GAA) repeat length and clinical features in Friedreich ataxia. *Am J Hum Genet*, **59** (3): 554-60.

Fortune MT, Vassilopoulos C, Coolbaugh MI, Siciliano MJ and Monckton DG (2000) Dramatic, expansion-biased, age-dependent, tissue-specific somatic mosaicism in a transgenic mouse model of triplet repeat instability. *Hum Mol Genet*, **9** (3): 439-45.

Frank-Kamenetskii MD and Mirkin SM (1995) Triplex DNA structures. *Annu Rev Biochem*, **64**: 65-95.

Fride E, Ponde D, Breuer A and Hanus L (2005) Peripheral, but not central effects of cannabidiol derivatives: Mediation by CB(1) and unidentified receptors. *Neuropharmacology*, **48** (8): 1117-29.

Fridovich I (1995) Superoxide radical and superoxide dismutases. *Annu Rev Biochem*, **64**: 97-112.

Gatchel JR and Zoghbi HY (2005) Diseases of unstable repeat expansion: mechanisms and common principles. *Nat Rev Genet*, **6** (10): 743-55.

Gellera C, Pareyson D, Castellotti B, Mazzucchelli F, Zappacosta B *et al.* (1997) Very late onset Friedreich's ataxia without cardiomyopathy is associated with limited GAA expansion in the X25 gene. *Neurology*, **49** (4): 1153-5.

Ghazizadeh M (2003) Cisplatin may induce frataxin expression. *J Nippon Med Sch*, **70** (4): 367-71.

Gomes-Pereira M, Foiry L, Nicole A, Huguet A, Junien C *et al.* (2007) CTG trinucleotide repeat "big jumps": large expansions, small mice. *PLoS Genet*, **3** (4): e52.

Gong JP, Onaivi ES, Ishiguro H, Liu QR, Tagliaferro PA *et al.* (2006) Cannabinoid CB2 receptors: immunohistochemical localization in rat brain. *Brain Res*, **1071** (1): 10-23.

Grabczyk E, Mancuso M and Sammarco MC (2007) A persistent RNA.DNA hybrid formed by transcription of the Friedreich ataxia triplet repeat in live bacteria, and by T7 RNAP in vitro. *Nucleic Acids Res*, **35** (16): 5351-9.

Grabczyk E and Usdin K (2000a) Alleviating transcript insufficiency caused by Friedreich's ataxia triplet repeats. *Nucleic Acids Res*, **28** (24): 4930-7.

Grabczyk E and Usdin K (2000b) The GAA•TTC triplet repeat expanded in Friedreich's ataxia impedes transcription elongation by T7 RNA polymerase in a length and supercoil dependent manner. *Nucleic Acids Res*, **28** (14): 2815-22.

Grant L, Sun J, Xu H, Subramony SH, Chaires JB *et al.* (2006) Rational selection of small molecules that increase transcription through the GAA repeats found in Friedreich's ataxia. *FEBS Lett*, **580** (22): 5399-405.

Greene E, Mahishi L, Entezam A, Kumari D and Usdin K (2007) Repeat-induced epigenetic changes in intron 1 of the frataxin gene and its consequences in Friedreich ataxia. *Nucleic Acids Res*, **35** (10): 3383-90.

Gueven N, Luff J, Peng C, Hosokawa K, Bottle SE *et al.* (2006) Dramatic extension of tumor latency and correction of neurobehavioral phenotype in Atm-mutant mice with a nitroxide antioxidant. *Free Radic Biol Med*, **41** (6): 992-1000.

Guzman M (2003) Cannabinoids: potential anticancer agents. *Nat Rev Cancer*, **3** (10): 745-55.

Hahn SM, Krishna CM and Mitchell JB (1994) New directions for free radical cancer research and medical applications. *Adv Exp Med Biol*, **366**: 241-51.

Hajos N, Ledent C and Freund TF (2001) Novel cannabinoid-sensitive receptor mediates inhibition of glutamatergic synaptic transmission in the hippocampus. *Neuroscience*, **106** (1): 1-4.

Hampson AJ, Grimaldi M, Axelrod J and Wink D (1998) Cannabidiol and (-)Delta9-tetrahydrocannabinol are neuroprotective antioxidants. *Proc Natl Acad Sci U S A*, **95** (14): 8268-73.

Hark AT, Schoenherr CJ, Katz DJ, Ingram RS, Levorse JM *et al.* (2000) CTCF mediates methylation-sensitive enhancer-blocking activity at the H19/Igf2 locus. *Nature*, **405** (6785): 486-9.

Hart PE, Lodi R, Rajagopalan B, Bradley JL, Crilley JG *et al.* (2005) Antioxidant treatment of patients with Friedreich ataxia: four-year follow-up. *Arch Neurol*, **62** (4): 621-6.

Hausse AO, Aggoun Y, Bonnet D, Sidi D, Munnich A *et al.* (2002) Idebenone and reduced cardiac hypertrophy in Friedreich's ataxia. *Heart*, **87** (4): 346-9.

Heidenfelder BL, Makhov AM and Topal MD (2003) Hairpin formation in Friedreich's ataxia triplet repeat expansion. *J Biol Chem*, **278** (4): 2425-31.

Herkenham M, Lynn AB, Johnson MR, Melvin LS, de Costa BR *et al.* (1991) Characterization and localization of cannabinoid receptors in rat brain: a quantitative in vitro autoradiographic study. *J Neurosci*, **11** (2): 563-83.

Herman D, Jenssen K, Burnett R, Soragni E, Perlman SL *et al.* (2006) Histone deacetylase inhibitors reverse gene silencing in Friedreich's ataxia. *Nat Chem Biol*, **2** (10): 551-8.

Hockly E, Richon VM, Woodman B, Smith DL, Zhou X *et al.* (2003) Suberoylanilide hydroxamic acid, a histone deacetylase inhibitor, ameliorates motor deficits in a mouse model of Huntington's disease. *Proc Natl Acad Sci U S A*, **100** (4): 2041-6.

Hollister LE (1974) Structure-activity relationships in man of cannabis constituents, and homologs and metabolites of delta9-tetrahydrocannabinol. *Pharmacology*, **11** (1): 3-11.

Hosokawa K, Chen P, Lavin FM and Bottle ES (2004) The impact of carboxy nitroxide antioxidants on irradiated ataxia telangiectasia cells. *Free Radic Biol Med*, **37** (7): 946-52.

Howlett AC, Barth F, Bonner TI, Cabral G, Casellas P *et al.* (2002) International Union of Pharmacology. XXVII. Classification of cannabinoid receptors. *Pharmacol Rev*, **54** (2): 161-202.

Hu F, Chou CJ and Gottesfeld JM (2009) Design and synthesis of novel hybrid benzamide-peptide histone deacetylase inhibitors. *Bioorg Med Chem Lett*, **19** (14): 3928-31.

Ishiguro H, Yamada K, Sawada H, Nishii K, Ichino N *et al.* (2001) Age-dependent and tissue-specific CAG repeat instability occurs in mouse knock-in for a mutant Huntington's disease gene. *J Neurosci Res*, **65** (4): 289-97.

Iuvone T, Esposito G, Esposito R, Santamaria R, Di Rosa M *et al.* (2004) Neuroprotective effect of cannabidiol, a non-psychoactive component from Cannabis sativa, on beta-amyloid-induced toxicity in PC12 cells. *J Neurochem*, **89** (1): 134-41.

Jauslin ML, Meier T, Smith RA and Murphy MP (2003) Mitochondria-targeted antioxidants protect Friedreich Ataxia fibroblasts from endogenous oxidative stress more effectively than untargeted antioxidants. *Faseb J*, **17** (13): 1972-4.

Jones G, Pertwee RG, Gill EW, Paton WD, Nilsson IM *et al.* (1974) Relative pharmacological potency in mice of optical isomers of delta 1-tetrahydrocannabinol. *Biochem Pharmacol*, **23** (2): 439-46.

Juan-Pico P, Fuentes E, Javier Bermudez-Silva F, Javier Diaz-Molina F, Ripoll C *et al.* (2006) Cannabinoid receptors regulate Ca(2+) signals and insulin secretion in pancreatic beta-cell. *Cell Calcium*, **39** (2): 155-62.

Julien B, Grenard P, Teixeira-Clerc F, Van Nhieu JT, Li L *et al.* (2005) Antifibrogenic role of the cannabinoid receptor CB2 in the liver. *Gastroenterology*, **128** (3): 742-55.

Kanduri C, Pant V, Loukinov D, Pugacheva E, Qi CF *et al.* (2000) Functional association of CTCF with the insulator upstream of the H19 gene is parent of origin-specific and methylation-sensitive. *Curr Biol*, **10** (14): 853-6.

Kang SH, Vieira K and Bungert J (2002) Combining chromatin immunoprecipitation and DNA footprinting: a novel method to analyze protein-DNA interactions in vivo. *Nucleic Acids Res*, **30** (10): e44.

Kaytor MD, Burright EN, Duvick LA, Zoghbi HY and Orr HT (1997) Increased trinucleotide repeat instability with advanced maternal age. *Hum Mol Genet*, **6** (12): 2135-9.

Kennedy L and Shelbourne PF (2000) Dramatic mutation instability in HD mouse striatum: does polyglutamine load contribute to cell-specific vulnerability in Huntington's disease? *Hum Mol Genet*, **9** (17): 2539-44.

Khaspekov LG, Brenz Verca MS, Frumkina LE, Hermann H, Marsicano G *et al.* (2004) Involvement of brain-derived neurotrophic factor in cannabinoid receptor-dependent protection against excitotoxicity. *Eur J Neurosci*, **19** (7): 1691-8.

Kim TH, Abdullaev ZK, Smith AD, Ching KA, Loukinov DI *et al.* (2007) Analysis of the vertebrate insulator protein CTCF-binding sites in the human genome. *Cell*, **128** (6): 1231-45.

Klenova E (2007) *Search for CTCF/DNA binding sites*. Molecular Medicine Group, Department of Biological Sciences, University of Essex. Accessed 27 March, 2008, from <http://www.essex.ac.uk/bs/molonc/spa.htm>.

Klenova EM, Morse HC, 3rd, Ohlsson R and Lobanenkov VV (2002) The novel BORIS + CTCF gene family is uniquely involved in the epigenetics of normal biology and cancer. *Semin Cancer Biol*, **12** (5): 399-414.

Klenova EM, Nicolas RH, Paterson HF, Carne AF, Heath CM *et al.* (1993) CTCF, a conserved nuclear factor required for optimal transcriptional activity of the chicken c-myc gene, is an 11-Zn-finger protein differentially expressed in multiple forms. *Mol Cell Biol*, **13** (12): 7612-24.

Kosutic J and Zamurovic D (2005) High-dose beta-blocker hypertrophic cardiomyopathy therapy in a patient with Friedreich ataxia. *Pediatr Cardiol*, **26** (5): 727-30.

Koutnikova H, Campuzano V, Foury F, Dolle P, Cazzalini O *et al.* (1997) Studies of human, mouse and yeast homologues indicate a mitochondrial function for frataxin. *Nat Genet*, **16** (4): 345-51.

Kouzarides T (2007) Chromatin modifications and their function. *Cell*, **128** (4): 693-705.

Kovtun IV, Liu Y, Bjoras M, Klungland A, Wilson SH *et al.* (2007) OGG1 initiates age-dependent CAG trinucleotide expansion in somatic cells. *Nature*, **447** (7143): 447-52.

Kuo PH, Carlson KR, Christensen I, Girardi M and Heald PW (2008) FDG-PET/CT for the evaluation of response to therapy of cutaneous T-cell lymphoma to vorinostat (suberoylanilide hydroxamic acid, SAHA) in a phase II trial. *Mol Imaging Biol*, **10** (6): 306-14.

Ladd PD, Smith LE, Rabaia NA, Moore JM, Georges SA *et al.* (2007) An antisense transcript spanning the CGG repeat region of FMR1 is upregulated in premutation carriers but silenced in full mutation individuals. *Hum Mol Genet*, **16** (24): 3174-87.

Lastres-Becker I, De Miguel R and Fernandez-Ruiz JJ (2003) The endocannabinoid system and Huntington's disease. *Curr Drug Targets CNS Neurol Disord*, **2** (5): 335-47.

Lavin MF (2008) Ataxia-telangiectasia: from a rare disorder to a paradigm for cell signalling and cancer. *Nat Rev Mol Cell Biol*, **9** (10): 759-69.

Lawrence DK and Gill EW (1975) The effects of delta1-tetrahydrocannabinol and other cannabinoids on spin-labeled liposomes and their relationship to mechanisms of general anesthesia. *Mol Pharmacol*, **11** (5): 595-602.

Lee KK and Workman JL (2007) Histone acetyltransferase complexes: one size doesn't fit all. *Nat Rev Mol Cell Biol*, **8** (4): 284-95.

LeProust EM, Pearson CE, Sinden RR and Gao X (2000) Unexpected formation of parallel duplex in GAA and TTC trinucleotide repeats of Friedreich's ataxia. *J Mol Biol*, **302** (5): 1063-80.

Lewis A and Murrell A (2004) Genomic imprinting: CTCF protects the boundaries. *Curr Biol*, **14** (7): R284-6.

Lhatoo SD, Rao DG, Kane NM and Ormerod IE (2001) Very late onset Friedreich's presenting as spastic tetraparesis without ataxia or neuropathy. *Neurology*, **56** (12): 1776-7.

Li K, Besse EK, Ha D, Kovtunovych G and Rouault TA (2008) Iron-dependent regulation of frataxin expression: implications for treatment of Friedreich ataxia. *Hum Mol Genet*, **17** (15): 2265-73.

Liao MJ, Yin C, Barlow C, Wynshaw-Boris A and van Dyke T (1999) Atm is dispensable for p53 apoptosis and tumor suppression triggered by cell cycle dysfunction. *Mol Cell Biol*, **19** (4): 3095-102.

Libby RT, Hagerman KA, Pineda VV, Lau R, Cho DH *et al.* (2008) CTCF cis-regulates trinucleotide repeat instability in an epigenetic manner: a novel basis for mutational hot spot determination. *PLoS Genet*, **4** (11): e1000257.

Libby RT, Monckton DG, Fu YH, Martinez RA, McAbney JP *et al.* (2003) Genomic context drives SCA7 CAG repeat instability, while expressed SCA7 cDNAs are intergenerationally and somatically stable in transgenic mice. *Hum Mol Genet*, **12** (1): 41-50.

Lloret A, Dragileva E, Teed A, Espinola J, Fossale E *et al.* (2006) Genetic background modifies nuclear mutant huntingtin accumulation and HD CAG repeat instability in Huntington's disease knock-in mice. *Hum Mol Genet*, **15** (12): 2015-24.

Lobanenkov VV, Nicolas RH, Adler VV, Paterson H, Klenova EM *et al.* (1990) A novel sequence-specific DNA binding protein which interacts with three regularly spaced direct repeats of the CCCTC-motif in the 5'-flanking sequence of the chicken c-myc gene. *Oncogene*, **5** (12): 1743-53.

Lodi R, Hart PE, Rajagopalan B, Taylor DJ, Crilley JG *et al.* (2001a) Antioxidant treatment improves in vivo cardiac and skeletal muscle bioenergetics in patients with Friedreich's ataxia. *Ann Neurol*, **49** (5): 590-6.

Lodi R, Rajagopalan B, Blamire AM, Cooper JM, Davies CH *et al.* (2001b) Cardiac energetics are abnormal in Friedreich ataxia patients in the absence of cardiac dysfunction and hypertrophy: an in vivo 31P magnetic resonance spectroscopy study. *Cardiovasc Res*, **52** (1): 111-9.

Lorenzetti D, Watase K, Xu B, Matzuk MM, Orr HT *et al.* (2000) Repeat instability and motor incoordination in mice with a targeted expanded CAG repeat in the Sca1 locus. *Hum Mol Genet*, **9** (5): 779-85.

Lutz B (2002) Molecular biology of cannabinoid receptors. *Prostaglandins Leukot Essent Fatty Acids*, **66** (2-3): 123-42.

Mangiarini L, Sathasivam K, Mahal A, Mott R, Seller M *et al.* (1997) Instability of highly expanded CAG repeats in mice transgenic for the Huntington's disease mutation. *Nat Genet*, **15** (2): 197-200.

Marian AJ and Roberts R (1995) Molecular genetics of hypertrophic cardiomyopathy. *Annu Rev Med*, **46**: 213-22.

Mariotti C, Solari A, Torta D, Marano L, Fiorentini C *et al.* (2003) Idebenone treatment in Friedreich patients: one-year-long randomized placebo-controlled trial. *Neurology*, **60** (10): 1676-9.

Marsicano G, Goodenough S, Monory K, Hermann H, Eder M *et al.* (2003) CB1 cannabinoid receptors and on-demand defense against excitotoxicity. *Science*, **302** (5642): 84-8.

Marsicano G, Moosmann B, Hermann H, Lutz B and Behl C (2002) Neuroprotective properties of cannabinoids against oxidative stress: role of the cannabinoid receptor CB1. *J Neurochem*, **80** (3): 448-56.

Martens JH, O'Sullivan RJ, Braunschweig U, Opravil S, Radolf M *et al.* (2005) The profile of repeat-associated histone lysine methylation states in the mouse epigenome. *EMBO J*, **24** (4): 800-12.

Matsuda LA, Lolait SJ, Brownstein MJ, Young AC and Bonner TI (1990) Structure of a cannabinoid receptor and functional expression of the cloned cDNA. *Nature*, **346** (6284): 561-4.

McDaniel DO, Keats B, Vedanarayanan VV and Subramony SH (2001) Sequence variation in GAA repeat expansions may cause differential phenotype display in Friedreich's ataxia. *Mov Disord*, **16** (6): 1153-8.

Mechoulam R (1986) The pharmacohistory of cannabis sativa. IN Mechoulam, R. (Ed.) *Cannabinoids as therapeutic agents.* Boca Raton, FL., CRC Press.

Mechoulam R, Ben-Shabat S, Hanus L, Ligumsky M, Kaminski NE *et al.* (1995) Identification of an endogenous 2-monoglyceride, present in canine gut, that binds to cannabinoid receptors. *Biochem Pharmacol*, **50** (1): 83-90.

Mechoulam R and Gaoni Y (1967) The absolute configuration of delta-1-tetrahydrocannabinol, the major active constituent of hashish. *Tetrahedron Lett*, **12**: 1109-11.

Mechoulam R, Parker LA and Gallily R (2002) Cannabidiol: an overview of some pharmacological aspects. *J Clin Pharmacol*, **42** (11 Suppl): 11S-19S.

Minucci S and Pelicci PG (2006) Histone deacetylase inhibitors and the promise of epigenetic (and more) treatments for cancer. *Nat Rev Cancer*, **6** (1): 38-51.

Miranda CJ, Santos MM, Ohshima K, Smith J, Li L *et al.* (2002) Frataxin knockin mouse. *FEBS Lett*, **512** (1-3): 291-7.

Molife LR, Attard G, Fong PC, Karavasilis V, Reid AH *et al.* (2009) Phase II, two-stage, single-arm trial of the histone deacetylase inhibitor (HDACi) romidepsin in metastatic castration-resistant prostate cancer (CRPC). *Ann Oncol*, **21** (1): 109-13.

Monckton DG, Coolbaugh MI, Ashizawa KT, Siciliano MJ and Caskey CT (1997) Hypermutable myotonic dystrophy CTG repeats in transgenic mice. *Nat Genet*, **15** (2): 193-6.

Monros E, Molto MD, Martinez F, Canizares J, Blanca J *et al.* (1997) Phenotype correlation and intergenerational dynamics of the Friedreich ataxia GAA trinucleotide repeat. *Am J Hum Genet*, **61** (1): 101-10.

Montermini L, Andermann E, Labuda M, Richter A, Pandolfo M *et al.* (1997a) The Friedreich ataxia GAA triplet repeat: premutation and normal alleles. *Hum Mol Genet*, **6** (8): 1261-6.

Montermini L, Kish SJ, Jiralerspong S, Lamarche JB and Pandolfo M (1997b) Somatic mosaicism for Friedreich's ataxia GAA triplet repeat expansions in the central nervous system. *Neurology*, **49** (2): 606-10.

Montermini L, Richter A, Morgan K, Justice CM, Julien D *et al.* (1997c) Phenotypic variability in Friedreich ataxia: role of the associated GAA triplet repeat expansion. *Ann Neurol*, **41** (5): 675-82.

Munro S, Thomas KL and Abu-Shaar M (1993) Molecular characterization of a peripheral receptor for cannabinoids. *Nature*, **365** (6441): 61-5.

Musco G, Stier G, Kolmerer B, Adinolfi S, Martin S *et al.* (2000) Towards a structural understanding of Friedreich's ataxia: the solution structure of frataxin. *Structure*, **8** (7): 695-707.

Nadler V, Mechoulam R and Sokolovsky M (1993) Blockade of 45Ca2+ influx through the N-methyl-D-aspartate receptor ion channel by the non-psychoactive cannabinoid HU-211. *Brain Res*, **622** (1-2): 79-85.

NCBI (2009) *Entrez Gene*. Accessed September, 2009, from <http://www.ncbi.nlm.nih.gov/sites/entrez?db=gene>.

Ofek O, Karsak M, Leclerc N, Fogel M, Frenkel B *et al.* (2006) Peripheral cannabinoid receptor, CB2, regulates bone mass. *Proc Natl Acad Sci U S A*, **103** (3): 696-701.

Ohlsson R, Renkawitz R and Lobanenkov V (2001) CTCF is a uniquely versatile transcription regulator linked to epigenetics and disease. *Trends Genet*, **17** (9): 520-7.

Ohshima K, Montermini L, Wells RD and Pandolfo M (1998) Inhibitory effects of expanded GAA.TTC triplet repeats from intron I of the Friedreich ataxia gene on transcription and replication in vivo. *J Biol Chem*, **273** (23): 14588-95.

Ohshima K, Sakamoto N, Labuda M, Poirier J, Moseley ML *et al.* (1999) A nonpathogenic GAAGGA repeat in the Friedreich gene: implications for pathogenesis. *Neurology*, **53** (8): 1854-7.

OMIM (2006) *Online Mendelian Inheritance in Man*. Accessed October, 2006, from <http://www.ncbi.nlm.nih.gov/entrez/dispomim.cgi?id=229300>.

Ostman-Smith I, Wettrell G and Riesenfeld T (1999) A cohort study of childhood hypertrophic cardiomyopathy: improved survival following high-dose beta-adrenoceptor antagonist treatment. *J Am Coll Cardiol*, **34** (6): 1813-22.

Ota H, Tokunaga E, Chang K, Hikasa M, Iijima K *et al.* (2006) Sirt1 inhibitor, Sirtinol, induces senescence-like growth arrest with attenuated Ras-MAPK signaling in human cancer cells. *Oncogene*, **25** (2): 176-85.

Otten AD and Tapscott SJ (1995) Triplet repeat expansion in myotonic dystrophy alters the adjacent chromatin structure. *Proc Natl Acad Sci U S A*, **92** (12): 5465-9.

Pacher P, Batkai S and Kunos G (2006) The endocannabinoid system as an emerging target of pharmacotherapy. *Pharmacol Rev*, **58** (3): 389-462.

Pandolfo M (1999) Molecular pathogenesis of Friedreich ataxia. *Arch Neurol*, **56** (10): 1201-8.

Pandolfo M (2002a) Iron metabolism and mitochondrial abnormalities in Friedreich ataxia. *Blood Cells Mol Dis*, **29** (3): 536-47; discussion 548-52.

Pandolfo M (2002b) The molecular basis of Friedreich ataxia. *Adv Exp Med Biol*, **516**: 99-118.

Pant V, Kurukuti S, Pugacheva E, Shamsuddin S, Mariano P *et al.* (2004) Mutation of a single CTCF target site within the H19 imprinting control region leads to loss of Igf2 imprinting and complex patterns of de novo methylation upon maternal inheritance. *Mol Cell Biol*, **24** (8): 3497-504.

Peier AM and Nelson DL (2002) Instability of a premutation-sized CGG repeat in FMR1 YAC transgenic mice. *Genomics*, **80** (4): 423-32.

Pertwee RG (2001) Cannabinoid receptors and pain. *Prog Neurobiol*, **63** (5): 569-611.

Pertwee RG (2002) Cannabinoids and multiple sclerosis. *Pharmacol Ther*, **95** (2): 165-74.

Pertwee RG, Stevenson LA, Elrick DB, Mechoulam R and Corbett AD (1992) Inhibitory effects of certain enantiomeric cannabinoids in the mouse vas deferens and the myenteric plexus preparation of guinea-pig small intestine. *Br J Pharmacol*, **105** (4): 980-4.

Pianese L, Cavalcanti F, De Michele G, Filla A, Campanella G *et al.* (1997) The effect of parental gender on the GAA dynamic mutation in the FRDA gene. *Am J Hum Genet*, **60** (2): 460-3.

Pook MA, Al-Mahdawi S, Carroll CJ, Cossee M, Puccio H *et al.* (2001) Rescue of the Friedreich's ataxia knockout mouse by human YAC transgenesis. *Neurogenetics*, **3** (4): 185-93.

Puccio H, Simon D, Cossee M, Criqui-Filipe P, Tiziano F *et al.* (2001) Mouse models for Friedreich ataxia exhibit cardiomyopathy, sensory nerve defect and Fe-S enzyme deficiency followed by intramitochondrial iron deposits. *Nat Genet*, **27** (2): 181-6.

Rada-Iglesias A, Enroth S, Ameur A, Koch CM, Clelland GK *et al.* (2007) Butyrate mediates decrease of histone acetylation centered on transcription start sites and down-regulation of associated genes. *Genome Res*, **17** (6): 708-19.

Radisky DC, Babcock MC and Kaplan J (1999) The yeast frataxin homologue mediates mitochondrial iron efflux. Evidence for a mitochondrial iron cycle. *J Biol Chem*, **274** (8): 4497-9.

Rai M, Soragni E, Jenssen K, Burnett R, Herman D *et al.* (2008) HDAC inhibitors correct frataxin deficiency in a Friedreich ataxia mouse model. *PLoS ONE*, **3** (4): e1958.

Raman C, McAllister SD, Rizvi G, Patel SG, Moore DH *et al.* (2004) Amyotrophic lateral sclerosis: delayed disease progression in mice by treatment with a cannabinoid. *Amyotroph Lateral Scler Other Motor Neuron Disord*, **5** (1): 33-9.

Ramirez BG, Blazquez C, Gomez del Pulgar T, Guzman M and de Ceballos ML (2005) Prevention of Alzheimer's disease pathology by cannabinoids: neuroprotection mediated by blockade of microglial activation. *J Neurosci*, **25** (8): 1904-13.

Recillas-Targa F, De La Rosa-Velazquez IA, Soto-Reyes E and Benitez-Bribiesca L (2006) Epigenetic boundaries of tumour suppressor gene promoters: the CTCF connection and its role in carcinogenesis. *J Cell Mol Med*, **10** (3): 554-68.

Recillas-Targa F, Pikaart MJ, Burgess-Beusse B, Bell AC, Litt MD *et al.* (2002) Position-effect protection and enhancer blocking by the chicken beta-globin insulator are separable activities. *Proc Natl Acad Sci U S A*, **99** (10): 6883-8.

Reid G, Metivier R, Lin CY, Denger S, Ibberson D *et al.* (2005) Multiple mechanisms induce transcriptional silencing of a subset of genes, including oestrogen receptor alpha, in response to deacetylase inhibition by valproic acid and trichostatin A. *Oncogene*, **24** (31): 4894-907.

Reik W (2007) Stability and flexibility of epigenetic gene regulation in mammalian development. *Nature*, **447** (7143): 425-32.

Richardson DR (2003) Friedreich's ataxia: iron chelators that target the mitochondrion as a therapeutic strategy? *Expert Opin Investig Drugs*, **12** (2): 235-45.

Richardson DR, Mouralian C, Ponka P and Becker E (2001) Development of potential iron chelators for the treatment of Friedreich's ataxia: ligands that mobilize mitochondrial iron. *Biochim Biophys Acta*, **1536** (2-3): 133-40.

Rinaldi-Carmona M, Barth F, Heaulme M, Shire D, Calandra B *et al.* (1994) SR141716A, a potent and selective antagonist of the brain cannabinoid receptor. *FEBS Lett*, **350** (2-3): 240-4.

Rinaldi-Carmona M, Barth F, Millan J, Derocq JM, Casellas P *et al.* (1998) SR 144528, the first potent and selective antagonist of the CB2 cannabinoid receptor. *J Pharmacol Exp Ther*, **284** (2): 644-50.

Ristow M, Mulder H, Pomplun D, Schulz TJ, Muller-Schmehl K *et al.* (2003) Frataxin deficiency in pancreatic islets causes diabetes due to loss of beta cell mass. *J Clin Invest*, **112** (4): 527-34.

Rothe N (2008) Gene regulation and epigenotype in Friedreich's ataxia. PhD thesis, Imperial College London.

Rozen S and Skaletsky HJ (2000) Primer3 on the WWW for general users and for biologist programmers. In: Krawetz S, Misener S (eds) *Bioinformatics Methods and Protocols: Methods in Molecular Biology.* Humana Press, Totowa, NJ, 365-386.

Russo E and Guy GW (2006) A tale of two cannabinoids: the therapeutic rationale for combining tetrahydrocannabinol and cannabidiol. *Med Hypotheses*, **66** (2): 234-46.

Rustin P, von Kleist-Retzow JC, Chantrel-Groussard K, Sidi D, Munnich A *et al.* (1999) Effect of idebenone on cardiomyopathy in Friedreich's ataxia: a preliminary study. *Lancet*, **354** (9177): 477-9.

Sakamoto N, Chastain PD, Parniewski P, Ohshima K, Pandolfo M *et al.* (1999) Sticky DNA: self-association properties of long GAA.TTC repeats in R.R.Y triplex structures from Friedreich's ataxia. *Mol Cell*, **3** (4): 465-75.

Sambrook J, Fritsch EF and Maniatis T (1989) *Molecular cloning: a laboratory manual*, New York, Cold Spring Harbor Laboratory.

Sarsero JP, Li L, Holloway TP, Voullaire L, Gazeas S *et al.* (2004) Human BAC-mediated rescue of the Friedreich ataxia knockout mutation in transgenic mice. *Mamm Genome*, **15** (5): 370-82.

Sarsero JP, Li L, Wardan H, Sitte K, Williamson R *et al.* (2003) Upregulation of expression from the FRDA genomic locus for the therapy of Friedreich ataxia. *J Gene Med*, **5** (1): 72-81.

Sato T, Oyake M, Nakamura K, Nakao K, Fukusima Y *et al.* (1999) Transgenic mice harboring a full-length human mutant DRPLA gene exhibit age-dependent intergenerational and somatic instabilities of CAG repeats comparable with those in DRPLA patients. *Hum Mol Genet*, **8** (1): 99-106.

Saveliev A, Everett C, Sharpe T, Webster Z and Festenstein R (2003) DNA triplet repeats mediate heterochromatin-protein-1-sensitive variegated gene silencing. *Nature*, **422** (6934): 909-13.

Schmucker S, Argentini M, Carelle-Calmels N, Martelli A and Puccio H (2008) The in vivo mitochondrial two-step maturation of human frataxin. *Hum Mol Genet*, **17** (22): 3521-31.

Schoenherr CJ, Levorse JM and Tilghman SM (2003) CTCF maintains differential methylation at the Igf2/H19 locus. *Nat Genet*, **33** (1): 66-9.

Schulz JB, Boesch S, Burk K, Durr A, Giunti P *et al.* (2009) Diagnosis and treatment of Friedreich ataxia: a European perspective. *Nat Rev Neurol*, **5** (4): 222-34.

Schulz JB, Dehmer T, Schols L, Mende H, Hardt C *et al.* (2000) Oxidative stress in patients with Friedreich ataxia. *Neurology*, **55** (11): 1719-21.

Seznec H, Lia-Baldini AS, Duros C, Fouquet C, Lacroix C *et al.* (2000) Transgenic mice carrying large human genomic sequences with expanded CTG repeat mimic closely the DM CTG repeat intergenerational and somatic instability. *Hum Mol Genet*, **9** (8): 1185-94.

Seznec H, Simon D, Bouton C, Reutenauer L, Hertzog A *et al.* (2005) Friedreich ataxia: the oxidative stress paradox. *Hum Mol Genet*, **14** (4): 463-74.

Sharma R, Bhatti S, Gomez M, Clark RM, Murray C *et al.* (2002) The GAA triplet-repeat sequence in Friedreich ataxia shows a high level of somatic instability in vivo, with a significant predilection for large contractions. *Hum Mol Genet*, **11** (18): 2175-87.

Shelbourne PF, Killeen N, Hevner RF, Johnston HM, Tecott L *et al.* (1999) A Huntington's disease CAG expansion at the murine Hdh locus is unstable and associated with behavioural abnormalities in mice. *Hum Mol Genet*, **8** (5): 763-74.

Simon D, Seznec H, Gansmuller A, Carelle N, Weber P *et al.* (2004) Friedreich ataxia mouse models with progressive cerebellar and sensory ataxia reveal autophagic neurodegeneration in dorsal root ganglia. *J Neurosci*, **24** (8): 1987-95.

Smith KJ, Bleyer AJ, Little WC and Sane DC (2003) The cardiovascular effects of erythropoietin. *Cardiovasc Res*, **59** (3): 538-48.

Soragni E, Herman D, Dent SY, Gottesfeld JM, Wells RD *et al.* (2008) Long intronic GAA*TTC repeats induce epigenetic changes and reporter gene silencing in a molecular model of Friedreich ataxia. *Nucleic Acids Res*, **36** (19): 6056-65.

Sorbi S, Forleo P, Cellini E, Piacentini S, Serio A *et al.* (2000) Atypical Friedreich ataxia with a very late onset and an unusual limited GAA repeat. *Arch Neurol*, **57** (9): 1380-2.

Stanley JL, Lincoln RJ, Brown TA, McDonald LM, Dawson GR *et al.* (2005) The mouse beam walking assay offers improved sensitivity over the mouse rotarod in determining motor coordination deficits induced by benzodiazepines. *J Psychopharmacol*, **19** (3): 221-7.

Sturm B, Bistrich U, Schranzhofer M, Sarsero JP, Rauen U *et al.* (2005a) Friedreich's ataxia, no changes in mitochondrial labile iron in human lymphoblasts and fibroblasts: a decrease in antioxidative capacity? *J Biol Chem*, **280** (8): 6701-8.

Sturm B, Stupphann D, Kaun C, Boesch S, Schranzhofer M *et al.* (2005b) Recombinant human erythropoietin: effects on frataxin expression in vitro. *Eur J Clin Invest*, **35** (11): 711-7.

Sugiura T, Kondo S, Sukagawa A, Nakane S, Shinoda A *et al.* (1995) 2-Arachidonoylglycerol: a possible endogenous cannabinoid receptor ligand in brain. *Biochem Biophys Res Commun*, **215** (1): 89-97.

Talbert PB and Henikoff S (2006) Spreading of silent chromatin: inaction at a distance. *Nat Rev Genet*, **7** (10): 793-803.

Thornton-Jones ZD, Vickers SP and Clifton PG (2005) The cannabinoid CB1 receptor antagonist SR141716A reduces appetitive and consummatory responses for food. *Psychopharmacology (Berl)*, **179** (2): 452-60.

Toft NJ, Winton DJ, Kelly J, Howard LA, Dekker M *et al.* (1999) Msh2 status modulates both apoptosis and mutation frequency in the murine small intestine. *Proc Natl Acad Sci U S A*, **96** (7): 3911-5.

Turano M, Tammaro A, De Biase I, Lo Casale MS, Ruggiero G *et al.* (2003) 3-Nitropropionic acid increases frataxin expression in human lymphoblasts and in transgenic rat PC12 cells. *Neurosci Lett*, **350** (3): 184-6.

van den Broek WJ, Nelen MR, Wansink DG, Coerwinkel MM, te Riele H *et al.* (2002) Somatic expansion behaviour of the (CTG)n repeat in myotonic dystrophy knock-in mice is differentially affected by Msh3 and Msh6 mismatch-repair proteins. *Hum Mol Genet*, **11** (2): 191-8.

Van Sickle MD, Duncan M, Kingsley PJ, Mouihate A, Urbani P *et al.* (2005) Identification and functional characterization of brainstem cannabinoid CB2 receptors. *Science*, **310** (5746): 329-32.

Voncken M, Ioannou P and Delatycki MB (2004) Friedreich ataxia-update on pathogenesis and possible therapies. *Neurogenetics*, **5** (1): 1-8.

Vostrov AA and Quitschke WW (1997) The zinc finger protein CTCF binds to the APBbeta domain of the amyloid beta-protein precursor promoter. Evidence for a role in transcriptional activation. *J Biol Chem*, **272** (52): 33353-9.

Wang Z and Storm DR (2006) Extraction of DNA from mouse tails. *Biotechniques*, **41** (4): 410, 412.

Watase K, Venken KJ, Sun Y, Orr HT and Zoghbi HY (2003) Regional differences of somatic CAG repeat instability do not account for selective neuronal vulnerability in a knock-in mouse model of SCA1. *Hum Mol Genet*, **12** (21): 2789-95.

Watase K and Zoghbi HY (2003) Modelling brain diseases in mice: the challenges of design and analysis. *Nat Rev Genet*, **4** (4): 296-307.

Wells RD (2008) DNA triplexes and Friedreich ataxia. *FASEB J*, **22** (6): 1625-34.

West AG, Gaszner M and Felsenfeld G (2002) Insulators: many functions, many mechanisms. *Genes Dev*, **16** (3): 271-88.

Wheeler VC, Auerbach W, White JK, Srinidhi J, Auerbach A *et al.* (1999) Length-dependent gametic CAG repeat instability in the Huntington's disease knock-in mouse. *Hum Mol Genet*, **8** (1): 115-22.

Yokota T, Igarashi K, Uchihara T, Jishage K, Tomita H *et al.* (2001) Delayed-onset ataxia in mice lacking alpha -tocopherol transfer protein: model for neuronal degeneration caused by chronic oxidative stress. *Proc Natl Acad Sci U S A*, **98** (26): 15185-90.

Yoo CB, Cheng JC and Jones PA (2004) Zebularine: a new drug for epigenetic therapy. *Biochem Soc Trans*, **32** (Pt 6): 910-2.

Youdim MB, Fridkin M and Zheng H (2004) Novel bifunctional drugs targeting monoamine oxidase inhibition and iron chelation as an approach to neuroprotection in Parkinson's disease and other neurodegenerative diseases. *J Neural Transm*, **111** (10-11): 1455-71.

Zaibak F, Kozlovski J, Vadolas J, Sarsero JP, Williamson R *et al.* (2009) Integration of functional bacterial artificial chromosomes into human cord blood-derived multipotent stem cells. *Gene Ther*, **16** (3): 404-14.

Appendix A – Additional data from cannabinoid drug studies

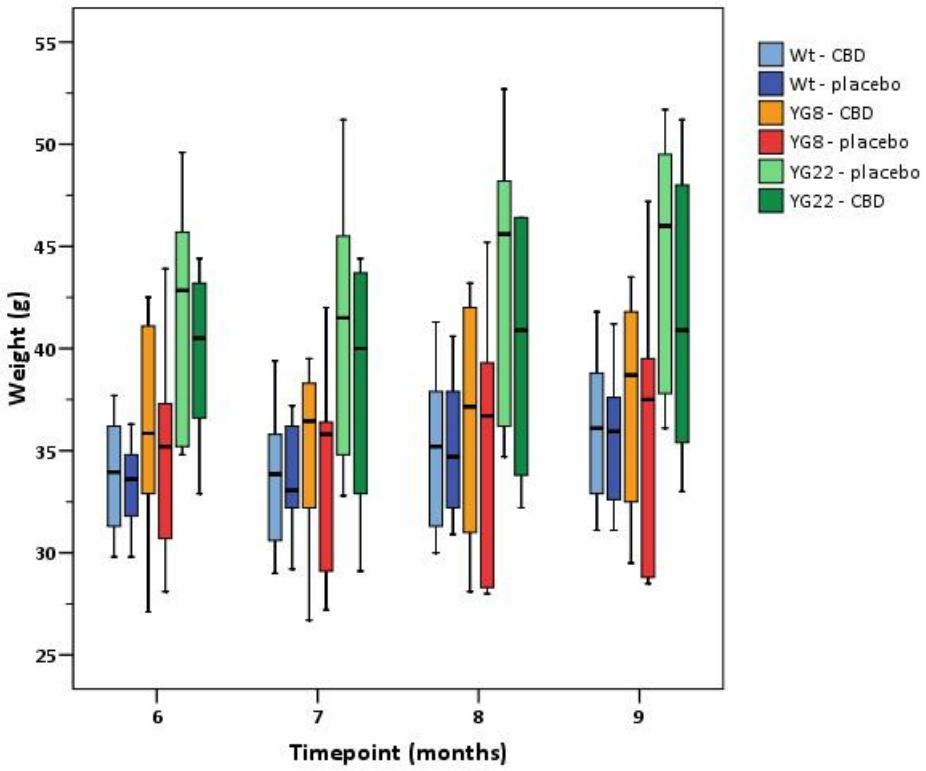

Figure A.1 – Boxplot of absolute weight during the 10mg/kg CBD study.

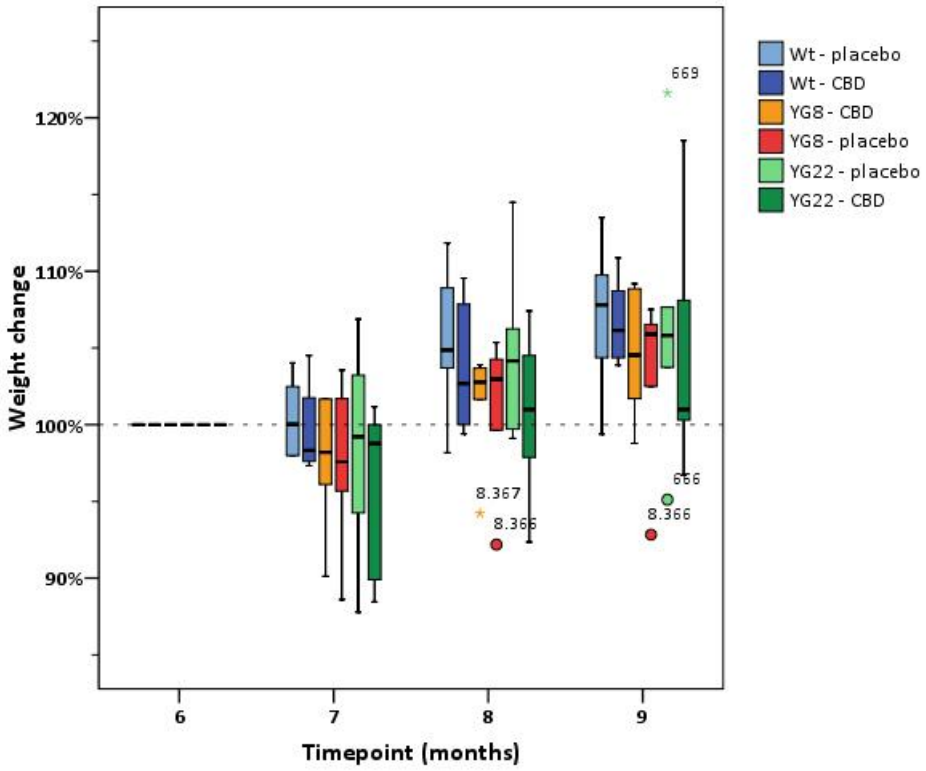

Figure A.2 – Boxplot of weight gain/loss during the 10mg/kg CBD study.

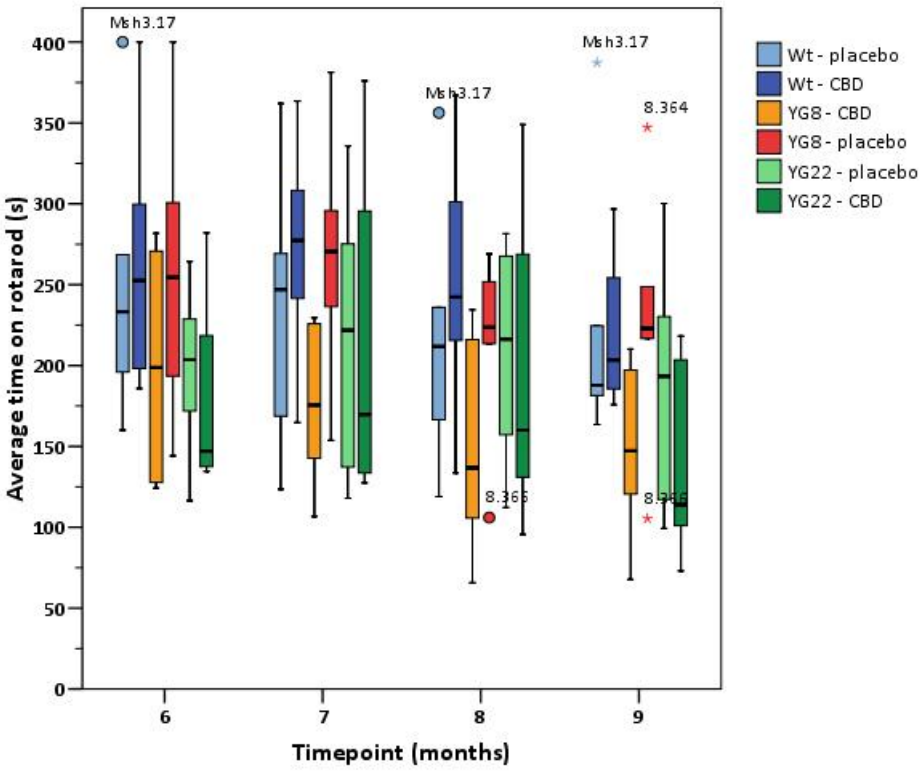

Figure A.3 – Boxplot of absolute rotarod performance during the 10mg/kg CBD study.

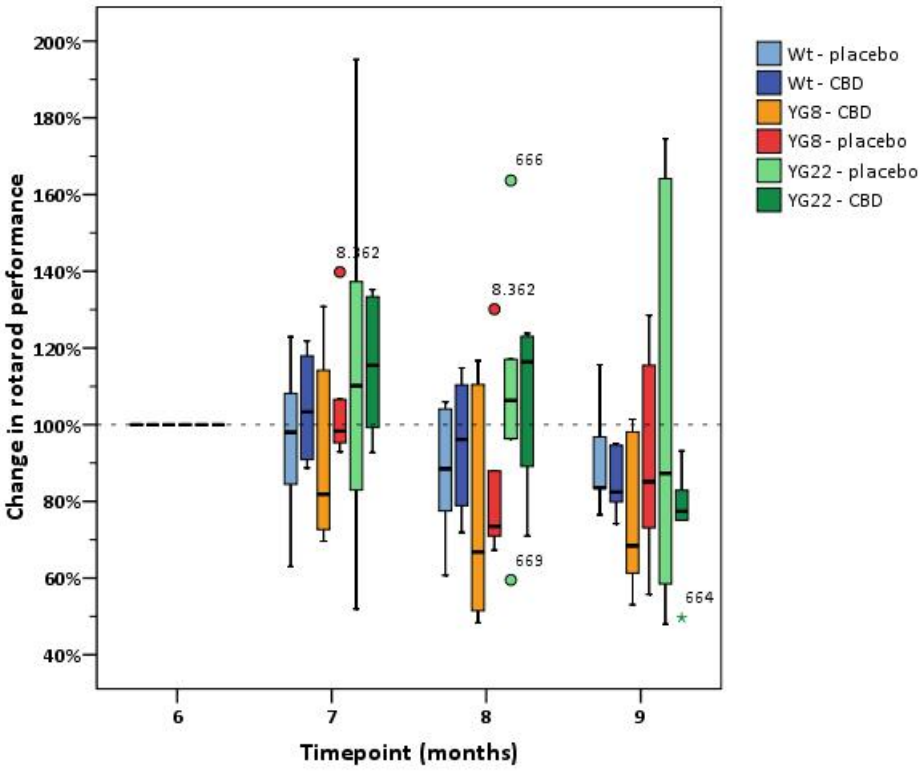

Figure A.4 – Boxplot of change in rotarod performance during the 10mg/kg CBD study.

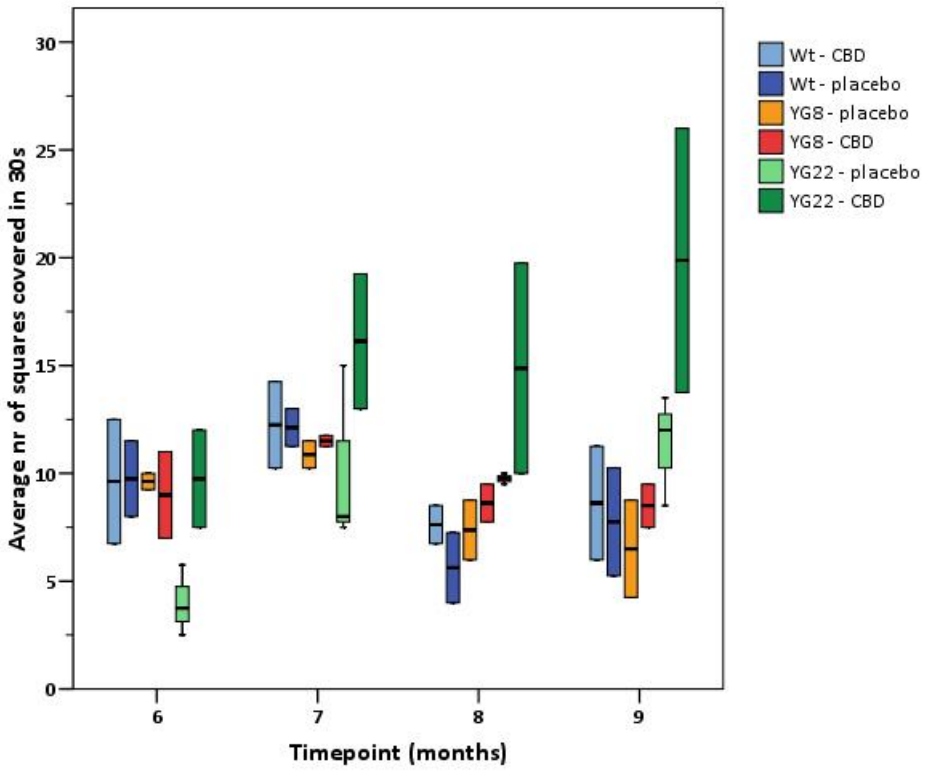

Figure A.5 – Boxplot of absolute locomotor activity during the 10mg/kg CBD study.

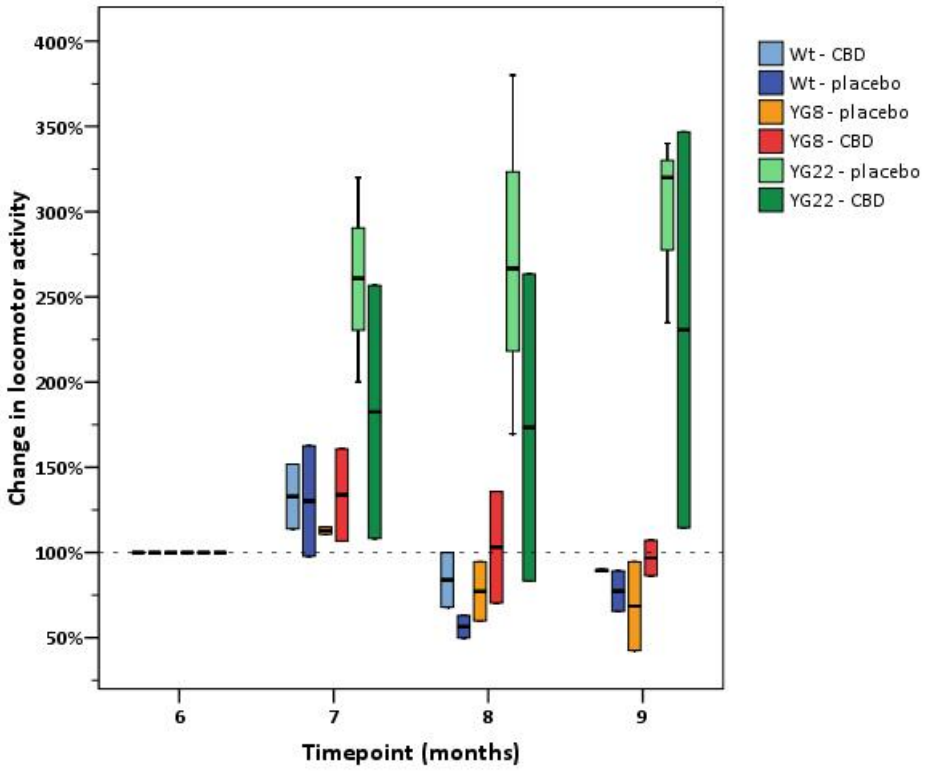

Figure A.6 – Boxplot of change in locomotor activity during the 10mg/kg CBD study.

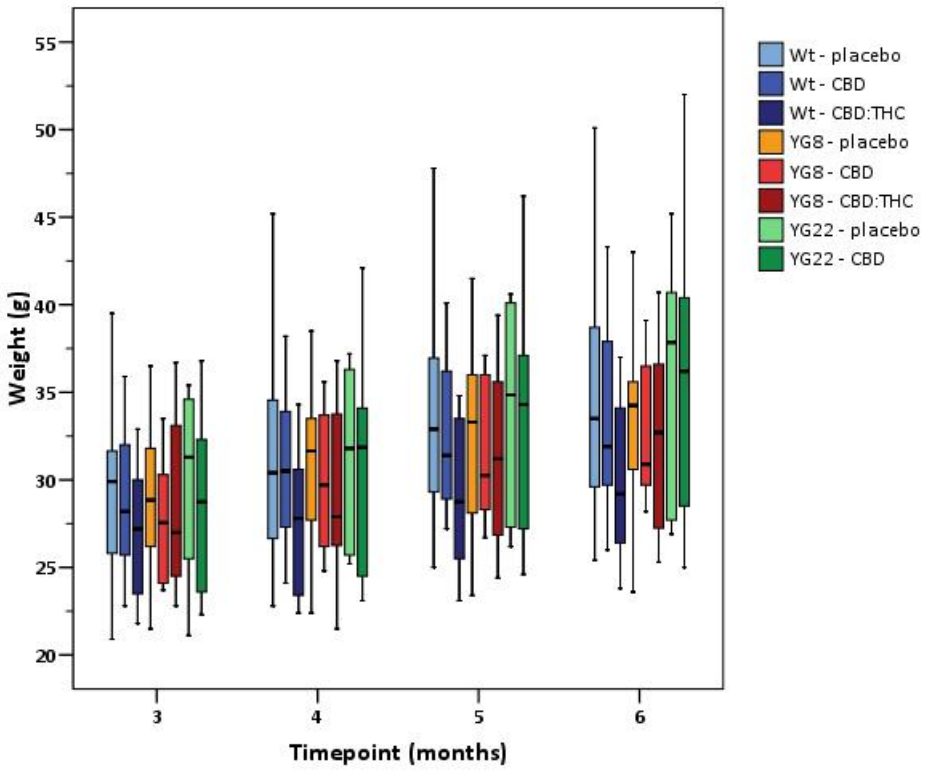

Figure A.7 – Boxplot of absolute weight during the 20mg/kg CBD/CBD:THC studies.

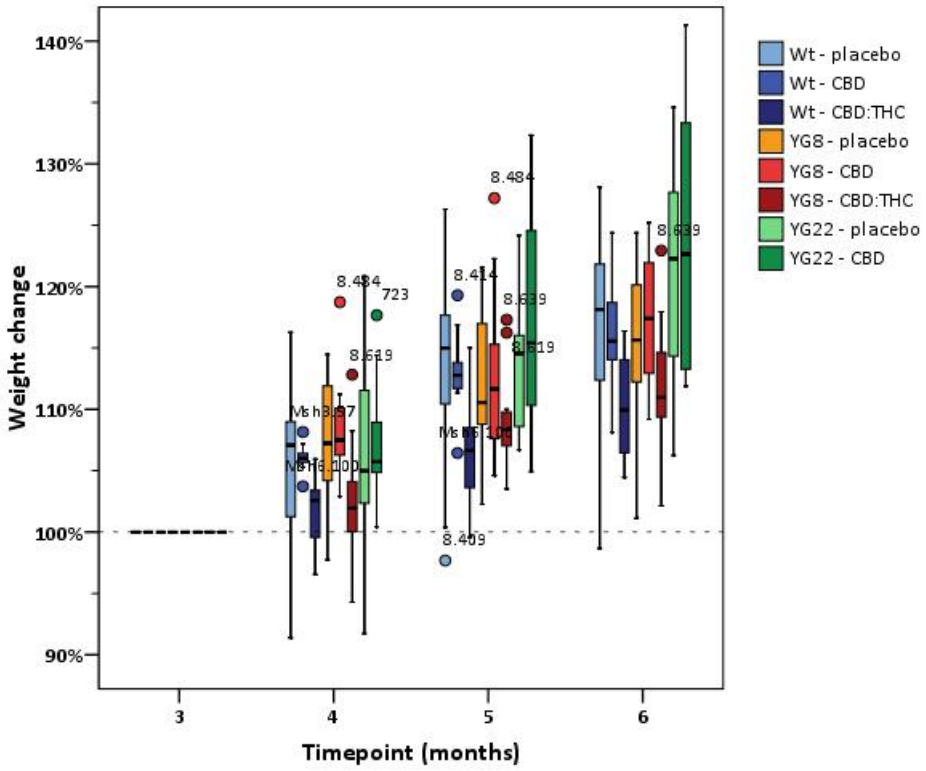

Figure A.8 – Boxplot of weight gain/loss during the 20mg/kg CBD/CBD:THC studies.

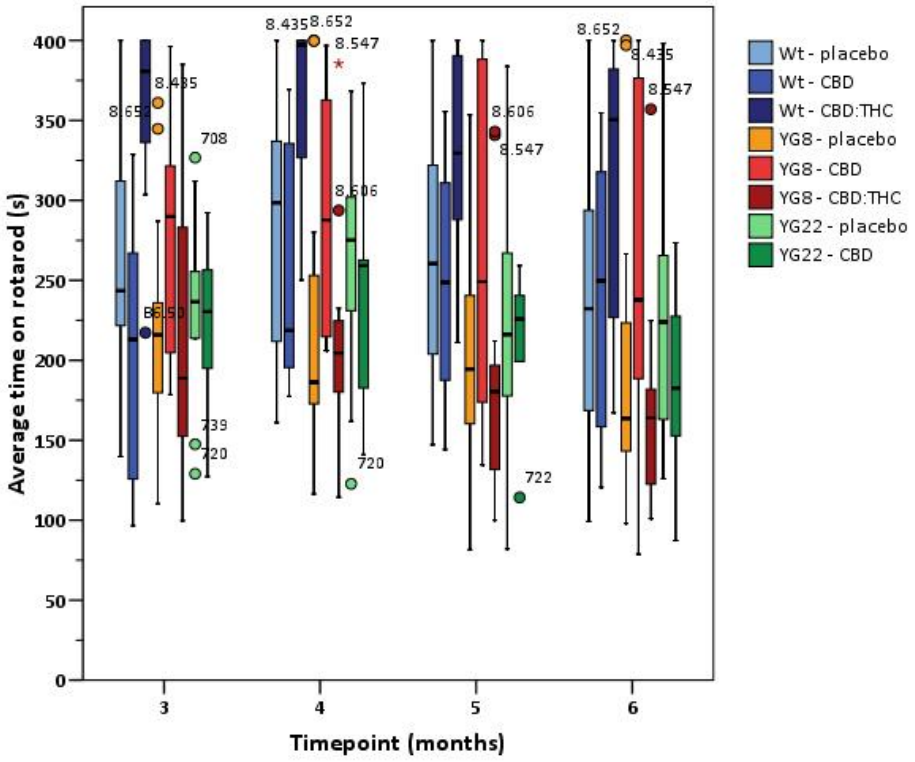

Figure A.9 – Boxplot of absolute rotarod performance during the 20mg/kg CBD/CBD:THC studies.

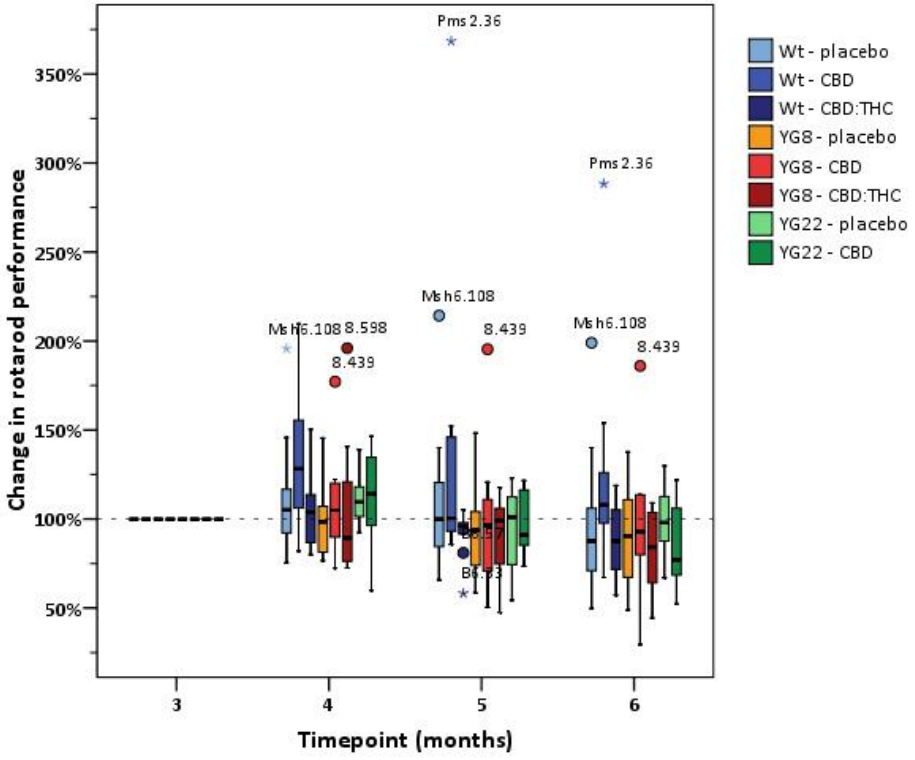

Figure A.10 – Boxplot of change in rotarod performance during the 20mg/kg CBD/CBD:THC studies.

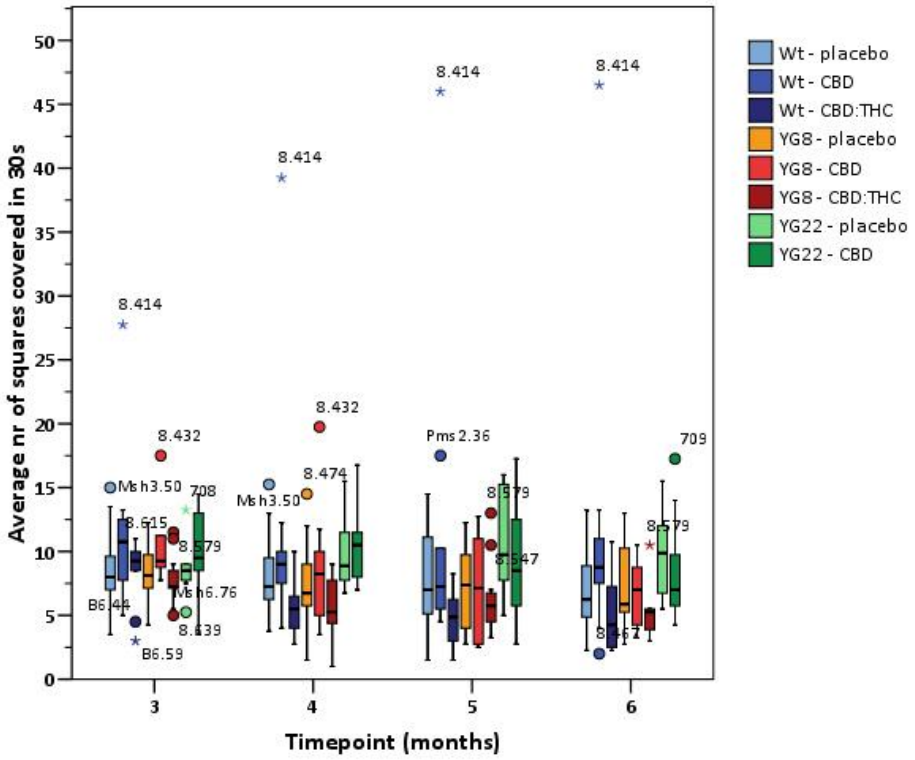

Figure A.11 – Boxplot of absolute locomotor activity during the 20mg/kg CBD/CBD:THC studies.

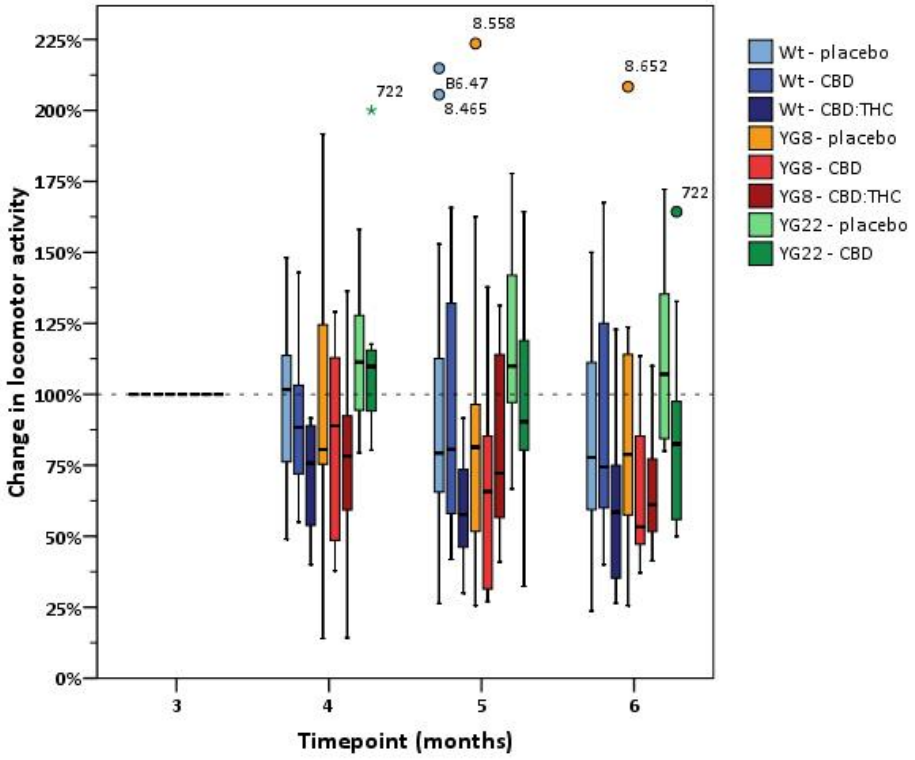

Figure A.12 – Boxplot of change in locomotor activity during the 20mg/kg CBD/CBD:THC studies.

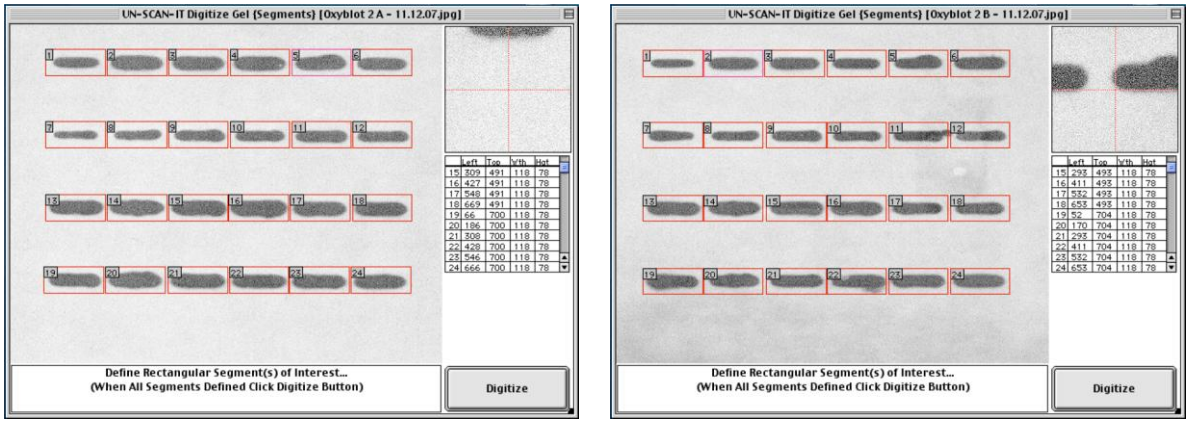

Figure A.13 – Screenshots of densitometry analysis performed to quantify levels of protein oxidation in the brain of mice from the 20mg/kg CBD/CBD:THC studies. (**A**) Blot A; (**B**) blot B. Samples were randomly loaded – see Table A.1 for key.

Table A.1 – List of samples used for the oxyblot analysis performed for the 20mg/kg CBD and CBD:THC studies.

Segment	Mouse ID	Study group
1	8.467	Wt - CBD
2	8.471	Wt - placebo
3	Msh6.100	Wt - CBD
4	762	Wt - placebo
5	Pms2.112	Wt - CBD
6	Msh6.113	Wt - placebo
7	8.484	YG8 - CBD
8	8.485	YG8 - placebo
9	8.439	YG8 - CBD
10	8.45	YG8 - placebo
11	8.496	YG8 - placebo
12	8.499	YG8 - CBD
13	B6.46	Wt - CBD:THC
14	B6.47	Wt - placebo
15	B6.48	Wt - CBD:THC
16	B6.49	Wt - placebo
17	B6.50	Wt - CBD:THC
18	B6.51	Wt - placebo
19	8.527	YG8 - CBD:THC
20	8.558	YG8 - placebo
21	8.547	YG8 - CBD:THC
22	8.564	YG8 - placebo
23	8.598	YG8 - CBD:THC
24	8.601	YG8 - placebo

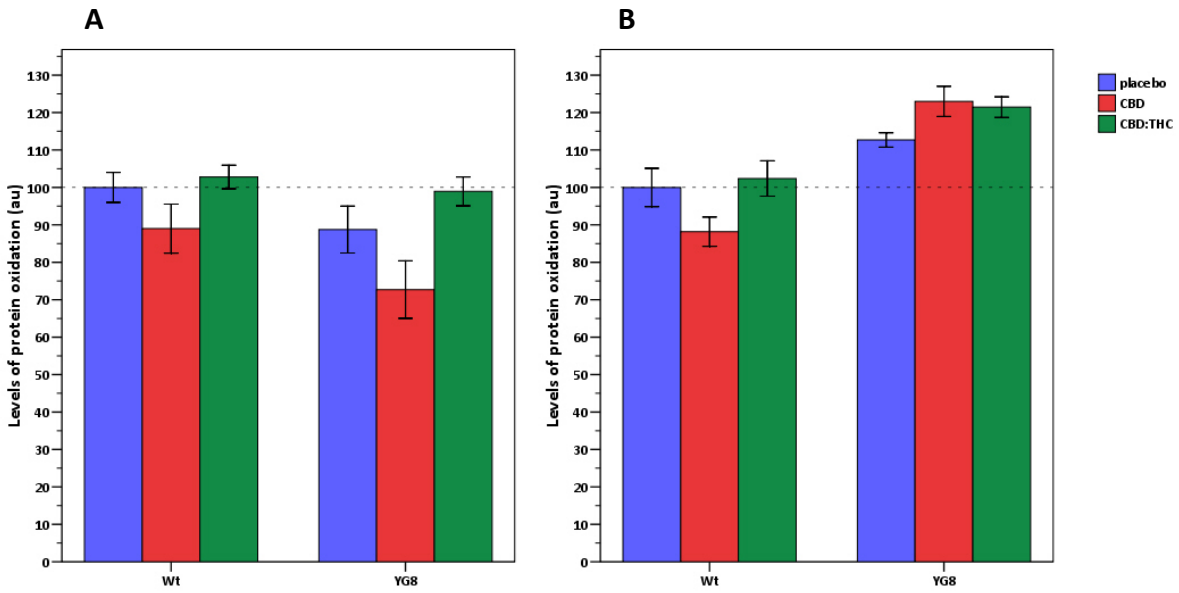

Figure A.14 – Levels of protein oxidation in the brain of mice from the 20mg/kg CBD/CBD:THC studies, as determined by Oxyblot analysis. (**A**) Blot A; (**B**) blot B. Placebo n=6, CBD n=3, CBD:THC n=3. (au = arbitrary units; error bars: +/- 1 SE)

Table A.2 – Independent samples *t*-test associated *p*-values of drug treatment effect on brain levels of protein oxidation during the 20mg/kg CBD and CBD:THC studies.

Genotype	Treatment (vs placebo)	*p*-value	
		blot A	blot B
Wt	CBD	0.175	0.180
	CBD:THC	0.668	0.777
YG8	CBD	0.169	0.032
	CBD:THC	0.319	0.034

Placebo n=6, CBD n=3, CBD:THC n=3

Table A.3 – Independent samples *t*-test associated *p*-values of genotype effect on brain levels of protein oxidation during the 20mg/kg CBD and CBD:THC studies.

Genotype	Treatment	*p*-value	
		blot A	blot B
Wt vs YG8	placebo	0.162	0.043
	CBD	0.182	0.003
	CBD:THC	0.483	0.025

Placebo n=6, CBD n=3, CBD:THC n=3

Appendix B – Additional data from CTMIO drug studies

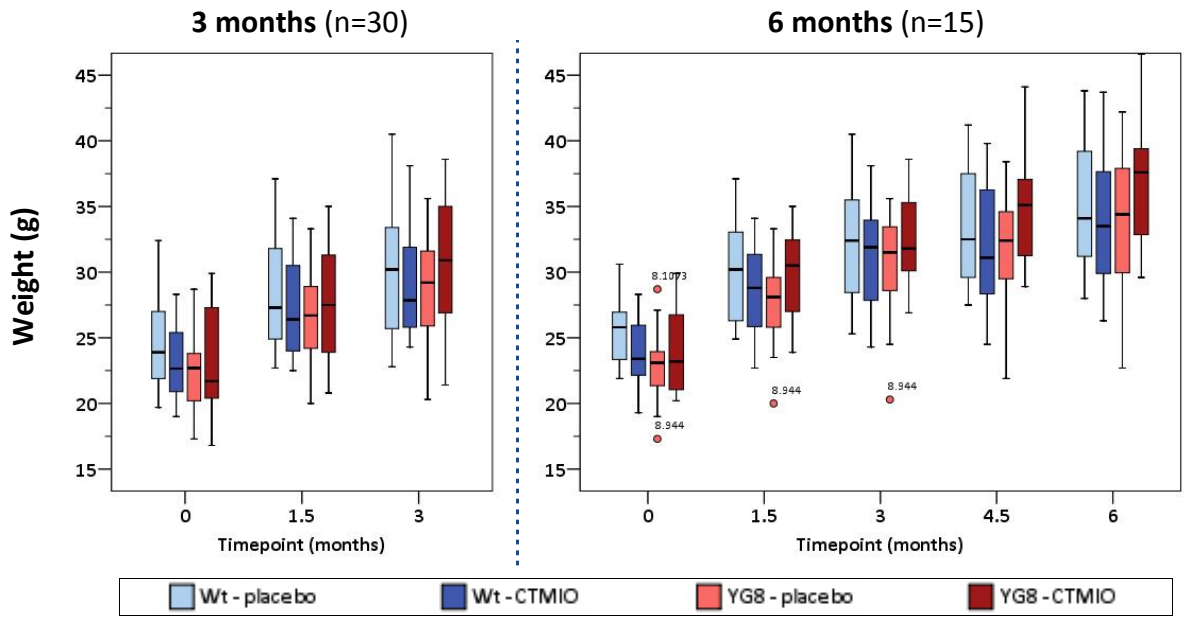

Figure B.1 – Boxplot of absolute weight during the CTMIO studies.

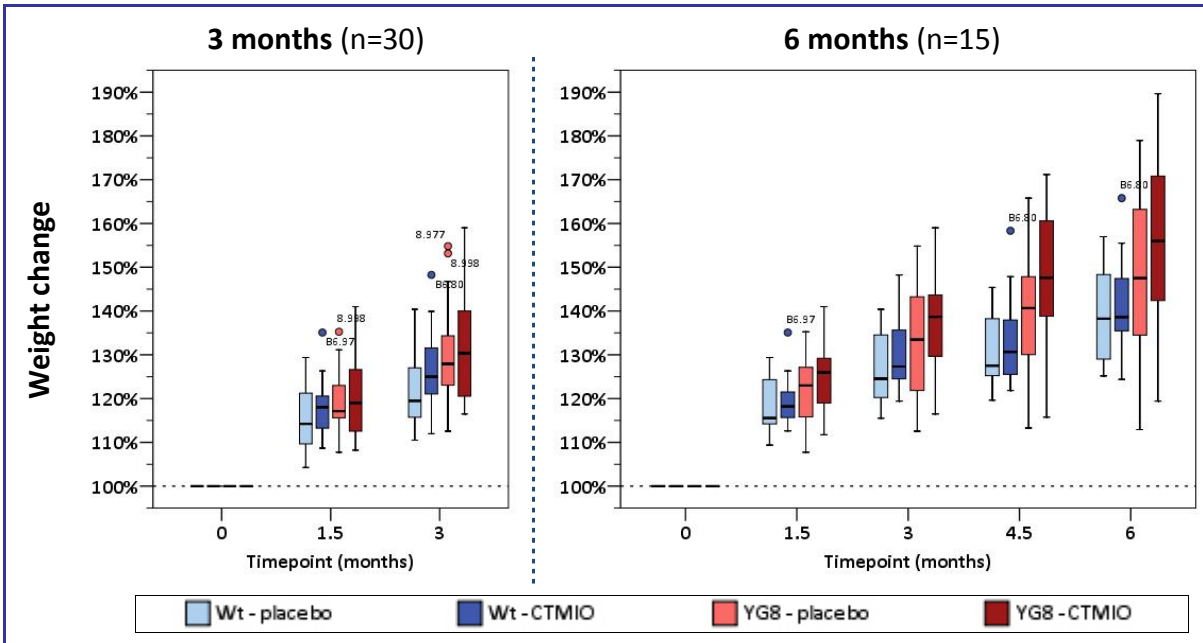

Figure B.2 – Boxplot of weight gain/loss during the CTMIO studies.

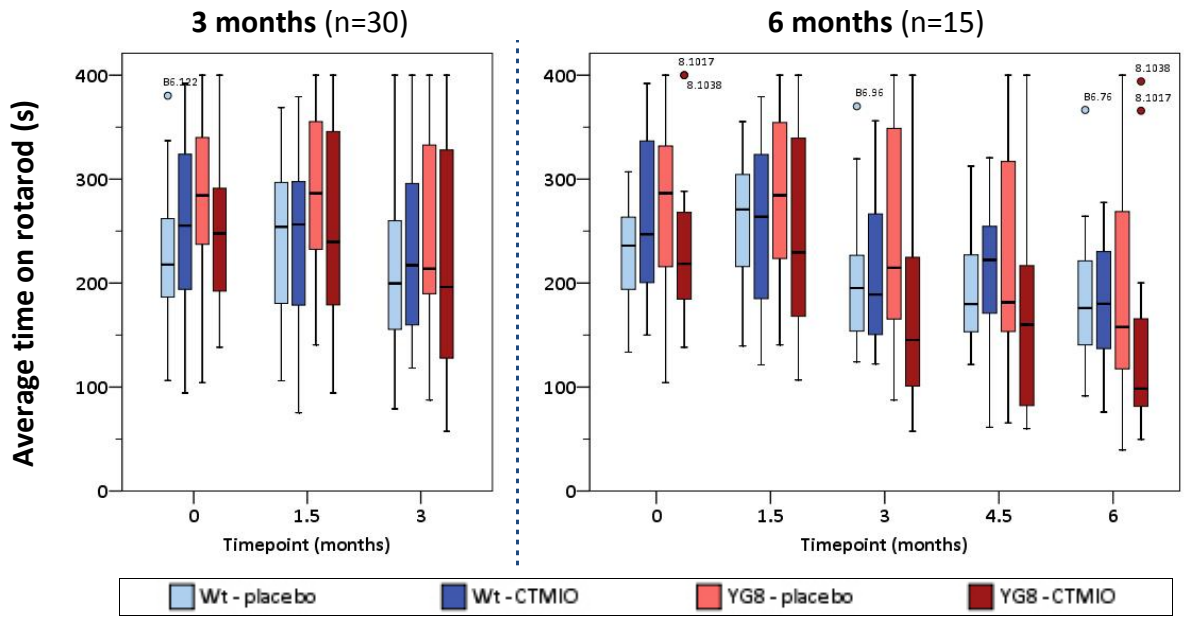

Figure B.3 – Boxplot of absolute rotarod performance during the CTMIO studies.

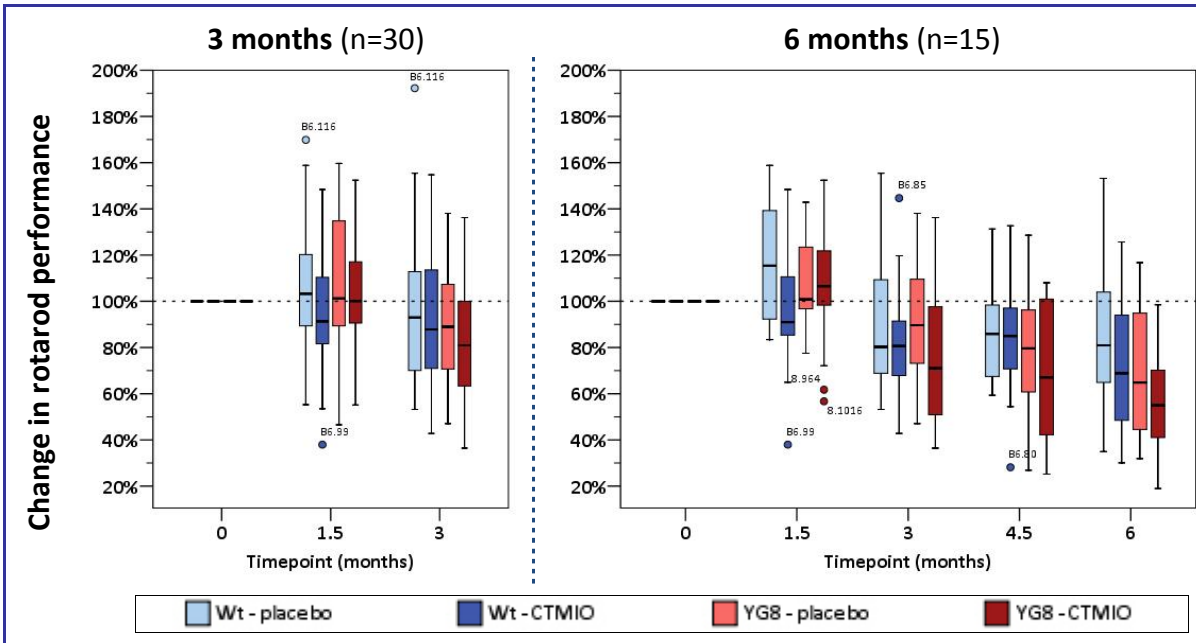

Figure B.4 – Boxplot of change in rotarod performance during the CTMIO studies.

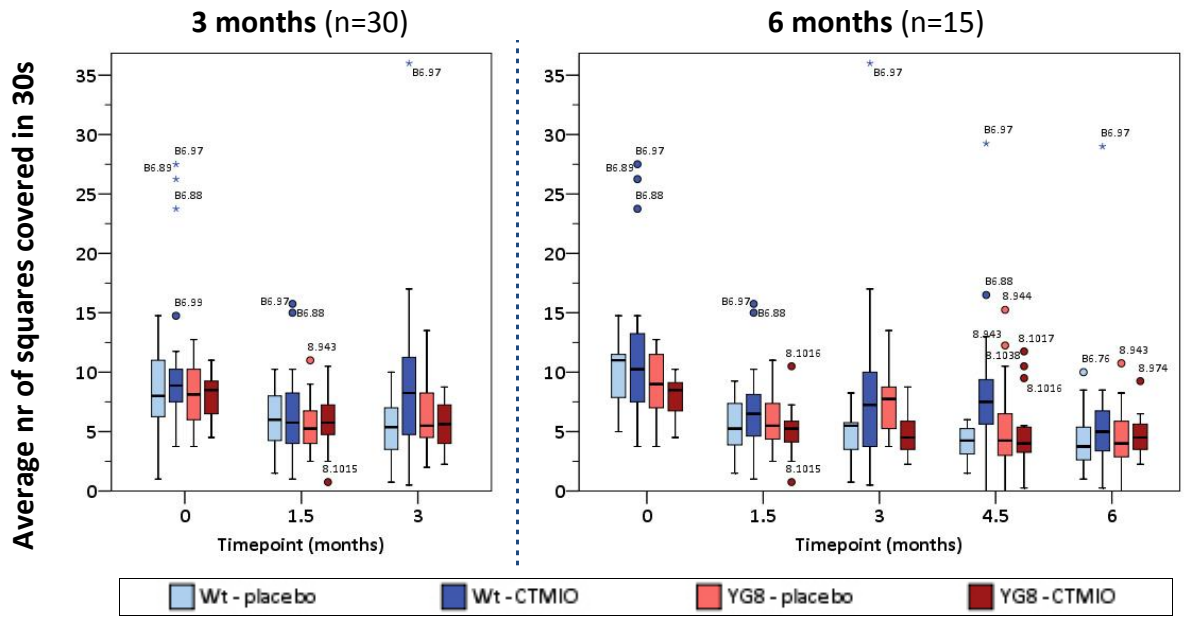

Figure B.5 – Boxplot of absolute locomotor activity during the CTMIO studies.

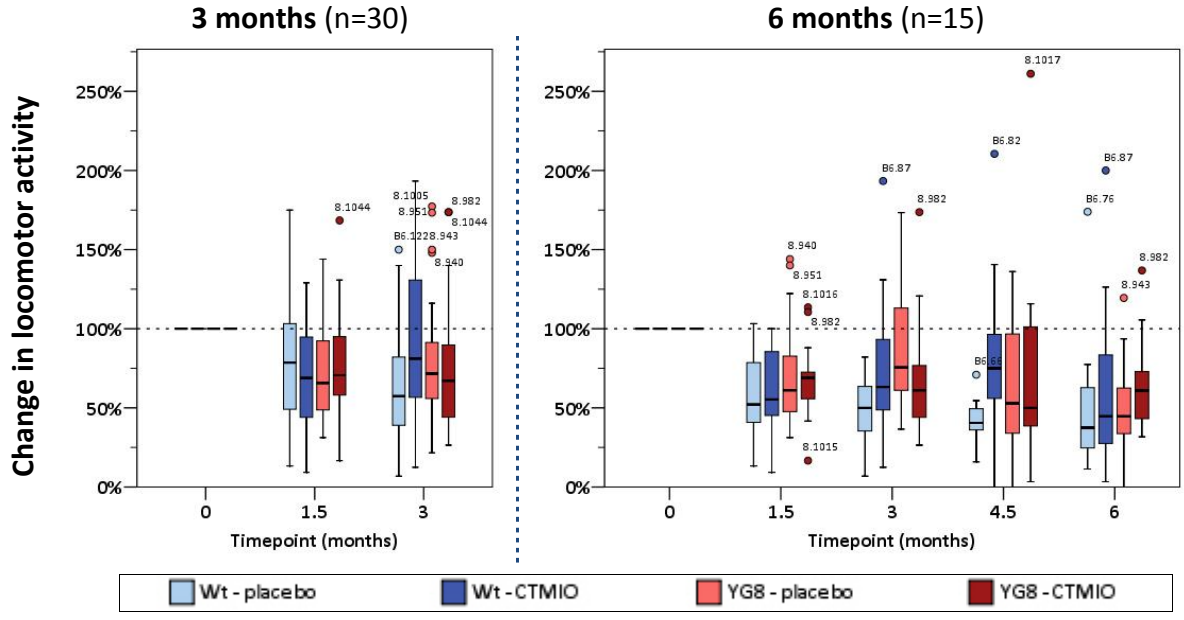

Figure B.6 – Boxplot of change in locomotor activity during the CTMIO studies.

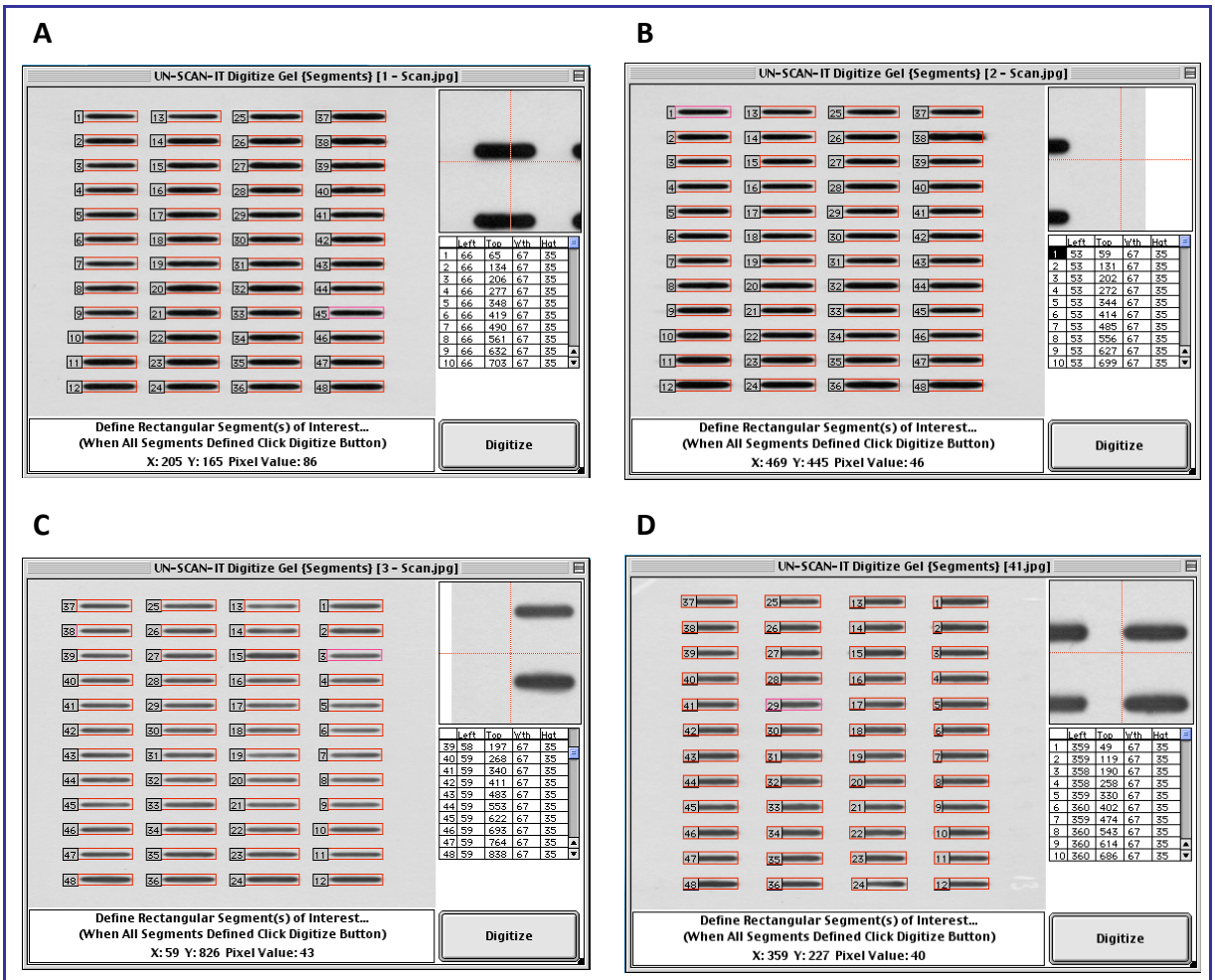

Figure B.7 – Screenshots of densitometry analysis performed to quantify levels of protein oxidation in the brain of mice from the CTMIO studies. (**A**) Blot 1; (**B**) blot 2; (**C**) blot 3; (**D**) blot 4.

Appendix C – Additional data from HDACi 106 drug studies

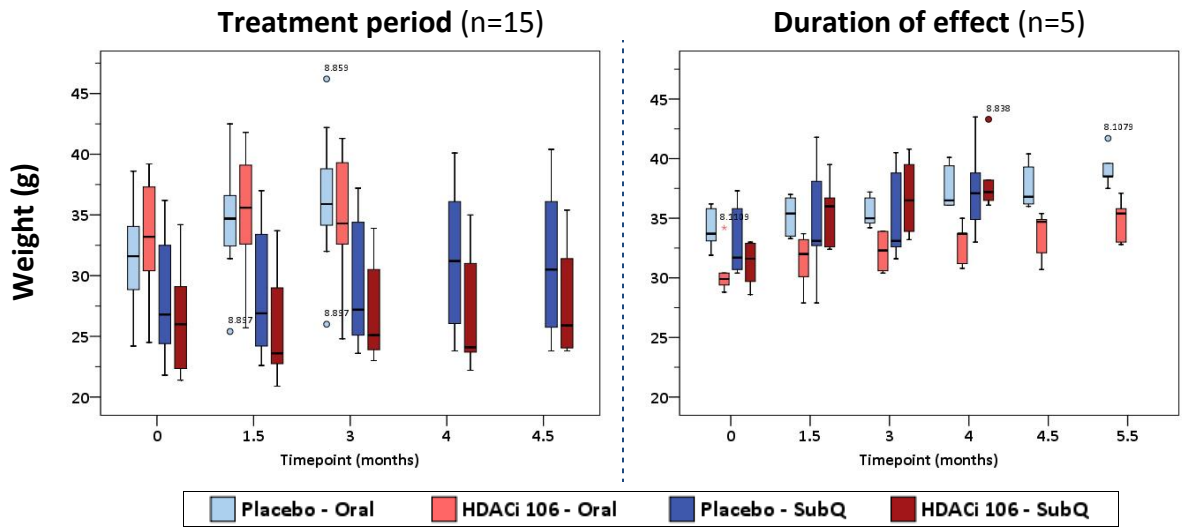

Figure C.1 – Boxplot of absolute weight during the HDACi 106 studies.

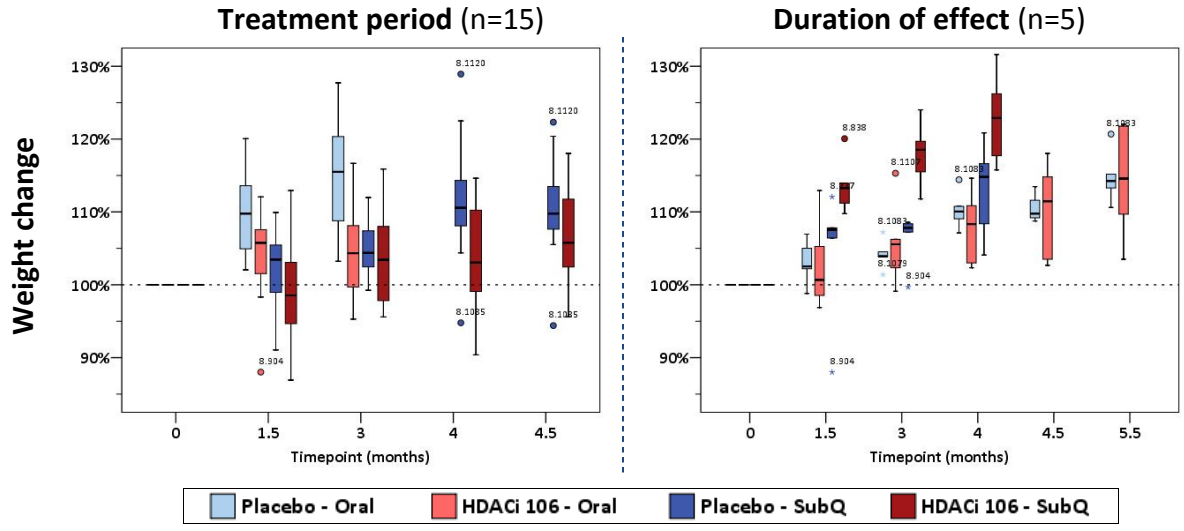

Figure C.2 – Boxplot of weight gain/loss during the HDACi 106 studies.

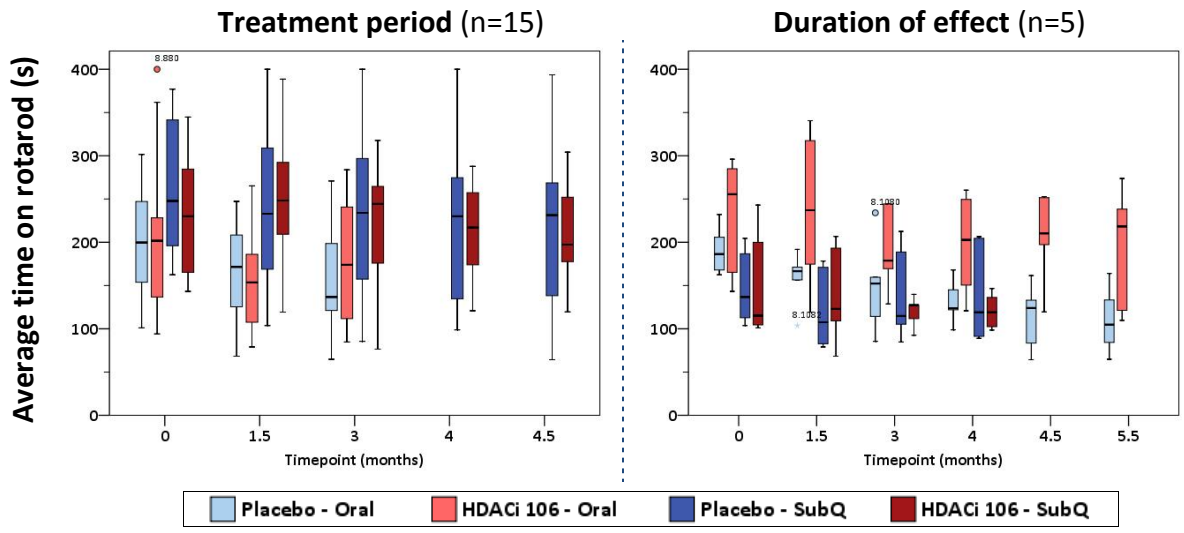

Figure C.3 – Boxplot of absolute rotarod performance during the HDACi 106 studies.

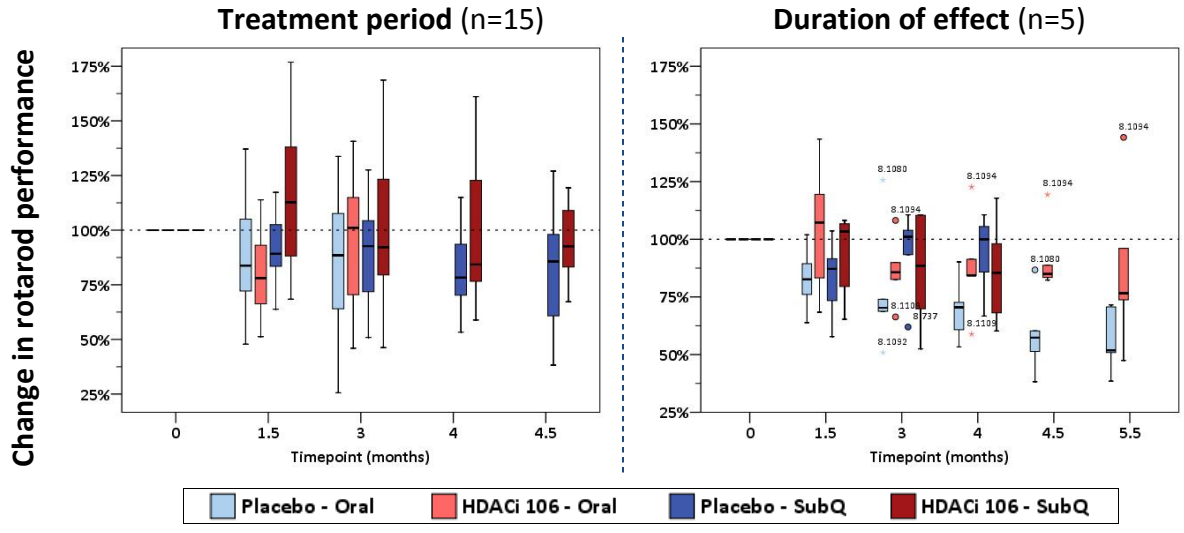

Figure C.4 – Boxplot of change in rotarod performance during the HDACi 106 studies.

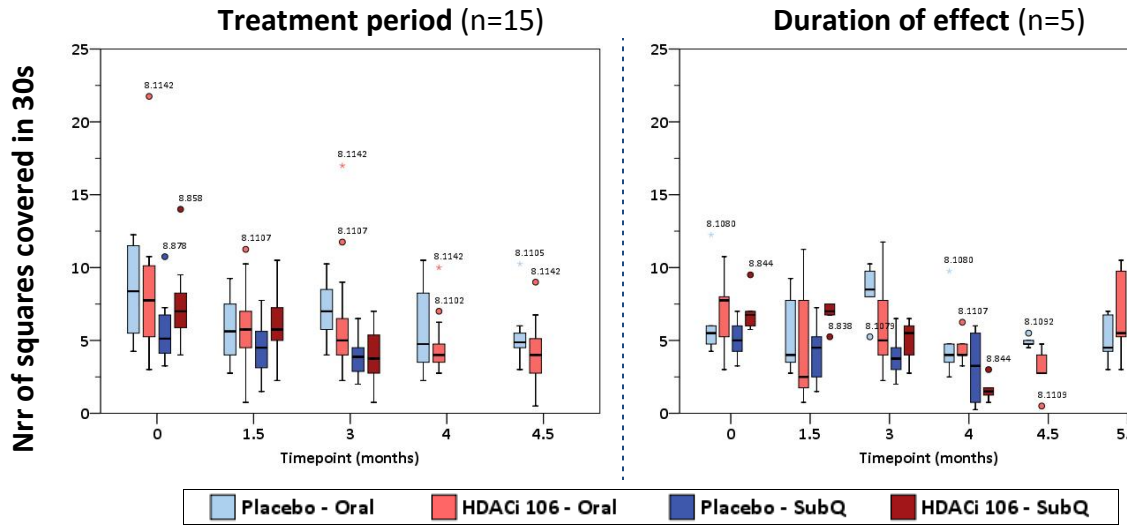

Figure C.5 – Boxplot of absolute locomotor activity during the HDACi 106 studies.

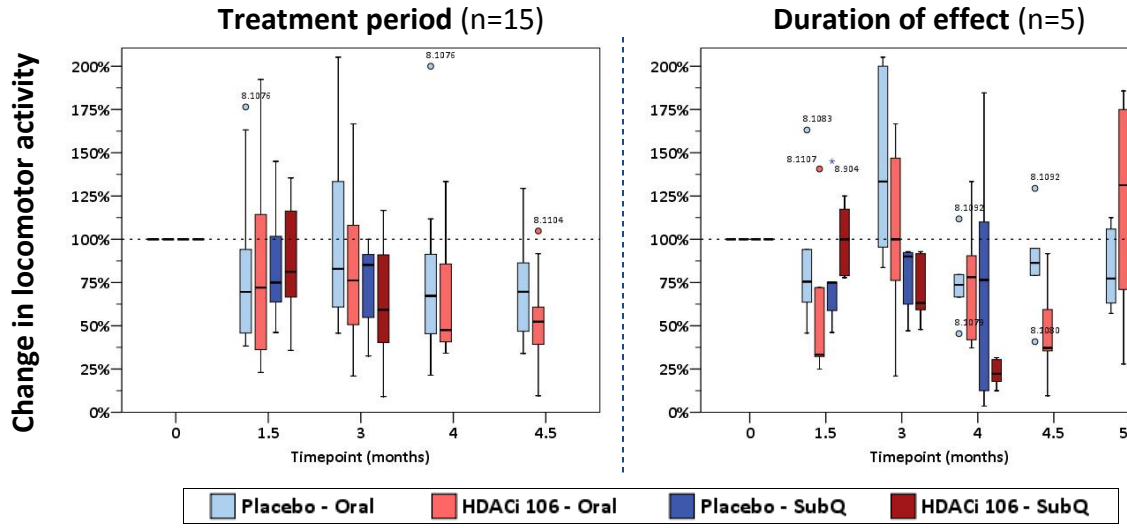

Figure C.6 – Boxplot of change in locomotor activity during the HDACi 106 studies.

Appendix D – Additional data from CTCF studies

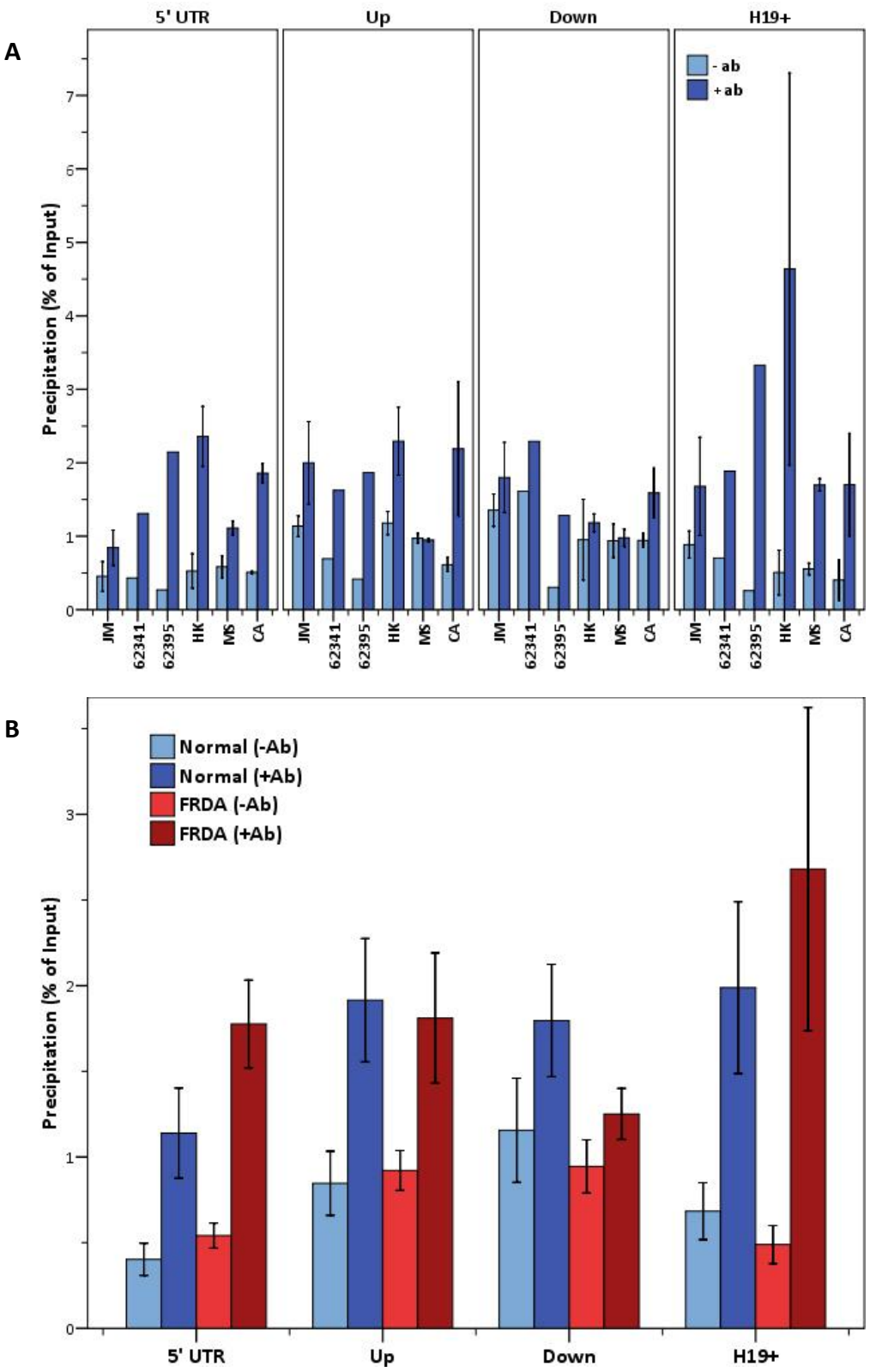

Figure D.1 – Precipitation levels following ChIP analysis of normal and FRDA cerebellum samples. Individual (**A**) and combined (**B**) levels of precipitation obtained with either anti-CTCF antibody (+ab) or IgG (-ab), displayed as percentage of input sample. Normal (n=4): JM (n=2), 62341 (n=1), 62395 (n=1); FRDA (n=6): HK (n=2), MS (n=2), CA (n=2).

(error bars: +/- 1 SE)

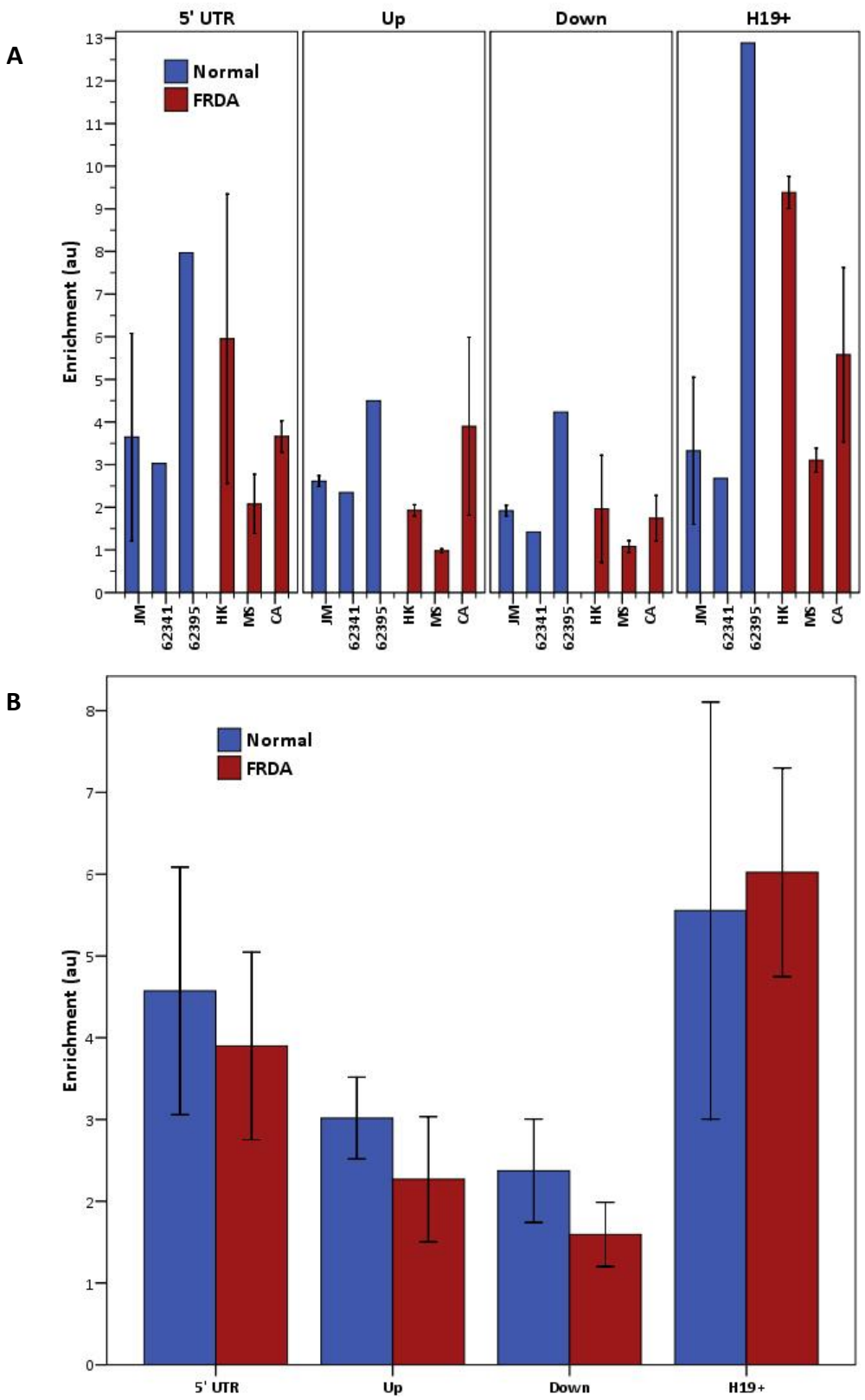

Figure D.2 – CTCF enrichment determined by ChIP analysis of normal and FRDA cerebellum samples. Individual (**A**) and combined (**B**) levels of enrichment obtained following subtraction of –ab values and normalization to input sample. Normal (n=4): JM (n=2), 62341 (n=1), 62395 (n=1); FRDA (n=6): HK (n=2), MS (n=2), CA (n=2).

(au = arbitrary units; error bars: +/- 1 SE)

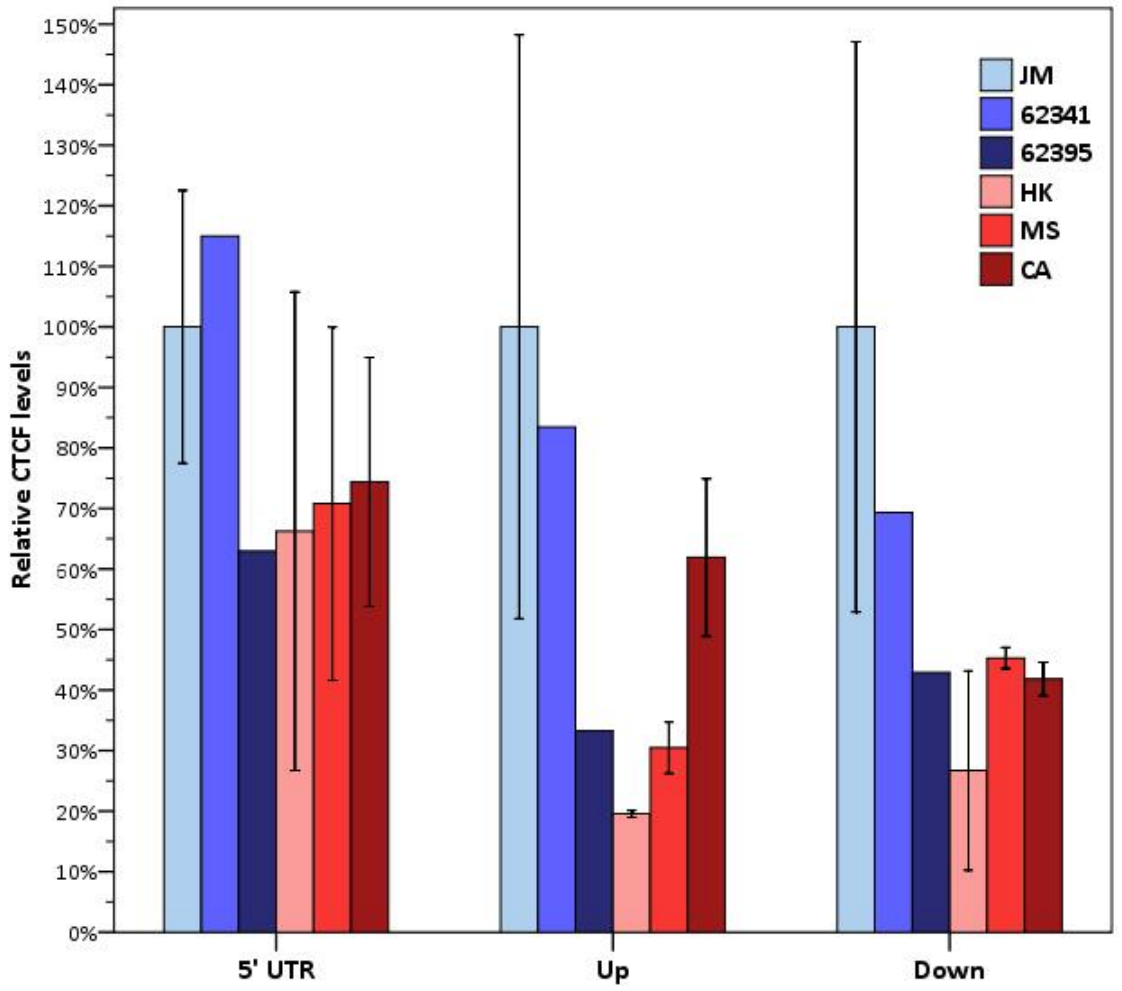

Figure D.3 – Relative CTCF levels determined in the *FXN* gene. CTCF levels were normalised to input and minus antibody samples, and finally determined in relation to a previously described CTCF-binding control region in the human *H19* gene. Normal: JM (n=2), 62341 (n=1), 62395 (n=1); FRDA: HK (n=2), MS (n=2), CA (n=2). (error bars: +/- 1 SE)

Appendix E – Journal publications

Available online at www.sciencedirect.com
ScienceDirect
Genomics 88 (2006) 580–590
GENOMICS
www.elsevier.com/locate/ygeno

GAA repeat expansion mutation mouse models of Friedreich ataxia exhibit oxidative stress leading to progressive neuronal and cardiac pathology

Sahar Al-Mahdawi [a], Ricardo Mouro Pinto [a], Dhaval Varshney [a], Lorraine Lawrence [b], Margaret B. Lowrie [b], Sian Hughes [c], Zoe Webster [d], Julian Blake [e], J. Mark Cooper [f], Rosalind King [f], Mark A. Pook [a,*]

[a] *Biosciences, School of Health Sciences & Social Care, Brunel University, Uxbridge UB8 3PH, UK*
[b] *Imperial College London, Exhibition Road, London, UK*
[c] *Rockefeller Building, University College London, London, UK*
[d] *Embryonic Stem Cell Facility, MRC CSC, Hammersmith Hospital, DuCane Road, London, UK*
[e] *Department of Clinical Neurophysiology, Norfolk and Norwich University Hospital, Norwich, UK*
[f] *Department of Clinical Neurosciences, Royal Free & University College Medical School, Rowland Hill Street, London, UK*

Received 9 March 2006; accepted 27 June 2006
Available online 17 August 2006

Abstract

Friedreich ataxia (FRDA) is a neurodegenerative disorder caused by an unstable GAA repeat expansion mutation within intron 1 of the *FXN* gene. However, the origins of the GAA repeat expansion, its unstable dynamics within different cells and tissues, and its effects on frataxin expression are not yet completely understood. Therefore, we have chosen to generate representative FRDA mouse models by using the human *FXN* GAA repeat expansion itself as the genetically modified mutation. We have previously reported the establishment of two lines of human *FXN* YAC transgenic mice that contain unstable GAA repeat expansions within the appropriate genomic context. We now describe the generation of FRDA mouse models by crossbreeding of both lines of human *FXN* YAC transgenic mice with heterozygous *Fxn* knockout mice. The resultant FRDA mice that express only human-derived frataxin show comparatively reduced levels of frataxin mRNA and protein expression, decreased aconitase activity, and oxidative stress, leading to progressive neurodegenerative and cardiac pathological phenotypes. Coordination deficits are present, as measured by accelerating rotarod analysis, together with a progressive decrease in locomotor activity and increase in weight. Large vacuoles are detected within neurons of the dorsal root ganglia (DRG), predominantly within the lumbar regions in 6-month-old mice, but spreading to the cervical regions after 1 year of age. Secondary demyelination of large axons is also detected within the lumbar roots of older mice. Lipofuscin deposition is increased in both DRG neurons and cardiomyocytes, and iron deposition is detected in cardiomyocytes after 1 year of age. These mice represent the first GAA repeat expansion-based FRDA mouse models that exhibit progressive FRDA-like pathology and thus will be of use in testing potential therapeutic strategies, particularly GAA repeat-based strategies.

Keywords: Friedreich ataxia; FRDA; *FXN*; Frataxin; GAA repeat; Mouse model

Friedreich ataxia (FRDA) is an autosomal recessive neurodegenerative disorder that is predominantly caused by a homozygous GAA repeat expansion mutation within intron 1 of the *FXN* gene (formerly *FRDA*) [1]. Normal individuals have 5 to 30 GAA repeat sequences, whereas affected individuals have from approximately 70 to more than 1000 GAA triplets [2]. The effect of the GAA expansion mutation is to reduce greatly the expression of frataxin [3], a mitochondrial protein that interacts with succinate dehydrogenase complex subunits [4] and acts both as an iron chaperone in iron–sulfur clusters and heme biosynthesis [5–8] and as an iron detoxifier [9]. A direct correlation has been identified between the size of the smaller of the two GAA repeat mutations (and hence the level of residual frataxin expression) and the age of onset and severity of FRDA disease phenotype [3,10–12]. Evidence suggests that the GAA repeat expansion may have its effect by adopting an abnormal triplex structure that interferes with *FXN* gene transcription

* Corresponding author. Fax: +44 1895 274348.
E-mail address: Mark.Pook@brunel.ac.uk (M.A. Pook).

0888-7543/$ - see front matter © 2006 Elsevier Inc. All rights reserved.
doi:10.1016/j.ygeno.2006.06.015

[13,14], possibly by the formation of a sticky DNA complex that sequesters transcription factors [15]. It has also been suggested that GAA repeats may produce a heterochromatin-mediated gene silencing effect [16].

The generation of a representative mouse model of FRDA is considered important for the further understanding of disease pathology and the testing of potential therapeutic strategies. Thus far, strategies have been based on various gene-targeting approaches to modify the homologous mouse *Fxn* gene. Initially, *Fxn* knockout mice were shown to be embryonic lethal in the homozygous state [17]. Several Cre/*loxP* conditional knockout mice have subsequently been generated. These have each been shown to reproduce some pathological features of FRDA, including dysfunction of large sensory neurons, cardiodegeneration, diabetes, deficiency of Fe–S-containing enzymes, oxidative stress, and mitochondrial iron accumulation [18–21]. Despite these successes, conditional knockout models are by their nature selective in the tissues that contain loss or decreased levels of frataxin and they do not address the question of GAA repeat mutation dynamics. A different gene-targeting approach is to introduce a GAA repeat mutation into the mouse *Fxn* locus. However, this GAA repeat knock-in strategy is somewhat hampered by the fact that the *Fxn* intron 1 region of the mouse does not normally contain a GAA repeat sequence. Indeed, knock-in of a 230-GAA repeat sequence into the *Fxn* intron 1 has not reproduced triplet repeat instability in mice, although it did result in decreased frataxin production [22].

We hypothesized that a human genomic *FXN* transgene that contained a GAA repeat expansion at the correct intronic position would enable both GAA repeat instability and reduced frataxin expression to be obtained within the one single model. Our previous work demonstrated that a wild-type *FXN* YAC transgene could successfully rescue the embryonic lethal phenotype of the *Fxn* knockout mouse [17], indicating that the YAC contained the necessary regulatory elements for appropriate human frataxin expression in a frataxin null mouse [23]. We have subsequently generated two lines of human *FXN* YAC transgenic mice containing GAA repeat expansions derived from FRDA patient DNA that exhibit intergenerational and somatic instability of the GAA repeat [24]. We now describe the generation of GAA repeat expansion-based FRDA mouse models by crossbreeding of these *FXN* YAC transgenic mice with heterozygous *Fxn* knockout mice. Offspring are produced that express comparatively reduced levels of human-derived frataxin and rescue the homozygous *Fxn* knockout embryonic lethality. We detect FRDA-like biochemical, histopathological, and functional losses that will allow these mouse models to be used for testing effective FRDA therapeutic strategies.

Results

Human GAA expansion-containing FXN YAC transgenes rescue FRDA knockout embryonic lethality

Two lines of human *FXN* YAC transgenic mice that contain GAA repeat expansions of approximately 190 repeats or 190+ 90 repeats, designated YG22 and YG8, respectively, have previously been described [24]. To determine the viability of each GAA *FXN* transgene, we set up crosses between YG22 or YG8 mice (FXN^+, $Fxn^{+/+}$) and heterozygous *Fxn* knockout mice ($Fxn^{+/-}$) [17]. The FXN^+, $Fxn^{+/-}$ offspring from these crosses were further bred with $Fxn^{+/-}$ mice to generate FXN^+, $Fxn^{-/-}$ "rescues." Correct Mendelian ratios of rescue mice to overall offspring number were obtained from both YG22 and YG8 crosses ($p>0.25$ in each case), indicating functional frataxin derived from both GAA repeat-containing transgenes. The rescue mice from both lines exhibit a normal life span, with mice surviving up to at least 2 years of age.

Decreases in frataxin mRNA and protein expression

To determine the levels of frataxin mRNA expression in YG22 and YG8 rescue and transgenic mice we performed semiquantitative RT-PCR using primers that recognize both human and mouse frataxin cDNA, followed by digestion with human-specific and mouse-specific restriction enzymes. The DNA products were standardized by comparison with mouse *Hprt* RT-PCR controls and were then determined as a percentage of wild-type mouse values. The results confirmed the presence of human-only frataxin mRNA transcripts in both YG22 and YG8 rescue mice (Fig. 1A). The levels of transgenic *FXN* mRNA expression compared to endogenous mouse *Fxn* mRNA revealed decreases in all YG22 and YG8 rescue mouse tissues (Fig. 1B). The greatest, and statistically significant, decreases were detected in the cerebellum of both YG22 (62%) and YG8 (57%) rescues, together with the skeletal muscle of YG8 rescues (57%). This contrasted with YG22 and YG8 transgenic mouse samples, which all showed increases (101 to 145%) in overall frataxin mRNA expression, with approximately equal contributions from transgenic and endogenous frataxin mRNA.

To determine the levels of human frataxin expression in YG22 and YG8 rescue mice we used an anti-human recombinant mature frataxin antibody (α-hmfxn) in Western blot analysis of several different tissue lysates. Our initial analysis of equalized unaffected human and wild-type mouse skeletal muscle samples indicated that the α-hmfxn antibody reacts strongly with human frataxin to give a band of 18 kDa, but reacts only weakly with mouse frataxin to give a slightly larger band of 19 kDa (Fig. 2A). We determined the ratio of human to mouse signal intensities to be 2.3:1. Thus, although a direct comparison between the human frataxin levels in the YG22 and YG8 rescue mice and wild-type mouse frataxin levels was not possible, we were able to calculate the comparative levels of human frataxin indirectly. Analysis of our results (Fig. 2B–2D) revealed comparative frataxin levels of 67 and 86% in the cerebellum, 45 and 52% in the heart, and 23 and 23% in the skeletal muscle of YG22 and YG8 rescue mice, respectively, when standardized to an anti-porin mitochondrial antibody control ($p<0.01$ for all, except YG8 cerebellum, which was not significant). These frataxin expression levels were further decreased to 67 and 42% in cerebellum, 37 and 25% in heart, and 10 and 9% in skeletal muscle of YG22 and YG8 rescue

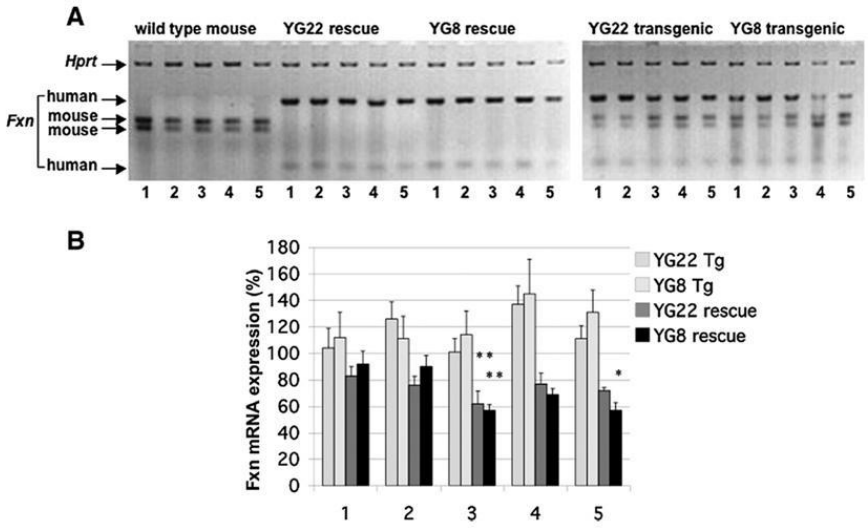

Fig. 1. mRNA expression analysis. (A) A representative RT-PCR image showing restriction-digested human frataxin products (112 and 29 bp) and mouse frataxin products (75 and 64 bp), together with mouse *Hprt* controls. mRNA samples were isolated from tissues of wild-type, YG22 rescue, YG8 rescue, YG22 transgenic, and YG8 transgenic mice (lanes 1, cerebrum; 2, brain stem; 3, cerebellum; 4, heart; 5, skeletal muscle). (B) Levels of frataxin mRNA expression as a percentage value of wild-type mouse expression. Values were generated by determining the means of six different RT-PCR experiments, each normalized to *Hprt*. Error bars indicate SEM. $^{*}p<0.05$, $^{**}p<0.01$.

mice, respectively, when standardized to an anti-actin antibody control ($p<0.01$ for all). This suggests that there is both a decrease in the relative amount of frataxin within the mitochondria and an overall decrease in mitochondria within the cells of these tissues, especially within the YG8 cerebellar and heart tissues compared with the corresponding YG22 tissues. Some confirmation of this latter point comes from our finding of variably decreased (60–90%) levels of porin in all YG22 and YG8 cerebellum, heart, and skeletal muscle tissues, compared with wild-type controls (data not shown). In contrast, the levels of frataxin in the cerebrum and brain stem from both YG22 and YG8 rescue mice are not similarly reduced, but show increases of between 1 and 2 times the endogenous mouse levels when standardized to porin and levels of 0.7 to 2.2 times when standardized to actin (Figs. 2B–2D). These data suggest an increased amount of frataxin within the mitochondria of the cerebrum and brain stem of both mice, with an approximately normal number of mitochondria in YG22, but a decrease in YG8. The fluctuating decreased or increased levels of frataxin protein that we determined in different rescue mouse tissues contrasts with our finding of constant decreased frataxin mRNA levels in all rescue mouse tissues. This discrepancy may be explained by tissue-dependent variations in posttranscriptional and posttranslational effects on transgenic frataxin protein production.

To investigate potential antioxidant changes, comparative levels of the antioxidant enzymes, CuZnSOD and MnSOD, were also determined from the same tissue lysates (Figs. 2B, 2E, and 2F). CuZnSOD showed increases of up to 166% in cerebrum, brain stem, cerebellum, and heart of both YG22 and YG8 rescue mice compared with wild-type controls and normalized with actin, although changes were not to a significant level. However, a significant decrease in CuZnSOD was detected in the skeletal muscle of both YG22 and YG8 rescue mice (40 and 22%, respectively, $p<0.01$ for each). MnSOD showed increases of up to 146% in all tissues (with the exception of YG8 skeletal muscle, which was decreased to 80%) compared with wild-type controls and normalized with porin, although changes were not to a significant level.

Neurobehavioral deficits

The coordination ability of the YG22 and YG8 rescue mice was shown to be impaired from the age of 3 months as determined by reduced performance on an accelerating rotarod treadmill compared with wild-type littermate controls ($p<0.01$) (Fig. 3A). However, the degree of impairment did not extend to overt ataxia in either line of mice up to the age of 2 years. Muscle strength, assessed by a forelimb grip strength test, was decreased in YG22 rescues from 9 months of age ($p<0.01$), but no significant changes were detected in the YG8 rescues (Fig. 3B). Locomotor activity, assessed by examining the unrestricted movement of mice in an open field, was decreased in both lines. The YG22 rescues showed a decreased trend in locomotor activity from 6 months of age, but no statistically significant difference was seen until 1 year ($p<0.05$). YG8 rescues, on the other hand, showed a significant decrease in locomotor activity from 6 months of age ($p<0.05$) (Fig. 3C). Both YG22 and YG8 lines demonstrated an increase in weight, with statistically significant differences detected in YG22 rescues from 6 months

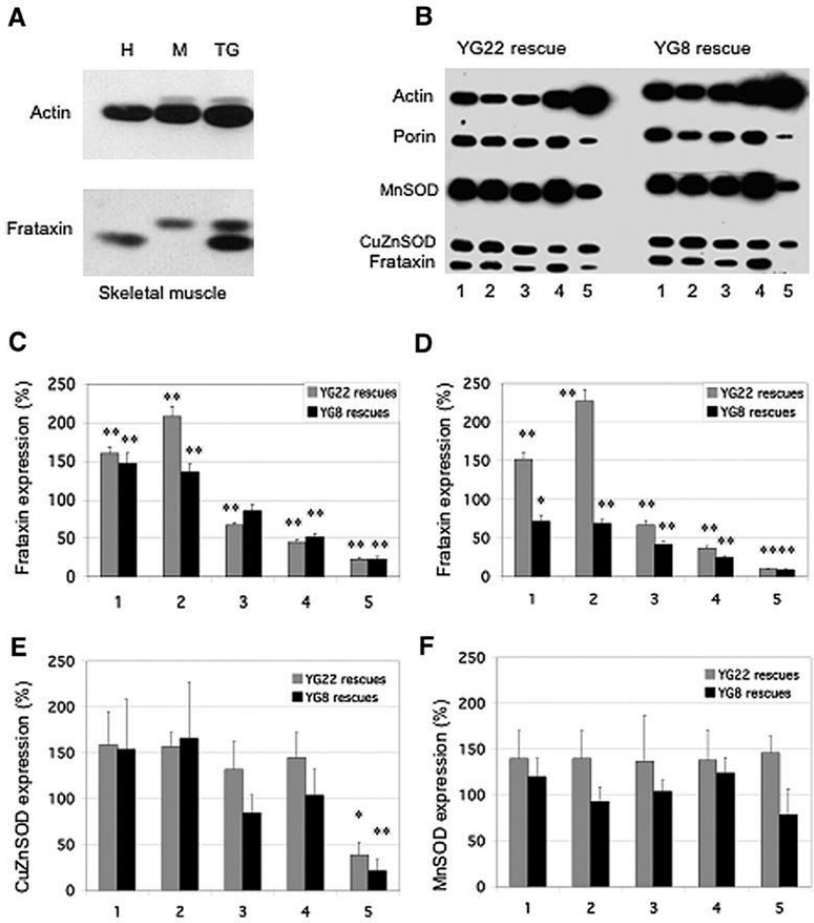

Fig. 2. Frataxin and antioxidant enzyme expression levels in YG22 and YG8 rescue mice. (A) Western blot showing comparative levels of frataxin relative to actin in skeletal muscle samples from human (H), wild-type mouse (M), and YG22 transgenic mouse (TG). (B) Western blot of YG22 and YG8 rescue mouse tissue lysates (lanes 1, cerebrum; 2, brain stem; 3, cerebellum; 4, heart; 5, skeletal muscle) hybridized with antibodies against frataxin, actin, porin, MnSOD, and CuZnSOD. The very low levels of YG8 skeletal muscle frataxin, which appear to be negative in this image, were revealed upon longer exposure. (C, D) Levels of transgenic human frataxin expression as a percentage value of endogenous wild-type mouse frataxin expression, (C) relative to porin controls or (D) relative to actin controls ($n=5–8$). Tissues 1–5 are as described for (B). (E) Levels of CuZnSOD in rescue mice as a percentage value of wild-type mouse expression, normalized to actin ($n=3–7$). Tissues 1–5 are as described for (B). (F) Levels of MnSOD in rescue mice as a percentage value of wild-type mouse expression, normalized to porin ($n=3–6$). Tissues 1–5 are as described for (B). Error bars indicate SEM. $*p<0.05$, $**p<0.01$.

of age ($p<0.01$) and in YG8 rescues from 9 months of age ($p<0.01$) (Fig. 3D). One reason for the observed gain in weights may be the decreased locomotor activity identified in the mice.

Electrophysiological analysis

Motor and sensory nerve conduction studies were performed on the sciatic and caudal nerves of 9- to 14-month-old YG22 rescue and wild-type control mice and 20-month-old YG8 rescue and wild-type control mice. Decreases in both the sensory action potential and the sensory conduction velocity of the older YG8 rescue mice were detected (Fig. 4), although not to statistical significance. However, no sensory nerve conduction changes were detected in the younger YG22 rescues, and no motor nerve conduction changes were detected in either line of mice (data not shown). Taken together, these findings suggest a mild, progressive peripheral sensory neuropathy, which is consistent with an FRDA phenotype.

Histological abnormalities in the dorsal root ganglia (DRG) and heart

To detect possible neuronal histopathology in the YG22 and YG8 rescue mice, we examined sections of brain, spinal cord, and DRG from eight YG22 rescues, six YG8 rescues, and three wild-type mice. By performing H&E staining and anti-calbindin

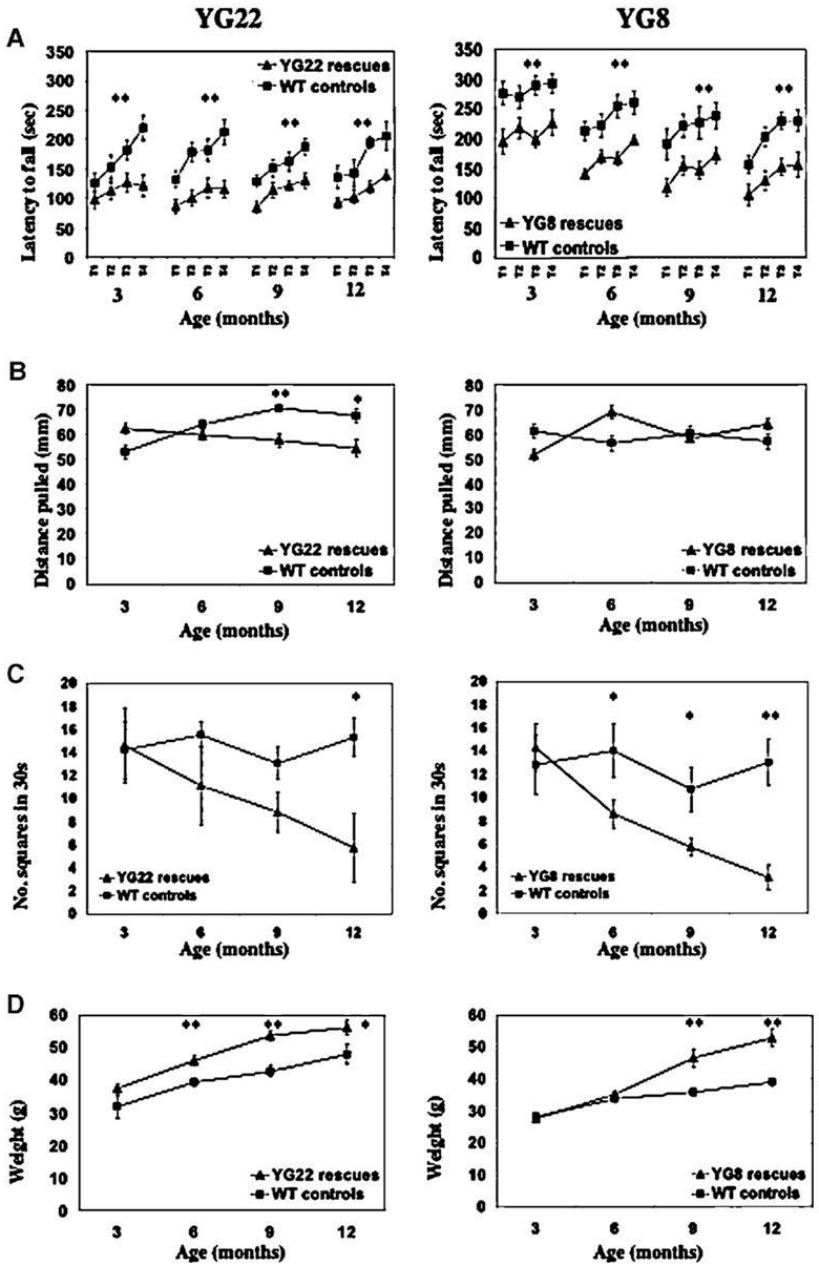

Fig. 3. Functional studies of 3-, 6-, 9-, and 12-month-old YG22 and YG8 rescue mice, compared with wild-type controls. (A) Rotarod analysis of YG22 and YG8 rescue mice compared with wild-type littermate controls shows a coordination deficit in both rescue mice from 3 months of age ($n = 10$ and 9, respectively). However, a direct comparison between YG22 and YG8 experiments is not possible due to the use of different rotarod acceleration rate settings carried out at different periods of time. (B) Grip strength analysis shows a weakness in YG22 rescues only from 9 months of age ($n = 6–10$). (C) Locomotor analysis identifies a progressive decrease in the mobility of both rescue mice ($n = 6–8$ and 7–13, respectively). (D) Weight increases are detected in both rescue mice ($n = 6–16$). Error bars indicate SEM. $^{*}p < 0.05$, $^{**}p < 0.01$.

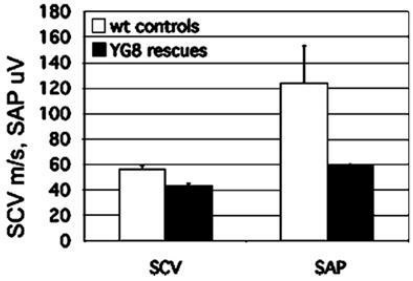

Fig. 4. Sensory nerve conduction studies of 20-month-old YG8 rescue mice and wild-type controls showing a decrease in sensory conduction velocity (SCV) and sensory action potential (SAP), although not to significance ($n=2$).

immunohistology, we did not identify any of the cerebellar Purkinje cell abnormalities or granule cell losses that have previously been reported for frataxin conditional knockout mice [20]. Neither did we detect any abnormalities in the brain or spinal cord regions of either line of mice. However, we did identify pathological changes in the DRG. Prominent giant vacuoles were identified in the large sensory neuronal cell bodies of the DRG in both YG8 and YG22 rescue mice but not in wild-type controls (Fig. 5A). The vacuoles are round, single or multiple, and appear to be empty. We also detected peripheral margination of the nucleus in many large neuronal cell bodies, with or without vacuoles, suggestive of the process of central chromatolysis. These findings indicate specific degeneration of cells that also are a primary site of pathology in FRDA patients. Interestingly, the occurrence of DRG vacuoles shows a progressive position-dependent profile, which is similar in both lines of mice. Between the ages of 6 months to 1 year, vacuoles are detected only in the DRG of the lumbar region, but after 1 year of age, vacuoles also become apparent within DRG of the cervical region. Approximately 60% of the lumbar DRG sections from YG22 rescues and 70% of the lumbar DRG sections from YG8 rescues have cells containing vacuoles, with one to seven cells affected in each DRG section. In contrast, only 16% of the cervical DRG sections have vacuoles, and the vacuoles are detected in only one cell per DRG section. This profile resembles the distal-to-proximal "dying-back" phenomenon of neurodegeneration that is observed in FRDA patients.

To determine potential hypertrophic cardiomyopathy, the heart weight/body weight ratio was determined and the heart examined for histopathology by H&E, trichrome Masson, and Perl's staining. No increase in heart weight to body weight ratio was identified and no myofibril disarray or fibrosis was observed to suggest cardiomyopathy (data not shown). However, Perl's staining identified iron deposition within the heart, but only from the oldest (14–18 months) YG22 rescue mice studied (Fig. 5B). In these cases, Perl's staining of the cardiomyocytes was prominent but sparse, consistent with similar findings in FRDA patients.

Ultrastructure pathology

Ultrastructure examination of lumbar DRG from 20-month-old YG8 rescue mice by electron microscopy confirmed the presence of large vacuoles within the large neuronal cell bodies (Fig. 6A), as previously detected by light microscopy. Chromatolysis was also confirmed by the finding of dispersion of the rough endoplasmic reticulum ribosomes, leaving regions of the cell devoid of any cytoplasmic organelles (Fig. 6B). Lipofuscin deposition, which represents a lysosomal protein polymer arising from iron-catalyzed oxidation, was pronounced in DRG neurons (Fig. 6C). Other changes within the lumbar DRG included the finding of swelling and secondary demyelination of large axons (Figs. 6D and 6E). These pathological changes are all in keeping with oxidative stress and mitochondrial dysfunction of degenerating large DRG neurons, which are then attempting to regenerate by activation of protein synthesis. Ultrastructure examination of the heart identified patches of lipofuscin deposition and lysosomes, together with an accumulation of dispersed free glycogen, disrupting the regular arrays of mitochondria within the cardiomyocytes (Fig. 6F). Lipofuscin deposition is a recognized feature within FRDA cardiomyocytes and dispersed free glycogen accumulation leading to myofibril distortion has been found in other forms of hypertrophic cardiomyopathy [25].

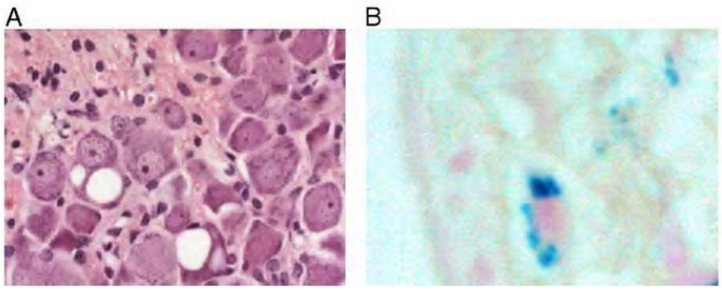

Fig. 5. Neuronal and cardiac histopathology. (A) H&E-stained section of lumbar DRG from a representative YG22 rescue mouse over 1 year of age, showing two neurons containing large vacuoles. Original magnification 400×. (B) Perl's staining of a heart section from a representative YG22 rescue mouse over 1 year of age, showing characteristic blue staining indicating iron deposition. Original magnification 600×.

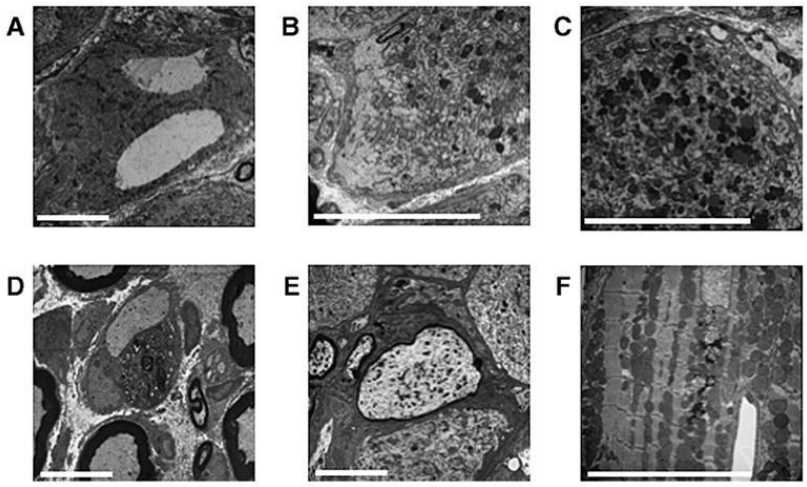

Fig. 6. (A–E) Electron micrographs of lumbar DRG from 20-month-old YG8 rescue mice showing examples of: (A) giant vacuoles, (B) chromatolysis, and (C) lipofuscin deposits within the large neuronal cell bodies. Also detected within the lumbar DRG are instances of: (D) complete demyelination of a large axon with its associated Schwann cell and (E) large axonal swelling with reduced myelination. (F) Electron micrograph of cardiac muscle from a 20-month-old YG8 rescue mouse showing lipofuscin deposition and lysosomes disrupting an ordered array of mitochondria. Scale bars represent 10 μm.

Decreased aconitase activity and mitochondrial respiratory chain function

Previous studies of FRDA patient and mouse model tissues have demonstrated impaired activity of the iron–sulfur cluster (ISC)-containing aconitase enzyme and mitochondrial respiratory chain (MRC) complexes I, II, and III, but not the non-ISC-containing MRC complex IV [18,26]. Examination of heart tissue samples from 6-month-old YG8 rescue mice detected a decrease in aconitase activity to approximately 66% of wild-type mouse levels ($p<0.05$) (Fig. 7). Decreases in MRC complex I and II/III activity were also detected (79 and 75% of controls, respectively), although not to significant levels. In contrast, isolated MRC complex II and MRC complex IV activities showed no change. These data are in general agreement with the previous reports of FRDA patient and mouse model samples. However, the isolated MRC complex II activity was not decreased in the YG8 rescue mice, as has previously been described in conditional knockout mouse models [18,20]. Therefore, it is possible that the level of frataxin reduction in these samples is only just sufficient to induce changes in the most sensitive enzyme, aconitase. The impaired aconitase activity may be due to either reduced ISC formation or oxidative damage.

Oxidative stress

To detect potential oxidative stress in our FRDA models, we determined the levels of oxidized proteins and malondialdehyde (MDA; a marker of lipoperoxides) in YG22 and YG8 rescue mouse cerebrum, cerebellum, heart, and skeletal muscle tissues compared with wild-type controls. Oxidized proteins were increased in all samples from both YG22 and YG8 rescue mice (Fig. 8A). The most prominent significant increases were

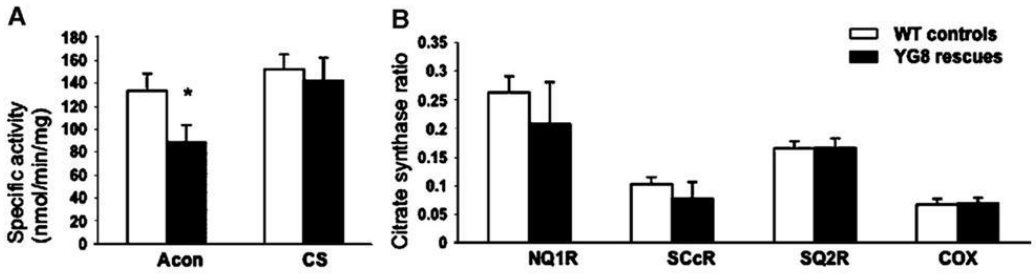

Fig. 7. Mitochondrial respiratory chain and aconitase activities in heart tissue from 6-month-old YG8 rescue mutant and control mice. (A) The specific activities of aconitase (Acon) and citrate synthase (CS). CS activities were divided by 10 ($n=6$). (B) The mitochondrial respiratory chain (MRC) activities expressed as a ratio with citrate synthase; MRC I, NADH coenzyme Q1 reductase (NQ1R); MRC II/III, succinate cytochrome *c* reductase (SCcR); MRC II, succinate coenzyme Q2 reductase (SQ2R); and MRC IV, cytochrome oxidase (COX). COX/CS ratio was multiplied by a factor of 10 ($n=4$). Activities are expressed as means±SEM. *$p=0.03$.

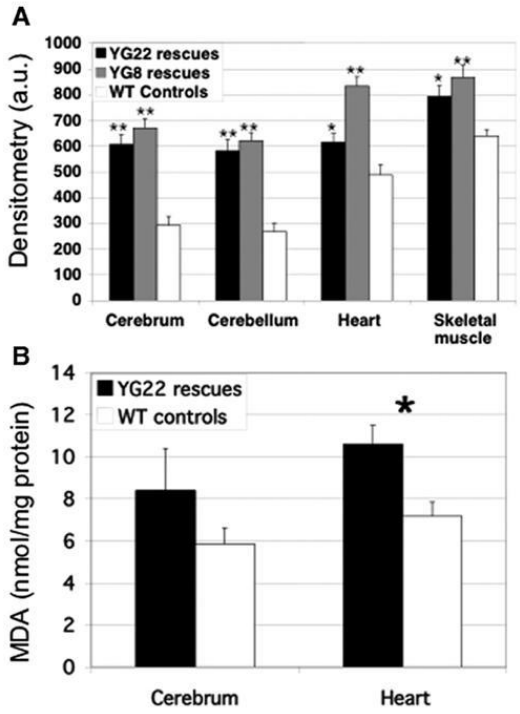

Fig. 8. Oxidative stress. (A) Oxyblot analysis detects protein oxidation in cerebrum, cerebellum, heart, and skeletal muscle tissues of 6- to 9-month old YG22 and YG8 rescue mice, compared with wild-type controls, measured in arbitrary units (a.u.) of densitometry ($n=8$–12). Error bars indicate SEM. *$p<0.05$, **$p<0.01$. (B) TBARS analysis shows levels of MDA (nmol/mg of protein) as a marker of lipoperoxidation in YG22 cerebrum and heart tissue compared with wild-type controls ($n=6$). Error bars indicate SEM. *$p<0.05$.

detected in the cerebrum and cerebellum of both lines ($p<0.01$), with lesser, but still significant, increases also detected in the heart and skeletal muscle of both YG8 ($p<0.01$) and YG22 ($p<0.05$) mice. The finding of increased oxidized proteins in the YG22 cerebrum is somewhat at odds with our previous finding of an increased level of frataxin protein in this tissue, suggesting reduced functional efficiency of the transgenic human frataxin protein. Increased lipid peroxidation, as determined by MDA levels, was also detected in cerebrum and heart samples from YG22 rescue mice, but only the heart showed a statistically significant increase ($p<0.05$) (Fig. 8B).

Discussion

Although the exact mechanisms that cause FRDA are still under investigation, several specific features of FRDA molecular pathology are now well established. Thus, the majority of FRDA patients are homozygous for GAA repeat expansion mutations within intron 1 of the *FXN* gene, leading to decreased levels of frataxin, subsequent oxidative stress, iron deposition, and ultimately neurodegeneration, primarily in the large sensory neurons of the DRG, and hypertrophic cardiomyopathy. We have been able to recapitulate many such features of FRDA disease in the mouse by establishing two lines of model mice that express frataxin only from GAA repeat expansion-containing *FXN* transgenes.

We have previously shown that the GAA repeat somatic instability pattern in our YG22 and YG8 transgenic mice closely resembles the GAA repeat dynamics in FRDA patients [24]. Our initial interpretation of the Western blot data from this study, which showed a more intense signal from the human frataxin compared to the mouse frataxin, led us to speculate on likely overexpression of human frataxin in YG22 or YG8 knockout rescue mice [24]. However, we have now demonstrated that both YG22 and YG8 rescue mice express comparatively decreased levels of human frataxin mRNA in all tissues and decreased levels of human frataxin protein in at least some tissues compared with endogenous mouse levels. Overall the YG8 rescue mice demonstrate slightly less frataxin mRNA and protein expression, combined with marginally higher amounts of protein oxidation, compared with the YG22 mice. Therefore, it is possible that the additional 90 GAA repeats in the YG8 line are responsible for producing a slightly more severe phenotype. Previous GAA expansion mutation knock-in studies have shown that mice expressing 25–36% endogenous mouse frataxin levels do not show an obvious pathological phenotype [22], although a clear microarray gene expression phenotype has been determined [27]. These mouse frataxin levels are similar to the human frataxin levels that we have determined in our heart samples. However, due to its slightly different amino acid composition, human frataxin may not function at 100% of endogenous mouse frataxin efficiency. Therefore, the levels of frataxin that we see here (67 and 42% in cerebellum, 37 and 25% in heart, and 10 and 9% in skeletal muscle of YG22 and YG8 rescue mice, respectively) may in fact represent an even more "functional" decrease, resulting in the pathological phenotype that we describe.

Age-related somatic increases in GAA repeats have previously been detected in the cerebrum, brain stem, and cerebellum of both YG22 and YG8 transgenic mice, but no such increases were detected in the heart or skeletal muscle [24]. Therefore, the pattern of frataxin expression in our YG22 and YG8 rescue mice (highest in cerebrum and brain stem, lowest in skeletal muscle) is not likely to be entirely due to somatic increases in GAA repeat expansions. A similar pattern of "high brain and low skeletal muscle" frataxin expression has been reported in lines of human *FXN* BAC transgenic mice that contain normal-sized GAA repeats [28]. Thus, unknown tissue-specific regulatory factors would appear to be acting on human *FXN* transgenes within the context of the mouse. As yet there are insufficient data available on human tissue samples to determine if a similar differential pattern of frataxin expression is present in FRDA and thus how representative our mouse models are in this regard.

That being said, the differentially reduced levels of frataxin in our mouse models are sufficient to induce a mild FRDA-like pathological phenotype. Impaired aconitase activity, oxidative stress, and functional deficits are apparent, although not severe, and neuronal histopathology and iron deposition within the

heart are later progressive effects. This phenotype is indicative of the early effects of FRDA pathology that precede overt ataxia and the later development of hypertrophic cardiomyopathy. Indeed, these mild mouse models can be considered representative of the less severe, later onset cases of FRDA. The 190 and 190+90 GAA repeat expansion mutation sizes within our mouse models are also in keeping with the cases of later onset FRDA that have smaller GAA allele sizes of fewer than 200 repeats [29–33].

The vacuoles identified in the DRG of our mouse models appear similar to those in the "Cb" neuron-specific frataxin conditional knockout model reported by Simon et al. [20]. However, an additional finding within our models is the progression of vacuolar pathology from affected distal lumbar regions at only 6 months of age to more proximal cervical regions at 13–15 months. This resembles the dying-back phenomenon of neurodegeneration that is observed in FRDA patients. Although, to our knowledge, DRG vacuoles have not been described in FRDA patients, loss of large sensory DRG cell bodies is a hallmark of the disease. Thus, it is likely that we are identifying a milder or earlier effect in our mouse models, before the DRG neurons degenerate and are lost completely. The identification of lipofuscin deposition, chromatolysis, and swelling and demyelination of axons in the DRG can be explained by cells that are suffering from chronic oxidative damage. In this sense, our FRDA mouse models are similar to the mouse model of ataxia with vitamin E deficiency, which shows lipofuscin deposition in DRG of mice over 1 year of age, indicating chronic oxidative stress [34]. Although frataxin conditional knockout mouse models have reproduced many other features of FRDA pathology, there is currently some debate concerning oxidative stress status. Studies of neuronal and cardiac conditional knockout models indicate no, or insignificant, oxidative stress [35,36], whereas pancreatic and hepatic conditional knockout models demonstrate distinct oxidative stress [19,21]. Our own models demonstrate an obvious, but not severe, degree of oxidative stress. This may be due to the fact that our models have residual frataxin in all tissues, which may also be the case with the pancreatic and hepatic knockout models, but not the neuronal and cardiac knockout models, which have complete frataxin loss in specific tissues. Our mice also have a mitochondrial respiratory chain that shows only a slight overall functional deficit and, therefore, continues to produce damaging free radicals. The greater loss of aconitase activity than MRC complex activity deficits suggests that aconitase impairment is a prominent early feature, even in mild cases of FRDA. The increases that we found in CuZnSOD and MnSOD are generally consistent with a reaction to oxidative stress in our FRDA mouse model tissues. However, where there is the greatest decrease in frataxin (i.e., skeletal muscle) we actually see a decrease in both CuZnSOD and MnSOD. This indicates a different susceptibility or handling of this tissue to mild oxidative stress. The identification of iron deposition in the hearts of only our older mice confirms the later onset aspect of this pathology, as previously described for cardiac frataxin conditional knockout mouse mutants [18].

Understanding that FRDA is caused by an unstable GAA repeat sequence, leading to decreased levels of frataxin, has given rise to novel ideas for frataxin-increasing therapies. We believe that we have generated a GAA-repeat-based mouse model of FRDA that would be suitable for the investigation of many different therapeutic strategies. These include the possible use of iron chelators and antioxidants, targeted preferentially to the mitochondria [37,38], as well as novel drugs aimed at up-regulation of frataxin expression, such as hemin, butyric acid, and cisplatin [39,40]. However, the fact that our FRDA mouse models have been generated by the introduction of a GAA repeat expansion mutation also makes them amenable to novel therapeutic strategies aimed at interacting with and modifying the GAA repeat expansion itself.

Materials and methods

Production and genotyping of genetically modified mice

GAA repeat expansion-containing YG8 and YG22 transgenic mice [24] were first crossed with heterozygous *Fxn* knockout mice [17] to produce mice containing both the transgene and the knockout allele. A second cross with heterozygous *Fxn* knockout mice then produced viable FRDA model mice containing the human *FXN* transgene on an *Fxn* null background. Genotyping of GAA repeats and *Fxn* allele status was performed as previously described [24].

mRNA and protein expression analysis

mRNA was isolated and RT-PCR amplified for 25 cycles using human/mouse frataxin exon 3/4 primers FRT1 and RRTII, followed by digestion with mouse-specific *Bst*XI and human-specific *Afl*III restriction enzymes as previously described [23]. Mouse *Hprt* RT-PCR was also carried out for 25 cycles using the primers and conditions described by Puccio et al. [18]. DNA products were resolved in 3% agarose gels and UV images were analyzed by UN-SCAN-IT (Silk Scientific Corp.) densitometry.

Frataxin Western blot analysis was carried out using a recombinant anti-mature frataxin antibody (G. Isaya, Mayo Clinic) as previously described [23]. Other immunodetection was carried on the same Western blots using antibodies against actin (Sigma), porin (Cambridge Bioscience), MnSOD (Abcam), and CuZnSOD (Abcam). Densitometry was carried out using UN-SCAN-IT software (Silk Scientific Corp.).

Functional studies

Rotarod analysis was performed using a Ugo-Basille 7650 accelerating rotarod treadmill apparatus. Mutant and control littermate mice ages 3, 6, 9, and 12 months (n=5–10) were placed on the rod and four trials were performed with the speed of the rotation gradually increasing from 4 to 40 rpm over a period of approximately 3–5 min. A period of 10 min rest was given between each trial. The time taken for each mouse to fall from the rod was recorded. Grip strength was assessed by holding mice by the base of the tail, while their forepaws gripped onto a horizontal bar that was attached to a tension spring. The mice were gently pulled backward until they let go of the bar and the distance pulled in millimeters was recorded. Locomotor activity was assessed by placing the mice in a gridded open-field Perspex box and the number of gridded squares entered by the mouse over a period of 20 s was recorded.

Electrophysiology

Electrophysiological recordings were carried out on anesthetized 20-month-old YG8 rescue mice, 9- to 14-month-old YG22 rescue mice, and wild-type controls. Motor nerve conduction was investigated by placing electrodes in the hind-paw muscle and stimulating the sciatic nerve. Measurements of amplitude,

distal latency, and proximal latency were taken, and the motor conduction velocity was then determined. Sensory nerve conduction was investigated by placing electrodes at two positions in the tail skin and stimulating the caudal nerve. Measurements of the sensory action potential were taken, and the sensory conduction velocity was then determined.

Histology

For histological preparations, terminally anesthetized mice were fixed by intracardial perfusion with 4% paraformaldehyde in phosphate-buffered saline (PBS). The fixed mouse tissues were dissected, embedded in paraffin wax, and sectioned by standard methods. Sections were deparaffinized with Histoclear (National Diagnostics) and slides were stained with hematoxylin and eosin or trichrome Masson stains. Perl's technique was used to detect ferric iron as previously described [17].

Electron microscopy

Mice of 20 months of age were perfused via a cannula in the heart with 1% glutaraldehyde and 1% paraformaldehyde plus 1% dextran, all in 0.1 M PIPES buffer. Tissues were dissected out, fixed for several hours in the same solution, and then postfixed overnight in 1% osmium tetroxide +1.5% potassium ferricyanide and 3% sodium iodate. Tissues were then dehydrated through increasing concentrations of ethanol and embedded in Durcupan via 1,2-epoxy propane. Thin sections for light microscopy were stained with thionin and acridine orange and ultrathin sections for electron microscopy were contrasted with uranyl acetate and lead citrate.

Biochemical measurements

Dissected mouse heart tissues were snap-frozen in liquid nitrogen. Mitochondrial respiratory chain and aconitase activities were determined as previously described [26].

Oxidative stress

Protein lysates were prepared according to Campuzano et al. [3]. For each assay, 10 μg of protein was used and the concentration was determined by using the BCA Protein Assay Reagent Kit (Pierce). Proteins were then modified by the use of the OxyBlot Protein Oxidation Detection Kit (Chemicon International). Duplicate samples were used for each assay and controls of unmodified samples were also included. After the assay was performed according to the manufacturer's instructions, each sample was diluted to 100 μl in 1× Laemmli buffer [41], with 2-mercaptoethanol and no added glycerol. Samples were then applied to a slot-blot apparatus and washed with the same buffer, followed by electroblot transfer buffer. The filters were air-dried and treated with the antibody provided in the kit and subsequently visualized on X-OMAT X-ray film. Densitometry was performed using UN-SCAN-IT software (Silk Scientific Corp.) and the final values were calculated as ratios to the protein concentration used per assay.

TBARS (thiobarbituric acid-reactive substances) assay for MDA

Using a modification of the method described by Ledwozyw et al. [42], brain and heart tissues from wild-type and mutant mice were homogenized to 20% (w/v) in Dulbecco's PBS. Samples were then centrifuged at 2000*g* for 10 min and supernatants were collected. Each supernatant (0.1 ml) was mixed with 20% (w/v) trichloroacetic acid in 0.6 M HCl and left at room temperature for 15 min. This was then mixed with thiobarbituric acid (TBA; prepared by dissolving 0.5 g of TBA in 6 ml of 1 M NaOH and then adding 69 ml of water). The mixture was then heated to 100°C for 30 min, cooled to room temperature for 10 min, and then extracted with 0.8 ml of *n*-butanol. Samples were vortexed and then centrifuged at 1500*g* for 10 min. The upper organic phase was collected and the absorbance of each sample was determined at 532 nm vs *n*-butanol. The concentration of MDA (which forms an adduct with TBA) was determined from a standard curve, obtained from using different concentrations of MDA (Aldrich). The protein concentration of each tissue homogenate supernatant was determined by the BCA Protein Assay (Pierce) and the final value of MDA in each tissue was presented as nmol/mg of protein used.

Statistical analysis

Mendelian ratios were determined using χ^2 analysis, rotarod analysis was carried out using ANOVA with repeated measures, and all other functional, mRNA, Western blot, oxyblot, TBARS, and enzyme activities were analyzed using the Student *t* test.

Acknowledgments

We thank Michel Koenig and Helene Puccio (INSERM) for the *Fxn* knockout mice and helpful discussion, Grazia Isaya (Mayo Clinic and Foundation) for the kind gift of anti-human recombinant mature frataxin antibody, and Sebastian Brandner (UCL) for analysis of neuronal histological data. This work was supported by The Wellcome Trust, Friedreich's Ataxia Research Alliance, Seek A Miracle/Muscular Dystrophy Association, and Ataxia, UK. S.A. is supported by The Wellcome Trust (Grant 070235).

References

[1] V. Campuzano, L. Montermini, M.D. Molto, L. Pianese, M. Cossee, F. Cavalcanti, E. Monros, F. Rodius, F. Duclos, A. Monticelli, F. Zara, J. Canizares, H. Koutnikova, S.I. Bidichandani, C. Gellera, A. Brice, P. Trouillas, G. De Michele, A. Filla, R. De Frutos, F. Palau, P.I. Patel, S. Di Donato, J.L. Mandel, S. Cocozza, M. Koenig, M. Pandolfo, Friedreich's ataxia: autosomal recessive disease caused by an intronic GAA triplet repeat expansion, Science 271 (1996) 1423–1427.

[2] M. Pandolfo, The molecular basis of Friedreich ataxia, Adv. Exp. Med. Biol. 516 (2002) 99–118.

[3] V. Campuzano, L. Montermini, Y. Lutz, L. Cova, C. Hindelang, S. Jiralerspong, Y. Trottier, S.J. Kish, B. Faucheux, P. Trouillas, F.J. Authier, A. Durr, J.L. Mandel, A. Vescovi, M. Pandolfo, M. Koenig, Frataxin is reduced in Friedreich ataxia patients and is associated with mitochondrial membranes, Hum. Mol. Genet. 6 (1997) 1771–1780.

[4] P. Gonzalez-Cabo, R.P. Vazquez-Manrique, M.A. Garcia-Gimeno, P. Sanz, F. Palau, Frataxin interacts functionally with mitochondrial electron transport chain proteins, Hum. Mol. Genet. 14 (2005) 2091–2098.

[5] A.L. Bulteau, H.A. O'Neill, M.C. Kennedy, M. Ikeda-Saito, G. Isaya, L.I. Szweda, Frataxin acts as an iron chaperone protein to modulate mitochondrial aconitase activity, Science 305 (2004) 242–245.

[6] J. Gerber, U. Muhlenhoff, R. Lill, An interaction between frataxin and Isu1/Nfs1 that is crucial for Fe/S cluster synthesis on Isu1, EMBO Rep. 4 (2003) 906–911.

[7] T. Yoon, J.A. Cowan, Frataxin-mediated iron delivery to ferrochelatase in the final step of heme biosynthesis, J. Biol. Chem. 279 (2004) 25943–25946.

[8] R.A. Schoenfeld, E. Napoli, A. Wong, S. Zhan, L. Reutenauer, D. Morin, A.R. Buckpitt, F. Taroni, B. Lonnerdal, M. Ristow, H. Puccio, G.A. Cortopassi, Frataxin deficiency alters heme pathway transcripts and decreases mitochondrial heme metabolites in mammalian cells, Hum. Mol. Genet. 14 (2005) 3787–3799.

[9] O. Gakh, S. Park, G. Liu, L. Macomber, J.A. Imlay, G.C. Ferreira, G. Isaya, Mitochondrial iron detoxification is a primary function of frataxin that limits oxidative damage and preserves cell longevity, Hum. Mol. Genet. 15 (2005) 467–479.

[10] A. Durr, M. Cossee, Y. Agid, V. Campuzano, C. Mignard, C. Penet, J.L. Mandel, A. Brice, M. Koenig, Clinical and genetic abnormalities in patients with Friedreich's ataxia, N. Engl. J. Med. 335 (1996) 1169–1175.

[11] A. Filla, G. De Michele, F. Cavalcanti, L. Pianese, A. Monticelli, G. Campanella, S. Cocozza, The relationship between trinucleotide (GAA)

repeat length and clinical features in Friedreich ataxia, Am. J. Hum. Genet. 59 (1996) 554–560.
[12] E. Monros, M.D. Molto, F. Martinez, J. Canizares, J. Blanca, J.J. Vilchez, F. Prieto, R. de Frutos, F. Palau, Phenotype correlation and intergenerational dynamics of the Friedreich ataxia GAA trinucleotide repeat, Am. J. Hum. Genet. 61 (1997) 101–110.
[13] S.I. Bidichandani, T. Ashizawa, P.I. Patel, The GAA triplet-repeat expansion in Friedreich ataxia interferes with transcription and may be associated with an unusual DNA structure, Am. J. Hum. Genet. 62 (1998) 111–121.
[14] E. Grabczyk, K. Usdin, The GAA*TTC triplet repeat expanded in Friedreich's ataxia impedes transcription elongation by T7 RNA polymerase in a length and supercoil dependent manner, Nucleic Acids Res. 28 (2000) 2815–2822.
[15] N. Sakamoto, K. Ohshima, L. Montermini, M. Pandolfo, R.D. Wells, Sticky DNA, a self-associated complex formed at long GAA*TTC repeats in intron 1 of the frataxin gene, inhibits transcription, J. Biol. Chem. 276 (2001) 27171–27177.
[16] A. Saveliev, C. Everett, T. Sharpe, Z. Webster, R. Festenstein, DNA triplet repeats mediate heterochromatin-protein-1-sensitive variegated gene silencing, Nature 422 (2003) 909–913.
[17] M. Cossee, H. Puccio, A. Gansmuller, H. Koutnikova, A. Dierich, M. LeMeur, K. Fischbeck, P. Dolle, M. Koenig, Inactivation of the Friedreich ataxia mouse gene leads to early embryonic lethality without iron accumulation, Hum. Mol. Genet. 9 (2000) 1219–1226.
[18] H. Puccio, D. Simon, M. Cossee, P. Criqui-Filipe, F. Tiziano, J. Melki, C. Hindelang, R. Matyas, P. Rustin, M. Koenig, Mouse models for Friedreich ataxia exhibit cardiomyopathy, sensory nerve defect and Fe–S enzyme deficiency followed by intramitochondrial iron deposits, Nat. Genet. 27 (2001) 181–186.
[19] M. Ristow, H. Mulder, D. Pomplun, T.J. Schulz, K. Muller-Schmehl, A. Krause, M. Fex, H. Puccio, J. Muller, F. Isken, J. Spranger, D. Muller-Wieland, M.A. Magnuson, M. Mohlig, M. Koenig, A.F. Pfeiffer, Frataxin deficiency in pancreatic islets causes diabetes due to loss of beta cell mass, J. Clin. Invest. 112 (2003) 527–534.
[20] D. Simon, H. Seznec, A. Gansmuller, N. Carelle, P. Weber, D. Metzger, P. Rustin, M. Koenig, H. Puccio, Friedreich ataxia mouse models with progressive cerebellar and sensory ataxia reveal autophagic neurodegeneration in dorsal root ganglia, J. Neurosci. 24 (2004) 1987–1995.
[21] R. Thierbach, T.J. Schulz, F. Isken, A. Voigt, B. Mietzner, G. Drewes, J.C. von Kleist-Retzow, R.J. Wiesner, M.A. Magnuson, H. Puccio, A.F. Pfeiffer, P. Steinberg, M. Ristow, Targeted disruption of hepatic frataxin expression causes impaired mitochondrial function, decreased life span and tumor growth in mice, Hum. Mol. Genet. 14 (2005) 3857–3864.
[22] C.J. Miranda, M.M. Santos, K. Ohshima, J. Smith, L. Li, M. Bunting, M. Cossee, M. Koenig, J. Sequeiros, J. Kaplan, M. Pandolfo, Frataxin knockin mouse, FEBS Lett 512 (2002) 291–297.
[23] M.A. Pook, S. Al-Mahdawi, C.J. Carroll, M. Cossee, H. Puccio, L. Lawrence, P. Clark, M.B. Lowrie, J.L. Bradley, J.M. Cooper, M. Koenig, S. Chamberlain, Rescue of the Friedreich's ataxia knockout mouse by human YAC transgenesis, Neurogenetics 3 (2001) 185–193.
[24] S. Al-Mahdawi, R.M. Pinto, P. Ruddle, C. Carroll, Z. Webster, M. Pook, GAA repeat instability in Friedreich ataxia YAC transgenic mice, Genomics 84 (2004) 301–310.
[25] A. Verloes, M. Massin, J. Lombert, B. Grattagliano, D. Soyeur, J. Rigo, L. Koulischer, F. van Hoof, Nosology of lysosomal glycogen storage diseases without in vitro acid maltase deficiency: delineation of a neonatal form, Am. J. Med. Genet. 72 (1997) 135–142.
[26] J.L. Bradley, J.C. Blake, S. Chamberlain, P.K. Thomas, J.M. Cooper, A.H. Schapira, Clinical, biochemical and molecular genetic correlations in Friedreich's ataxia, Hum. Mol. Genet. 9 (2000) 275–282.
[27] G. Coppola, S.-H. Choi, M.M. Santos, C.J. Miranda, D. Tentler, E.M. Wexler, M. Pandolfo, D.H. Geschwind, Gene expression profiling in frataxin deficient mice: microarray evidence for significant expression changes without detectable neurodegeneration, Neurobiol. Dis. 22 (2006) 302–311.
[28] J.P. Sarsero, L. Li, T.P. Holloway, L. Voullaire, S. Gazeas, K.J. Fowler, D.M. Kirby, D.R. Thorburn, A. Galle, S. Cheema, M. Koenig, R. Williamson, P.A. Ioannou, Human BAC-mediated rescue of the Friedreich ataxia knockout mutation in transgenic mice, Mamm. Genome 15 (2004) 370–382.
[29] J. Berciano, I. Mateo, C. De Pablos, J.M. Polo, O. Combarros, Friedreich ataxia with minimal GAA expansion presenting as adult-onset spastic ataxia, J. Neurol. Sci. 194 (2002) 75–82.
[30] C. Gellera, D. Pareyson, B. Castellotti, F. Mazzucchelli, B. Zappacosta, M. Pandolfo, S. Di Donato, Very late onset Friedreich's ataxia without cardiomyopathy is associated with limited GAA expansion in the ×25 gene, Neurology 49 (1997) 1153–1155.
[31] S.D. Lhatoo, D.G. Rao, N.M. Kane, I.E. Ormerod, Very late onset Friedreich's presenting as spastic tetraparesis without ataxia or neuropathy, Neurology 56 (2001) 1776–1777.
[32] D.O. McDaniel, B. Keats, V.V. Vedanarayanan, S.H. Subramony, Sequence variation in GAA repeat expansions may cause differential phenotype display in Friedreich's ataxia, Mov. Disord. 16 (2001) 1153–1158.
[33] S. Sorbi, P. Forleo, E. Cellini, S. Piacentini, A. Serio, B. Guarnieri, C. Petruzzi, Atypical Friedreich ataxia with a very late onset and an unusual limited GAA repeat, Arch. Neurol. 57 (2000) 1380–1382.
[34] T. Yokota, K. Igarashi, T. Uchihara, K. Jishage, H. Tomita, A. Inaba, Y. Li, H. Suzuki, H. Mizusawa, H. Arai, Delayed-onset ataxia in mice lacking α-tocopherol transfer protein: model for neuronal degeneration caused by chronic oxidative stress, Proc. Natl. Acad. Sci. USA 98 (2001) 15185–15190.
[35] H. Seznec, D. Simon, C. Bouton, L. Reutenauer, A. Hertzog, P. Golik, V. Procaccio, M. Patel, J.C. Drapier, M. Koenig, H. Puccio, Friedreich ataxia: the oxidative stress paradox, Hum. Mol. Genet. 14 (2005) 463–474.
[36] H. Seznec, D. Simon, L. Monassier, P. Criqui-Filipe, A. Gansmuller, P. Rustin, M. Koenig, H. Puccio, Idebenone delays the onset of cardiac functional alteration without correction of Fe–S enzymes deficit in a mouse model for Friedreich ataxia, Hum. Mol. Genet. 13 (2004) 1017–1024.
[37] M.L. Jauslin, T. Meier, R.A. Smith, M.P. Murphy, Mitochondria-targeted antioxidants protect Friedreich ataxia fibroblasts from endogenous oxidative stress more effectively than untargeted antioxidants, FASEB J. 17 (2003) 1972–1974.
[38] D.R. Richardson, C. Mouralian, P. Ponka, E. Becker, Development of potential iron chelators for the treatment of Friedreich's ataxia: ligands that mobilize mitochondrial iron, Biochim. Biophys. Acta 1536 (2001) 133–140.
[39] J.P. Sarsero, L. Li, H. Wardan, K. Sitte, R. Williamson, P.A. Ioannou, Upregulation of expression from the FRDA genomic locus for the therapy of Friedreich ataxia, J. Gene Med. 5 (2003) 72–81.
[40] M. Voncken, P. Ioannou, M.B. Delatycki, Friedreich ataxia—update on pathogenesis and possible therapies, Neurogenetics 5 (2004) 1–8.
[41] U.K. Laemmli, Cleavage of structural proteins during the assembly of the head of bacteriophage T4, Nature 227 (1970) 680.
[42] A.M.J. Ledwozyw, A. Stepien, A. Kadziolka, The relationship between plasma triglycerides, cholesterol, total lipids and lipid peroxidation products during human atherosclerosis, Clin. Chim. Acta 155 (1986) 275–284.

Human Molecular Genetics, 2008, Vol. 17, No. 5 **735–746**
doi:10.1093/hmg/ddm346
Advance Access published on November 27, 2007

The Friedreich ataxia GAA repeat expansion mutation induces comparable epigenetic changes in human and transgenic mouse brain and heart tissues

Sahar Al-Mahdawi, Ricardo Mouro Pinto, Ozama Ismail, Dhaval Varshney, Stefania Lymperi, Chiranjeevi Sandi, Daniah Trabzuni and Mark Pook*

Hereditary Ataxia Group, Centre for Cell & Chromosome Biology and Brunel Institute of Cancer Genetics & Pharmacogenomics, Division of Biosciences, School of Health Sciences & Social Care, Brunel University, Uxbridge UB8 3PH, UK

Received September 20, 2007; Revised November 17, 2007; Accepted November 25, 2007

Friedreich ataxia (FRDA) is caused by a homozygous GAA repeat expansion mutation within intron 1 of the *FXN* gene, leading to reduced expression of frataxin protein. Evidence suggests that the mutation may induce epigenetic changes and heterochromatin formation, thereby impeding gene transcription. In particular, studies using FRDA patient blood and lymphoblastoid cell lines have detected increased DNA methylation of specific CpG sites upstream of the GAA repeat and histone modifications in regions flanking the GAA repeat. In this report we show that such epigenetic changes are also present in FRDA patient brain, cerebellum and heart tissues, the primary affected systems of the disorder. Bisulfite sequence analysis of the *FXN* flanking GAA regions reveals a shift in the FRDA DNA methylation profile, with upstream CpG sites becoming consistently hypermethylated and downstream CpG sites becoming consistently hypomethylated. We also identify differential DNA methylation at three specific CpG sites within the *FXN* promoter and one CpG site within exon 1. Furthermore, we show by chromatin immunoprecipitation analysis that there is overall decreased histone H3K9 acetylation together with increased H3K9 methylation of FRDA brain tissue. Further studies of brain, cerebellum and heart tissues from our GAA repeat expansion-containing FRDA YAC transgenic mice reveal comparable epigenetic changes to those detected in FRDA patient tissue. We have thus developed a mouse model that will be a valuable resource for future therapeutic studies targeting epigenetic modifications of the *FXN* gene to increase frataxin expression.

INTRODUCTION

FRDA is an autosomal recessive neurodegenerative disorder that is predominantly caused by a homozygous GAA repeat expansion mutation within intron 1 of the *FXN* gene (1). Normal individuals have 5–30 GAA repeat sequences, whereas affected individuals have from approximately 70 to more than 1000 GAA triplets (2). The GAA repeat shows somatic instability, with progressive expansion throughout life, particularly in the cerebellum and dorsal root ganglia (DRG) (3–5). The effect of the GAA expansion mutation is to reduce the expression of frataxin (6), a mitochondrial protein that acts as an iron chaperone in iron–sulphur cluster and heme biosynthesis (7–9). Frataxin insufficiency leads to oxidative stress, mitochondrial iron accumulation and resultant cell death, with the primary site of pathology being in the large sensory neurons of the DRG and the dentate nucleus of the cerebellum (10). The outcome is progressive spinocerebellar neurodegeneration, causing symptoms of ataxia, dysarthria, muscle weakness and sensory loss, together with cardiomyopathy and diabetes. At present there is no effective treatment for FRDA, and affected individuals

*To whom correspondence should be addressed. Tel: +44 1895267243; Fax: +44 1895274348; Email: mark.pook@brunel.ac.uk

generally die in early adulthood from the associated heart disease.

Preclinical and clinical trials using antioxidants and iron chelators have demonstrated some limited success in alleviating FRDA heart pathology (11–16). However, a more effective overall therapeutic strategy may be to target the immediate effects of the GAA repeat expansion mutation to restore normal levels of frataxin expression. The exact mechanism by which the GAA repeat expansion leads to decreased frataxin expression is unknown, but several models have been put forward. First, it has been suggested that the GAA repeat expansion may adopt abnormal DNA or DNA/RNA hybrid structures that interfere with *FXN* gene transcription (17–20). Secondly, there is evidence that GAA repeat expansions produce a heterochromatin-mediated gene silencing effect (21). Epigenetic mechanisms, such as DNA methylation and the associated deacetylation and methylation of histones are known to affect gene expression by chromatin remodelling (22), and these epigenetic changes are likely to underpin any GAA repeat-induced heterochromatin-mediated gene silencing effects. In support of this hypothesis, research has recently shown increased DNA methylation of three specific CpG sites immediately upstream of the expanded GAA repeat sequence in FRDA patient lymphoblastoid cell lines and primary lymphocytes, and one of the three CpG sites was identified as an important enhancer of frataxin expression (23). Other studies have identified specific histone modifications that are associated with gene silencing within the GAA repeat expansion-flanking regions of the *FXN* intron 1 sequence in FRDA lymphoblastoid cell lines and primary lymphocytes (23,24). These changes include deacetylation of histone H3 and H4 lysine residues and increased di- and trimethylation of H3K9. Based on the hypothesis that the acetylation state of the core histones is responsible for gene silencing, novel histone deacetylase (HDAC) inhibitor compounds have been developed and have been shown to increase *FXN* transcription in FRDA lymphoblastoid cells and primary lymphocytes (24).

These previous epigenetic studies have provided valuable insights into the possible mechanism of GAA-induced transcription inhibition, but they do not address the issue of whether such epigenetic changes are actually present in the most clinically relevant FRDA tissues. Therefore, we decided to investigate epigenetic profiles of the *FXN* gene in FRDA patient autopsy brain, cerebellum and heart tissue. By bisulfite sequencing and ChIP analysis we now report changes in DNA methylation and histone modifications that are consistent with inhibition of *FXN* transcription. With a view to future epigenetic-based FRDA therapies, we also investigated the *FXN* epigenetic profiles within brain, cerebellum and heart tissue from our Y47, YG8 and YG22 FRDA YAC transgenic mouse models (25–27). We find that the GAA repeat expansion-containing FRDA mouse models (YG8 and YG22) exhibit comparable epigenetic changes to those detected in FRDA patient tissue. Therefore, these are excellent FRDA mouse models in which to investigate the therapeutic effects of epigenetically acting compounds, such as novel HDAC inhibitors or DNA methylation inhibitors.

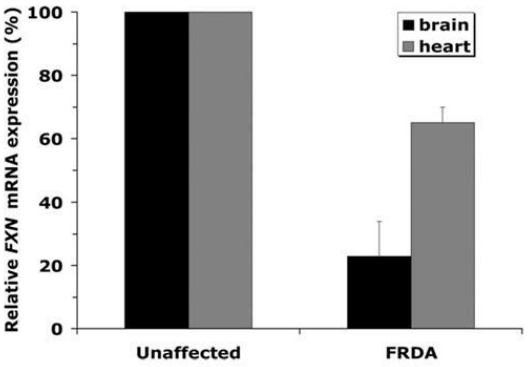

Figure 1. Quantitative RT–PCR analysis of *FXN* mRNA isolated from brain and heart autopsy samples of two FRDA patients (750/650 and 700/700 GAA repeats) and two unaffected individuals. The mean values of FRDA patient tissue data are normalized to the mean *FXN* mRNA level of the unaffected individuals taken as 100%. Two individual cDNA samples were analysed for each tissue and each reaction was carried out in triplicate. Bars represent SEMs.

RESULTS

FXN gene DNA methylation profiles are distinctly altered in human FRDA brain and heart tissues

A previous investigation of the *FXN* gene in FRDA patient lymphoblastoid cell lines and blood samples has detected hypermethylation at three specific CpG sites immediately upstream of the expanded GAA repeat sequence. One of the three CpG sites was further identified as an important enhancer element for frataxin expression (23). This same study also reported a lack of any DNA methylation in the promoter region of either FRDA or unaffected cells.

However, cultured cells are known to often develop non-physiological DNA methylation profiles. Furthermore, FRDA is a systemic disorder that is known to have differentially affected tissues and cell types. Therefore, we chose to investigate the DNA methylation status in two of the primary affected tissues in FRDA, namely brain and heart. We obtained brain and heart autopsy tissues from two FRDA patients (GAA repeat sizes of 750/650 and 700/700) and two unaffected individuals, and we first determined the *FXN* transcription levels of the samples by quantitative RT–PCR. The FRDA brain and heart samples showed mean values of 23 and 65% *FXN* expression, respectively, compared with the unaffected samples (Fig. 1). We then analysed the DNA methylation status of the samples by performing bisulfite sequence analysis of three regions of the *FXN* gene: (i) a 475 bp sequence that encompasses part of the *FXN* promoter, exon 1 and start of intron 1, containing 59 CpG sites; (ii) a 286 bp sequence upstream of the GAA repeat, containing 8 CpG sites and (iii) a 275 bp sequence downstream of the GAA repeat, containing 12 CpG sites (Fig. 2). A comparison of the bisulfite sequences from the FRDA patient and control brain and heart tissues reveals a certain degree of DNA methylation in all eight of the upstream GAA CpG sites (Fig. 3C and D) and all 12 of the downstream GAA CpG sites (Fig. 3E and F). However, the data show a

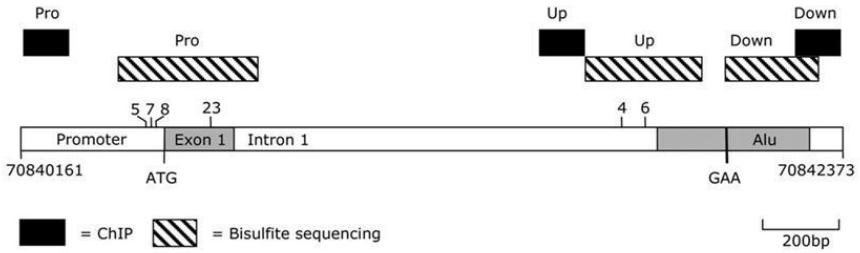

Figure 2. Schematic representation of 2.2 kb at the 5′ end of the *FXN* gene, indicating the promoter/exon 1 (Pro), upstream GAA (Up) and downstream GAA (Down) regions that were analysed by ChIP (black boxes) and bisulfite sequencing (hatched boxes). Numbers above indicate the position of CpG sites within the promoter and upstream GAA regions. The positions of the ATG translation start codon, exon 1 open reading frame and GAA repeat sequence within the Alu repeat sequence are shown. Numbers below indicate the chromosome 9 base pair numbering according to the 2006 build of the UCSC human DNA sequence database.

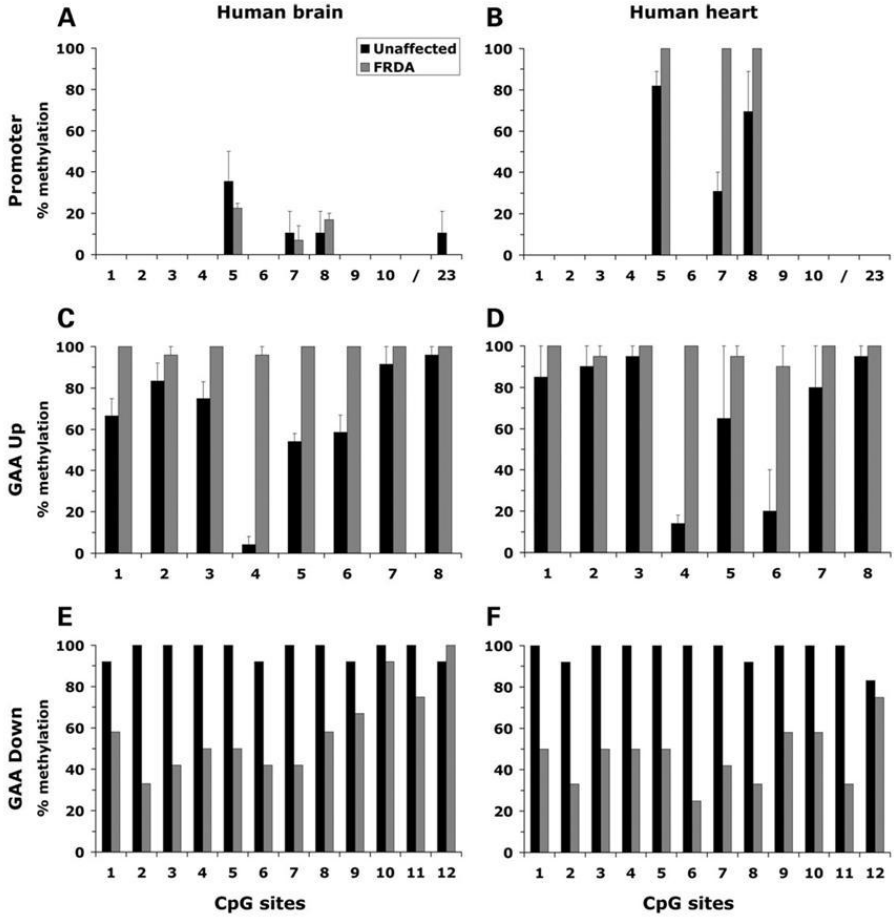

Figure 3. DNA methylation analysis of the *FXN* promoter (**A** and **B**), upstream GAA (**C** and **D**) and downstream GAA (**E** and **F**) regions of human brain and heart tissues. In each case for the *FXN* promoter and upstream GAA regions the mean percentage (+SEM) of methylated CpG sites is shown as determined from the analysis of two FRDA patients and two unaffected individuals, with 7–12 independent cloned DNA sequences analysed for each. For the downstream region the percentage of methylated CpG sites has been determined from one FRDA patient and one unaffected individual (12 independent cloned DNA sequences analysed for each). Only eleven CpG sites are represented for the promoter region (A and B), as sites 11–22 and 24–59 did not show any methylation in either FRDA or unaffected samples in brain or heart. FRDA brain tissues and both FRDA and unaffected heart tissues did not show any DNA methylation at CpG site 23.

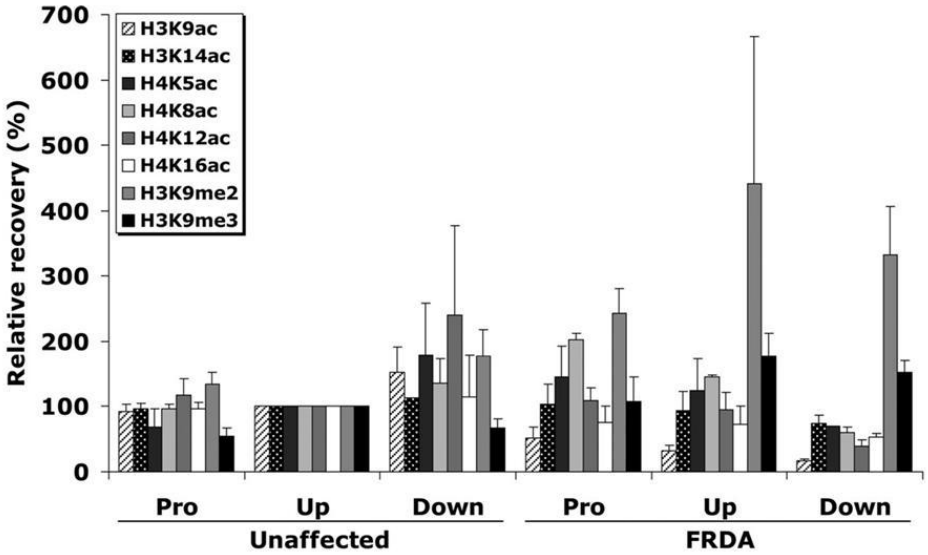

Figure 4. Analysis of histone modifications in human brain tissue. ChIP quantitative PCR results for the *FXN* promoter/exon1 (Pro), upstream GAA (Up) and downstream GAA (Down) amplified regions are represented as the relative amount of immunoprecipitated DNA compared with input DNA, having taken negligible −Ab control values into account. *FXN* values were normalized with human *GAPDH* and all values have been adjusted so that all of the Upstream GAA mean values from the unaffected individuals are 100%. In each case two individual ChIP samples from two FRDA patients and two unaffected controls were analysed in triplicate. The means and SEMs of these values are shown.

consistent shift in the DNA methylation pattern around the GAA repeat in both tissue types. The FRDA upstream GAA CpG sites are comparatively hypermethylated, whereas the FRDA downstream GAA CpG sites are comparatively hypomethylated (Fig. 3C–F). The greatest increases in DNA methylation within the upstream GAA region are seen at CpG sites 4, 5 and 6, the latter of which corresponds to the previously described E-box enhancer element (23). We observed 100% methylation at CpG site 6 in FRDA brain tissues (*FXN* mRNA level of 23%, Fig. 1) compared with a mean value of 90% methylation in heart tissue (*FXN* mRNA level of 65%, Fig. 1). Thus, the upstream GAA DNA methylation changes in both FRDA brain and heart are consistent with their proposed roles in inhibition of *FXN* transcription. However, the finding of decreased DNA methylation in the downstream GAA region (Fig. 3E and F) is somewhat unexpected, since all of the 12 CpG sites fall within an Alu repeat sequence and such sequences are usually repressed by heavy DNA methylation.

Another particularly interesting finding was the identification of differential DNA methylation at three specific CpG sites within the *FXN* promoter (sites 5, 7 and 8) and one CpG site within exon 1 (site 23) (Fig. 3A and B). All of the other 55 CpG sites in the total of 59 CpG sites analysed show complete lack of DNA methylation, as to be expected for a CpG island that is situated at the start of a gene. CpG sites 5, 7 and 8 show incomplete methylation in the unaffected heart, but complete methylation in the FRDA heart (Fig. 3B). Therefore, these CpG sites may be involved in reducing initiation of *FXN* gene transcription in FRDA heart. However, the DNA methylation pattern is different in brain tissue. Here we identified mean values of 10–35% DNA methylation at the four CpG sites in the unaffected tissues, but very little overall change of DNA methylation in FRDA tissues, or even loss of methylation at CpG sites 5 and 23 (Fig. 3A). Furthermore, the fact that we have identified some degree of DNA methylation at all in this region contrasts with the previous report that DNA methylation is absent in the *FXN* promoter region of both FRDA and unaffected lymphoblastoid cells (23). Therefore, we have shown that the influence of DNA methylation on *FXN* gene expression is likely to be complex, with some similarities (CpG site usage) but also some distinct differences (degree of CpG methylation) identified between different somatic tissues.

FXN gene histone modifications are altered in human FRDA brain tissue

Previous studies of the promoter, upstream GAA and downstream GAA regions of the *FXN* gene have identified specific histone modifications that are associated with gene silencing within the GAA repeat expansion-flanking regions of the *FXN* intron 1 sequence in FRDA lymphoblastoid cell lines and primary lymphocytes (23,24). We have now investigated acetylated histone H3 and H4 and methylated histone H3K9 modifications by ChIP analysis of the *FXN* promoter, upstream GAA and downstream GAA regions (Fig. 2) in autopsy brain tissues from two FRDA patients and two unaffected individuals. Our results show overall decreased histone H3 and H4 acetylation of FRDA brain tissue, particularly in the downstream GAA region (Fig.4). All of the six acetylated histone residues that we have examined show a GAA-induced gradient of

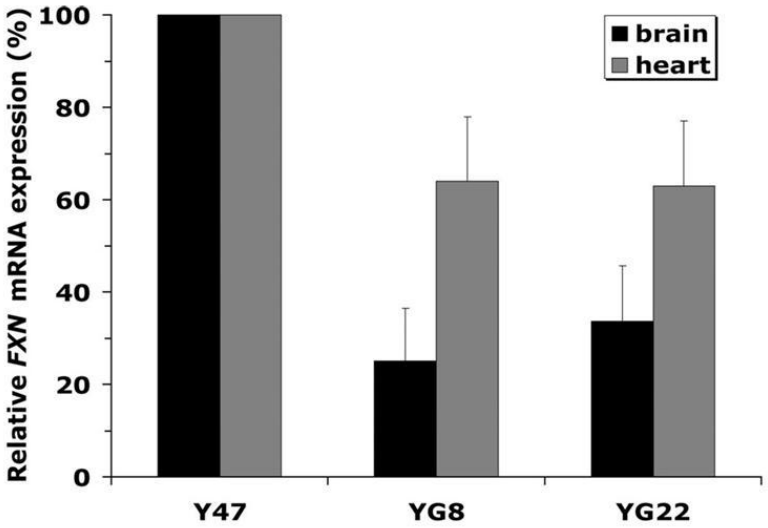

Figure 5. Quantitative RT–PCR analysis of transgenic *FXN* mRNA isolated from Y47 (9 GAA), YG8 (190+90 GAA) and YG22 (190 GAA) mouse brain and heart tissues. Data are normalized to the mean *FXN* mRNA level found in the non-GAA transgenic control samples taken as 100%. Two individual cDNA samples were analysed for each tissue from two mice of each line and each reaction was carried out in triplicate. The means and SEMs of these values are shown.

comparative acetylation that is highest in the *FXN* promoter and lowest in the downstream GAA region. The single most altered histone residue is H3K9, which exhibits progressive decreases in acetylation to comparative levels of 56, 32 and 11% in the *FXN* promoter, upstream GAA and downstream GAA regions, respectively. There is also a consistently increased H3K9 di- and tri-methylation of FRDA brain tissue in all three of the *FXN* gene regions (Fig. 4). These changes concur with the previous findings of increased H3K9 di- and tri-methylation in the upstream GAA region of other cell types (23,24). However, we have now extended these studies to show that in FRDA brain the H3K9 di- and tri-methylation spreads to both *FXN* promoter and downstream GAA regions.

DNA methylation profiles of *FXN* transgenic mouse brain and heart tissues resemble the profiles of human tissue

Having determined the epigenetic profiles around the human *FXN* gene, we then investigated the epigenetic profiles of the *FXN* transgene in brain and heart tissue isolated from YG8 and YG22 GAA repeat expansion-containing *FXN* YAC transgenic mice (26) compared with Y47 normal-sized GAA repeat-containing *FXN* YAC transgenic mice (27). Initial determination of *FXN* transgene expression showed YG8 (90+190 GAA repeats) and YG22 (190 GAA repeats) to have mean decreased mRNA levels of ~26 and 35% in brain and 57 and 56% in heart compared with Y47 (Fig. 5). Thus, inhibition of *FXN* expression in transgenic mouse brain and heart was comparable with the mean values of 23 and 65% observed in the human FRDA brain and heart samples, respectively (Fig. 1). DNA methylation analysis was then performed on the GAA repeat expansion-containing YG8 and YG22 GAA repeat transgenic mouse tissue samples compared with the Y47 non-GAA repeat controls (3–4 individual mice for each group). As the mouse transgenes consist of entire human *FXN* gene sequence, we were able to investigate the DNA methylation profiles of exactly the same three regions of the *FXN* gene that we had previously analysed in human tissue (Fig. 2). Our data show that the DNA methylation profiles of upstream GAA regions of both YG8 and YG22 transgenic mouse brain and heart tissues closely resemble those found in human tissues (Fig. 6C and D). Namely, there is a consistent hypermethylation of the upstream GAA region induced by the GAA repeat expansion, with the most prominent hypermethylation at CpG sites 4, 5 and 6. However, the degree of DNA methylation at CpG sites 4 and 6 in YG8 and YG22 transgenic mouse brain tissue is less than that observed in FRDA human brain tissue, and indeed YG8 shows no difference at all at CpG site 6. The downstream GAA region differs from the human situation in that there is hypermethylation at all CpG sites, which is retained upon introduction of the GAA repeat expansion (Fig. 6E and F). Thus, there is no GAA-induced decrease in DNA methylation as detected in the human tissues. The promoter/exon 1 regions of the *FXN* transgenes in both mouse brain and heart tissues show a similarity to the human tissues in that DNA methylation is found at only four specific CpG sites: 5, 7, 8 and 23 (Fig. 6A and B). However, the changes in the DNA profiles of these four CpG sites upon introduction of the GAA repeat expansion differ markedly from those found in the human tissues. This time, the brain tissue shows either no change (CpG sites 5 and 7) or an increase (CpG sites 8 and 23) in DNA methylation, whereas the heart tissue shows an overall decrease in DNA methylation. Assessment of the entire mouse DNA methylation data indicates a similar overall DNA methylation profile around the start of the *FXN* gene that is consistent with inhibition of *FXN* transcription.

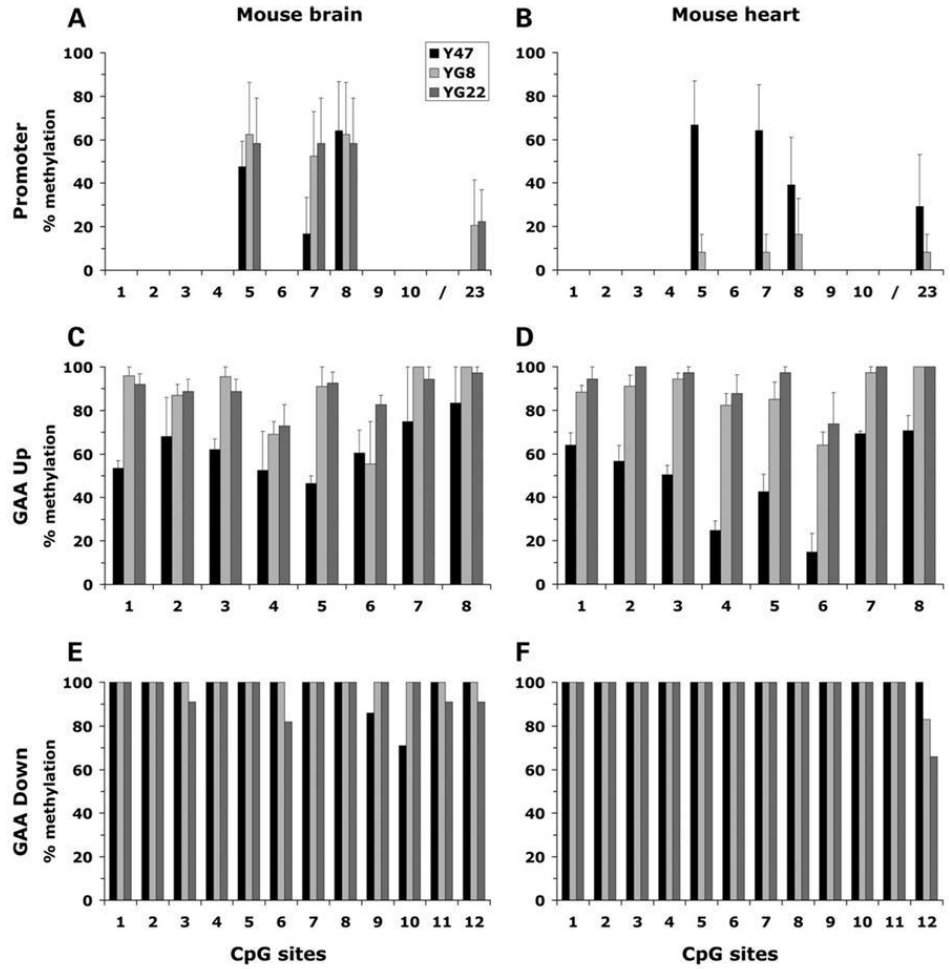

Figure 6. DNA methylation analysis of the *FXN* promoter (**A** and **B**), upstream GAA (**C** and **D**) and downstream GAA (**E** and **F**) regions of Y47 (black columns), YG8 (light grey columns) and YG22 (dark grey columns) transgenic mouse brain and heart tissues. In each case for the *FXN* promoter and upstream GAA regions, the mean percentage value (+SEM) of methylated CpG sites is shown as determined from the analysis of 7–12 independent cloned DNA sequences from each of 3–4 mice per group. For the downstream region the percentages of methylated CpG sites have been determined from one Y47, YG8 and YG22 mouse (12 independent cloned DNA sequences analysed for each). Only eleven CpG sites are represented for the promoter region, as sites 11–22 and 24–59 did not show any methylation in either FRDA or unaffected samples in brain or heart. Y47 brain tissues did not show any DNA methylation at CpG site 23, while YG22 heart tissues did not show any DNA methylation at any CpG site within the promoter region.

However, there are also some specific differences, which may result from epigenetic-control or transcriptional-control variations between the human and the mouse that will require further investigation.

DNA methylation profiles of the upstream GAA region in *FXN* human and transgenic mouse cerebellar tissues are comparable and more severely altered than in other brain tissue

To investigate potential variation within distinct regions of the brain we further analysed the DNA methylation profiles within the upstream GAA region of cerebellar tissue from one FRDA patient compared with an unaffected control and two individual mice from each of the YG8 and YG22 lines compared with the Y47 control line. We chose to investigate the cerebellum because this structure is known to be involved in FRDA pathology (10) and we ourselves have observed increased GAA repeat instability primarily within the cerebellum of both human FRDA patient and FRDA transgenic mouse tissues (3,5,25). The results (shown in Fig. 7) reveal similar DNA methylation changes to those observed in both human and mouse brain tissues. However, the degree of hypermethylation change in the GAA repeat expansion-containing human and

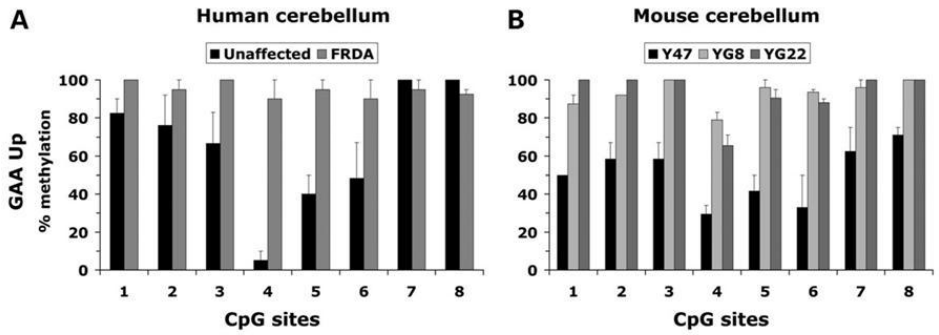

Figure 7. DNA methylation analysis of the upstream GAA regions of human (**A**) and transgenic mouse (**B**) cerebellar tissue. (A) In each case the mean percentage (+ SEM) of methylated CpG sites is shown as determined from the analysis of two FRDA patients (black columns) and two unaffected individuals (grey columns) with 10 independent cloned DNA sequences analysed for each. (B) Y47 (11 GAA) (black columns), YG8 (190+90 GAA) (light grey columns) and YG22 (190 GAA) (dark grey columns) transgenic mouse brain and heart tissues. In each case the mean percentage value (+SEM) of methylated CpG sites is shown as determined from the analysis of 7–12 independent cloned DNA sequences from each of two mice per group.

mouse cerebellar tissue is more severe, particularly at CpG sites 4, 5 and 6, compared with that seen in the brain tissues as a whole (Fig. 7A compared with Fig. 3C, and Fig. 7B compared with Fig. 6C). We have previously shown that frataxin expression in cerebellar tissue is reduced at both mRNA and protein levels compared with brain and brain stem tissue in our *FXN* transgenic mice (26). Therefore, the DNA hypermethylation patterns that we have now observed concur with the hypothesis that the upstream GAA region (CpG sites 4–6 in particular) is somehow involved in down-regulation of frataxin transcription.

Histone modifications of *FXN* transgenic mouse brain tissue are comparable with histone modifications of human tissue

Acetylated histone H3 and H4 and di- and tri-methylated histone H3K9 modifications were detected by ChIP analysis of the three regions of the *FXN* transgene (Fig. 2) in brain tissue isolated from both YG8 and YG22 GAA repeat expansion-containing *FXN* YAC transgenic mice (26) and Y47 normal-sized GAA repeat-containing *FXN* YAC transgenic mice (27). Our results show overall GAA repeat-induced decreases in histone H3K9 acetylation and increases in H3K9 methylation for both YG8 and YG22 transgenic mice (Fig. 8), as we previously identified in human FRDA tissue (Fig. 4). However, the level of deacetylation in the transgenic mouse tissue was not as great as that seen in the human tissue, possibly as a consequence of the smaller transgenic GAA repeat expansion sizes (190+90 for YG8 mice and 190 for YG22 mice, compared with 750/650 and 700/700 for FRDA patients). Also, H4K16 acetylation is actually increased in all three *FXN* transgene regions of YG8 mouse tissue compared with Y47. Furthermore, H4K8 acetylation and H4K12 acetylation are increased in all three *FXN* transgene regions of YG22 mouse tissue compared with Y47, which is somewhat different to the finding in human tissues. The greatest consistent histone residue changes that we found between the non-GAA (Y47) and both of the GAA (YG8 and YG22) transgenic brain tissue samples were decreases in acetylated H3K9 and increases in di- and tri-methylated H3K9. The H4K12 residue also showed a significant degree of deacetylation, but only in the YG8 transgenic tissue. All of these major histone residue changes in mouse brain tissue reflect the GAA repeat-induced histone residue changes that we detected in human tissue. Furthermore, as with the human samples, we similarly identified a GAA repeat-induced gradient of decreased H3K9 acetylation in both YG8 and YG22 transgenic mouse tissues, with the highest comparative levels of acetylation in the *FXN* promoter and the lowest comparative levels in the downstream GAA region. The increases in H3K9 di- and tri-methylation were consistent throughout all of the three *FXN* gene regions in both YG8 and YG22 transgenic mice, once again agreeing with our findings in human FRDA tissue.

DISCUSSION

For the consideration of future FRDA therapy, it is first essential to understand the mechanism of GAA-induced inhibition of *FXN* gene transcription. Previous studies of FRDA have implicated epigenetic changes, including the detection of increased DNA methylation of specific CpG sites upstream of the GAA repeat and histone modifications in regions flanking the GAA repeat that are both consistent with transcription inhibition (23,24). However, no DNA or histone methylation changes have previously been identified in the *FXN* promoter or downstream GAA regions, and clinically relevant FRDA brain and heart tissues have not previously been investigated. Different trinucleotide repeat expansion mutations have been shown to induce *cis*-acting epigenetic changes in several other human disorders (28,29). Thus, DNA methylation of the CGG repeat upstream of the *FMR1* gene has been identified as a main epigenetic switch in Fragile X syndrome, with histone acetylation playing an ancillary role (30). Decreased Sp1 interaction associated with DNA hypermethylation upstream of the CTG repeat in the *DMPK* gene has also been reported for congenital myotonic dystrophy type 1 (29). Furthermore, both CTG and GAA repeat expansions have

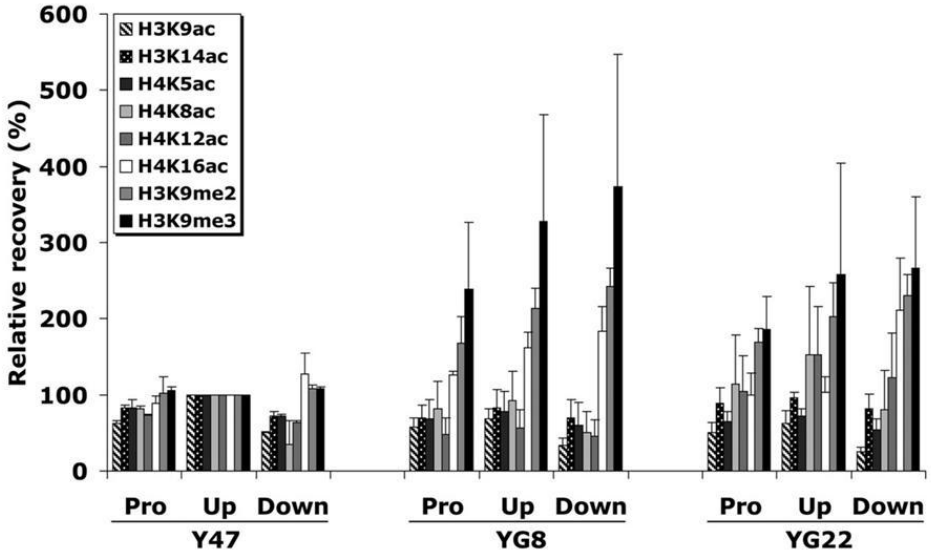

Figure 8. Analysis of histone modifications in transgenic mouse brain tissues. ChIP quantitative PCR results for the transgenic *FXN* promoter/exon1 (Pro), upstream GAA (Up) and downstream GAA (Down) amplified regions are represented as the relative amount of immunoprecipitated DNA compared with input DNA, having taken negligible −Ab control values into account. *FXN* values were normalized with mouse *GAPDH* and all values have been adjusted so that all of the upstream GAA values from the non-GAA transgenic mouse tissues (Y47) are 100%. In each case two individual ChIP samples were analysed in triplicate from each of two mice per group. The means and SEMs of these values are shown.

been shown to induce similar heterochromatin formation by position effect variegation studies of transgenic mice (21). However, it is still uncertain if different trinucleotide repeat sequences produce similar overall epigenetic effects or not.

Our investigations of the *FXN* gene in both FRDA human and transgenic mouse brain, cerebellum and heart tissues have now confirmed the presence of previously described DNA methylation changes (23) in the upstream GAA region of these clinically important tissues. Furthermore, our data have revealed an overall shift in the DNA methylation profile, moving from hypomethylation in the downstream GAA region towards hypermethylation in the upstream GAA region. This shift in DNA methylation profile could be explained by the known position of the GAA repeat within an Alu sequence, since Alu sequences have been shown to act as methylation centres leading to bi-directional spread of DNA methylation (31). Thus, the hypermethylation detected in the FRDA upstream GAA region may be due to the GAA repeat mutation enhancing the effect of a putative methylation centre at the 5′ end of the Alu sequence. At the same time, the addition of the GAA repeat sequence would put extra distance between the methylation centre at the 5′ end of the Alu sequence and the downstream GAA region. This may impede the spread of methylation to the downstream region when the distance is large enough (e.g. 2.25 kb for 750 human GAA repeats), but not when the distance is smaller (e.g. 600 bp for 190 transgenic mouse GAA repeats).

We have additionally identified differential DNA methylation at four specific CpG sites within the *FXN* promoter and exon 1 regions that have not previously been reported. The three CpG sites within the promoter region (sites 5, 7 and 8) are immediately upstream of the ATG translation start site, at nucleotide positions −27, −18 and −11, respectively. CpG sites 5 and 7 are also contained within Sp1 transcription factor binding sites (32). Interestingly, the region between −64 and the start of translation has previously been suggested to contain sequences important for positive regulation of frataxin production, although no candidate sequences were identified (33). Therefore, the three differentially methylated CpG sites that we have now uncovered in the *FXN* promoter, and in particular the two Sp1 recognition sites, are likely to represent these important regulatory sequences.

In comparison with other instances of trinucleotide repeat-induced DNA methylation changes that inhibit transcription (28,29), one would have predicted general hypermethylation to be associated with the FRDA GAA repeat expansion mutation. However, we actually identified three occurrences in human tissues (promoter and downstream GAA regions in brain, and downstream GAA region in heart) and one occurrence in mouse tissues (promoter region in heart) where there was in fact GAA repeat expansion-induced decrease in DNA methylation. This suggests the possible occurrence of demethylation and resultant active *FXN* gene expression, at least for some cells within the tissue. DNA demethylation has previously been shown to occur both passively due to DNA replication upon cell division (34) and actively in a process that may involve RNA (35), although the DNA demethylating activity has yet to be identified. DNA demethylation has also previously been associated with processes of DNA damage and repair. The formation of 8-OH-dG by oxidative DNA damage has been shown to affect the activity of human DNA methyltransferase and

inhibit CpG methylation (36), and DNA demethylation has also been shown to occur as a result of homologous recombination repair of DNA damaged by double-strand breaks (37). However, DNA demethylation has not previously been considered for FRDA. A close inspection of our data reveals that potential DNA demethylation in the *FXN* promoter region occurs when the degree of DNA hypermethylation change in the upstream GAA region is greatest. Therefore, we now propose that the shutdown of transcription due to major epigenetic changes at the upstream GAA region may result in attempts to upregulate *FXN* transcription by Sp1 binding and subsequent DNA demethylation in the promoter region. In support of this proposal, Sp1 binding is known to occur independent of CpG methylation status (32), but at the same time has been shown to inhibit CpG methylation (38). Furthermore, DNA demethylation has previously been shown to occur when there are few methylated CpG sites within a CpG island, but not when all of the CpG sites are methylated (39), which is exactly the situation that we find for the *FXN* promoter region. However, the GAA repeat expansion-induced decreases in DNA methylation at the *FXN* promoter are not consistent throughout all human and mouse brain and heart tissues, suggesting the involvement of other factors. Such factors may include differential susceptibility of the brain and heart tissues to DNA damage and/or GAA repeat instability. Indeed, FRDA is a disorder that is known to involve both oxidative DNA damage (40) and somatic instability of GAA repeats (3–5). Therefore, cells that are initially methylated at the *FXN* promoter region may lose this methylation as part of the GAA repeat instability process, wherein demethylation subsequent to DNA damage repair (37) may be selected for due to beneficial effect of *FXN* expression and hence cell viability. The GAA repeat expansion-induced decreases in DNA methylation that we have observed in the downstream GAA region of human tissues, but not transgenic mouse tissues, are more likely due to differently sized GAA repeats within the Alu sequence, as we have previously discussed. However, potential DNA demethylation in this downstream GAA region could also indirectly lead to an increase in *FXN* transcription due to the removal of inhibitory effects on RNA polymerase II elongation.

Our investigations of histone modifications within *FXN* gene in both FRDA human and transgenic mouse brain tissues have now confirmed the changes previously reported for H3K9 deacetylation in the *FXN* promoter, upstream GAA and downstream GAA regions and H3K9 methylation in the upstream GAA region (23,24). Furthermore, we have extended the H3K9 methylation analysis to include the *FXN* promoter and downstream GAA regions that to our knowledge have not previously been reported for any FRDA tissue. Our findings from both human and transgenic mouse tissues indicate significant H3K9 deacetylation, which becomes more severe upon progression from the *FXN* promoter, through the upstream GAA region to the downstream GAA region. This correlates well with the results for both di- and tri-methylation of H3K9, which show a generally similar gradient of progressive increase from the *FXN* promoter, through the upstream GAA region, to the downstream GAA region. The only exception is the very high level of di-methylated H3K9 in the upstream GAA region of human FRDA brain tissue, which is higher than that in the downstream GAA region. All of the H3K9 changes correlate well with the DNA methylation changes in both human and transgenic mouse brain tissues. Thus, the patterns of progressively increasing H3K9 deacetylation and increasing H3K9 di- and tri-methylation in transgenic mouse brain correspond exactly to the pattern of increasing DNA methylation. Similarly, the patterns of progressively increasing H3K9 deacetylation and increasing H3K9 tri-methylation in human FRDA brain with a peak of H3K9 di-methylation in the upstream GAA region equate very well to the corresponding DNA methylation profiles. Therefore, our combined data thus far indicate major roles for DNA methylation, histone H3K9 deacetylation and histone H3K9 methylation in the inhibition of *FXN* transcription in brain and heart tissues, with a less prominent role for deacetylation of other histone residues. The more severe epigenetic changes within the *FXN* intron 1 region compared with the promoter region support a hypothesis of transcription inhibition due to interference with elongation rather than initiation. Further work will be required to determine the exact relationships between DNA methylation, histone acetylation and methylation, heterochromatin formation and transcription inhibition. However, our results are consistent with the generally described pathway for gene inactivation wherein initial histone H3K9 deacetylation leads to H3K9 methylation, recruitment of HP1, histone deacetylases, DNA methyltransferases and eventual long-term shut down of transcription by DNA methylation (41). However, this situation is not likely to be universal for all trinucleotide repeat disorders, as highlighted by research on the *FMR1* gene which has shown both histone deacetylation and H3K9 methylation in the absence of DNA methylation without interfering in active gene transcription (42).

For now, the exact mechanism by which the GAA repeat mutation inhibits frataxin expression remains elusive. However, accumulating evidence, including the findings of this report, now highlights the importance of epigenetic changes that lead to heterochromatin formation. The epigenetic changes that we and others have now identified in FRDA do not in any way negate the importance of any abnormal DNA or DNA/RNA hybrid structures in the inhibition of frataxin expression, but rather suggest the involvement of several combined mechanisms. Indeed the existence of abnormal DNA structures may help to explain why the GAA repeat mutation induces epigenetic changes in the first place. Thus, there are reports that non-B DNA structures such as hairpins may induce DNA methylation (43,44), and GAA repeats have been shown to form hairpins (45). Alternatively, small double-stranded RNA (dsRNA) has also been shown to induce transcriptional gene silencing through a mechanism that involves DNA methylation (46,47). However, dsRNA has failed to induce DNA methylation in a study of mouse oocytes (48) and dsRNA targeted to the *HD* gene does not induce DNA methylation at the target huntingtin genomic locus in human cells (49). Thus, further studies are still required to identify any possible involvement of non-B DNA structures (such as GAA hairpins or triplex structures), DNA/RNA hybrids or dsRNA in the establishment of epigenetic changes and heterochromatin formation in FRDA.

In light of the epigenetic changes that we and others have identified in FRDA tissues and cells, several novel epigenetic-

based therapeutic approaches can now be considered for FRDA. First, HDAC inhibitors can be used, and indeed these have already shown considerable promise by increasing acetylation of histones and thereby increasing *FXN* transcription in FRDA cells (24). Secondly, pharmacological approaches could be taken to decrease H3K9 methylation, as have recently been described for the combined use of mithramycin and cystamine in Huntington disease mice (50). Thirdly, therapies to decrease DNA methylation should now be considered for FRDA, as have previously been tried for other trinucleotide repeat disorders. In particular, 5-azadeoxycytidine (5-azadC) has been shown to remove DNA methylation of the CCG repeat expansion, increase H3 and H4 acetylation, decrease H3K9 methylation, increase H3K4 methylation and reactivate the *FMR1* gene (30,51). Combined HDAC inhibitor and 5-azadC treatment has also been shown to synergistically increase *FMR1* gene activity (52). Finally, short dsRNA molecules complementary to promoter sequences have recently been shown to induce gene activation (53,54), and such approaches may also prove effective in increasing *FXN* transcription. Our identification of a transgenic FRDA mouse model that shows comparable epigenetic changes to those seen in FRDA patients will now provide a valuable resource in the study of all such epigenetic-based FRDA therapies.

MATERIALS AND METHODS

Tissues

Human brain, cerebellum and heart tissue samples were obtained from autopsies of two FRDA patients (750/650 and 700/700 GAA repeats) and two non-FRDA individuals, in accordance with UK Human Tissue Authority ethical guidelines. Mouse brain and heart tissues were dissected from our previously reported *FXN* YAC transgenic mouse models: Y47 (two copies of nine GAA repeats); YG8 (2 copies of 90 and 190 GAA repeats) and YG22 (1 copy of 190 GAA repeats) (25,27).

mRNA expression analysis

Total RNA was isolated from frozen tissues by homogenization with Trizol (Invitrogen) and cDNA was then prepared by using AMV Reverse transcriptase (Invitrogen) with oligo-dT primers. Levels of human or mouse transgenic *FXN* mRNA expression were assessed by quantitative RT–PCR using an ABI7400 sequencer and SYBR® Green (Applied Biosystems) with the following primers: FxnRTF 5′-CAGAGGAAACGCTGGAC TCT-3′ and FxnRTR 5′-AGCCAGATTTGCTTGTTTGGC-3′ (24). Human *GAPDH* or mouse *Gapdh* RT–PCR primers were used as control standards: human: GapdhhF 5′-GAAGG TGAAGGTCGGAGT-3′ and GapdhhR 5′-GAAGATGGTGA TGGGATTTC-3′ mouse GapdhmF 5′-ACCCAGAAGACTG TGGATGG-3′ and GapdhmR 5′-GGATGCAGGGATGAT GTTCT-3′.

Bisulfite sequencing

Genomic DNA was isolated from frozen tissue by standard phenol/chloroform extraction and ethanol precipitation. Two micrograms of genomic DNA was digested with *Eco*RI prior to bisulfite treatment using the CpGenome kit (Calbiochem). Nested PCR was carried out on bisulfite-treated DNA to amplify three regions of the *FXN* gene using the following primers: Pro 1st primer pair: SL1F1 5′-TAGTTTTTAA GTTTTTTTTGTTTAG-3′ and SL1R1 5′-CAAAACAAAAT ATCCCCTTTTC-3′; Pro 2nd primer pair: SL1F2 5′-GTTTT TTTATAGAAGAGTGTTTG-3′ and SL1R2 5′-CAAAAACC AATATAAATACAACC-3′; Up 1st primer pair: F1G 5′-GAG GGATTTGTTTGGGTAAAG-3′ and R1G 5′-ATACTAAAT TTCACCATATTAACC-3′; Up 2nd primer pair: F2G 5′-GA TTTGTTTGGGTAAAGGTTAG-3′ and R2G 5′-CTCCCAA AATACTAAAATTATAAAC-3′; Down 1st primer pair: NH1F 5′-AAGAAGAAGAAGAAAATAAAGAAAAG-3′ and SLGR2 5′-TCCTAAAAAAAATCTAAAAACCATC-3′; Down 2nd primer pair: NH2F 5′-AGAAGAAGAAAATAAA GAAAAGTTAG-3′ and SLGR1 5′-AAAACCATCATAAC CACACTTAC-3′. PCR products were then resolved on agarose gels, purified with Geneclean (BIO101) and cloned into pCR4.0 (Invitrogen) prior to DNA sequencing. A minimum of seven clones were sequenced for each tissue sample.

ChIP analysis

Histone modifications at the three *FXN* gene regions were detected by ChIP analysis of FRDA human and mouse tissues. This procedure involved initial cross-linking of DNA and protein by formaldehyde treatment of homogenized frozen tissue samples. DNA was then sheared by sonication, followed by immunoprecipitation with commercially available anti-histone and anti-acetylated histone H3 and H4 antibodies: H3K9ac, H3K14ac, H4K5ac, H4K8ac, H4K12ac, H4K16ac and H3K9me2 (Upstate), and H3K9me3 (Diagenode). For each experiment, normal rabbit serum (SIGMA) was used as a minus antibody immunoprecipitation control. After reversal of cross-linking, quantitative RT–PCR amplification of the resultant co-immunoprecipitated DNA was carried out with SYBR® Green in an ABI7400 sequencer (Applied Biosystems) using three sets of *FXN* primers (Pro, Up and Down) and human *GAPDH* control for the human samples as previously described (24). For the analysis of transgenic mouse samples, the same three sets of *FXN* primers were used together with the following mouse *Gapdh* control primers: GapdhMF, 5′-TGACAAGAGGGCGAGCG-3′ and GapdhMR, 5′-GGAAGCCGAAGTCAGGAAC-3′. Each tissue sample was subjected to two independent ChIP procedures, followed by triplicate quantitative PCR analysis.

Conflict of Interest statement. None declared.

FUNDING

This research has been supported by the Friedreich's Ataxia Research Alliance (FARA), the National Ataxia Foundation (NAF), Ataxia UK, GoFAR and the King Faisal Specialist Hospital and Research Center, KSA.

REFERENCES

1. Campuzano, V., Montermini, L., Molto, M.D., Pianese, L., Cossee, M., Cavalcanti, F., Monros, E., Rodius, F., Duclos, F., Monticelli, A. *et al.* (1996) Friedreich's ataxia: autosomal recessive disease caused by an intronic GAA triplet repeat expansion. *Science*, **271**, 1423–1427.
2. Pandolfo, M. (2002) The molecular basis of Friedreich ataxia. *Adv. Exp. Med. Biol.*, **516**, 99–118.
3. Clark, R.M., De Biase, I., Malykhina, A.P., Al-Mahdawi, S., Pook, M. and Bidichandani, S.I. (2006) The GAA triplet-repeat is unstable in the context of the human FXN locus and displays age-dependent expansions in cerebellum and DRG in a transgenic mouse model. *Hum. Genet*, **120**, 633–640.
4. De Biase, I., Rasmussen, A., Endres, D., Al-Mahdawi, S., Monticelli, A., Cocozza, S., Pook, M. and Bidichandani, S.I. (2007) Progressive GAA expansions in dorsal root ganglia of Friedreich's ataxia patients. *Ann. Neurol.*, **61**, 55–60.
5. De Biase, I., Rasmussen, A., Monticelli, A., Al-Mahdawi, S., Pook, M., Cocozza, S. and Bidichandani, S.I. (2007) Somatic instability of the expanded GAA triplet-repeat sequence in Friedreich ataxia progresses throughout life. *Genomics*, **90**, 1–5.
6. Campuzano, V., Montermini, L., Lutz, Y., Cova, L., Hindelang, C., Jiralerspong, S., Trottier, Y., Kish, S.J., Faucheux, B., Trouillas, P. *et al.* (1997) Frataxin is reduced in Friedreich ataxia patients and is associated with mitochondrial membranes. *Hum. Mol. Genet.*, **6**, 1771–1780.
7. Bulteau, A.L., O'Neill, H.A., Kennedy, M.C., Ikeda-Saito, M., Isaya, G. and Szweda, L.I. (2004) Frataxin acts as an iron chaperone protein to modulate mitochondrial aconitase activity. *Science*, **305**, 242–245.
8. Gerber, J., Muhlenhoff, U. and Lill, R. (2003) An interaction between frataxin and Isu1/Nfs1 that is crucial for Fe/S cluster synthesis on Isu1. *EMBO Rep.*, **4**, 906–911.
9. Yoon, T. and Cowan, J.A. (2004) Frataxin-mediated iron delivery to ferrochelatase in the final step of heme biosynthesis. *J. Biol. Chem.*, **279**, 25943–25946.
10. Koeppen, A.H., Michael, S.C., Knutson, M.D., Haile, D.J., Qian, J., Levi, S., Santambrogio, P., Garrick, M.D. and Lamarche, J.B. (2007) The dentate nucleus in Friedreich's ataxia: the role of iron-responsive proteins. *Acta. Neuropathol.*, **114**, 163–173.
11. Hart, P.E., Lodi, R., Rajagopalan, B., Bradley, J.L., Crilley, J.G., Turner, C., Blamire, A.M., Manners, D., Styles, P., Schapira, A.H. *et al.* (2005) Antioxidant treatment of patients with Friedreich ataxia: four-year follow-up. *Arch. Neurol.*, **62**, 621–626.
12. Mariotti, C., Solari, A., Torta, D., Marano, L., Fiorentini, C. and Di Donato, S. (2003) Idebenone treatment in Friedreich patients: one-year-long randomized placebo-controlled trial. *Neurology*, **60**, 1676–1679.
13. Richardson, D.R., Mouralian, C., Ponka, P. and Becker, E. (2001) Development of potential iron chelators for the treatment of Friedreich's ataxia: ligands that mobilize mitochondrial iron. *Biochim. Biophys. Acta.*, **1536**, 133–140.
14. Rustin, P., Rotig, A., Munnich, A. and Sidi, D. (2002) Heart hypertrophy and function are improved by idebenone in Friedreich's ataxia. *Free Radic. Res*, **36**, 467–469.
15. Schols, L., Vorgerd, M., Schillings, M., Skipka, G. and Zange, J. (2001) Idebenone in patients with Friedreich ataxia. *Neurosci. Lett*, **306**, 169–172.
16. Seznec, H., Simon, D., Monassier, L., Criqui-Filipe, P., Gansmuller, A., Rustin, P., Koenig, M. and Puccio, H. (2004) Idebenone delays the onset of cardiac functional alteration without correction of Fe-S enzymes deficit in a mouse model for Friedreich ataxia. *Hum. Mol. Genet*, **13**, 1017–1024.
17. Bidichandani, S.I., Ashizawa, T. and Patel, P.I. (1998) The GAA triplet-repeat expansion in Friedreich ataxia interferes with transcription and may be associated with an unusual DNA structure. *Am. J. Hum. Genet*, **62**, 111–121.
18. Grabczyk, E., Mancuso, M. and Sammarco, M.C. (2007) A persistent RNA·DNA hybrid formed by transcription of the Friedreich ataxia triplet repeat in live bacteria, and by T7 RNAP *in vitro*. *Nucleic Acids Res.*, **35**, 5351–5359.
19. Grabczyk, E. and Usdin, K. (2000) The GAA*TTC triplet repeat expanded in Friedreich's ataxia impedes transcription elongation by T7 RNA polymerase in a length and supercoil dependent manner. *Nucleic Acids Res.*, **28**, 2815–2822.
20. Sakamoto, N., Ohshima, K., Montermini, L., Pandolfo, M. and Wells, R.D. (2001) Sticky DNA, a self-associated complex formed at long GAA*TTC repeats in intron 1 of the frataxin gene, inhibits transcription. *J. Biol. Chem*, **276**, 27171–27177.
21. Saveliev, A., Everett, C., Sharpe, T., Webster, Z. and Festenstein, R. (2003) DNA triplet repeats mediate heterochromatin-protein-1-sensitive variegated gene silencing. *Nature*, **422**, 909–913.
22. Egger, G., Liang, G., Aparicio, A. and Jones, P.A. (2004) Epigenetics in human disease and prospects for epigenetic therapy. *Nature*, **429**, 457–463.
23. Greene, E., Mahishi, L., Entezam, A., Kumari, D. and Usdin, K. (2007) Repeat-induced epigenetic changes in intron 1 of the frataxin gene and its consequences in Friedreich ataxia. *Nucleic Acids Res.*, **35**, 3383–3390.
24. Herman, D., Jenssen, K., Burnett, R., Soragni, E., Perlman, S.L. and Gottesfeld, J.M. (2006) Histone deacetylase inhibitors reverse gene silencing in Friedreich's ataxia. *Nat. Chem. Biol.*, **2**, 551–558.
25. Al-Mahdawi, S., Pinto, R.M., Ruddle, P., Carroll, C., Webster, Z. and Pook, M. (2004) GAA repeat instability in Friedreich ataxia YAC transgenic mice. *Genomics*, **84**, 301–310.
26. Al-Mahdawi, S., Pinto, R.M., Varshney, D., Lawrence, L., Lowrie, M.B., Hughes, S., Webster, Z., Blake, J., Cooper, J.M., King, R. *et al.* (2006) GAA repeat expansion mutation mouse models of Friedreich ataxia exhibit oxidative stress leading to progressive neuronal and cardiac pathology. *Genomics*, **88**, 580–590.
27. Pook, M.A., Al-Mahdawi, S., Carroll, C.J., Cossee, M., Puccio, H., Lawrence, L., Clark, P., Lowrie, M.B., Bradley, J.L., Cooper, J.M. *et al.* (2001) Rescue of the Friedreich's ataxia knockout mouse by human YAC transgenesis. *Neurogenetics*, **3**, 185–193.
28. Greene, E., Handa, V., Kumari, D. and Usdin, K. (2003) Transcription defects induced by repeat expansion: fragile X syndrome, FRAXE mental retardation, progressive myoclonus epilepsy type 1, and Friedreich ataxia. *Cytogenet. Genome Res.*, **100**, 65–76.
29. Steinbach, P., Glaser, D., Vogel, W., Wolf, M. and Schwemmle, S. (1998) The DMPK gene of severely affected myotonic dystrophy patients is hypermethylated proximal to the largely expanded CTG repeat. *Am. J. Hum. Genet*, **62**, 278–285.
30. Tabolacci, E., Pietrobono, R., Moscato, U., Oostra, B.A., Chiurazzi, P. and Neri, G. (2005) Differential epigenetic modifications in the FMR1 gene of the fragile X syndrome after reactivating pharmacological treatments. *Eur. J. Hum. Genet*, **13**, 641–648.
31. Graff, J.R., Herman, J.G., Myohanen, S., Baylin, S.B. and Vertino, P.M. (1997) Mapping patterns of CpG island methylation in normal and neoplastic cells implicates both upstream and downstream regions in *de novo* methylation. *J. Biol. Chem*, **272**, 22322–22329.
32. Clark, S.J., Harrison, J. and Molloy, P.L. (1997) Sp1 binding is inhibited by (m)Cp(m)CpG methylation. *Gene*, **195**, 67–71.
33. Greene, E., Entezam, A., Kumari, D. and Usdin, K. (2005) Ancient repeated DNA elements and the regulation of the human frataxin promoter. *Genomics*, **85**, 221–230.
34. Matsuo, K., Silke, J., Georgiev, O., Marti, P., Giovannini, N. and Rungger, D. (1998) An embryonic demethylation mechanism involving binding of transcription factors to replicating DNA. *EMBO J.*, **17**, 1446–1453.
35. Weiss, A., Keshet, I., Razin, A. and Cedar, H. (1996) DNA demethylation in vitro: involvement of RNA. *Cell*, **86**, 709–718.
36. Turk, P.W., Laayoun, A., Smith, S.S. and Weitzman, S.A. (1995) DNA adduct 8-hydroxyl-2′-deoxyguanosine (8-hydroxyguanine) affects function of human DNA methyltransferase. *Carcinogenesis*, **16**, 1253–1255.
37. Cuozzo, C., Porcellini, A., Angrisano, T., Morano, A., Lee, B., Pardo, A.D., Messina, S., Iuliano, R., Fusco, A., Santillo, M.R. *et al.* (2007) DNA damage, homology-directed repair, and DNA methylation. *PLoS Genet.*, **3**, e110. First published on 22 May 2007, 10.1371/pgen.0030110.
38. Macleod, D., Charlton, J., Mullins, J. and Bird, A.P. (1994) Sp1 sites in the mouse aprt gene promoter are required to prevent methylation of the CpG island. *Genes. Dev*, **8**, 2282–2292.
39. Choi, Y.C. and Chae, C.B. (1993) Demethylation of somatic and testis-specific histone H2A and H2B genes in F9 embryonal carcinoma cells. *Mol. Cell. Biol.*, **13**, 5538–5548.
40. Schulz, J.B., Dehmer, T., Schols, L., Mende, H., Hardt, C., Vorgerd, M., Burk, K., Matson, W., Dichgans, J., Beal, M.F. *et al.* (2000) Oxidative stress in patients with Friedreich ataxia. *Neurology*, **55**, 1719–1721.

41. D'Alessio, A.C. and Szyf, M. (2006) Epigenetic tete-a-tete: the bilateral relationship between chromatin modifications and DNA methylation. *Biochem. Cell Biol.*, **84**, 463–476.
42. Pietrobono, R., Tabolacci, E., Zalfa, F., Zito, I., Terracciano, A., Moscato, U., Bagni, C., Oostra, B., Chiurazzi, P. and Neri, G. (2005) Molecular dissection of the events leading to inactivation of the FMR1 gene. *Hum. Mol. Genet*, **14**, 267–277.
43. Chen, X., Mariappan, S.V., Catasti, P., Ratliff, R., Moyzis, R.K., Laayoun, A., Smith, S.S., Bradbury, E.M. and Gupta, G. (1995) Hairpins are formed by the single DNA strands of the fragile X triplet repeats: structure and biological implications. *Proc. Natl Acad. Sci. USA*, **92**, 5199–5203.
44. Laayoun, A. and Smith, S.S. (1995) Methylation of slipped duplexes, snapbacks and cruciforms by human DNA(cytosine-5)methyltransferase. *Nucleic Acids Res.*, **23**, 1584–1589.
45. Heidenfelder, B.L., Makhov, A.M. and Topal, M.D. (2003) Hairpin formation in Friedreich's ataxia triplet repeat expansion. *J. Biol. Chem.*, **278**, 2425–2431.
46. Kawasaki, H. and Taira, K. (2004) Induction of DNA methylation and gene silencing by short interfering RNAs in human cells. *Nature*, **431**, 211–217.
47. Morris, K.V., Chan, S.W., Jacobsen, S.E. and Looney, D.J. (2004) Small interfering RNA-induced transcriptional gene silencing in human cells. *Science*, **305**, 1289–1292.
48. Svoboda, P., Stein, P., Filipowicz, W. and Schultz, R.M. (2004) Lack of homologous sequence-specific DNA methylation in response to stable dsRNA expression in mouse oocytes. *Nucleic Acids Res.*, **32**, 3601–3606.
49. Park, C.W., Chen, Z., Kren, B.T. and Steer, C.J. (2004) Double-stranded siRNA targeted to the huntingtin gene does not induce DNA methylation. *Biochem. Biophys. Res. Commun.*, **323**, 275–280.
50. Ryu, H., Lee, J., Hagerty, S.W., Soh, B.Y., McAlpin, S.E., Cormier, K.A., Smith, K.M. and Ferrante, R.J. (2006) ESET/SETDB1 gene expression and histone H3 (K9) trimethylation in Huntington's disease. *Proc. Natl Acad. Sci. USA*, **103**, 19176–19181.
51. Pietrobono, R., Pomponi, M.G., Tabolacci, E., Oostra, B., Chiurazzi, P. and Neri, G. (2002) Quantitative analysis of DNA demethylation and transcriptional reactivation of the FMR1 gene in fragile X cells treated with 5-azadeoxycytidine. *Nucleic Acids Res.*, **30**, 3278–3285.
52. Chiurazzi, P., Pomponi, M.G., Pietrobono, R., Bakker, C.E., Neri, G. and Oostra, B.A. (1999) Synergistic effect of histone hyperacetylation and DNA demethylation in the reactivation of the FMR1 gene. *Hum. Mol. Genet*, **8**, 2317–2323.
53. Janowski, B.A., Younger, S.T., Hardy, D.B., Ram, R., Huffman, K.E. and Corey, D.R. (2007) Activating gene expression in mammalian cells with promoter-targeted duplex RNAs. *Nat. Chem. Biol.*, **3**, 166–173.
54. Li, L.C., Okino, S.T., Zhao, H., Pookot, D., Place, R.F., Urakami, S., Enokida, H. and Dahiya, R. (2006) Small dsRNAs induce transcriptional activation in human cells. *Proc. Natl Acad. Sci. USA*, **103**, 17337–17342.

Appendix F – Posters presented

Cannabinoid therapeutic testing of a Friedreich ataxia mouse model

Ricardo Mouro Pinto, Sahar Al-Mahdawi, Mark Pook – Ataxia Research Group, CCCB/BICGP,
Division of Biosciences, School of Health Sciences & Social Care, Brunel University, Uxbridge, UK

Abstract

The potential neuroprotective effect of cannabinoids is being investigated in a Friedreich ataxia mouse model. Preliminary results from functional studies suggest that treatment with the cannabinoids CBD and THC does not improve the FRDA-like phenotype. However, histological and biochemical analysis are still needed to confirm if more subtle effects are present.

Friedreich ataxia (FRDA) [1]

FRDA is a rare, genetic, neurodegenerative, life-shortening disorder. It is the most common of the hereditary ataxias in the UK with an estimated prevalence of 1-2 in 50,000. Typically the disease manifests around puberty.

Symptoms:

- muscle weakness and loss of coordination (ataxia)
- vision impairment, hearing loss, and slurred speech
- skeletal abnormalities (scoliosis, pes cavus)
- increased risk of diabetes
- serious heart condition (cardiomyopathy)

Genetics: [2]

- mode of inheritance is autosomal recessive
- the gene (*FXN*) encodes a protein called frataxin
- most common genetic mutation (98%) is the unstable hyperexpansion of a GAA triplet repeat in the first intron of the *FXN* gene
- results in a deficiency of mitochondrial frataxin

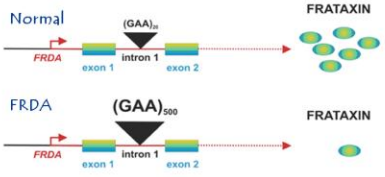

Pathogenesis and therapy: [2]

Reduced levels of frataxin result in mitochondrial dysfunction. There is currently no effective treatment for FRDA. The growing understanding of the role of frataxin and the disease pathogenesis has led to the consideration of 4 primary potential therapeutic targets.

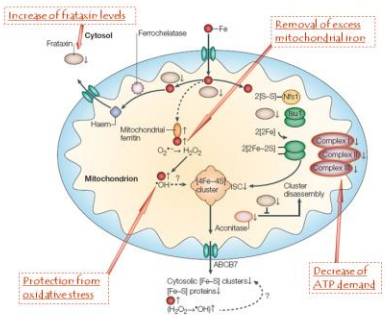

Cannabinoids as potential therapeutics for FRDA:

Cannabinoids are a group of compounds present in Cannabis (*Cannabis sativa L*). The cannabinoids Cannabidiol (CBD) and Δ^9-tetrahydrocannabinol (THC) have antioxidant activity, indicating that they may be effective in preventing and/or treating the development of FRDA.

FRDA mouse model [3]

- Human *FXN* transgene containing the GAA expansion mutation, in a null background
- 2 lines: Yg8 (GAA_{190+90}) & Yg22 (GAA_{190})
- Mild FRDA-like pathological phenotype:
  - decreased levels of frataxin
  - mild oxidative stress
  - progressive coordination defect
  - histological abnormalities in the dorsal root ganglia (DRG) (A) and heart (B)

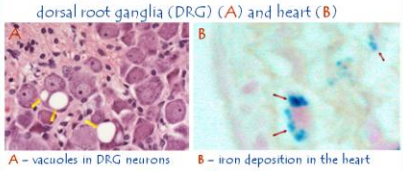

A – vacuoles in DRG neurons B – iron deposition in the heart

Aim of study

Examine the potential neuroprotective effects of the cannabinoids CBD and THC in FRDA by performing drug trials on the FRDA mouse model available.

Cannabinoid therapeutic testing

Dose* (mg/kg)	Period (months)	Drug	Number of mice used		
			Wt	Yg8	Yg22
10	6-9	Placebo	6	5	6
		CBD	6	6	5
20	3-6	Placebo	19	18	10
		CBD	9	10	10
		CBD:THC	10	11	-

*Intraperitoneal dose administered twice weekly

Key indicators being investigated:

- Functional studies
  - weight measurement
  - coordination analysis
  - locomotor activity analysis
- Histological analysis of DRG sections
- Biochemical analysis in various tissues
  - oxidative stress
  - aconitase activity
  - mitochondrial respiratory chain complexes activity

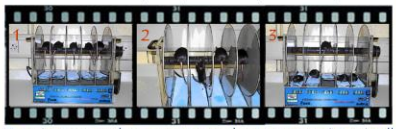

Coordination analysis using an accelerating rotarod treadmill apparatus. The time taken for each mouse to fall is recorded.

Preliminary results

So far, only functional studies have been performed:

- 10 and 20 mg/kg CBD treatment (6-9 and 3-6 months of age, respectively) appears to have no beneficial nor detrimental effects;
- 20 mg/kg CBD:THC treatment (3-6 months of age) not only seems to cause a subtle decrease in weight, as well as having an apparent detrimental effect on rotarod performance and locomotor activity, in both wild type and Yg8 rescue mice.

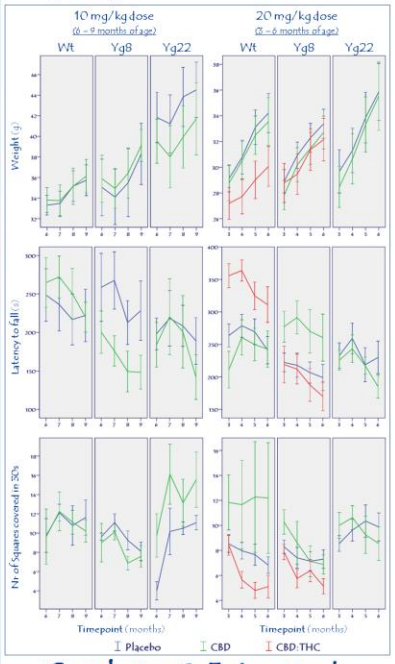

Conclusion & Future work

To this point, based on functional studies, none of the three cannabinoid treatment regimes show any overt beneficial effect on the FRDA mice. In fact, only detrimental effects seem to be detected with the CBD:THC treatment in both wild type and FRDA mice. Nevertheless, it is still necessary to examine potential histological and biochemical alterations.

Alternative therapeutic agents are also being considered for future drug trials, namely the antioxidant CTMIO and a class of histone deacetylase inhibitors.

Brunel UNIVERSITY WEST LONDON

Acknowledgments:

- This study is sponsored by Ataxia UK
- CBD and THC provided by GW Pharmaceuticals

References:

1. Pandolfo, M. (2002) *Adv Exp Med Biol* 516: 99-118
2. Gatchel, J.R. and Zoghbi, H.I. (2005) *Nat Rev Genet* 6(10): 743-55
3. Al-Mahdawi, S. *et al* (2006) *Genomics* 88: 580-590

Poster presented at the 57th ASHG Annual Meeting (2007), San Diego, USA

Analysis of CTCF binding to the *FXN* gene in Friedreich ataxia

Ricardo Mouro Pinto, Chiranjeevi Sandi, Sahar Al-Mahdawi and Mark Pook – Hereditary Ataxia Research Group, CCCB/BICGP, Division of Biosciences, School of Health Sciences & Social Care, Brunel University, Uxbridge, UK

Abstract

Recent findings suggest a heterochromatin-mediated silencing of the *FXN* gene in Friedreich ataxia. CTCF is a well reported DNA insulator and recent findings implicate CTCF in instability of trinucleotide repeat tracts. In this study we propose that CTCF may play a role in FRDA, since CTCF sites identified in the *FXN* gene have reduced levels of CTCF in FRDA.

Friedreich ataxia (FRDA) [1]

FRDA is a rare, genetic, neurodegenerative, life-shortening disorder, typically manifesting around puberty, with an estimated prevalence of 1 in 50,000.

Main symptoms:

- muscle weakness and loss of coordination (ataxia);
- vision impairment, hearing loss, and slurred speech;
- skeletal abnormalities and cardiomyopathy

Genetic features: [2]

- mode of inheritance is autosomal recessive
- the gene (*FXN*) encodes a protein called frataxin
- most common genetic mutation (98%) is the unstable hyperexpansion of a GAA triplet repeat in the first intron of the *FXN* gene
- results in a deficiency of mitochondrial frataxin:

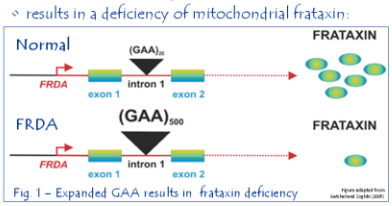

Fig. 1 – Expanded GAA results in frataxin deficiency

Mechanisms for reduced frataxin expression in FRDA: [3]

- GAA repeats are susceptible to forming triplexes, with inhibitory effects on transcription.
- Recent evidence suggests that GAA repeat expansions produce a heterochromatin-mediated silencing effect: [4]

↓ H3 & H4 acetylation	Up- and downstream of GAA
↑ H3K9 di- & trimethylation	
↑ DNA methylation	Upstream of GAA

Fig. 2 – Heterochromatin mediated silencing in FRDA

CCCTC-binding factor (CTCF) [5]

- CTCF is a DNA insulator, being therefore able to modulate gene expression:
  - Enhancer blocking activity
  - Heterochromatin barrier activity
- CTCF binding has also been shown to flank trinucleotide repeat tracts at various disease loci and has been specifically implicated in *cis*-regulation of CAG repeat instability in SCA7 mice, where loss of CTCF binding promoted repeat instability.

Hypothesis

CTCF binding may affect *FXN* gene expression and/or GAA repeat instability in FRDA.

Aim of study

- Identify potential CTCF binding sites in the *FXN* gene
- Investigate if the levels of CTCF bound to these sites differed in normal sized vs expanded GAA *FXN* genes.

Methods

- Identification of potential CTCF binding sites in *FXN*:
  - a 3kb region of the *FXN* gene (70840164 to 70843163, NC_000009, GI: 89161216), spanning the entire 5' UTR, exon 1 and some of intron 1 including the GAA repeat (Fig. 3), was screened *in silico* [6] for potential CTCF binding sites. 3 *FXN* regions were identified: *FXN* 5' UTR; upstream and downstream of the GAA repeat.

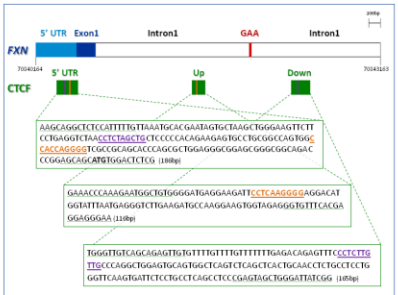

Fig. 3 – Diagram of *FXN* region screened *in silico* and putative CTCF binding sites identified (sense and anti-sense). The *FXN* regions analysed by EMSA and ChIP are also shown (green) along with the respective sequences (including primer sequences).

- Electrophoretic Mobility Shift Assay (EMSA) [7]
  - PCR products from the 3 *FXN* sites (Fig. 3) and from a previously identified human CTCF-binding site in *H19* [8] were gene cleaned and γ-^{32}P 5' end-labeled. Binding reactions were performed using recombinant full length CTCF (Abnova). 'Supershift' assays were performed by adding to the binding reaction an anti-CTCF antibody (Upstate). Reaction mixtures with a final volume of 10µl were incubated for 30-45mins at RT and then analyzed by 5% nondenaturing PAGE.
- Chromatin immunoprecipitation (ChIP) [4]
  - CTCF levels were investigated by ChIP in the 3 *FXN* sites using human cerebellum tissues from 3 normal and 3 FRDA individuals. Immunoprecipitation was carried out using an anti-CTCF antibody (Upstate). For each experiment, normal rabbit serum (SIGMA) was used as a 'minus antibody' immunoprecipitation control. Relative quantitative PCR amplification was carried out with SYBR® Green in an AB17400 sequencer (Applied Biosystems). CTCF values were normalised to input and minus antibody samples, and finally determined in relation to a control region in the human *H19* gene [8], previously identified as a CTCF binding site.

Results

- 4 candidate CTCF binding sites were detected *in silico* in 3 regions of the *FXN* gene (Fig. 3): 5' UTR, upstream and downstream of the GAA repeat.
- EMSA confirms binding of CTCF to the 5' UTR region, but fails to identify CTCF binding to both regions analysed up- and downstream of the repeat:

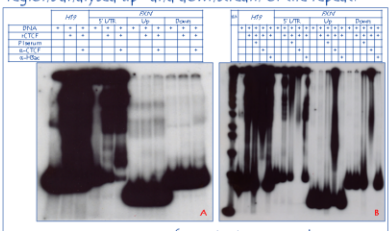

Fig. 4 – EMSA investigation of CTCF binding sites in the *FXN* gene. In gel A the α-CTCF was added 10mins after binding was initiated, while in gel B it was present in the reaction from the start.

- ChIP analysis has shown CTCF enrichment at all *FXN* sites investigated (Fig. 5 A) and after normalisation to *H19* a trend was observed, towards lower CTCF levels present in FRDA samples (Fig. 5 B & C):

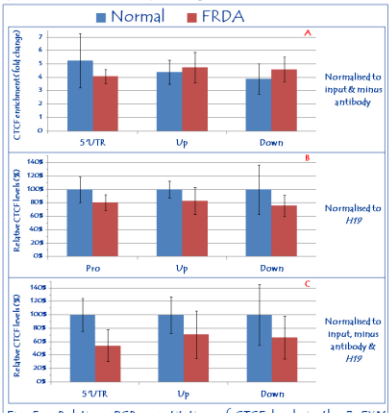

Fig. 5 – Relative qPCR quantitation of CTCF levels in the 3 *FXN* regions, of normal and FRDA human cerebellum, by ChIP analysis.

Conclusion

Thus far, our findings suggest that CTCF may play a role in the development of FRDA, by exposing the FXN gene to heterochromatin formation, and may also explain the age-related somatic instability of expanded GAA repeat tracts, which is prominent in FRDA brain, and especially cerebellum, tissues.

Brunel UNIVERSITY WEST LONDON

Acknowledgments:

- Ataxia UK
- FARA
- GoFAR
- MDA (USA)

References:

1. Pandolfo, M. (2002) *Adv Exp Med Biol* **516**: 99-118
2. Gatchel, J.R. and Zoghbi, H.I. (2005) *Nat Rev Genet* **6**(10): 743-55
3. Festenstein, R. (2006) *Nat Chem Biology* **2**: 512 – 513
4. Al-Mahdawi, S. *et al* (2008) *Hum Molec Genet* **17**(5): 735-746
5. Libby, R.T. *et al* (2008) *PLoS Genet* **4**(11)
6. http://www.essex.ac.uk/bs/molonc/spa.htm
7. Filippova, G.N. *et al* (2001) *Nat Genet* **28**: 335-343
8. Burke, L.J. *et al* (2005) *EMBO J.* **24**(18): 3291-300

Poster presented at the 6th International Conference on Unstable Microsatellites and Human Disease (2009), Guanacaste, Costa Rica